

DISS. ETH NO. 25434

***Modelling Microbial Life
in Unsaturated Soil under Spatial Gradients***

A thesis submitted to attain the degree of
DOCTOR OF SCIENCES of ETH ZURICH

(Dr. sc. ETH Zurich)

presented by

MINSU KIM

*MSc in Physics
Seoul National University
MSc in Complex Systems Science
Erasmus Mundus degree of
University of Gothenburg and University of Warwick*

born on 10.06.1984

citizen of Republic of Korea

accepted on the recommendation of

Prof. Dr. Dani Or, ETH Zurich

Dr. Osnat Gillor, Ben Gurion University of the Negev, IL

Prof. Dr. Jan van der Meer, University of Lausanne

2018

DOCTORAL THESIS

**Modelling Microbial Life in Unsaturated Soil under
Spatial Gradients**

Author:
Minsu KIM

Supervisor:
Prof. Dr. Dani OR

Soil and Terrestrial Environmental Physics (STEP)
Department of Environmental Systems Science (USYS)
ETH Zürich

Abstract

Doctor of Sciences of ETH Zurich (Dr. sc. ETH Zurich)

Modelling Microbial Life in Unsaturated Soil under Spatial Gradients

by Minsu KIM

Microbial activity in soil plays an important role in a wide range of ecosystem services ranging from nutrient cycling to nitrogen fixation and degradation of pollutants. Despite their importance, a quantitative description of microbial processes in soil remains lacking due to soil structural complexity, dynamic changes in nutrient composition and availability, and remarkable adaptation of microbial communities to spatially and temporally varying environments at all scales. The study developed a mechanistic model for microbial life in soil-like domains that aims to disentangle physical, chemical, and microbiological interactions and provides new insights into ecological functionality. A spatially-resolved model of microbial dynamics is developed on abstracted rough soil surfaces. The idealised representation preserves the salient features of soil micro-hydrology and supports upscaling of diffusion supported trophic interactions and biogeochemical fluxes. A key feature in the modelling framework is the coupling of individual-based representations of microbial cells inhabiting heterogeneous soil domains where effects of spatial heterogeneity, dynamic environmental conditions and spatial gradients of moisture and temperature affect microbial community interactions. The modelling framework was applied to ecological questions such as quantifying the spatial self-organisation of multi-taxa community under various hydration conditions, predicting soil microbial diversity dynamics in response to sudden wetting and drying, and estimating rates of carbon and nitrogen cycling performed by microbial communities. The spatial scalability of the model provides the means to consider nuanced interactions between climates, soil and microbial communities under a range of conditions. The modelling framework was extended to representing biological soil crusts (biocrusts) in arid regions where sharp near-surface gradients of temperature, light, and nutrient shape the spatial distribution of microorganisms and biogeochemical functioning of these important desert ecosystems. The study elucidated microbial community organisation in biocrusts, and its feedback on modifying physical and chemical properties and biologically produced gas emission dynamics. The findings from the mechanistic model highlight the importance of processes at the microscale in affecting globally relevant biogeochemical fluxes, specifically, biotic-abiotic interactions and emissions of reactive gases (e.g. HONO and NH₃) from soil systems. The model provides an important building block towards advancing predictive capabilities for biocrusts functions; the insights enhance understanding of large-scale carbon and nitrogen cycles from near-surface processes and their potential responses to changing climate.

Zusammenfassung

Doktor der Naturwissenschaften ETH Zürich (Dr. sc. ETH Zürich)

Modellierung des mikrobiellen Lebens in ungesättigtem Boden unter Einwirkung räumlicher Gradienten

von Minsu KIM

Mikrobielle Aktivität spielt eine wichtige Rolle für eine Vielzahl von Ökosystemdienstleistungen, vom Nährstoffkreislauf wie die Fixierung von Stickstoff bis zum Abbau von Schadstoffen. Trotz ihrer Wichtigkeit fehlt eine quantitative Beschreibung von mikrobiellen Prozessen im Boden auf Grund der Komplexität der Bodenstruktur, der Dynamik von Nährstoffzusammensetzung und Verfügbarkeit, sowie der ausserordentlichen Anpassungsfähigkeit der mikrobiellen Gemeinschaft in einer räumlich und zeitlich variablen Umwelt über alle Skalen hinweg. In dieser Studie wurde ein mechanistisches Modell für mikrobielles Leben in bodenartigen Domänen entwickelt, um physikalische und chemische Prozesse von mikrobiellen Interaktionen zu trennen und neue Einsichten in die ökologische Funktionalität zu geben. Das räumlich aufgelöste Modell der mikrobiellen Dynamik basiert auf einer abstrakten Repräsentation rauer Bodenoberflächen. Die idealisierte Repräsentation konserviert die hervorstechenden Eigenschaften der Mikrohydrologie und ermöglicht die Hochskalierung von auf der Diffusion basierenden trophischen Interaktionen und biogeochemischen Zyklen. Eine grundlegende Eigenschaft der Modellstruktur ist die Verkoppelung einer individuenbasierten Repräsentation der mikrobiellen Zellen, welche eine heterogene Bodendomäne bewohnen, in welcher Effekte der räumlichen Heterogenität, dynamische Umweltbedingungen und räumliche Gradienten von Bodenfeuchte und Temperatur die Interaktionen in der mikrobiellen Gemeinschaft beeinflussen. Das Modell wurde auf ökologische Fragestellungen wie die Quantifizierung der räumlichen Selbstorganisation einer mikrobiellen Gemeinschaft bestehend aus einer Vielzahl von Taxa unter variablen hydrologischen Bedingungen angewandt und sagt die Dynamik der bodenmikrobiellen Diversität als Konsequenz eines plötzlichen Benetzungs-Trockenheitszyklus, sowie die Raten des Kohlenstoff- und Stickstoffkreislaufs, voraus. Die räumliche Skalierbarkeit des Modells ermöglicht die Berücksichtigung nuancierter Interaktionen zwischen Klima, Boden und mikrobiellen Gemeinschaften für eine Vielzahl an Bedingungen. Das Rahmenkonzept wurde erweitert,

um bi-ologische Bodenkrusten in ariden Gebieten darzustellen, wo starke Gradienten von Tem-peratur, Licht und Nährstoffen in Nähe der Bodenoberfläche die räumliche Verteilung der Mikroorganismen und biogeochemischen Funktionen dieser wichtigen Wüstenökosysteme bestimmt. Diese Studie verdeutlicht die Organisation der mikrobiellen Gemeinschaft in bi-ologischen Bodenkrusten und deren Rückkopplung auf die Modifikation von physikalis-chen und chemischen Eigenschaften, welche die Dynamik der Produktion biologischer Gasem-misionen bestimmen. Die Ergebnisse des mechanistischen Modells heben die Wichtigkeit von kleinskaligen Prozessen und deren Einfluss auf global relevante biochemische Stoff-flüsse, mit Augenmerk auf biotisch-abiotische Interaktionen und Emissionen reaktiver Gase (z.b. HONO und NH_3) aus Bodensystemen, hervor. Das Modell stellt einen wesentlichen Baustein dar, um Funktionen der biologischen Bodenkrusten vorherzusagen. Diese Ein-sichten verbessern das Verständnis von grossskaligen Kohlen- und Stickstoffzyklen in Bodenoberflächennähe und deren potentiellen Reaktionen auf klimatische Veränderung.

Acknowledgements

It has been a very long time since I have been dreaming of this moment and it is about to happen. During my stay in Switzerland, I have met many nice people who directly and indirectly helped and encouraged me to continue/complete my PhD.

I must start this acknowledgement by mentioning Prof. Dr. Dani Or. I am grateful to Dani, who has provided me generous support for my doctoral study. His guidance with immense knowledge on soil and his patience helped me to overcome numerous obstacles I have been facing through my research. Indeed, it was sometimes difficult and frustrating, but very very special. I am deeply grateful to Dani for allowing me to work with him and giving me a chance to learn from him.

Besides my advisor, I would like to thank my thesis committee members: Prof. Dr. Jan van der Meer and Dr. Osnat Gillor, for accepting to participate the committee after all years of rescheduling the defense and for providing me valuable comments and questions.

As a PhD student, I had a lot to learn from other researchers, Dr. Olga Ilie, Dr. Iso Christl, Prof. Dr. Martin Schroth, and Michi Simmler, who provided me, the chemistry-newbie, essential insights on soil chemistry. Dr. Bettina Weber from Max Planck Institute also provided me helpful discussion regarding processes in biocrusts together with HONO emission dataset from her work.

I would like to thank all my colleagues and friends in STEP. Dr. Peter Lehmann, Dr. Andreas Papritz, Dr. Stanislaus Schymanski, Dr. Gang Wang, and Dr. Robin Tecon were always kind to answer my scientific questions. Dani Breitenstein was the most important person in my laboratory life, who could literally solve any technical issues during my experiments. I cannot imagine my model scripts running and providing valid results without having the strong IT support by Daniel Baumann and Madlene Nussbaum. My work was discussed with members of SoilBugs, Ali Ebrahimi, Hannah Kleyer, Benedict Borer, and Sami Ben Said. Learning from Siul Ruiz, Frouke Hoogland, Linfeng Fan, Milad Aminzadeh, Erfan Haghighi, Jonas von Rütte, Gernot Michlmayr, and Franziska Möbius about their research on soil at different scales was always fun. Dr. Leonardo Ramirez-Lopez, Dr. Liliana Montano Herrera, Sabine Dürig, and Hans Wunderli also should be mentioned.

I am grateful for my siblings, Minju, Minie, Minsung, and my parents, Chongkyu and Sangrye, who have provided me emotional support throughout my life. I am also grateful for my new family members, Flurina, Christoph, and Irene, who encouraged me to finish the final work of this PhD thesis.

Finally, there is Sāmi Bickel, my colleague, my friend, and my family, my all-time-stimulant to enthusiastic debates and discussion about scientific and non-scientific topics from microbial life in earth to our lives on the Earth. In the end, we even have made the decision to continue these activities and fun in the rest of our life resulting this thesis and our baby Lia at the same time.

Sam, we have a lot more fun things to do together! Are you ready?

Zurich, 2019

Minsu Kim

Contents

Abstract	iii
Zusammenfassung	vi
Acknowledgements	vii
1 Introduction	1
1.1 Microbial life and function in soil	1
1.2 Mechanistic modelling of microbial life in unsaturated soils	3
1.3 Organisation of this thesis	5
2 Rough Surface Patch Model	11
2.1 Introduction	11
2.2 Representing soil rough surfaces	12
2.2.1 A patch	12
2.2.2 Diffusion process on rough surface domain	17
2.3 Microbial growth on rough surfaces	17
2.4 Hydration and fragmentation of aqueous habitats	19
2.4.1 Chemotactic microbial locomotion on rough surfaces.	20
2.4.2 Fragmentation of aquatic habitats on surfaces	21
2.5 Results	22
2.5.1 Effective water film thickness of rough surfaces	22
2.5.2 Microbial cell mean flagellated propulsion speed	23
2.5.3 Microbial dispersion rates	25
2.6 Discussion	28
3 Microbial Interactions on Soil Rough Surfaces	35
3.1 Introduction	35
3.2 Methods: Rough Surface Patch Model (RSPM) with multiple species	35
3.2.1 Assigning different “species” within the reaction diffusion equation	35
3.2.2 Assigning trophic interactions among multiple species	37
3.2.3 Measures of microbial diversity	37
3.2.4 Sporulation and germination processes in IBM	38
3.3 Results	39
3.3.1 Microbial community trophic interactions	39
3.3.2 Hydration effects on microbial diversity and onset of coexistence	43
3.3.3 Surface roughness (texture) effects on microbial diversity	44

3.3.4	Microbial diversity dynamics during a hydration event	46
3.4	Discussion	47
4	Microbial Community Response to Hydration-Desiccation Cycles in Desert Soil	55
4.1	Introduction	55
4.2	Methods and Materials	57
4.2.1	Soil-sampling scheme	57
4.2.2	RNA extraction and reverse transcription	57
4.2.3	Quantitative PCR (qPCR)	58
4.2.4	Taxonomic analysis	58
4.2.5	Non-metric multidimensional scaling	58
4.2.6	Modelling microbial growth on hydrated surfaces	58
4.2.7	Measuring microbial diversity	60
4.3	Results	61
4.3.1	Community composition changes during a rainfall event: Field obser- vations	61
4.3.2	Community diversity metrics during a rainfall event: Field observations	62
4.3.3	Microbial community dynamics during a rainfall event: model predic- tions	64
4.4	Discussion	64
5	Hydration Status and Diurnal Trophic Interactions Shape Microbial Community Function in Desert Biocrusts	73
5.1	Introduction	73
5.2	A mechanistic model of desert biocrusts	75
5.2.1	The biocrust physical domain	75
5.2.2	Environmental boundary conditions	78
	Light irradiance on the surface	78
	Temperature dynamics	79
5.2.3	Biocrust biogeochemical processes: mass transfer/inorganic C and N partitioning	79
	Gas diffusion with the biocrust	79
	Mass transfer between gas and liquid	80
	Dissociation of chemical substances	81
5.2.4	Microbial community in desert biocrust ecosystem	82
	Microbial community and trophic interactions	82
	Temperature-dependent microbial growth	83
	pH feedback	85
	Microbial growth rates	85
5.2.5	Microbial EPS production	86
	EPS production and transport properties	86
5.2.6	Diffusion reaction equation at the biocrust scale	87
5.2.7	Evaluation of the proposed mechanistic Desert Biocrust Model (DBM)	88

5.2.8	Physical domain and boundary conditions for nutrients	88
5.3	Results	89
5.3.1	Steady state of geochemical traits within the biocrust (no biological activity)	89
5.3.2	Microbial activity effects on the biocrust chemical environment	90
5.3.3	Vertical stratification of microbial functional groups	92
5.3.4	Fully saturated biocrusts: comparing model predictions with observations	94
5.3.5	Diurnal cycles of gaseous efflux from saturated biocrusts	94
5.4	Discussion	97
5.4.1	Spatial and temporal variations in local pH within unsaturated biocrusts	97
5.4.2	Microbial community stratification within biocrusts	98
5.4.3	Complex trophic interactions of microbial community within biocrusts	99
5.4.4	Gaseous efflux from desert biocrusts	100
5.4.5	Assumptions and limitations of the desert biocrust model (DBM) . . .	100
5.5	Summary and conclusions	102
6	The Role of Localised pH on HONO and NH₃ Emissions from Drying Soils and Biocrusts	111
6.1	Introduction	111
6.2	Results and Discussion	114
6.2.1	Soil hydration represented by water contents and water film thickness distributions	114
6.2.2	Time scales of physicochemical processes in unsaturated soils	114
6.2.3	Mean soil pH vs. local aqueous film pH	116
6.2.4	Spatially resolved pH measurements of drying soils	117
6.2.5	Predicting emissions dynamics from drying biocrusts	117
6.2.6	HONO and NH ₃ emissions under different desiccation rates and atmospheric ammonia levels	120
6.3	Methods and Materials	121
6.3.1	The desert biocrust mathematical model	121
6.3.2	Experimental setup for localised pH	121
7	Conclusions and outlook	129
7.1	Summary and concluding remarks	129
7.2	Outlook for future research	131
A	Individual-Based Model of Microbial Life on Hydrated Rough Soil Surfaces	139
A.1	A patch	139
A.2	The effective water film thickness and the degree of saturation	140
A.3	Connectivity of within patch aqueous habitats.	142
A.4	Diffusion process on rough surface patch model	143
A.5	Microbial growth	145

A.5.1	Metabolism	145
A.5.2	Cell division.	146
A.5.3	Death.	146
A.6	Swimming speed.	146
A.7	Chemotactic Motion.	147
A.8	Parameters used for physical domain	151
A.9	Parameters used for IBM	152
A.10	Parameters used for diversity dynamics	153
B	Microbial Community Response to Hydration-Desiccation Cycles	157
B.1	Average water contents	157
B.2	Chemical analysis of the soil samples	158
B.3	Statistical analysis of the soil chemical composition	159
B.4	Used primers	161
B.5	MiSeq sequencing analysis	161
B.6	Average qPCR counts of rRNA units	162
B.7	Analysis of similarity (ANOSIM) test.	163
B.8	Richness and evenness per category	164
C	The Model of Microbial Life under Hdration-Desiccation Cycles	167
C.1	Aqueous phase and gas phase in the physical domain	167
C.2	Parameters used to generate roughness domain for the modified RSPM.	170
C.3	Diffusion processes through the profile	170
C.4	Environmental conditions: temperature	171
C.5	Individual based description of microbial growth on the heterogeneous domain	172
C.6	Temperature dependent microbial growth	175
C.7	Active cells and potentially active cells before and after wetting event	177
D	Hydration Status and Diurnal Trophic Interactions Shape	
	Microbial Community Function in Desert Biocrusts	181
D.1	Biocrust temperature distribution and dynamics	181
D.2	Modelling of chemical reactions within biocrusts	181
D.3	Activity of photoautotrophs	186
D.3.1	Photosynthesis and dark respiration	186
D.3.2	Nitrogen fixation and dynamic yields	186
D.3.3	EPS production	190
D.4	Stoichiometry and rates of biological processes	191
D.5	Overview of parameters used in this study	196
D.6	Simulated chemical environment of a fully saturated biocrusts	200
E	Mechanistic Model of Biocrusts under Dynamic Hydration Conditions	205
E.1	Mechanistic model of biological soil crusts	205
E.1.1	Diffusion processes in the model domain	205

E.1.2	A set of chemical reactions between gas and liquid phases	206
	Gas-liquid partitioning under Henry's law	206
	Acid-base model and local pH determination	207
	Analytic solution of local pH under Henry's and acid-base equilibria .	208
E.1.3	Estimation of gaseous efflux	208
E.2	pH measurements of drying soils	210
E.2.1	Experimental set-up	210
	Use of a planar optode and a microelectrode	210
	Sample preparation	210
	Control of the composition of gas phase	210
	Monitoring hydration conditions	210
E.3	Supplementary figures	211

List of Figures

2.1	A conceptual diagram of the definition of a patch.	13
2.2	A comparison of effective water film thickness distribution between smooth and rough surface domain.	16
2.3	The effective water film thickness of the rough surface domain as a single patch for different hydration conditions	23
2.4	Microbial locomotion in rough surface patch model	24
2.5	Microbial dispersion on rough surfaces	26
2.6	Colony expansion rate	28
3.1	Scheme of the individual-based modelling (IBM)	40
3.2	Examples of spatial patterns arising from different microbial consortia on rough surfaces for different hydration conditions	42
3.3	Microbial population diversity and coexistence index (CI)	45
3.4	Roughness effects on microbial population diversity for different hydration conditions	46
3.5	Microbial diversity dynamics during a wetting-drying cycle	48
4.1	Microbial community response to a hydration cycle	62
4.2	Microbial diversity dynamics during a hydration cycle	63
4.3	Model prediction: effect of hydration dynamics on the soil microbial community	65
5.1	A schematic of the physical domain and environmental conditions of the desert biocrust model (DBM).	77
5.2	Key microbial functional groups and biogeochemical interactions within the desert biocrust model.	84
5.3	Aqueous-phase distribution affects diffusion pathways and geochemical conditions (no biological activity)	90
5.4	Diurnal distributions of chemical constituents in the desert biocrust.	91
5.5	Diurnal shifts in microbial activity and spatial distributions in desert biocrusts	93
5.6	Diurnal variations in microbial activity within saturated biocrusts.	95
5.7	Oxygen and pH profiles within saturated biocrusts.	96
5.8	Gas effluxes from saturated biocrusts.	97
6.1	A schematic of HONO and NH ₃ emissions caused by biotic and abiotic factors in an unsaturated soil/desert biocrust	112
6.2	Changes in abiotic conditions while drying soils in the model	115

6.3	Changes in pH under wet-dry cycles are monitored with a planar optode and a microelectrode	118
6.4	Direct measurement of pH localisation and dynamics during desiccation of quartz sand of different textures under different atmospheric pCO ₂ levels . .	119
6.5	Dynamic processes during biocrust desiccation as predicted by the desert biocrusts model (DBM)	123
6.6	HONO and NH ₃ gaseous emissions during biocrust drying	124
7.1	Separating abiotic contributions from CO ₂ efflux measured from biological crusts.	133
7.2	Diurnal dynamics of CO ₂ and HONO	134
7.3	Interplay between CO ₂ and HONO on microbially mediated surfaces	136
A.1	Effects of surface tension on effective water film thickness	142
A.2	A schematic diagram of flux calculation	144
A.3	A diagram for microbial locomotion	150
B.1	Average water contents	157
B.2	Chemical analysis of the soil samples from the field	159
B.3	Linear model fit of chemical parameters	160
B.4	qPCR	162
B.5	Analysis of similarity (ANOSIM) test	163
B.6	Comparison of the richness and evenness	164
C.1	The abstract physical domain in the modified RSPM	168
C.2	Dynamics of temperature profile	173
C.3	A schematic of the soil profile domain	174
D.1	Activity of photoautotrophs	187
D.2	Modelling the relation of nitrogen fixation and photosynthesis	189
D.3	Modelled EPS production under various hydration conditions and its role on diffusion processes	191
D.4	Diurnal distributions of chemical constituents in the unsaturated biocrust . .	201
E.1	Analytic solutions of pH	209
E.2	An example of the physical domain and the scheme for local pH calculation .	211
E.3	HONO and NH ₃ emissions from simulated desiccation of biocrusts under various conditions	212
E.4	Vertical patterns of pH changes observed using a planar optode	213

List of Tables

5.1	A summary of the desert biocrust model (DBM)	76
A.1	Parameters for rough surface domain	151
A.2	Parameters for Individual Based Modelling (IBM)	152
A.3	Parameters for individual-based modelling (IBM) in diversity dynamics	153
B.1	Primes Targeting 16S rRNA	161
C.1	Parameters for the extended RSPM	170
C.2	Parameters for individual-based modelling (IBM) for aerobic and anaerobic species	176
C.3	Parameters for temperature dependent growth	177
D.1	Henry's law constants of gaseous elements and partial pressures in the atmosphere	182
D.2	Acid-base reactions in the desert biocrust model	184
D.3	Stoichiometry and kinetics of chemical reactions	184
D.4	Acid dissociation constants	185
D.5	Stoichiometry of microbial reactions	193
D.6	Monod coefficients for growth rates	194
D.7	Microbial growth rate of functional groups	195
D.8	Overview of control parameters	197
D.9	Overview of parameters (1)	198
D.9	Overview of parameters (2)	199

To Moggie.

Chapter 1

Introduction

1.1 Microbial life and function in soil

Soil microbial processes drive some of the most globally significant biogeochemical cycles (carbon, nitrogen), affect key nutrient cycling in soils including emissions of green house gases and trace reactive gases, purification of water, and contribute to a range of other ecosystem services (Lawton, 1994; Houghton, 2007; Falkowski, Fenchel, and Delong, 2008; Bardgett, Freeman, and Ostle, 2008; Graham et al., 2012; Ferrenberg, Reed, and Belnap, 2015). These essential functions for life on Earth rely on highly abundant and diverse microorganisms in soil. Advances in molecular biology enabled quantification of this unparalleled diversity of microbial life making soil the most biologically active compartment of the biosphere (Whitman, Coleman, and Wiebe, 1998; Horner-Devine, Carney, and Bohannan, 2004; Gans, Wolinsky, and Dunbar, 2005; Elsas, Jansson, and Trevors, 2006; Roesch et al., 2007; Quince, Curtis, and Sloan, 2008). The complex soil matrix supports and maintains this immense microbial diversity within physically and chemically distinctive microhabitats that are in constant state of change (Young and Ritz, 1998; Ranjard and Richaume, 2001; Torsvik and Øvreås, 2002; Curtis and Sloan, 2004; Becker et al., 2006; Or et al., 2007; Holden, Ritz, Young, et al., 2011; Crawford et al., 2012).

Advances in molecular techniques are not yet mirrored in similar progress in quantitative description of the interactions between microbial life and the physical and chemical soil environment. An important obstacle to mechanistic representation is the disparity in scales of microbial processes from the level of interacting cells (at pores and surfaces of soil grains) and the scale of ecologically relevant processes (soil profile to landscapes) (Manzoni and Porporato, 2009; Vereecken et al., 2016; Li et al., 2017). Field scale studies of soil microbial ecology have focused on disentangling complex processes and often rely on empirical relations between microbial activity and various provisional and regulatory services (Costanza et al., 1998; Jeffery et al., 2010; Tikhonovich and Provorov, 2011; Garbisu, Alkorta, and Epelde, 2011; Bardgett, Freeman, and Ostle, 2008; Graham et al., 2012). Based on these empirical relations, it has been argued that it is possible to represent soil microbial functions at the ecosystem scale without the need to consider fine details of microbial interactions at the micro scale (Andrén, Brussaard, and Clarholm, 1999). However, the rapid advances in metagenomics tools and technological advances in imaging (e.g., micro-computed tomography, nuclear magnetic resonance, nano-secondary ion mass spectrometry, etc.) have

revealed the critical importance of microenvironment in shaping microbial diversity, activity, and functioning within the complex soil structure (Grundmann et al., 2001; Young et al., 2008; Holden, Ritz, Young, et al., 2011; Vos et al., 2013; Ebrahimi and Or, 2018). Physical and chemical conditions that affect microbial cells may vary drastically from pore to pore at micro-metric scales (Grundmann and Debouzie, 2000; Ruamps, Nunan, and Chenu, 2011; Raynaud and Nunan, 2014) suggesting that, firstly, the high microbial diversity is supported by distinctive niches in soil microstructures and, secondly, process representation at these scales has a pivotal role for quantifying fluxes and processes that manifest at larger scales (Ebrahimi and Or, 2017; Ebrahimi and Or, 2018).

Advances in molecular-genetic based methods and rapid expansion in identification of microbial taxa enable us to gain knowledge on vast diversity of microorganisms in soil (e.g., a teaspoon of soil, almost $\sim 10^9$ cells (genomes) with $\sim 10^{12}$ genes of about $\sim 10^4$ OTUs can be found) (Torsvik and Øvreås, 2002; Roesch et al., 2007). Furthermore, advances in sequencing technology (metagenomics and transcriptomics) enable characterisation of microbial community composition and in some cases present state of function based on the relative abundance of genes and their expression (Sharon and Banfield, 2013). This provides the relative activity of certain enzymes to others therefore indicates the potential functions performed by the community. However, these approaches are instrumental in quantifying soil diversity and functions and population dynamics of active organisms, and their application to resolving ecological questions have been limited (Griffiths et al., 2003; Vogel et al., 2003; Vogel et al., 2009; Bell et al., 2009; Delmont et al., 2012; Prosser, 2015).

A major obstacle to the effective utilisation of these genetic-based methods remains the dearth of quantitative frameworks for systematic interpretation of microbial interactions in their natural (albeit complex) soil environmental conditions (Prosser et al., 2007; Or et al., 2007; Tecon and Or, 2017). This has been summarized in Prosser, 2015 call for bridging the gap between genetic information and ecological functionality and the call for increasing the use of quantitative frameworks. Considering the dynamic and harsh conditions in soil, gene expression may be inhibited in the prevailing environmental conditions, such as limited water availability, temperature, pH, and substrate concentrations. This suggests that observations on spatial distribution of microorganisms and relevant substrates are necessary to delineate microbial activity together. Therefore, to link the metagenomics to ecosystem function or soil characteristics, improved mechanistic understandings of soil microenvironment and its spatio-temporal dynamics is of the essence.

Direct observation of microbial processes within the opaque soil matrix remains challenging with present methods (O'Donnell et al., 2007). There are several approaches to understand the physical, chemical properties in spatial context, such as the dissection of a single aggregate (Grundmann et al., 2001) and micro-computed tomography (μ CT) to configure water and gas distribution in a sample (Sammartino, Michel, and Capowiez, 2012) followed up with chemical analysis using ion-selective electrodes (for describing microenvironment without microbial activity) (Amman, 1988; Pedersen, Smets, and Dechesne, 2015). Some other methods attempt of visualising soils at micro-scale together with individual bacterial

cells using Electro-dispersive X-ray spectroscopy (EDS), atomic force microscopy (AFM), infrared spectroscopy (IRS), or Nano-secondary ion mass spectroscopy (NanoSIMS). One of the most promising recent development might be the application of NanoSIMS and Raman microspectroscopy to observe the *in situ* activity at the single cell level (of targeted groups) in soils (Eichorst et al., 2015). These methods are helpful to investigate the role of soil structure at microscale and sporadic distribution of microbial cells and their activity. However, most of cases are invasive and lacks the capability for temporal aspects of microbial activity in unsaturated soils.

The natural heterogeneity of soil pore matrix or surface roughness on grains implies the sparsely distributed microbial colonies in unsaturated soils as distribution of water is limited to the corners or cracks (Or and Tuller, 2000). Otherwise, water is absorbed onto the solid rough surfaces indicating the configuration of water film should govern the microbial interaction in unsaturated soils (Or et al., 2007; Tecon and Or, 2017). Furthermore, a mechanistic model of water configuration benefits to investigate temporal aspect of microbial life in soils as hydration condition in soil is in constant change. Some controlled experiments have attempted to study microbial life in soil pores using unsaturated porous ceramic surfaces (Dechesne et al., 2008; Tecon and Or, 2016; Kleyer, Tecon, and Or, 2017) or micro-fluidic pore networks to observe growth of microorganisms at small scales (Dai et al., 2013; Borer, Tecon, and Or, 2018), nevertheless, definitive studies of microbial function in real soil and their small scale biogeography remain challenging.

1.2 Mechanistic modelling of microbial life in unsaturated soils

Modelling tools could bridge gaps in present experimental limitations and quantitative description of microbial activity within soil. Various mechanistic modelling approaches have been proposed for spatio-temporal representation of microbial life including Individual Based Models (IBM), Lattice Boltzmann methods (LBM), and hybrid models such as IBM implemented within pore network models or on patchy surfaces (O'Donnell et al., 2007). In the context of microbial life in unsaturated soils, some modelling approaches have been used to elucidate relations between small-scale physical environments and roles of soil microbial communities in terrestrial ecosystems (Wang and Or, 2010; Long and Or, 2007; Ebrahimi and Or, 2014; Ebrahimi and Or, 2015; Ebrahimi and Or, 2017). These studies provided new insights into environmental factors, especially hydration conditions, that limit and promote soil bacterial life in an abstracted soil structure at very small scale (a few mm). The study presented in this thesis inherits and shares some of objectives and methodologies with the previous studies and extends the description further to possibilities of scaling-up to macroscopic systems that consider hydration, temperature and other gradients that shape natural populations (surface crusts, sharp fronts, etc.).

The mathematical modelling of microorganisms in soil is particularly challenging compared to other systems such as waste water treatment, lakes, sediments or other aqueous systems. This is due to the complex physical structure of soil pore spaces and dynamic processes under unsaturated conditions. As a complex porous medium, solid, liquid, and

gas phases coexist in soils and their distribution and connectivity are determined by constituting soil grains that are highly irregular in their sizes, shapes, and packing. Therefore, an abstract representation of soil domain is a prerequisite for modelling with the possible scalability before introducing biological or chemical processes. Continuum media models or pore-network models are common examples of such abstraction. Continuum representation of soil is useful for some application due to simple parameterisation and analytical tractability. However, such description may not be valid at small scales (smaller than the REV), thus it often applies to large domains (metre scale). Pore networks have been used to represent soil transport processes. They have the scale advantage and could be generalised based on universality principles of percolation theory (Berkowitz and Ewing, 1998; Hunt and Ewing, 2009; Manzoni et al., 2014). However, benefits of universality principles are bounded only to description of physical domain and microbial or chemical processes are not subjected to this scalability. Therefore, a numerical framework is required for connecting two scales of relevance to microbial activity and interaction (10^{-6} - 10^{-3} m) and measurable functionality of these processes (10^{-2} - 10^{-1} m). Furthermore, highly heterogeneous and dynamic nature of processes occurring in soil and the strong coupling between abiotic and biotic factors add challenges in many mathematical models (continuum and pore networks) due to the dynamic modification of the local environment which cannot be captured in static pictures.

To overcome modelling challenges while preserving cell-level description of microbial activity and their functions in soils, a model framework is proposed and presented in this thesis. In the proposed model, microbial life is described in a simple soil surface domain with an abstracted version of the real geometry. The abstracted soil domain of rough surfaces and simple soil pore spaces capture the micro-hydrology relevant to microbial life (Long and Or, 2007; Kim and Or, 2016). Unlike the previous approach (Long and Or, 2007) that uses an empirical relation for the hydration conditions, the model in this work describes the hydration conditions of rough surfaces depending on the energy state of water (matric potential) by implementing abstract geometry of roughness elements, that can retain water. This allows to investigate temporal aspects of soil hydration that shapes dynamics of physical, chemical, microbiological processes. The physical domain analogously represent a vertical cross-section of near surface soil layers (and biocrusts) including water/gas configuration, their influence on the microbial activity, and chemical environment at small scales. A key feature of the model is to link hydration conditions at sub-millimetre scales as local water film thickness, which governs the microbial activity, and at sample scales (soil representative volumes at sub-metre scales), which is measurable macroscopically as water contents.

To describe microbial activity on rough surfaces, Individual based model (IBM) was chosen to simulate individual cells throughout this study. IBM approach explicitly follows each individual, a single cell, with entities of interests such as size, biomass, age, growth property, and life history etc. (For the detailed reviews on this modelling approach, see Ferrer, Prats, and López, 2008 and Hellweger et al., 2016). This approach differs to population-based dynamics as it treats individual cells as discrete quantity. Therefore, it has a merit

to describe differences among individuals within a population growing in structured environments. Furthermore, a broad range of interaction patterns (competitive, mutualistic, or parasitic interactions) or adaptive processes under spatio-temporally varying environments can be also investigated by using IBM. In this work, employing IBM is especially beneficial because of the temporal aspect of the study, such as exploring dynamic response of microbial communities to a sudden wetting and changes in microbial activity under sharp gradients of hydration, light, and temperature within drying soils at near-surfaces. This integrated model of abstract soil hydrated surfaces and individual based model shows the emergence of their functionality as a community exhibiting a full-scale ecological system connecting the activity of an individual cell to its contribution to biogeochemical cycles.

1.3 Organisation of this thesis

This thesis focuses on the mechanistic model of microbial life in unsaturated soils and its applicability for soil microbial ecology. Especially, the role of water configuration on physical structures of unsaturated soil is the main interest of this study to address ecological questions in various environmental conditions. The modelling framework aimed at encompassing the description of soil microbial life and its functioning at difference scales and providing predictions of macroscopically observable measures, such as colony expansion rate, bacterial diversity dynamics, spatial distribution of chemical substances over the soil depth (yet centi-metric scale), and gaseous efflux driven by microbial activity. Microbial dynamics in desert soils and biological soil crusts (biocrusts) in arid lands were considered as example ecosystems for the model applications because of the minimal impacts of other organisms, such as plants, and strong influence of physical/chemical properties of unsaturated soils on microbial activity. Furthermore, the model was accustomed to resolve temporal dynamics under extreme environments, such as a sudden water availability from a natural rain event, high temperature variances in desert soils, and the resulting spatial gradient of hydration, substrate distribution, and temperature over the depth. Detailed description of the model and results for the model applications are provided in this thesis, organised with the following chapters:

To model microbial life in heterogeneous soils under various hydration conditions, firstly a spatial element of a rough soil surface was depicted as a collection of patches with different roughness properties. In Chapter 2, a detailed description of hydrated rough surface patch model is given. The model allows to calculate a micro-hydrological measure, the effective water film thickness, which directly affects the microbial life by altering their flagellar motility, aqueous habitat connectivity, and diffusion of substrates. On this abstract domain of rough soil surfaces, microbial growth was introduced by using the Individual Based Model (IBM) to investigate their behaviour on the hydrated rough surfaces (The chapter is partially excerpted from Kim and Or, 2016).

To address some questions of soil microbial ecology, in Chapter 3, the model was used to demonstrate multi-species/nutrient dynamics on unsaturated soil rough surfaces. Various forms of trophic dependencies (competition, mutualism) were applied in the model and the

model simulations exhibited spontaneous formations of microbial community patterns. In addition, soil microbial diversity metrics under various hydration conditions were investigated by using the capability of the model to represent many interacting species. The result highlights that hydration conditions on the rough surface regulates the degree of microbial interaction, thus alter the microbial diversity regardless of the simplest assumption made for the microbial community (species differences were only based on growth rate and substrate affinity) (The chapter is also partially excerpted from Kim and Or, 2016).

The rough surface patch model was extended to a vertical cross-section of soil domain to capture microbial life at the gas and liquid interface, which distinguishes soil from other aquatic ecosystems. The mass transfer from gas to liquid phase was introduced by combining gas percolation and Henry's law. By doing this, the surface model allows the other mode of transport of the gaseous substrate through the depth, such as oxygen, for aerobic microorganisms. The extended model was applied to predict the microbial community response to hydration-desiccation cycles in desert soil (Chapter 4). The model predicts the changes in liquid and gas phase configurations, which shape microbial community composition and diversity during and after a rain event. The decrease in diversity and the significant change in community composition were in agreement with field data. The results give an emphasis on the critical role for the fragmented aqueous habitat in maintaining microbial diversity dynamics (The chapter is published in Šťovíček et al., 2017).

In Chapter 5, the model was further developed for biological soil crusts (biocrusts) in arid land as a real ecological system. For not only qualitative but also quantitative comparisons, the modelling attempts of describing the functioning of microbial consortia within biocrusts. Especially, as an ecologically functioning unit, a simple microbial community of four essential groups was designed for carbon and nitrogen cycling; diazotrophic photoautotrophs, aerobic heterotrophs, anaerobic heterotrophs, and chemoautotrophs (nitrifiers). Together with various environmental factors, chemical processes for carbon and nitrogen compounds highlights the importance of mechanistic understanding of the microbial ecology within biocrusts (The chapter is published in Kim and Or, 2017.).

In Chapter 6, the desert biocrust model was applied to investigate the gaseous emission during drying soils/biocrusts. Especially, the roles of hydration dynamics and spatial heterogeneity of soil surfaces were evaluated to see emissions of pH related gaseous like nitrous acid (HONO) and ammonia (NH₃). This study reveals microscale processes of localised pH decrease during desiccation amplified by nitrification processes performed by microorganisms. The results highlight the power of mechanistic modelling to bridge micro-macro scales (The chapter is taken from Kim and Or, 2018).

The main results and conclusions are summarised in Chapter 7. From drawn conclusions, moreover, some potential extension and future directions are suggested accounting possible applications for the global model of large-scale carbon and nitrogen cycles and its response to changing climate.

References

- Amman, Daniel (1988). *Ion-selective micro-electrodes*. Springer Berlin.
- Andrén, Olof, Lijbert Brussaard, and Marianne Clarholm (1999). "Soil organism influence on ecosystem-level processes—bypassing the ecological hierarchy?" In: *Applied Soil Ecology* 11.2, pp. 177–188.
- Bardgett, Richard D, Chris Freeman, and Nicholas J Ostle (2008). "Microbial contributions to climate change through carbon cycle feedbacks". In: *The ISME Journal* 2.8, pp. 805–814.
- Becker, Joanna M et al. (2006). "Bacterial activity, community structure, and centimeter-scale spatial heterogeneity in contaminated soil". In: *Microbial Ecology* 51.2, pp. 220–231.
- Bell, Colin W et al. (2009). "Linking microbial community structure and function to seasonal differences in soil moisture and temperature in a Chihuahuan desert grassland". In: *Microbial Ecology* 58.4, pp. 827–842.
- Berkowitz, B. and R.P. Ewing (1998). "Percolation theory and network modeling applications in soil physics". In: *Surveys in Geophysics* 19.1, pp. 23–72.
- Borer, Benedict, Robin Tecon, and Dani Or (2018). "Spatial organization of bacterial populations in response to oxygen and carbon counter-gradients in pore networks". In: *Nature communications* 9.1, p. 769.
- Costanza, Robert et al. (1998). "The value of the world's ecosystem services and natural capital". In: *Nature* 387, pp. 253–260.
- Crawford, J.W. et al. (2012). "Microbial diversity affects self-organization of the soil–microbe system with consequences for function". In: *Journal of The Royal Society Interface* 9.71, pp. 1302–1310.
- Curtis, Thomas P and William T Sloan (2004). "Prokaryotic diversity and its limits: Microbial community structure in nature and implications for microbial ecology". In: *Current Opinion in Microbiology* 7.3, pp. 221–226.
- Dai, Jing et al. (2013). "Charting microbial phenotypes in multiplex nanoliter batch bioreactors". In: *Analytical chemistry* 85.12, pp. 5892–5899.
- Dechesne, Arnaud et al. (2008). "The porous surface model, a novel experimental system for online quantitative observation of microbial processes under unsaturated conditions". In: *Applied and Environmental Microbiology* 74.16, pp. 5195–5200.
- Delmont, Tom O et al. (2012). "Structure, fluctuation and magnitude of a natural grassland soil metagenome". In: *The ISME Journal* 6.9, pp. 1677–1687.
- Ebrahimi, Ali and Dani Or (2015). "Hydration and diffusion processes shape microbial community organization and function in model soil aggregates". In: *Water Resources Research*.
- (2017). "Mechanistic modeling of microbial interactions at pore to profile scale resolve methane emission dynamics from permafrost soil". In: *Journal of Geophysical Research: Biogeosciences* 122.5, pp. 1216–1238.
- (2018). "Dynamics of soil biogeochemical gas emissions shaped by remolded aggregate sizes and carbon configurations under hydration cycles". In: *Global change biology* 24.1, e378–e392.

- Ebrahimi, Ali N and Dani Or (2014). "Microbial dispersal in unsaturated porous media: Characteristics of motile bacterial cell motions in unsaturated angular pore networks". In: *Water Resources Research* 50.9, pp. 7406–7429.
- Eichorst, Stephanie A et al. (2015). "Advancements in the application of NanoSIMS and Raman microspectroscopy to investigate the activity of microbial cells in soils". In: *FEMS microbiology ecology* 91.10, fiv106.
- Elsas, Jan Dirk van, Janet K Jansson, and Jack T Trevors (2006). *Modern soil microbiology*. CRC Press.
- Falkowski, Paul G, Tom Fenchel, and Edward F Delong (2008). "The microbial engines that drive Earth's biogeochemical cycles". In: *Science* 320.5879, pp. 1034–1039.
- Ferrenberg, Scott, Sasha C Reed, and Jayne Belnap (2015). "Climate change and physical disturbance cause similar community shifts in biological soil crusts". In: *Proceedings of the National Academy of Sciences* 112.39, pp. 12116–12121.
- Ferrer, Jordi, Clara Prats, and Daniel López (2008). "Individual-based modelling: an essential tool for microbiology". In: *Journal of Biological Physics* 34.1-2, pp. 19–37.
- Gans, Jason, Murray Wolinsky, and John Dunbar (2005). "Computational improvements reveal great bacterial diversity and high metal toxicity in soil". In: *Science* 309.5739, pp. 1387–1390.
- Garbisu, Carlos, Itziar Alkorta, and Lur Epelde (2011). "Assessment of soil quality using microbial properties and attributes of ecological relevance". In: *Applied Soil Ecology* 49, pp. 1–4.
- Graham, David E et al. (2012). "Microbes in thawing permafrost: the unknown variable in the climate change equation". In: *The ISME Journal* 6.4, pp. 709–712.
- Griffiths, Robert I et al. (2003). "Influence of depth and sampling time on bacterial community structure in an upland grassland soil". In: *FEMS Microbiology Ecology* 43.1, pp. 35–43.
- Grundmann, GL and D Debouzie (2000). "Geostatistical analysis of the distribution of NH_4^+ and NO_2^- -oxidizing bacteria and serotypes at the millimeter scale along a soil transect". In: *FEMS Microbiology Ecology* 34.1, pp. 57–62.
- Grundmann, GL et al. (2001). "Spatial modeling of nitrifier microhabitats in soil". In: *Soil Science Society of America Journal* 65.6, pp. 1709–1716.
- Hellweger, Ferdi L et al. (2016). "Advancing microbial sciences by individual-based modelling". In: *Nature Reviews Microbiology*.
- Holden, P.A., K. Ritz, I. Young, et al. (2011). "How do the microhabitats framed by soil structure impact soil bacteria and the processes that they regulate?" In: *The Architecture and Biology of Soils: Life in Inner Space*, p. 118.
- Horner-Devine, M Claire, Karen M Carney, and Brendan JM Bohannon (2004). "An ecological perspective on bacterial biodiversity". In: *Proceedings of the Royal Society of London. Series B: Biological Sciences* 271.1535, pp. 113–122.
- Houghton, RA (2007). "Balancing the global carbon budget". In: *Annual Review of Earth and Planetary Sciences* 35, pp. 313–347.

- Hunt, Allen and Robert Ewing (2009). *Percolation theory for flow in porous media*. Vol. 771. Springer.
- Jeffery, Simon et al. (2010). *European atlas of soil biodiversity*. European Commission.
- Kim, Minsu and Dani Or (2016). "Individual-based model of microbial life on hydrated rough soil surfaces". In: *PLoS ONE* 11.1, e0147394.
- (2017). "Hydration status and diurnal trophic interactions shape microbial community function in desert biocrusts". In: *Biogeosciences* 14.23, pp. 5403–5424.
- (2018). "The role of localised pH on HONO and NH₃ emissions from drying soils and desert biocrusts". In: *in review*.
- Kleyer, Hannah, Robin Tecon, and Dani Or (2017). "Resolving species level changes in a representative soil bacterial community using microfluidic quantitative PCR". In: *Frontiers in microbiology* 8.
- Lawton, John H (1994). "What do species do in ecosystems?" In: *Oikos*, pp. 367–374.
- Li, Li et al. (2017). "Expanding the role of reactive transport models in critical zone processes". In: *Earth-science reviews* 165, pp. 280–301.
- Long, Tao. and Dani. Or (2007). "Microbial growth on partially saturated rough surfaces: Simulations in idealized roughness networks". In: *Water Resources Research* 43.2, W02409.
- Manzoni, Stefano and Amilcare Porporato (2009). "Soil carbon and nitrogen mineralization: theory and models across scales". In: *Soil Biology and Biochemistry* 41.7, pp. 1355–1379.
- Manzoni, Stefano et al. (2014). "A theoretical analysis of microbial eco-physiological and diffusion limitations to carbon cycling in drying soils". In: *Soil Biology and Biochemistry* 73, pp. 69–83.
- O'Donnell, A.G. et al. (2007). "Visualization, modelling and prediction in soil microbiology". In: *Nature Reviews Microbiology* 5.9, pp. 689–699.
- Or, Dani. and Markus Tuller (2000). "Flow in unsaturated fractured porous media: Hydraulic conductivity of rough surfaces". In: *Water Resources Research* 36.5, pp. 1165–1177.
- Or, Dani. et al. (2007). "Physical constraints affecting bacterial habitats and activity in unsaturated porous media—a review". In: *Advances in Water Resources* 30.6, pp. 1505–1527.
- Pedersen, Lasse L, Barth F Smets, and Arnaud Dechesne (2015). "Measuring biogeochemical heterogeneity at the micro scale in soils and sediments". In: *Soil Biology and Biochemistry* 90, pp. 122–138.
- Prosser, James I (2015). "Dispersing misconceptions and identifying opportunities for the use of 'omics' in soil microbial ecology". In: *Nature Reviews Microbiology*.
- Prosser, James I et al. (2007). "The role of ecological theory in microbial ecology". In: *Nature Reviews Microbiology* 5.5, pp. 384–392.
- Quince, Christopher, Thomas P Curtis, and William T Sloan (2008). "The rational exploration of microbial diversity". In: *The ISME Journal* 2.10, pp. 997–1006.
- Ranjard, L. and A. Richaume (2001). "Quantitative and qualitative microscale distribution of bacteria in soil". In: *Research in Microbiology* 152.8, pp. 707–716.
- Raynaud, Xavier and Naoise Nunan (2014). "Spatial ecology of bacteria at the microscale in soil". In: *PloS one* 9.1.

- Roesch, Luiz FW et al. (2007). "Pyrosequencing enumerates and contrasts soil microbial diversity". In: *The ISME Journal* 1.4, pp. 283–290.
- Ruamps, Léo Simon, Naoise Nunan, and Claire Chenu (2011). "Microbial biogeography at the soil pore scale". In: *Soil Biology and Biochemistry* 43.2, pp. 280–286.
- Sammartino, Stéphane, Eric Michel, and Yvan Capowiez (2012). "A novel method to visualize and characterize preferential flow in undisturbed soil cores by using multislice helical CT". In: *Vadose Zone Journal* 11.1, pp. 0–0.
- Sharon, Itai and Jillian F Banfield (2013). "Genomes from metagenomics". In: *Science* 342.6162, pp. 1057–1058.
- Šťovíček, Adam et al. (2017). "Microbial community response to hydration-desiccation cycles in desert soil". In: *Scientific Reports* 7.45735.
- Tecon, Robin and Dani Or (2016). "Bacterial flagellar motility on hydrated rough surfaces controlled by aqueous film thickness and connectedness". In: *Scientific reports* 6.
- (2017). "Biophysical processes supporting the diversity of microbial life in soil". In: *FEMS microbiology reviews* 41.5, pp. 599–623.
- Tikhonovich, IA and NA Provorov (2011). "Microbiology is the basis of sustainable agriculture: an opinion". In: *Annals of Applied Biology* 159.2, pp. 155–168.
- Torsvik, Vigdis and Lise Øvreås (2002). "Microbial diversity and function in soil: From genes to ecosystems". In: *Current Opinion in Microbiology* 5.3, pp. 240–245.
- Vereecken, Harry et al. (2016). "Modeling soil processes: Review, key challenges, and new perspectives". In: *Vadose zone journal* 15.5.
- Vogel, J et al. (2003). "Relationship between spatial and genetic distance in *Agrobacterium* spp. in 1 cubic centimeter of soil". In: *Applied and Environmental Microbiology* 69.3, pp. 1482–1487.
- Vogel, Timothy M et al. (2009). "TerraGenome: a consortium for the sequencing of a soil metagenome". In: *Nature Reviews Microbiology* 7.4, pp. 252–252.
- Vos, Michiel et al. (2013). "Micro-scale determinants of bacterial diversity in soil". In: *FEMS Microbiology Reviews* 37.6, pp. 936–954.
- Wang, Gang. and Dani. Or (2010). "Aqueous films limit bacterial cell motility and colony expansion on partially saturated rough surfaces". In: *Environmental Microbiology* 12.5, pp. 1363–1373.
- Whitman, William B, David C Coleman, and William J Wiebe (1998). "Prokaryotes: the unseen majority". In: *Proceedings of the National Academy of Sciences* 95.12, pp. 6578–6583.
- Young, IM and K Ritz (1998). "Can there be a contemporary ecological dimension to soil biology without a habitat?" In: *Soil Biology and Biochemistry* 30.10-11, pp. 1229–1232.
- Young, I.M. et al. (2008). "Microbial distribution in soils: Physics and scaling". In: *Advances in Agronomy* 100, pp. 81–121.

Chapter 2

Rough Surface Patch Model¹

2.1 Introduction

The necessity for quantitative modelling frameworks to advance environmental microbiology have been widely recognised (Prosser et al., 2007; Sutherland et al., 2013). In the context of microbial life in soil, various modelling approaches have been proposed and used to elucidate relations between small-scale physical properties and roles of soil microbial communities in terrestrial ecosystems (Wang and Or, 2010; Long and Or, 2007; Ebrahimi and Or, 2014). These studies provided new insights into environmental conditions that limit and promote soil bacterial life in an abstracted soil structure at very small scale (a few mm). The detailed description of pores in such models limit their upscaling to macroscopic systems that consider hydration, temperature and other gradients that shape natural populations (surface crusts, sharp fronts, etc.). To overcome this limitation while preserving cell-level description of microbial activity and their functions, we propose a rough surface patch model (RSPM) to represent natural hydrated surfaces.

The modelling domain discretises the physical domain into patches that (collectively) represent soil hydration conditions at a given matric potential ψ_m , such as effective water film thickness. A similar approach has been applied to model microbial life on pre-assigned two-dimensional roughness domain (Long and Or, 2009), however the approach was macroscopic without cell-level interactions. Soil water retention properties for each patch are described by the van Genuchten model (Van Genuchten, 1980) permitting consistent representation of other hydraulic functions for the patch such as unsaturated nutrient diffusion according to Millington and Quirk (Moldrup et al., 2003). While such parametric representation of rough surfaces overlooks pore scale geometrical detail (sub-patch scale), it provides useful links with characteristics of soils at the sample scale while preserving spatial heterogeneity among patches, which are critical for quantifying competition and co-existence in soil.

This study propose an alternative description, which connects the soil roughness property to hydration condition. Using a probability distribution function of surface porosity sizes, water film thickness, connectivity of aqueous habitats are calculated as relevant measures for microorganisms on soil rough surfaces.

¹This chapter is reorganised based on on the publication of Kim and Or, 2016.

2.2 Representing soil rough surfaces

2.2.1 A patch

The basic building block of the domain is a surface roughness patch that represents pore walls or surfaces of adjacent soil grains. Each patch contains subdomain roughness that is not explicitly represented. Instead, it is represented by self-affine and fractal properties of such water retaining surface geometries. A patch represents a multi-niche domain capable of hosting multiple species at a capacity defined by mean nutrient flux across its boundaries with neighbouring patches. The effective water film thickness and patch connectivity jointly determine local microbial cell dispersion rates (propelled by flagellated motion). The mean residence time of microbial cells in a patch varies with patch size and film thickness linked to water filled roughness (that vary with matric potential) and it can be estimated directly based on hydration conditions (For the detailed information, see Appendix A).

The nature of roughness in each patch is characterised by a surface porosity Φ (roughness space for storing water) and an exponent D for roughness element size distribution (See a diagram for the roughness domain depicted in Fig. 2.1). In contrast to the surface pore network models (Wang and Or, 2010; Long and Or, 2007), the rough patch contains no geometrical details (other than average or parametric properties : See Fig. 2.1A). However, we set a conceptual angular pore (with depth and sides r) and a smooth region as roughness elements for an explicit description of capillary force and its corner effect on surface pores. We assume that the surface pore is the shape of a square pyramid with base and depth r and the smooth surface is a completely smooth surface where water films are held by absorptive force only (Tuller, Or, and Dudley, 1999). The surface porosity Φ represents the fraction of the surface occupied by pores (angular depressions) relative to the entire patch domain (Fig. 2.1B). While Φ determines the proportion of surface pores on the domain, the exponent D controls the size distribution of roughness elements (the angular pyramid-shaped depressions). For spatial scalability considerations, we assume that the distribution of surface pore volumes follows a power-law distribution (Fig. 2.1C).

$$N(r) \sim r^{-D}, \quad (2.1)$$

where $N(r)$ is the surface pore size distribution with size r . Here, to avoid problems of divergence and to consider realistic roughness elements, upper and lower size cutoffs are introduced : $r_{\min} \leq r \leq r_{\max}$. r_{\min} is set to be 10^{-7} (m) to represent the minimum size of physical elements on the rough surface (related to the size of clay particle). r_{\max} varies depending on the scale of the domain and the largest roughness element. We note that the power-law nature of the pore size distribution is adopted from fractal models of soil for the purpose of up-scaling patch size for a given domain. Assuming Eq. (2.1) in its respective boundaries allows us to calculate hydration properties analytically and we thus use it for its simplicity. We call the exponent D as a fractal dimension for roughness measures.

Based on the fractal dimension D and the surface porosity Φ , the effective water film

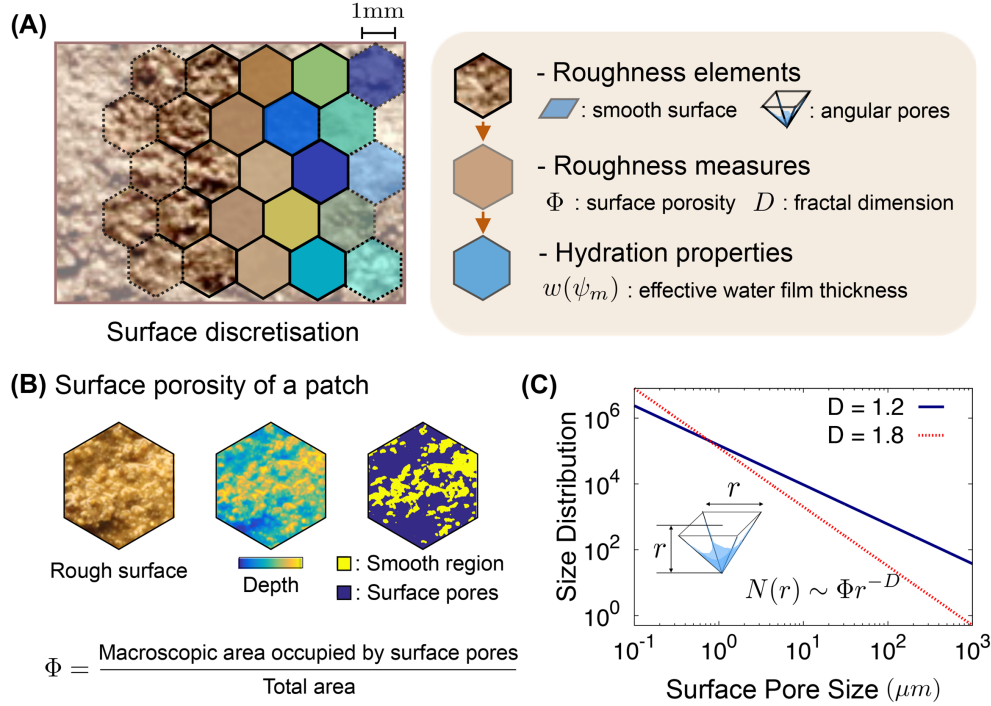


FIGURE 2.1: **A conceptual diagram of the definition of a patch.** (A) A rough soil surface domain is discretised with hexagonal patches representing subdomains. The brown and blue colour scale indicate the homogenisation of the roughness and hydration condition for each patch, respectively. To obtain the characteristics of patches we assume that a patch consists of roughness elements, a conceptual water-retaining pyramid-shaped pore and a smooth surface region. It allows us to calculate the amount of water held on the rough surface from the capillarity and van der Waals adsorptive forces at a certain relative humidity. Roughness of a patch is characterised with two measures, a surface porosity Φ and a fractal dimension D . The hydration condition of the patch can be represented as the effective water film thickness $w(\psi_m)$ as a function of the water matric potential ψ_m ; Eq. (2.2). (B) A rough surface domain would be comprised of various size of angular surface pores on the smooth surface. Surface porosity of a patch Φ determines the fraction of surface pores with respect to the patch domain (smooth surface+angular pores). (C) The fractal dimension D determines the size distribution of roughness elements for a patch, $N(r)$. It follows a power-law with a fractal dimension D . In the model, we assumed that the surface pore is the shape of a square pyramid with base r and height r (Larger pores indicate deeper pits on the rough surface).

thickness and the degree of saturation of a patch can be calculated by averaging the distribution of each element. For example, the effective water film thickness is defined as the value of the expected total amount of water at the water matric potential ψ_m , $\bar{V}(\psi_m)$, divided by the expected surface area of the patch, \bar{A} . Thus,

$$w_{\text{eff}}(\psi_m) = \frac{\bar{V}(\psi_m)}{\bar{A}} = \frac{\int_{r_{\min}}^{r_{\max}} [\Phi \mathcal{V}(r, \psi_m) + (1 - \Phi) h_\mu(\psi_m) r^2] r^{-(D+1)} dr}{\int_{r_{\min}}^{r_{\max}} r^2 r^{-(D+1)} dr}, \quad (2.2)$$

where $\mathcal{V}(r, \psi_m)$ is the amount of water which is held in an angular pore with size r and $h_\mu(\psi_m)$ is absorbed film thickness at ψ_m . When $\Phi \rightarrow 0$, the surface domain contains no angular pores thus only the contribution of van der Waals adsorptive forces would be left, which would determine the film thickness on that patch. On the other hand, when $\Phi \rightarrow 1$, the surface becomes very rough without any smooth area and the distribution of depth over the domain is purely given by the fractal dimension. The amount of water and effective water film thickness are calculated under considerations on physical properties of rough surfaces only; however, the model can be modified by considering chemical or biological agents that affect to the surface property. For instance, surfactant production by micro-organisms can alter the water-retention curve by lowering surface tension and increasing contact angle on the surface (Christofi and Ivshina, 2002; Rockhold et al., 2002). In this work, we did not consider these effects for sake of simplicity and calculated hydration property of surfaces with the surface tension of water, 72 mN.m^{-1} , and the contact angle as 0° (For the detailed calculations, see Appendix A).

Spatial variations and heterogeneity of the simulation domain are represented by assigning roughness measures to each patch drawn from a distribution of parameter values that preserve mean soil behaviour. As we have shown, a set of parameters $\{\Phi, D\}$ fully determines hydration properties of each patch in the model.

For the fractal dimension in the present work, we made an assumption that D is constant for the entire domain. Most of fractal models on soil structure distinguish fractal dimensions of mass D_m , pore volume D_p , and surface pore D_s in terms of size distributions (Gimenez et al., 1997; Ghanbarian-Alavijeh, Millán, and Huang, 2011). To simplify modelling the soil structure in the present work, we assume that $D = D_s = D_m - 1 = D_p - 1$ as a constant for the entire domain and analogously interpret that D determines different types or textures of soils (Tyler and Wheatcraft, 1992; Bird, Perrier, and Rieu, 2000; Huang and Zhang, 2005; Wang, Zhang, and Wang, 2005). For bulk soils, most of studies agree that sandy soils exhibit lower fractal dimension about $D_p \approx 2.4$ and higher clay contents increases D_p close to 3 (Tyler and Wheatcraft, 1992). Furthermore, some studies have provided measured data on fractal dimensions of soil surfaces to describe shape and form of natural objects as habitats of soil organisms such as micro-arthropod (Kampichler and Hauser, 1993; Kampichler, 1999), earthworms (Duhour et al., 2009), protozoa and bacterial species (Crawford, Ritz, and Young, 1993). Especially in the work of Kampichler and Hauser, 1993, the fractal dimension is measured from two-dimensional soil sections (in mm scales) by using image analysis technique. The size of patches (size of surface pores in our model) follows a power-law

distribution with $D \approx 1.4$. The work of Duhour et al., 2009 also measured the surface pore size distribution of the soil sections in cm scales and showed that D ranged between 1.32 and 1.70. The fractal dimension D for surface pore size distribution in RSPM is also in the range of $1 < D < 2$ and it can be connected with the surface fractal dimension describing the surface roughness (Mandelbrot, Passoja, and Paullay, 1984).

For the rough surface properties, the fractal dimension controls the specific surface area of the domain and the size distribution of surface pores. Thus, only one parameter, the surface porosity Φ , which is the proportion of area occupied by angular pores on the macroscopic surface area, is used to assign the heterogeneity of the roughness domain. However, any random spatial distribution of the local surface porosity cannot guarantee the persistence of up-scalability at the domain scale. To match the system domain with the real soil texture and surface roughness maintaining simple scalability, we assumed the surface porosity distribution follows the self-affine structure (Mandelbrot, Passoja, and Paullay, 1984; Scholz, 1995). Eq. (2.2) shows that the effective water film thickness of a patch is linearly dependent on surface porosity Φ . It implies that the length scale that we concern for substrate diffusion and microbial dispersion can be solely determined by Φ when D is constant. From the linear relation between the effective water film thickness and the surface porosity, we applied the definition of self-affinity relating the horizontal displacement Δr (distance) and the vertical displacement Δz (depth) (Pfeifer, 1984; Weiss, 2001),

$$\Delta z \sim \Delta w_{\text{eff}} \sim \Delta \Phi \sim (\Delta r)^H \equiv (\Delta r)^{3-Dp} = (\Delta r)^{2-D}, \quad (2.3)$$

where $H \in [0, 1]$ is the Hurst's exponent ($H = 2 - D$). The distribution of the surface porosity for the domain is obtained by implementing fractional Brownian surfaces (Mandelbrot and Van Ness, 1968; Stein, 2002) that preserve the relation, Eq. (2.3), with the mean value over the domain $\bar{\Phi}$ within a bounded region, $\Phi(\vec{r}) \in [0, 1]$. Typical examples of the surface domain for different roughness are given in Fig. 2.2.

In the figure, the roughness of the domain is depicted as the effective water film thickness distribution. As a patch model, each patch is assumed to be homogeneous inside and its roughness and hydration properties are averaged following the probability distribution. In terms of connectivity, we assumed the patch is a small replica of the entire domain (statistically self-similar to achieve the scalability) and the residence time of the microorganisms and the degree of interactions are determined by the global percolation probability of aqueous phase and the local surface porosity (This will be discussed in the section 2.4.). To sum up, the spatial heterogeneity of the local surface porosity with the self-affinity allows us to obtain distributions of available water (locally at the patch scale) in terms of saturation degree and effective water film thickness simultaneously with the representative roughness measures. This determines the local carrying capacity of microorganisms under a certain hydration condition and the nutrient flux from adjacent patches.

Effective water film thickness distribution at $\psi_m = -3.6\text{kPa}$

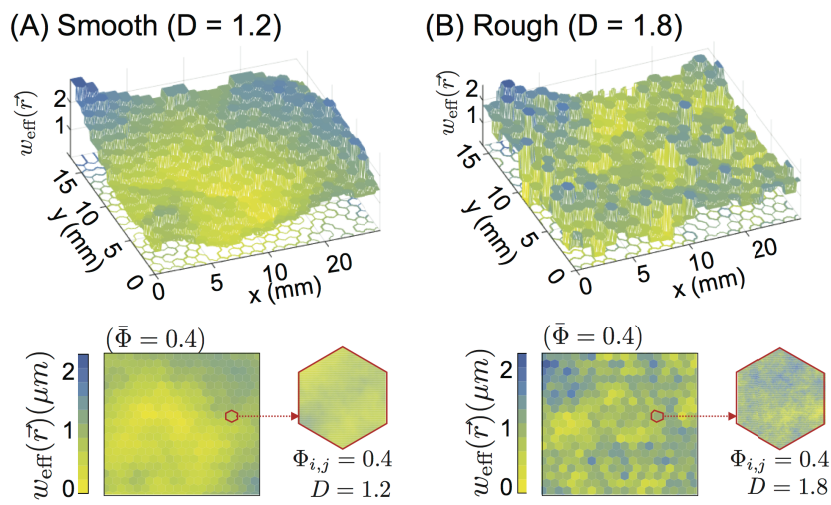


FIGURE 2.2: **A comparison of effective water film thickness distribution $w_{\text{eff}}(\vec{r})$ between smooth and rough surface domain.** Typical examples of rough surface domain are given as the effective water film thickness distribution at $\psi_m = -3.6\text{kPa}$. **(A)** a smooth surface domain ($D = 1.2$) and **(B)** a rough surface domain ($D = 1.8$) are provided for a comparison. To illustrate the role of the fractal dimension D for generating self-affine characteristics, the mean surface porosity of the domain is fixed as a constant for both cases ($\bar{\Phi} = 0.4$). A patch in the domain is assumed to be homogeneous inside for its roughness and hydration condition (effective water film thickness). However, to incorporate its roughness into the connectivity and tortuosity of the hydrological pathways in the patch, the global percolation probability of the domain and the local surface porosity $\Phi_{i,j}$ are considered to determine the residence time of microorganisms at the patch.

2.2.2 Diffusion process on rough surface domain

Nutrient diffusion variations and limitations at the micro-scale is an important mechanism for diverse microbial activity at small scales in soil. The nutrient flux to a physical niche determines the carrying capacity and various trophic interactions among species. The model links between micro-hydrology nutrient diffusion and dispersal of microorganisms on rough surfaces. In the model, transport properties on the rough surface are described explicitly and local conditions modify the development of microbial individuals. This modification at individual development would have a significant impact on community activity and this process regulates the spatial distribution of the microorganisms and the physical and chemical properties of the habitat.

Since we average microscopic details of the surface pore distribution and assume that hydration conditions are represented with effective water film thickness, the diffusion process is also described in terms of this parameter. The flux into a patch is estimated considering the cross section between adjacent patches based on their effective film thickness. In case that the effective film thickness among two neighbouring patches are different, we choose the minimum value of between them to guarantee that the joint cross sectional area is dictated by the thinner film. We apply Fick's law to calculate local substrate concentration, $C(\vec{r}, t)$, considering the reaction diffusion equation,

$$\frac{\partial C(\vec{r}, t)}{\partial t} = \nabla \cdot (D(\vec{r}) \nabla C(\vec{r}, t)) - \frac{1}{V_w(\vec{r})} f(b(\vec{r}), C(\vec{r}, t)), \quad (2.4)$$

where $D(\vec{r})$ is the apparent diffusion coefficient defined from the effective film thickness distribution of adjacent patches. Detailed calculation is presented in Appendix A. In Eq. (2.4), $f(b, C)$ is the total mass consumption by microorganisms with the total biomass b at the patch with the position \vec{r} . $V_w(\vec{r})$ is the volume of water in the patch (area of the patch \times the effective film thickness), thus the second term on r.h.s. indicates the change of concentration as a reaction term.

2.3 Microbial growth on rough surfaces

The present model employs Individual-Based Modelling (IBM) to describe dynamics of microbial activity on heterogeneous rough surface (DeAngelis, Gross, et al., 1992; Grimm et al., 2006). The IBM is capable of capturing interactions among cells competing for nutrients, or other forms of trophic dependencies such as mutualistic interactions between species (at the cell level). IBM represents cell-response to the physicochemical micro-environments with high spatial and temporal variations (DeAngelis and Mooij, 2005). Although implementation of IBM requires considerable parameterisation that distinguishes physiological traits of various species (often derived from experimental results), the trophic preferences and interactions among species give rise to emergence of spatial patterns and ecological functionality in complex spatial domains is a distinct advantage (Vlachos et al., 2004; Ginovart, López, and Gras, 2005; Ferrer, Prats, and López, 2008).

Life on the patchy rough surface merges IBM with the generalised physiological characteristics of bacterial cells, such as substrate uptake rates, metabolism, maintenance, reproduction, chemotactic motion, and death (Kreft, Booth, and Wimpenny, 1998). The growth of an individual cell is determined from the local concentration. Lack of nutrients for a certain period exhaust cell reserves and lead to cell death following rules based on previous studies (Kreft, Booth, and Wimpenny, 1998). The model is spatially explicit and includes microbial motility that is regulated by balancing the capillary force on surface and the chemotactic motion of the microbial cell.

Considering the substrate consumption rates by microbial cells, the reaction diffusion Eq. (2.4) can be rewritten explicitly as

$$\frac{\partial C(\vec{r}, t)}{\partial t} = \nabla \cdot (D(\vec{r}) \nabla C(\vec{r}, t)) - \frac{1}{V_w(\vec{r})} \sum_{i=1}^{N(\vec{r}, t)} f_p(\vec{r}) \frac{\mu_i(\vec{r}, t)}{Y_{\max}^i} b_i(\vec{r}, t), \quad (2.5)$$

where $N(\vec{r}, t)$ is the number of individual cells in the patch at \vec{r} , Y_{\max}^i is the maximum growth yield with respect to the substrate, and $b_i(\vec{r}, t)$ is the biomass of cell i at time t . This implies that the reaction term is the total consumption of the nutrient by every individual at the patch. μ_i is the specific growth rate of the microbial cell i defined with Monod growth function (Monod, 1942; Monod, 1949)

$$\mu_i(\vec{r}, t) = \frac{\mu_{\max}^i C(\vec{r}, t)}{K_{s,i} + C(\vec{r}, t)}, \quad (2.6)$$

where μ_{\max}^i , $K_{s,i}$ are the maximum growth rate and the half-saturation constant of the cell i , respectively. Here, although the Monod equation is generally used for population growth on batch culture, it is known that the single cell growth also follows the same Eq. (Dai et al., 2013). Monod growth can be extended in the model for multiple nutrients (Bader, 1978). When several nutrients are limiting the growth rate of the cell, the change of biomass b_i can be written as

$$\begin{aligned} \tilde{\mu}^i b_i &= \frac{db_i}{dt} = \left(\mu_{\max}^i \min\left[\frac{C_1}{K_{s,i}^1 + C_1}, \frac{C_2}{K_{s,i}^2 + C_2}, \dots\right] - m_i \right) b_i, \\ \tilde{\mu}^i &= \mu_{\max}^i \min\left[\frac{C_1}{K_{s,i}^1 + C_1}, \frac{C_2}{K_{s,i}^2 + C_2}, \dots\right] - m_i = \mu_i - m_i, \end{aligned} \quad (2.7)$$

where C_j indicates the j -th limiting nutrient, $K_{s,i}^j$ is the half saturation constant with respect to the nutrient j , and m_i is the maintenance rate of the cell i . Here, we assume that the maintenance rate of cell i is proportional to its maximum growth rate, $m_i \equiv \alpha_m \mu_{\max}^i$.

A similar reaction-diffusion formulation has been used in previous studies of microbial growth on roughness network models, and pore network models (Long and Or, 2009; Wang and Or, 2010; Ebrahimi and Or, 2014). Unlike previous studies, the patch definition of a spatial element is not a single niche and the model is scalable (capable of representing complex gradients over sub-metric scales), thus, the nutrient consumption within a patch also depends on roughness elements distribution and connections to the domain boundaries.

Although the nutrient concentration or hydration condition is assumed to be constant for all individuals located at the same patch, the accessibility to the substrate and the degree of interaction among cells is not uniform. Considering this, we introduce in equation (2.5) a factor $f_p(\vec{r})$ as the nutrients sharing factor. This factor considers the connectivity of the surface within a patch that cannot be expressed explicitly due to the spatial averaging representation (essential for effective upscaling). We assume that the nutrient sharing factor combines the deterministic microbial consumption rates with a local stochastic component via

$$f_p(\vec{r}) = \xi(\psi_m, \vec{r}) + \chi_p(1 - \xi(\psi_m, \vec{r})), \quad (2.8)$$

where χ_p is a random number drawn from a uniform distribution, $\mathcal{U}[0, 1]$. To consider different nutritional environments within a patch without burdening the computations with geometrical detail, we employ stochastic nutrient sharing assigned based on the level of local connectivity at the patch scale, $\xi(\psi_m, \vec{r}) \in [0, 1]$. The estimation of local connectivity within a patch will be discussed in the next section. For $\xi(\psi_m, \vec{r}) \rightarrow 1$, that is, when the local domain (a patch) is fully connected and microorganisms can access the entire region by flagellated motion with no restrictions of surface and other abiotic structures, the nutrient sharing factor becomes unity and consumption rates by each organism are determined solely by their respective growth function, Eq. (2.6). Under such conditions (static and fully connected) with many microbial species, the species with the highest μ_{\max}^i and the lowest $K_{s,i}$ will dominate the patch at long time scale (the patch represents a single niche) (Tilman, 1994; Tilman and Kareiva, 1997; Fahrig, 2003; Tilman, 1982; Smith, 1993). On the other hand, as $\xi(\psi_m, \vec{r}) \rightarrow 0$, a patch becomes highly fragmented or all the microorganisms become sessile and the consumption of nutrients for each species is diffusion based and stochastic. This stochasticity can be interpreted as unique spatial locations within a patch and reflect inherent irregularity of soil niches (even at the micro-scale) in terms of diffusion and other factors to locations where microorganisms are attached.

2.4 Hydration and fragmentation of aqueous habitats

Surface hydration conditions play an important role in all of the microbial life functions ranging from the control of diffusion rates, habitat connectivity to cell dispersion rates and ranges. Field scale models often treat microbial dispersion as passive convection or diffusion of passive substances (Yao, Habibian, and O'Melia, 1971; Corapcioglu and Haridas, 1984; Thullner and Schäfer, 1999; Murphy and Ginn, 2000; Thullner et al., 2002; Tufenkji, 2007). However, at the pore scale, microorganisms are not passive and actively seek nutrients and enhance their survivability by chemotaxis (Adler, 1966; Berg and Brown, 1972; Ford and Lauffenburger, 1991; Ford and Harvey, 2007). Microbial cells move on surfaces by various mechanisms including swimming and swarming by flagella, twitching, gliding, sliding, and darting (Harshey, 2003). Generally, surface motility is enhanced under wet conditions, especially for microbes propelled via flagellated motility where swimming speeds have shown to be sensitive to water film thickness (Dechesne et al., 2010; Wang and Or, 2010). While

cell swimming speed depends on physical properties (film thickness, cell sizes) (Ebrahimi and Or, 2014), chemotaxis determines the direction of swimming by chemical responses to nutrient concentrations or signals from other cells. The model applied the locomotion at a single-cell level based on hydration conditions and chemotaxis.

2.4.1 Chemotactic microbial locomotion on rough surfaces.

We employed the receptor model (Hillen and Painter, 2009) to derive the specific growth rate as the chemotactic potential. This approach allows consideration of chemotactic motion in response to gradients of multiple nutrients collapsed into a single scalar potential (motion towards the direction that produces the highest specific growth rate). (For more detailed explanations, see Appendix A). A biased-random walk approach is used with the probability to cross to adjacent patches defined by the composite chemotactic field derived from local specific growth rate

$$p_i(t) = \frac{w_i e^{\alpha(w_i) \vec{\nabla} \mu(t) \cdot \hat{e}_i}}{\sum_{j=1}^7 w_j e^{\alpha(w_j) \vec{\nabla} \mu(t) \cdot \hat{e}_j}}, \quad (2.9)$$

when $v(\psi_m) \neq 0$ and where α is the factor for the chemotactic motion, given by

$$\alpha \equiv \frac{\chi_0}{2\mu_{\max} v(\psi_m)}, \quad (2.10)$$

which balances the chemotactic sensitivity χ_0 and the swimming speed of a microbial cell $v(\psi_m)$. In Eq. (2.9), w_i denotes the effective film thickness of the nearest patch in the direction $i \in \{1, \dots, 7\}$ and $i = 7$ denotes the current patch where the cell locates. This implies that the motion in the patch depends on the local gradient of the chemotactic field and concurrently on the nutrient flux from different directions.

The swimming speed $v(\psi_m)$ is determined as a function of effective water film thickness $w(\psi_m)$ and it includes mechanical interaction between the surface and the microbial cell following the previous model (Wang and Or, 2010):

$$v(w(\psi_m)) = v_0 \frac{(F_M - F_\lambda(w(\psi_m)) - F_c(w(\psi_m)))}{F_M}, \quad (2.11)$$

where v_0 is the maximum swimming speed of a cell in bulk water. F_M , F_λ , F_c are flagellated propulsion, cell-surface hydrodynamic interaction, and capillary pinning force in the aqueous film, respectively. F_λ and F_c are the function of $w(\psi_m)$ that reflects the hydration condition and roughness element distribution. When $F_M - F_\lambda(w) - F_c(w) < 0$, the capillary force becomes dominant and swimming velocity ceases (i.e. the microbial cell becomes sessile). Application of chemotactically-driven biased random walk for microbial cell displacement determines the expected travelling length and the residence time within a patch. When the expected travelling length becomes longer than $l_p/\xi(\psi_m)$, the bacterial cell moves to the other patch based on cumulated location. We assume that the inverse of $\xi(\psi_m)$, the local connectivity of the patch, to be the tortuosity of the patch, $\tau(\psi_m) \equiv \frac{1}{\xi(\psi_m)}$.

The minimum residence time of a bacterial cell in a patch $T_r(\vec{r}, \psi_m)$ is defined to represent the contribution of surface roughness to microbial dispersion as a physical property regardless of the chemical conditions such as substrate concentration that controls the chemotactic behaviour. We define the averaged minimum residence time \bar{T}_r of the domain at ψ_m as following,

$$\bar{T}_r(\psi_m) = \frac{1}{\int_{\Omega} d\Omega} \int_{\Omega} \frac{l_p}{v(\vec{r}, \psi_m) \xi(\vec{r}, \psi_m)} d\Omega \quad (2.12)$$

where l_p is the size of a patch and Ω is the system domain. This is the spatial average of the time to travel the hydrological pathways with the speed $v(\vec{r}, \psi_m)$.

2.4.2 Fragmentation of aquatic habitats on surfaces

In our model, the notion of aqueous phase connectivity on the rough surface considers two aspects; nutrient diffusion via the liquid phase and microbial dispersion rates and ranges. The structural effect of hydrological connectivities for nutrients is already averaged in terms of effective film thickness (Or and Tuller, 2000). The connectivity for microbial dispersion is treated differently from nutrient diffusion especially as microbial cell sizes become comparable to surface film thickness under mild matric potential values (micro-meteric at a few kilopascal) that limit dispersion by surface capillarity long before nutrient (molecular scale) diffusion becomes limiting.

We thus define “aqueous habitats” as aqueous surface regions bounded by thin films (too thin to support flagellated motion, but sufficient to support nutrient diffusion) or physical ridges preventing accessibility of microbes external to the connected aqueous cluster - which may consists of several patches. Microbial motility within a habitat may be supported or suppressed by local (patch scale) water film thickness. In the proposed RSPM, the hydration status of each patch with respect to motility is defined as either motile or sessile based on two criteria: (1) microbial motility is enabled by a sufficiently thick aqueous film. In other words, a “motile” patch is defined on the basis that microbial swimming velocity, Eq. (2.11), is nonzero. (2) connectivity within the patch should be high enough so microbial cells can percolate through the patch. This can be calculated following the expected occupation probability of accessible surface pores by flagellated motion. This explains the effects of physical landscape that affects travelling pathways of microbial cells and determine the minimum residence time within a patch (For the detailed information, see Appendix A). Hence, a patch is classified as “motile” when flagellated motion is supported by water film and the occupation probability of accessible pore regions is higher than percolation threshold at the patch so the connectivity within the patch is not zero (i.e. $v(w(\vec{r}, \psi_m)) > 0$ and $T_r(\vec{r}, \psi_m)$ is finite.). When these two criterion were not satisfied, the patch would be a “sessile” patch. Aqueous habitats in RSPM represent the collection of motile patches that allows microbial migration between patches. The distribution of roughness measures and their hydration properties (ability to retain water), and shapes the size and connectivity of aquatic habitats of microorganisms at domain scale.

However, the occupation probability of accessible pore regions cannot be fulfilled to describe the local connectivity within a patch since the structural information (such as the

arrangement of surface pores) would be lost from the spatial averaging method with probability density function of element size ($\mathcal{N}(r) \sim \Phi r^{-D}$). To compensate this, we retrieve the spatial information of the patch by assuming the scale invariant property on local connectivity. To clarify, there are two distinctive concepts of connectedness; local connectivity (within a patch) and global connectivity of aqueous habitats (among patches). We defined the local connectivity $\xi(\psi_m, \vec{r})$ of the patch at \vec{r} by using the occupation probability of accessible pore regions of the patch $p(\psi_m, \vec{r})$ and the global percolation probability of aqueous habitats $P(\psi_m)$ that is the proportion of the largest cluster region to the entire domain.

$$\xi(\psi_m, \vec{r}) = \begin{cases} P(\psi_m) & \text{if } p(\psi_m, \vec{r}) > p_c(\vec{r}) \\ p(\psi_m, \vec{r})P(\psi_m) & \text{elsewhere} \end{cases},$$

where $p_c(\vec{r})$ is the percolation threshold of the patch on self-affine surface. Previous studies have shown that the percolation threshold p_c on a self-affine surface is dependent on the Hurst's exponent H (roughness parameter) and p_c is a stochastic variable with a mean value (ensemble averaged) $\langle p_c \rangle(H)$ and a variance $\sigma(H)$ regardless of system sizes (Isichenko, 1992; Schmittbuhl, Vilotte, and Roux, 1993; Du, Satik, and Yortsos, 1996; Sahimi, 1998). The mean value of $\langle p_c \rangle(H)$ monotonically decreases with H such that $\langle p_c \rangle(H = 0) = 0.5$ and $\langle p_c \rangle(H = 1) = 0.386$ (Prakash et al., 1992). For example, a self-affine domain with $H = 0.2$ ($D = 1.8$) would have a percolation threshold value around $\langle p_c \rangle(0.2) \sim 0.46 \pm 0.08$ regardless of system size (Du, Satik, and Yortsos, 1996). Thus, we draw a certain local percolation threshold value $p_c(\vec{r})$ for each patch from a normal distribution with mean $\langle p_c \rangle(H)$ and a variance $\sigma(H)$. $P(\psi_m)$ the global connectivity (i.e. the probability that a patch belongs to the percolating cluster of aqueous habitats) relates the local surface property and the global surface property in terms of roughness. (See detailed description in Appendix A).

2.5 Results

2.5.1 Effective water film thickness of rough surfaces

We first consider the physical properties of an individual patch. We examined relationships between the surface porosity Φ on the effective film thickness considering that surface porosity is used to generate modelling domain heterogeneity (spatial distribution of patches with different properties). Model predictions were compared with measurements of Tokunaga and Wan (Tokunaga and Wan, 1997) for film thickness measurements of a rough rock surface. In that study, the averaged film thickness was calculated by taking the difference between smooth- and rough-surface blocks and dividing by macroscopic surface area. The approach is used in our model definition of the effective film thickness. The linear averaging over the surface considers the contributions of very thick films and very thin films based on their surface pore distribution and depression of the surface.

In Fig. 2.3, a comparison with the model and the experimental data is given. The figure shows that the experimental data (Bishop Tuff, porous fractured rock with the sample size $\approx 50\text{mm}$) of effective water film thickness from Tokunaga and Wan, 1997 agree with the

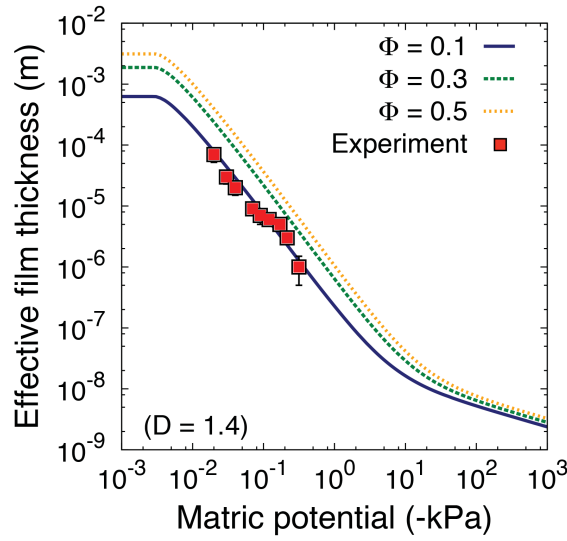


FIGURE 2.3: **The effective water film thickness of the rough surface domain as a single patch for different hydration conditions** (expressed by the matric potential of the aqueous phase). The surface porosity scales effective water film thickness when the fractal dimension is constant $D = 1.4$ ($D_p = 2.4$). When the surface porosity ($\Phi = 0.1$) is low the model agrees with the experimental data of Tokunaga and Wan, 1997. Here, we set the largest roughness element size $r_{\max} = 50$ mm as a possible representation of the surface depression of the sample rock used in the experiment (Tokunaga and Wan, 1997).

model when the surface has a relatively low surface porosity ($\Phi = 0.1$) when $D = 1.4$. Additionally, one can observe that the effective water film thickness at saturation reaches a certain value (when $\psi_m \rightarrow 0$). The value is statistically averaged with water-filled pores and absorbed water film over the domain. As the surface becomes drier, surface pores gradually become desaturated and only absorbed film ($w_{\text{eff}} \rightarrow$ a few nanometres, a few number of water molecular layers) remains on the surface and held by van der Waals forces, $\psi_m \ll -10^3$ kPa (Tuller and Or, 2005).

2.5.2 Microbial cell mean flagellated propulsion speed

The effective film thickness determines the microbial swimming speed on the surface. At local patch scale, the roughness defines how a patch affects the mean swimming velocity, thus determines the mean residence time at the given patch. A typical result of the mean swimming speed for different roughness measures is given in Fig. 2.4A. The figure shows the effect of surface porosity when D is constant and the capillary pinning force for flagella movement; the reduction of maximum swimming speed. Unlike the previous studies on the roughness network model (Long and Or, 2007; Wang and Or, 2010), assigning channel angles or height is not necessary since the effective water film thickness already averages the heterogeneous surface domain by using the probability distribution function of the surface pore sizes. The result shows that surface capillary force plays the most dominant role for microbial motility. The experimental data on a porous ceramic plate of Dechesne et al.,

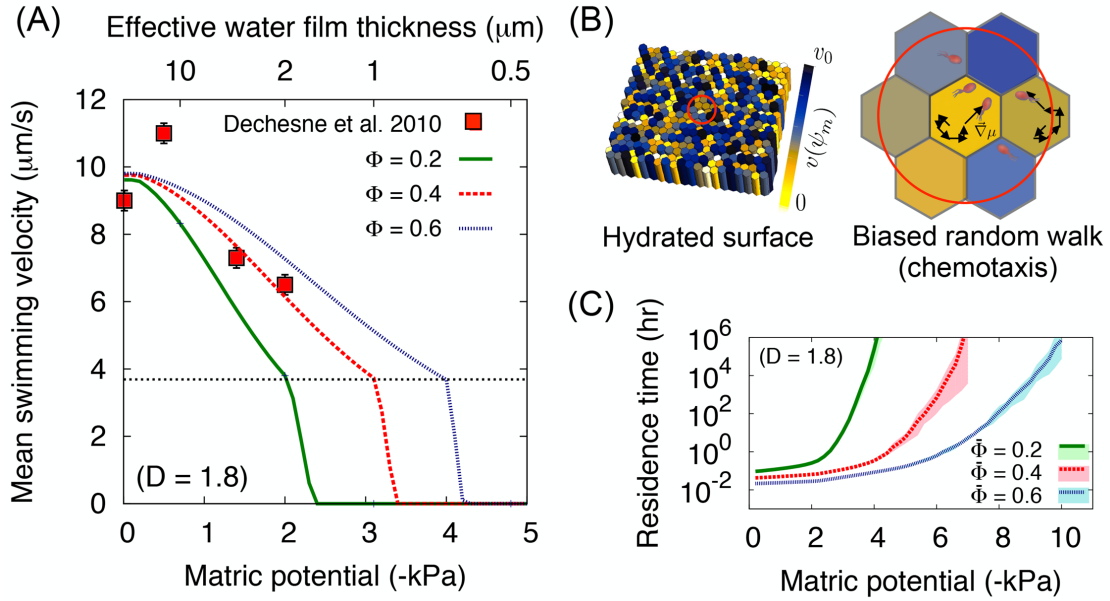


FIGURE 2.4: **Microbial locomotion in rough surface patch model** (A) The mean flagellated swimming velocity on the surface with different surface porosities for different hydration conditions expressed by matric potential (bottom axis) and effective water film thickness when $\Phi = 0.4$ (top axis). For comparison, we fixed the fractal dimension $D = 1.8$ and varied the surface porosity from 0.2 to 0.6. Measured values (red squares) from the work of Dechesne et al., 2010, the mean microbial swimming velocity on the porous ceramic plate, show good agreement with the model when the surface porosity is about 0.4. Black dotted horizontal line indicates the onset of capillary force. The swimming speed at the bulk water is given as $v_0 = 14 \mu\text{m/s}$ (Berg and Brown, 1972). The roughness effect and the surface porosity reduce the mean swimming velocity to about $10 \mu\text{m/s}$ even at the very wet case. (B) Heterogeneity of roughness patches on the domain can be mapped to the swimming velocity field for micro-organisms. Yellow-blue scale indicates the mean swimming speed. In a patch, the microbial locomotion follows the biased random walk following the probability to cross to adjacent patches, Eq. (2.9). (C) The averaged minimum residence time at a patch \bar{T}_r (assuming patch size $l_p = 500 \mu\text{m}$) varies for different roughness measures, Eq. (2.12). For a surface with constant fractal dimension, the averaged minimum residence time at a patch is higher when the surface porosity $\bar{\Phi}$ is lower. The shaded area indicate the lower and upper values from 5 sample domains with the same mean roughness measures $\{\bar{\Phi}, D\}$.

2010 agree well with the model surface of $D = 1.8$ and $\Phi = 0.4$. Here, we fixed $r_{\max} = 10^{-3}$ m considering the size of ceramic surface used by (Dechesne et al., 2010) and the absence of large roughness elements unlike natural rocks like Bishop Tuff used in the previous section (Tokunaga and Wan, 1997).

Considering that the mean swimming speed in the experiment of (Dechesne et al., 2010) is obtained by averaging swimming speeds of microbial cells during phases of significant motility over the entire domain, it is reasonable to expect that spatial heterogeneity was also averaged. This implies that the spatial average, ensemble average for simulations, and statistical average of individual motion for many cells (at population level) would behave identically.

So far, we have shown properties of an individual patch as an element of the physical domain. The model agrees with experimental data of effective water film thickness and the mean motile cells swimming velocity. For this physical property analysis, the size of patch does not play any role since the effective water film thickness and mean swimming velocity are intensive quantities, in other words, these values are independent of system size because a probability distribution (described with $\{\Phi, D\}$) is used for spatial averaging. However, to simulate dynamics of microbial populations, assigning the size of patch is necessary. In the model, we set the size of a hexagonal patch as $500\mu\text{m}$, both for computational purposes and for a comparison with the experimental data. The physical domain of the model is comprised of 100×100 hexagonal patches and thus the entire domain size is about 5 cm. In addition, we include surface spatial heterogeneity by applying different roughness parameters for each patch. For simulations, the fractal dimension is fixed, $D = 1.8$ and the heterogeneity of the surface porosity are assigned to represent a self-affine roughness when $H = 0.2$ with the mean surface porosity of all patches, $\bar{\Phi} = 0.4$ (See Fig. 2.2A for an example domain mapped to the effective film thickness distribution). The surface porosity distribution determines the swimming velocity field that controls the microbial dispersion rate by balancing capillarity and the chemotaxis (described as a biased-random walk) (See Fig. 2.4B).

The effect of surface porosity on the minimum residence time of microbial cells with a patch of size $l_p = 500\mu\text{m}$ for different hydration conditions (matric potential values) is depicted in Fig. 2.4C. The results show that lower surface porosities results in an increased residence times. The residence time diverges at a certain ψ_m due to the onset of capillary pinning forces and the fragmentation of the aqueous habitats. However, \bar{T}_r represents only the minimum residence time of microbial cells. In the model, the actual residence time varies depending on the substrate diffusion and the nutrient concentration of each patch. The actual dispersal of microbial cells and their distributions are highly dependent on the chemotaxis as we illustrate in the next section.

2.5.3 Microbial dispersion rates

We considered microbial population dynamics at the domain scale and their spatial distributions on the rough surface. In Fig. 2.5, simulated values of microbial colony expansion rates are given. Fig. 2.5A shows a typical example of microbial colony dispersion pattern

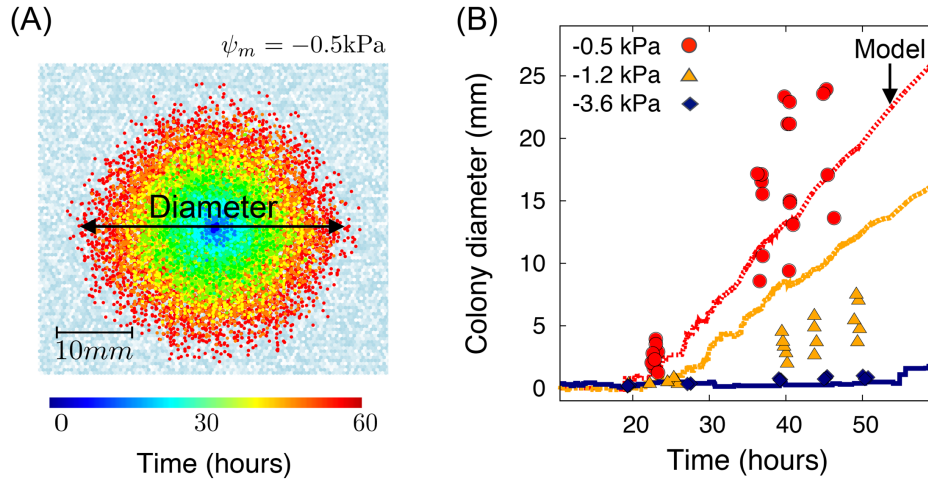


FIGURE 2.5: **Microbial dispersion on rough surfaces** (A) Simulated colony expansion of motile bacterial cells grown in a surface at $\psi_m = -0.5 \text{ kPa}$. The white-greyblue colour scale indicate the effective water film thickness distribution (blue=motile, white=sessile), Here, we did not use self-affine domain for the local surface porosity distribution to reflect the experimental setting of Dechesne et al., 2008. The initial nutrient concentration was given $C(\vec{r}, 0) = C_0 = 1 \text{ mg/L}$ and the boundary condition was to maintain concentration at the boundary. (B) The time evolution of colony diameter (or the maximum microbial dispersion distance) is given from simulated results (-0.5, -1.0, and -3.0 kPa, these values were chosen to cover various hydration conditions to cover globally connected, locally connected, and fragmented habitats) and experimental results (-0.5, -1.2, and -3.6 kPa) for hydrated surfaces at three values of matric potential. Lines in different colours indicate simulated results. Filled symbols indicate the experimental results from Dechesne et al., 2008.

on the RSPM. For the colony dispersion calculation for the domain, we made no use of local self-affine surface for the local surface porosity distribution. In order to compare simulations with the experiments that used porous ceramic surface following the mono-scale size distribution without any small or large grain, we used a random distribution of surface porosities for each patch drawn from the uniform distribution, $\mathcal{U}[0, 1]$. On the simulated surface domain, the nutrient concentration across the domain was given to be constant, $C(\vec{r}, t = 0) = C_0 = 1 \text{ mg/L}$. We maintained the constant concentration only at the boundary of the domain, $C(\vec{r}, t)|_{\text{boundary}} = C_0$. 100 microbial cells were inoculated at four patches at the centre of the domain, and their dispersion is observed over the simulation time of 60 hours. The hydration conditions during the simulation time were constant and determined by a matric potential value of $\psi_m = -0.5 \text{ kPa}$ (static hydration condition). We also measured the time evolution of the maximum microbial dispersion distance deduced from radial colony expansion rates (as in the experiments of (Dechesne et al., 2008) for three different matric potential (See Fig. 2.5B). For the comparison, we used the physical properties of an individual patch and compared the heterogenous domain, preserving the average surface porosity $\bar{\Phi}$. The comparison of simulations with experimental results were in good agreement, showing that the hydration conditions control the colony expansion rates on surfaces.

Additionally, we have developed an analytical approach for the colony expansion rate

for uniformly distributed surface porosity as the most simple case. In the model, the chemotactic movement of each microorganism is described by a biased-random walk. From the tumbling probability following the growth rate field as a chemotactic field, we earlier derived the jumping probability of an individual cell, Eq. (2.9), that can determine the microbial dispersion rate on the domain scale. For the calculation at population level, the effective average velocity under the chemotactic field is obtained by assuming isotropic movement of a cell (again, a patch is assumed to be homogenised inside). The nutrient concentration field $C(\vec{r})$ is mapped to the growth rate field, $\mu(C(\vec{r})) \equiv \mu(\vec{r})$, and the gradient of the growth rate field is assumed to be a chemotactic field. This allows us to simplify the individual chemotactic locomotion when multiple nutrients are considered for the microbial growth (for the detailed derivation, see Appendix A). By assuming that the mean isotropic trajectory duration, $T(u)$, is the same as the mean run time towards the direction \hat{x} , where u is the directional cosine of the chemotactic field direction (i.e. $u \equiv \frac{\nabla\mu \cdot \hat{x}}{|\nabla\mu|}$), the effective chemotactic velocity at population level can be calculated as follows (Lovely and Dahlquist, 1975; Othmer, Dunbar, and Alt, 1988):

$$\vec{v}_{\text{eff}}(\psi_m) = \vec{v}(\psi_m) \frac{\int_{-1}^1 u T(u) du}{\int_{-1}^1 T(u) du} = v(\psi_m) \frac{I_1(\alpha |\nabla\mu|)}{I_0(\alpha |\nabla\mu|)} \frac{\nabla\mu}{|\nabla\mu|} \equiv v(\psi_m) \vec{R}_c(\alpha, \mu), \quad (2.13)$$

where $v(\psi_m)$ is the mean swimming velocity of a cell under capillary pinning force, $T(u) = t_0 e^{\alpha |\nabla\mu| u}$ is the running time in direction u with t_0 , the mean run time in the absence of a chemical attractant, and $I_\nu(x)$ is the modified Bessel function of the first kind. Here we introduced the chemotactic retardation factor $R_c(\alpha, \mu)$ that controls the effective swimming speed as a result of chemotaxis. The chemotactic factor α is a function of $v(\psi_m)$ and $|\nabla\mu|$ as in Eq. (2.10), which changes over time depending on the local concentration. This means that the effective velocity of chemotaxis reaches the mean swimming velocity when $\alpha |\nabla\mu| \gg 1$ (strong chemotaxis), and it reaches to 0 when $\alpha |\nabla\mu| \rightarrow 0$ (no chemotaxis; uniform distribution of direction). From the chemotactic retardation factor, expected residence time under the chemotactic field at a patch can be calculated

$$T^*(\psi_m) = \frac{\tau(\psi_m) l_p}{v_{\text{eff}}^*(\psi_m)} = \frac{l_p}{v_{\text{eff}}^*(\psi_m) \xi(\psi_m)} = \frac{\bar{T}_r(\psi_m)}{R_c(\alpha^*, \mu^*)}, \quad (2.14)$$

where $v_{\text{eff}}^*(\psi_m)$ indicates the effective velocity at steady state (i.e. $\alpha |\nabla\mu|$ is constant over time) and $\bar{T}_r(\psi_m)$ is the averaged minimum residence time at a patch. From the mean residence time at a patch, the microbial dispersion rate, or the expansion rate of a chemotactic ring on the rough surface can be approximately written as

$$R(t) = \int_0^t T_r(\psi_m) \vec{v}_{\text{eff}}(\psi_m, \tau) \cdot \frac{\nabla\mu}{|\nabla\mu|} d\tau. \quad (2.15)$$

Fig. 2.6 compares the analytically predicted colony dispersion rates (based on Eq. (2.15)) with simulations and measurements by (Dechesne et al., 2008) as well as the simulated

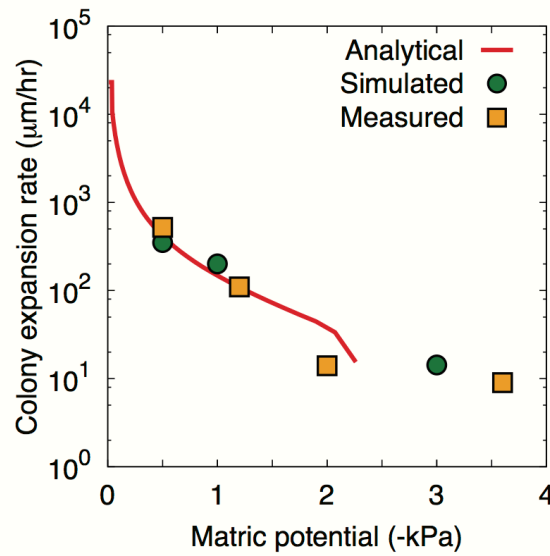


FIGURE 2.6: **Colony expansion rate.** Colony expansion rates for analytical results, surface patch model results (three matric potentials were chosen to cover various hydration conditions representing globally connected, locally connected, and fragmented habitats), and experimental results are compared. Analytic results are calculated based on Eq. (2.15). In analytical results, the average value of the surface porosity ($\bar{\Phi} = 0.5$) is used as a representative value of the domain and the expansion rate becomes zero since the flagellated movement is disabled due to the capillary forces at about -2kPa . The simulation results of RSPM show non-zero colony expansion rate up to about -3kPa because of the heterogeneity of the domain.

data from IBM. The results show that the colony expansion rate by the flagellated motility decreases exponentially from about $500\mu\text{m/hr}$ at -0.5kPa to $12.5\mu\text{m/hr}$ at -2kPa . Furthermore, the analytical prediction agrees with the experimental results. This implies that decomposition of physical, chemical, biological factors can be used to describe microbial dispersion. First, we calculated effective swimming velocity, which is driven from the hydrated rough surfaces with capillarity. Second, the biased random walk as chemotactic behaviour of a cell provides the net displacement towards the nutrient source. Third, considering the connectivity and tortuosity of the cell movement, it modifies the actual travelling distance that microbial cell traverses.

2.6 Discussion

The study presented a new and scalable modelling approach (termed the rough surface patch model, RSPM) for quantitative representation of microbial life on hydrated rough (soil) surfaces. The key element of water retention is encapsulated in patch roughness properties that collectively honours soil water retention properties and aqueous phase distribution with matric potential. Two roughness parameters, fractal dimension D and surface porosity Φ were used to derive the scale invariant surface pore size distribution. By using the probability density of surface pore sizes in a patch, the effective water film thickness is obtained as an indicator of roughness and regulator of nutrient diffusion and microbial

dispersion for various hydration conditions. The approach provides a scalable domain (via patch size) that preserves cell-level interactions without explicit representation of pore level aqueous phase distribution that limited the scales of previous models. Despite the simplification of soil surface structure with patch representation, the model manages to capture the effects of complex aqueous phase on nutrient transport, microbial growth and community interactions. The simple representation of surfaces as patches enable simple computations for ecological modelling at sub-metric scales and for days to months time frames. Finally, larger simulation domain permits considerations of temperature and hydration gradients known to affect microbial ecology near interfaces (i.e., soil surface, desert crust etc.) (Ettema and Wardle, 2002; Holden, Ritz, Young, et al., 2011). Patchy distribution of the microbial community and spatial heterogeneity can also be connected to the bacterial biodiversity across scales (Becker et al., 2006).

The modelling framework employs Individual based modelling (IBM) on the RSPM to describe cell-level microbial interactions in heterogeneous and time-variant environments. The IBM formulation provides an important tool to mechanistically account for multiple species growth with various biological characteristics and their trophic interactions (Kreft, Booth, and Wimpenny, 1998). The IBM also provides a simple means for considering individual cell motion. Each individual motion is influenced by local environments (at patch scale) and the dispersion of the population (at domain scale) emerges as an integrated effect of nutrient diffusion processes, biological growth, and chemotactic behaviour. The previous works on roughness networks succeed in showing numerically and analytically that the behaviour of population, such as the self-organisation that arises from the collection of individual movements (Dechesne et al., 2010; Wang and Or, 2010; Wang and Or, 2014). This allows insight into the relation between dynamics on microscopic as well as macroscopic levels. IBM is a useful tool to bridge the gap between individual cell response and emergent behaviour of populations for various environmental conditions. However, the approach involves heavy computational burden in maintaining each individual life history as the domain and time span increase. Thus, individual based modelling at scales larger than a few centimetres remain limited. There are several attempts at dealing with large numbers of individuals such as using “super-individuals” or reducing a spatial model to a representative space (Hellweger and Bucci, 2009). Although these approaches show a promise in computational biology, the upscaling from cell level to population behaviour remains poorly understood.

Based on the analysis at the population level (total number of individual at a patch), the importance of patch size in the model becomes apparent. This is because the approach considers averaging (with respect to surface properties and reducing aqueous phase distribution to film thickness) across length scales varying from 10^{-7} to 10^{-3} m. There are several criteria with respect to upscaling microbial growth on the patch model: First, the size of patches should be larger than a few micrometres considering the niches of microorganisms. Since the physical size of microorganisms is about $1 \sim 10 \mu\text{m}$, the size of patch should

be larger than this to host several individuals. Second, considering that a patch is a homogenised subdomain, the diffusion rate of nutrients is also an important factor for choosing the size of an element. The diffusion coefficient of nutrients is of the order of $10^{-10}\text{m}^2/\text{s}$. When the size of a patch is l_p , the time for a nutrient molecule to diffuse through a patch is about $t = l_p^2/4D$ which should be comparable with the persistence time for a microbial population. Assuming that the colony expansion rate is around $5\text{ mm/hr} \approx 10^{-6}\text{m/s}$ (the wet case) (Dechesne et al., 2010), the size of patch should be around 1mm. This may define an upper limit for the patch and model scale. Although the system size is scalable for the physical properties, the length scale of the microbial dispersion limits the size of a spatial element. However, compared presently available network models mimicking a small pore size explicitly (Long and Or, 2007; Wang and Or, 2010; Ebrahimi and Or, 2014), the patchy approach enables us to upscale up to a relatively larger scale.

In summary, we developed a rough surface patch model to describe microbial life in soils with a possibility of upscaling spatially to cm scales and temporally to the scale of months. The model predicts the effective water film thickness distribution at a given hydration condition over the domain, therefore microbial dispersion, carrying capacity of patch, and aqueous habitats distribution. In the next chapter, we discuss the application of this model to address some questions in microbial ecology.

References

- Adler, Julius (1966). "Chemotaxis in bacteria". In: *Science* 153.737, pp. 708–716.
- Bader, FG (1978). "Analysis of double-substrate limited growth". In: *Biotechnology and Bioengineering* 20.2, pp. 183–202.
- Becker, Joanna M et al. (2006). "Bacterial activity, community structure, and centimeter-scale spatial heterogeneity in contaminated soil". In: *Microbial Ecology* 51.2, pp. 220–231.
- Berg, Howard C and Douglas A Brown (1972). "Chemotaxis in *Escherichia coli* analysed by three-dimensional tracking". In: *Nature* 239.5374, pp. 500–504.
- Bird, NRA, Edith Perrier, and Michel Rieu (2000). "The water retention function for a model of soil structure with pore and solid fractal distributions". In: *European Journal of Soil Science* 51.1, pp. 55–63.
- Christofi, N and IB Ivshina (2002). "Microbial surfactants and their use in field studies of soil remediation". In: *Journal of Applied Microbiology* 93.6, pp. 915–929.
- Corapcioglu, M Yavuz and A Haridas (1984). "Transport and fate of microorganisms in porous media: a theoretical investigation". In: *Journal of Hydrology* 72.1, pp. 149–169.
- Crawford, John W, Karl Ritz, and Iain M Young (1993). "Quantification of fungal morphology, gaseous transport and microbial dynamics in soil: an integrated framework utilising fractal geometry". In: *Geoderma* 56.1, pp. 157–172.
- Dai, Jing et al. (2013). "Charting microbial phenotypes in multiplex nanoliter batch bioreactors". In: *Analytical chemistry* 85.12, pp. 5892–5899.
- DeAngelis, Donald L and Wolf M Mooij (2005). "Individual-based modeling of ecological and evolutionary processes". In: *Annual Review of Ecology, Evolution, and Systematics*, pp. 147–168.
- DeAngelis, Donald Lee, Louis J Gross, et al. (1992). *Individual-based models and approaches in ecology: populations, communities and ecosystems*. 1st. Chapman & Hall.
- Dechesne, Arnaud et al. (2008). "The porous surface model, a novel experimental system for online quantitative observation of microbial processes under unsaturated conditions". In: *Applied and Environmental Microbiology* 74.16, pp. 5195–5200.
- Dechesne, Arnaud et al. (2010). "Hydration-controlled bacterial motility and dispersal on surfaces". In: *Proceedings of the National Academy of Sciences* 107.32, pp. 14369–14372.
- Du, C, C Satik, and YC Yortsos (1996). "Percolation in a fractional Brownian motion lattice". In: *AIChE Journal* 42.8, pp. 2392–2395.
- Duhour, Andrés et al. (2009). "Response of earthworm communities to soil disturbance: Fractal dimension of soil and species rank–abundance curves". In: *Applied Soil Ecology* 43.1, pp. 83–88.
- Ebrahimi, Ali N and Dani Or (2014). "Microbial dispersal in unsaturated porous media: Characteristics of motile bacterial cell motions in unsaturated angular pore networks". In: *Water Resources Research* 50.9, pp. 7406–7429.
- Ettema, Christien H and David A Wardle (2002). "Spatial soil ecology". In: *Trends in Ecology & Evolution* 17.4, pp. 177–183.

- Fahrig, Lenore (2003). "Effects of habitat fragmentation on biodiversity". In: *Annual Review of Ecology, Evolution, and Systematics*, pp. 487–515.
- Ferrer, Jordi, Clara Prats, and Daniel López (2008). "Individual-based modelling: an essential tool for microbiology". In: *Journal of Biological Physics* 34.1-2, pp. 19–37.
- Ford, Roseanne M and Ronald W Harvey (2007). "Role of chemotaxis in the transport of bacteria through saturated porous media". In: *Advances in Water Resources* 30.6, pp. 1608–1617.
- Ford, Roseanne M and Douglas A Lauffenburger (1991). "Measurement of bacterial random motility and chemotaxis coefficients: II. Application of single-cell-based mathematical model". In: *Biotechnology and Bioengineering* 37.7, pp. 661–672.
- Ghanbarian-Alavijeh, Behzad, Humberto Millán, and Guanhua Huang (2011). "A review of fractal, prefractal and pore-solid-fractal models for parameterizing the soil water retention curve". In: *Canadian Journal of Soil Science* 91.1, pp. 1–14.
- Gimenez, D et al. (1997). "Fractal models for predicting soil hydraulic properties: a review". In: *Engineering Geology* 48.3, pp. 161–183.
- Ginovart, Marta, Daniel López, and Anna Gras (2005). "Individual-based modelling of microbial activity to study mineralization of C and N and nitrification process in soil". In: *Nonlinear Analysis: Real World Applications* 6.4, pp. 773–795.
- Grimm, Volker et al. (2006). "A standard protocol for describing individual-based and agent-based models". In: *Ecological Modelling* 198.1, pp. 115–126.
- Harshey, Rasika M (2003). "Bacterial motility on a surface: many ways to a common goal". In: *Annual Reviews in Microbiology* 57.1, pp. 249–273.
- Hellweger, Ferdi L and Vanni Bucci (2009). "A bunch of tiny individuals : Individual-based modeling for microbes". In: *Ecological Modelling* 220.1, pp. 8–22.
- Hillen, Thomas and Kevin J Painter (2009). "A user's guide to PDE models for chemotaxis". In: *Journal of Mathematical Biology* 58.1-2, pp. 183–217.
- Holden, P.A., K. Ritz, I. Young, et al. (2011). "How do the microhabitats framed by soil structure impact soil bacteria and the processes that they regulate?" In: *The Architecture and Biology of Soils: Life in Inner Space*, p. 118.
- Huang, Guanhua and Renduo Zhang (2005). "Evaluation of soil water retention curve with the pore–solid fractal model". In: *Geoderma* 127.1, pp. 52–61.
- Isichenko, Michael B (1992). "Percolation, statistical topography, and transport in random media". In: *Reviews of Modern Physics* 64.4, p. 961.
- Kampichler, Ch and M Hauser (1993). "Roughness of soil pore surface and its effect on available habitat space of microarthropods". In: *Geoderma* 56.1, pp. 223–232.
- Kampichler, Christian (1999). "Fractal concepts in studies of soil fauna". In: *Geoderma* 88.3, pp. 283–300.
- Kim, Minsu and Dani Or (2016). "Individual-based model of microbial life on hydrated rough soil surfaces". In: *PLoS ONE* 11.1, e0147394.
- Kreft, Jan-Ulrich, Ginger Booth, and Julian WT Wimpenny (1998). "BacSim, a simulator for individual-based modelling of bacterial colony growth". In: *Microbiology* 144.12, pp. 3275–3287.

- Long, Tao. and Dani. Or (2007). "Microbial growth on partially saturated rough surfaces: Simulations in idealized roughness networks". In: *Water Resources Research* 43.2, W02409.
- (2009). "Dynamics of microbial growth and coexistence on variably saturated rough surfaces". In: *Microbial Ecology* 58.2, pp. 262–275.
- Lovely, Peter S and FW Dahlquist (1975). "Statistical measures of bacterial motility and chemotaxis". In: *Journal of Theoretical Biology* 50.2, pp. 477–496.
- Mandelbrot, Benoit B, Dann E Passoja, and Alvin J Paullay (1984). "Fractal character of fracture surfaces of metals". In: *Nature* 308, pp. 721–722.
- Mandelbrot, Benoit B and John W Van Ness (1968). "Fractional Brownian motions, fractional noises and applications". In: *SIAM Review* 10.4, pp. 422–437.
- Moldrup, P. et al. (2003). "Modeling diffusion and reaction in soils: X. A unifying model for solute and gas diffusivity in unsaturated soil". In: *Soil Science* 168.5, pp. 321–337.
- Monod, Jacques (1942). "Recherches sur la croissance des cultures bacteriennes". In: *Hermann and Cie, Paris*.
- (1949). "The growth of bacterial cultures". In: *Annual Reviews in Microbiology* 3.1, pp. 371–394.
- Murphy, Ellyn M and Timothy R Ginn (2000). "Modeling microbial processes in porous media". In: *Hydrogeology Journal* 8.1, pp. 142–158.
- Or, Dani. and Markus Tuller (2000). "Flow in unsaturated fractured porous media: Hydraulic conductivity of rough surfaces". In: *Water Resources Research* 36.5, pp. 1165–1177.
- Othmer, Hans G, Steven R Dunbar, and Wolfgang Alt (1988). "Models of dispersal in biological systems". In: *Journal of Mathematical Biology* 26.3, pp. 263–298.
- Pfeifer, Peter (1984). "Fractal dimension as working tool for surface-roughness problems". In: *Applications of Surface Science* 18.1, pp. 146–164.
- Prakash, Sona et al. (1992). "Structural and dynamical properties of long-range correlated percolation". In: *Physical Review A* 46.4, R1724.
- Prosser, James I et al. (2007). "The role of ecological theory in microbial ecology". In: *Nature Reviews Microbiology* 5.5, pp. 384–392.
- Rockhold, Mark L et al. (2002). "Considerations for modeling bacterial-induced changes in hydraulic properties of variably saturated porous media". In: *Advances in Water Resources* 25.5, pp. 477–495.
- Sahimi, Muhammad (1998). "Non-linear and non-local transport processes in heterogeneous media: from long-range correlated percolation to fracture and materials breakdown". In: *Physics Reports* 306.4, pp. 213–395.
- Schmittbuhl, Jean, J-P Vilotte, and Stéphane Roux (1993). "Percolation through self-affine surfaces". In: *Journal of Physics A: Mathematical and General* 26.22, p. 6115.
- Scholz, Christopher (1995). "Scaling invariance of crack surfaces". In: *Journal of Geophysical Research* 100.B4, pp. 5953–5973.
- Smith, Val H (1993). "Implications of resource-ratio theory for microbial ecology". In: *Advances in Microbial Ecology*. Springer, pp. 1–37.
- Stein, Michael L (2002). "Fast and exact simulation of fractional Brownian surfaces". In: *Journal of Computational and Graphical Statistics* 11.3, pp. 587–599.

- Sutherland, William J et al. (2013). "Identification of 100 fundamental ecological questions". In: *Journal of Ecology* 101.1, pp. 58–67.
- Thullner, Martin and Wolfgang Schäfer (1999). "Modeling of a field experiment on bioremediation of chlorobenzenes in groundwater". In: *Bioremediation Journal* 3.3, pp. 247–267.
- Thullner, Martin et al. (2002). "Interaction between water flow and spatial distribution of microbial growth in a two-dimensional flow field in saturated porous media". In: *Journal of Contaminant Hydrology* 58.3, pp. 169–189.
- Tilman, David (1982). *Resource Competition and Community Structure*. Princeton University Press Princeton, NJ.
- (1994). "Competition and biodiversity in spatially structured habitats". In: *Ecology* 75.1, pp. 2–16.
- Tilman, David and Peter M Kareiva (1997). *Spatial ecology: the role of space in population dynamics and interspecific interactions*. Vol. 30. Princeton University Press.
- Tokunaga, Tetsu K and Jiamin Wan (1997). "Water film flow along fracture surfaces of porous rock". In: *Water Resources Research* 33.6, pp. 1287–1295.
- Tufenkji, Nathalie (2007). "Modeling microbial transport in porous media: Traditional approaches and recent developments". In: *Advances in Water Resources* 30.6, pp. 1455–1469.
- Tuller, Markus and Dani Or (2005). "Water films and scaling of soil characteristic curves at low water contents". In: *Water Resources Research* 41.9.
- Tuller, Markus, Dani Or, and Lynn M Dudley (1999). "Adsorption and capillary condensation in porous media: Liquid retention and interfacial configurations in angular pores". In: *Water Resources Research* 35.7, pp. 1949–1964.
- Tyler, Scott W and Stephen W Wheatcraft (1992). "Fractal scaling of soil particle-size distributions: Analysis and limitations". In: *Soil Science Society of America Journal* 56.2, pp. 362–369.
- Van Genuchten, M Th (1980). "A closed-form equation for predicting the hydraulic conductivity of unsaturated soils". In: *Soil Science Society of America Journal* 44.5, pp. 892–898.
- Vlachos, C et al. (2004). "Individual-based modelling of bacterial ecologies and evolution". In: *Comparative and Functional Genomics* 5.1, pp. 100–104.
- Wang, Gang. and Dani. Or (2010). "Aqueous films limit bacterial cell motility and colony expansion on partially saturated rough surfaces". In: *Environmental Microbiology* 12.5, pp. 1363–1373.
- Wang, Gang and Dani Or (2014). "Trophic interactions induce spatial self-organization of microbial consortia on rough surfaces". In: *Scientific Reports* 4.
- Wang, Kang, Renduo Zhang, and Fuqin Wang (2005). "Testing the pore-solid fractal model for the soil water retention function". In: *Soil Science Society of America Journal* 69.3, pp. 776–782.
- Weiss, Jérôme (2001). "Self-affinity of fracture surfaces and implications on a possible size effect on fracture energy". In: *International Journal of Fracture* 109.4, pp. 365–381.
- Yao, Kuan-Mu, Mohammad T Habibian, and Charles R O'Melia (1971). "Water and waste water filtration. Concepts and applications". In: *Environmental Science & Technology* 5.11, pp. 1105–1112.

Chapter 3

Microbial Interactions on Soil Rough Surfaces¹

3.1 Introduction

In Chapter 2, the Rough Surface Patch Model (RSPM) has been introduced and applied to modelling of single population growth on rough surfaces. In the model, cell level microbial interactions are considered within individual-based formulation including dispersion and colonial growth. The Individual based model (IBM) enables a simple application of multiple species interaction on such domains by assigning different physiological properties to individual cells. For example, various trophic dependencies, such as competition, mutualism, are the one of important capability of the model. High diversity found in soils thanks to complex soil structures can be also investigated by tracking the changes in relative abundances of pre-assigned multiple species. In this chapter, some applications of the model framework are provided, especially in a context of various hydration conditions of different soils.

3.2 Methods: Rough Surface Patch Model (RSPM) with multiple species

3.2.1 Assigning different “species” within the reaction diffusion equation

Microbial activity can be added to the RSPM by using the IBM as it was described in the previous chapter. The RSPM allows to generate dynamic environmental conditions and the IBM examines cell-level responses to it. Since the IBM is suitable for describing microbial behaviour in a heterogeneous and time-variant environment, combining these two models can be interpreted as an *in silico* experiment based on physical models. Each individual in the IBM represents a microbial cell possessing intrinsic parameters, that indicate its physiological characteristics, such as cell-size, specific growth rate, nutrient affinity, etc. (Kreft, Booth, and Wimpenny, 1998). As an addition to previous IBM models, the model proposed here is spatially explicit and includes motility of cells as they are able to actively explore

¹This chapter is partially excerpted from the publication of Kim and Or, 2016.

the domain. The motility of a cell is regulated by the chemotactic response to substrate concentrations and the swimming velocity on capillary surfaces. For its locomotion and net displacement, we used a biased random walk approach on the rough surface (Fig. 2.4).

For the model of interacting multiple species with multiple nutrients, the reaction diffusion equation, Eq. (2.5), can be simply extended since the description is given with individual cells.

$$\frac{\partial C_j(\vec{r}, t)}{\partial t} = \nabla \cdot (D_j(\vec{r}, t) \nabla C_j(\vec{r}, t)) - \frac{1}{V_w(\vec{r}, t)} \sum_{i=1}^{N(\vec{r}, t)} f_p(\vec{r}, t) \frac{\mu_i(\vec{r}, t)}{Y_{\max_j^i}} b_i(t), \quad (3.1)$$

where $C_j(\vec{r}, t)$ is the local concentration, $D_j(\vec{r}, t)$ is the local diffusion coefficient of the limiting/inhibiting substrate j and $V_w(\vec{r}, t)$ is the amount of water in a given patch at time t . The second term on the right-hand side is the reaction term calculating the total substrate consumption by microbial cells in the patch. $N(\vec{r}, t)$ is the total number of individuals at \vec{r} , $Y_{\max_j^i}$ is the species-specific maximum growth yield on the substrate j , $b_i(t)$ is the biomass, and $\mu_i(\vec{r}, t)$ is the growth rate of cell i at time t .

We assign each cell to a microbial species (or a taxon) i and its growth rate with limiting substrates by using Monod-type growth kinetics as a function of the substrate concentrations (Monod, 1942; Monod, 1949):

$$\mu_i(\vec{r}) = \mu_{\max}^i \min[f_i^1(\vec{r}), f_i^2(\vec{r}), \dots] \quad (3.2)$$

where $f_i^j(\vec{r}) = \frac{C_j(\vec{r})}{K_{S,i}^j + C_j(\vec{r})}$ (when nutrient j is a nutrient for the growth) or $f_i^j(\vec{r}) = \frac{K_{I,i}^j}{K_{I,i}^j + C_j(\vec{r})}$ (when nutrient j is an inhibitor for the growth) and μ_{\max}^i , $K_S^i/K_{I,i}^j$ are the maximum growth rate and half-saturation/inhibition constant of species i respect to the substrate j , respectively. Here, the individual growth rate at the small pore scale is assumed to be the same as the population growth rate in batch culture (Dai et al., 2013). Accordingly, the growth of an individual cell, that belongs to the species i , can be written as:

$$\begin{aligned} \frac{db_i(t)}{dt} &= (f_p(\vec{r}) \mu_{\max}^i \min[f_i^1(\vec{r}), f_i^2(\vec{r}), \dots] - m_i) b_i(t) \\ &= \mu_{\max}^i (f_p(\vec{r}) \min[f_i^1(\vec{r}), f_i^2(\vec{r}), \dots] - \alpha) b_i(t) = \tilde{\mu}^i(\vec{r}, t) b_i(t), \end{aligned} \quad (3.3)$$

where m_i is the maintenance rate of cell i and it is assumed to be linearly proportional to the maximum growth rate (i.e. $m_i = \alpha \mu_{\max}^i$). $\tilde{\mu}^i(\vec{r}, t)$ is the apparent growth rate of species i at \vec{r} and t as a result of nutrient concentration fields. For the application of the model for multiple species representing a microbial community in the model, each species are assigned as a set of different Monod parameters and yields, $\{\mu_{\max}^i, K_{s,j}^i, Y_{\max_j^i}\}$ in Eqs. (3.1). These physiological parameters can be drawn from a wide range of reported literature values.

3.2.2 Assigning trophic interactions among multiple species

An important application of the model involves cell-level trophic interactions among multiple species in the microbial community inhabiting the domain. The spontaneous spatial organisation of interdependent species has been studied for several trophic interactions based on the roughness network model (Wang and Or, 2014). The study has provided a systematic evaluation of the emergence of spatial organisation of motile microbial communities. Following this previous work, in this study, we choose competition and mutualism as the two representative forms of microbial interactions, allowing us to elucidate the spatial organisation of different microbial consortia under different surface hydrations and roughness.

For the competitive trophic interactions, we considered a simple case with two species and two nutrients; each species requires these two obligatory nutrients at different ratios and affinities (Wang and Or, 2014). The growth rate is determined by these two limiting nutrients based on the Eq. (3.3). We assign preferences (or higher affinities) of nutrients for each species by applying different maximum yields $Y_{\max,j}^i$ of species i on nutrient j where $i, j \in \{1, 2\}$ (Two species competing for two limiting nutrients). To reflect given preferences, species 1 prefers nutrient 1 and species 2 prefers nutrient 2 as shown in Fig. 3.2 with thick arrows, maximum yields should satisfy the conditions, $Y_{\max,1}^1 < Y_{\max,2}^1$ and $Y_{\max,1}^2 > Y_{\max,2}^2$, meaning that the nutrient with lower conversion rate (maximum yield) to microbial biomass is preferred.

For the mutualistic interactions, one species consumes the by-product of the other species that, in turn, may inhibit the producer's growth if not consumed. In other words, the initial producer (species 1) needs the other species to reduce the local concentration of its by-product and the consumer (species 2) needs species 1 for its growth. Here, we introduced the by-product yield β for species 1. The net growth of species 1 is given as $\mu_{\text{eff}} = (1 - \beta)\tilde{\mu}^1 = (1 - \beta)(\mu_1 - m_1)$ and the by-product yield rate would be $\Delta N_2 = \beta\mu_1 b_1 \Delta t$. For the sake of simplicity, we assume that other physiological parameters are equal between species and we ignore individual variances of cell size, cell velocity, and chemotactic sensitivity. Parameters used in simulations are given in Table A.2.

3.2.3 Measures of microbial diversity

Using the rough surface patch model (RSPM) and the IBM, variations in microbial community diversity with respect to hydration conditions and nutrient levels are investigated. For this, we assign physiological characteristics of multiple species before (numerical) inoculation on the rough surface domain. Then, the changes in species relative abundances result dynamics of microbial diversity of the system. To avoid the complex definition of microbial species, distinctive species are simply assigned by different Monod parameters of the growth function according to Eq. (2.6) (Used parameters can be found in Table A.2). Due to the moderate range of growth rate values (0.44 to 1.23 hr⁻¹ for *E. coli*), uniformly distributed values are used for the maximum growth rate μ_{\max} (Senn et al., 1994). Meanwhile, logarithmically distributed values for the half saturation constant K_s are used due to their wide spread variation (e.g. *E. coli* exhibits K_s values ranging from 40 $\mu\text{g.L}^{-1}$ up to 99 mg.L^{-1}) (Senn

et al., 1994). Differences in assigned Monod parameters imply different nutrient consumption patterns and ecological strategies spanning the range from “pseudo-copiotrophic” to “pseudo-oligotrophic” by covering a wide range of the parameter space (Zelenev, Van Bruggen, and Semenov, 2005). For the diversity calculations, other properties such as cell size and shape, motility, chemotactic sensitivity, and substrate yields were assumed equal for all species. Any functional diversity or complex trophic interactions were not included in this hypothetical scenario. To represent the most simplistic interaction, the model simulates the system with multiple species competing for a single nutrient diffusing through the aqueous phase (we consider other nutrients non-limiting). From the dynamics of the microbial population inhabiting the surface (species distinguished based on Eq. (A.21)), the time evolution of microbial diversity and the coexistence index at the steady state are investigated under various hydration conditions and two different inoculation schemes.

We employed a Shannon index, H as an indicator of the microbial diversity on the surface,

$$H(t) = - \sum_{i=1}^{N_s} p_i(t) \ln p_i(t). \quad (3.4)$$

The index is defined with the relative abundances $p_i(t) \equiv \frac{N_i(t)}{\sum_{i=1}^{N_s} N_i(t)}$, where $N_i(t)$ is the total number of individuals of species $i \in \{1, \dots, N_s\}$ at time t and N_s is the number of species on the domain that is interpreted as microbial richness. Furthermore, the normalised Shannon index (Shannon index divided with the $\ln N_s$) represents the population evenness (a.k.a. Pielou’s index) (Pielou, 1966; Jost, 2006; Colwell, 2009; Tuomisto, 2012; Jost, 2010). When the number of species is fixed (no extinction or migration), the richness is assumed to be constant and normalised Shannon index reflects the changes in evenness for different conditions ($H_D = 1$ indicates the highest evenness and all populations are equally distributed for the entire domain.). Meanwhile, when the number of species is not constant due to changes in external environmental conditions, the richness cannot be constant, thus the normalising denominator becomes a dynamic variable. In such case, the changes in richness and evenness should be tracked simultaneously to examine “appropriate” diversity dynamics.

3.2.4 Sporulation and germination processes in IBM

The model aims at describing microbial community behaviour under a wide range of matric potential, changes from several kPa to MPa; in other words, the domain can be exposed to very wet conditions after a wetting event and to very dry conditions after prolonged desiccation. As the soil dries after wetting, the effective water-film thickness can be reduced from 10^{-5} m to 10^{-9} m (See Fig. 2.3). This implies that the amount of nutrient flux to a certain location will also be reduced by several orders of magnitude due to thinning of the water film. In the model simulations, this suppresses microbial growth and leads to species extinct in the long term. To prevent this complete extinction of species during simulated drying in the model, sporulation and germination processes can be included as a survival strategy for microorganisms during desiccation.

Depletion of nutrients is the most important trigger for sporulation (Bär et al., 2002). In the model, when a cell is starved (i.e., negative growth rate) for a certain duration, it generates an endospore with a constant failure rate. In our simulations, the delay to initiation of sporulation is set at 5 h (Losick, Youngman, and Piggot, 1986). In the case of the domesticated *Bacillus subtilis* about 50-70% of the cells make the commit to sporulation under starvation stress (Schultz et al., 2009). In addition, the decision to sporulate at the cell-level is known to be stochastic and irreversible (Narula et al., 2012). In the model, we set a constant failure rate of 0.5 for all individuals. This means that half of the microbial cells will successfully sporulate and the others will remain in a vegetative state and eventually die out leading to cell-lysis when the starvation is prolonged. Note that this safety mechanism in the model is merely to control the efficiency of the “storage effect” of seeds over wetting-drying cycles. If a spore is generated, it will be stored in that location in a seed bank during the desiccation period (Lennon and Jones, 2011). This enables us to track changes in microbial interactions in different hydration states without allowing extinction of certain species during the hydration cycles.

Environmental conditions must become favourable for spore germination thereby ensuring a microorganism’s survival. At the single-cell level, two germination conditions are assumed to guarantee high survival possibility: (1) the local concentration of nutrients should be high enough to ensure positive growth rate (no starvation) and (2) the germination process is also defined as a stochastic process so spores can distribute the risk of extinction from waking up simultaneously. For instance, since timing and magnitude of rainfall are uncertain, the microorganism’s germination response should be made cautiously and thus sharing risks increases the probability of species survival. To simulate this stochastic process, we used a time-dependent probability function based on a timely ordered germination process at the individual spore level, such as micro lag time and micro-germination time (Leblanc and Lefebvre, 1984).

The IBM allows to include this decision process of individual cells for sporulation and germination (See Figure 3.1). It should be noted that in the model, this sporulation is considered a numerical construct to preserve the tail of the distribution from becoming irreversibly extinct. It helps to retain rare members in the microbial community while focusing on the main populations, and the model is able to track dynamics of microbial diversity under various hydration cycles.

3.3 Results

3.3.1 Microbial community trophic interactions

We generated a rough surface domain with the mean porosity $\bar{\Phi} = 0.4$ and $D = 1.2$ as a representative domain and well-mixed two species populations (50 individuals per species) were inoculated at the centre (four patches) of the domain. In the simulations, the nutrient concentration across the domain was given constant, $C(\vec{r}, t = 0) = C_0 = 0.2$ mg/L, and we maintained the constant concentration only at the boundary of the domain, $C(\vec{r}, t)|_{\text{boundary}} =$

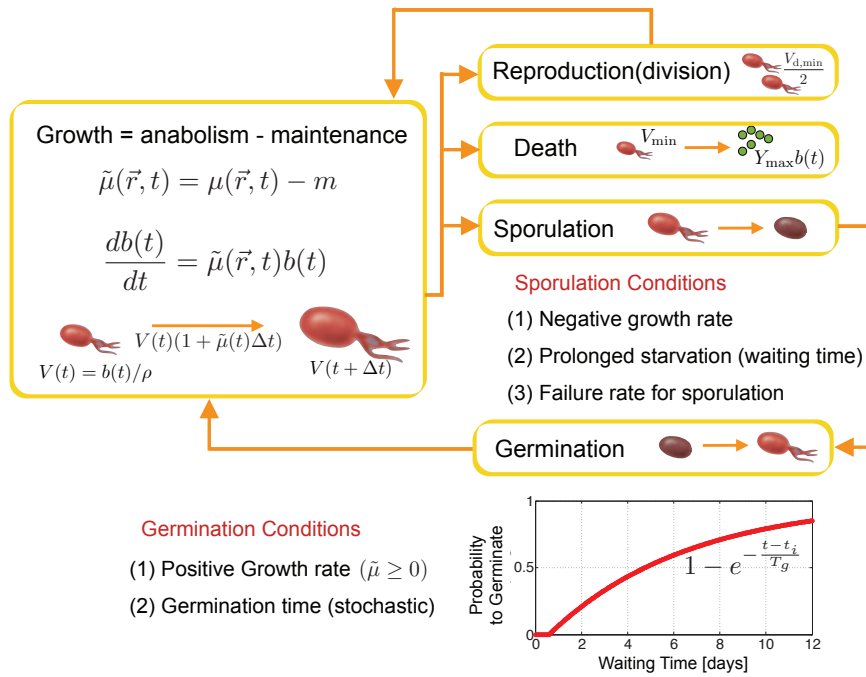


FIGURE 3.1: Scheme of the individual-based modelling (IBM). The initial work on IBM (Wang and Or, 2012; Kreft, Booth, and Wimpenny, 1998) is extended to include the process of sporulation and germination. While cell growth follows the rule from the previous model, when a microbial cell experiences prolonged starvation conditions, the agent has a chance to form a spore with a failure probability (in the simulation, this is one 0.5). For the germination, two conditions must be satisfied: the first is a nutrient condition that yields positive growth rates, the second is the stochastic waiting time. The germination process is assumed to be a stochastic process following a waiting-time dependent probability with the average germination time T_g . In the simulations, we assumed it to be 2 days. t_i indicates the time to onset of the germination process which is about 10% of the average germination time.

C_0 . The hydration conditions during the simulation time were constant and determined by matric potential value of $\psi_m = -0.5$ kPa and $\psi_m = -3.6$ kPa for the wet and dry cases, respectively (static hydration condition). $\psi_m = -3.6$ kPa is used as the drier case to guarantee the local connectivity so the spatial pattern can be observed. Fig. 3.2 depicts the resulting spatial self-organisation for four different cases (wet-dry; competition-mutualism).

For the competitive interaction, Fig. 3.2A and Fig. 3.2C, one can observe the spatial segregation of two species due to their nutrient consumption yields that lead them to occupy segregated sectors on the chemotactic band (the travelling band propagating from the inoculation point to the nutrient source that locates at the boundary of the domain). For the wet case, Fig. 3.2A, the double travelling bands of species 1 (blue) and species 2 (red) can be observed. Travelling bands are spatially divided into several sectors, one with species 1 being ahead and species 2 following and the other with vice versa. The following species makes small sectors inside of the travelling band. Some previous studies on chemotaxis show that, under certain conditions, a second band can be seen following the first when the nutrients are not depleted by the first band and the remaining amount of nutrients are sufficient to support an internal microbial band (Adler, 1966; Adler, 1973; Keller and Segel, 1971). These

studies considered only one species and these double bands are composed of two species. In this study, we observe two-layered travelling bands of two competing species. After the first travelling band appears at the boundary, microbial cells in the band induce a steep gradient in the concentration of nutrients. Since the maximum yields of species on nutrients are different, the created gradients of each nutrients become different and it would make directionally biased motions for each species. This effect generates the second band with different species to the first band. After emergence of the two travelling bands, microbial cells within the sectors cannot experience the strong gradient of nutrients because most of the nutrients are depleted by cells in the travelling bands. Hence internally remaining cells wander within the sectors. For the drier case, Fig. 3.2C, the double bands disappeared and a single travelling band forms with several small sectors of different species. These sectors are the results of competition between two species over the limited diffusing nutrients. As the system becomes dryer, the water film thickness is reduced affecting diffusion and thus consumption rates of nutrients. Although the gradient of nutrient concentration at the boundary of travelling band is similar to the wetter cases, the flux from the outside to the bands becomes smaller due to a thinner and fragmented water film. Each cell competes with others to occupy the front line leading to many smaller sectors at the travelling band. Since two nutrients are also obligatory for each species, these two species have to locate themselves at optimal positions that balance competition and cooperation simultaneously. The competition implies that they remain stay close to each other so that one species can consume the remaining nutrients after the consumption of other species. The results show that the differences in trophic interaction will affect to their spatial formation of colonies to optimise their consumptions based on physical processes such as diffusion of each nutrients. Unlike the results from roughness network model (Wang and Or, 2014), we did not observe complete segregation since the chemotactic behaviour includes higher degree of stochasticity as microbial locomotion is described with two-dimensional biased-random walk.

For the mutualistic interaction (Fig. 3.2B, Fig. 3.2D), the spatial organisation was not as strong as the competitive interactions and the pattern reflects the simplicity of the model interaction. Since species 1 (blue) degrades the primary nutrient (N1) and produces the by-product that can be used by species 2 (red) for growth, species 2 follows the chemotactic band of the species 1. In addition, the growth of species 2 requires consumption of inhibiting substance (N2), which would help species 1 by reducing local N2 concentration.

The ratio of the population size in aqueous habitats was analysed for wet and dry cases. For the wet case, Fig. 3.2B, species 1 grows better than species 2. For the dry case, Fig. 3.2D, the relative abundance becomes inverted. It shows that the degree of mutualistic interaction (assigned with the by-product yield β) and the hydration condition that mediates the effective diffusion of inhibiting substances as well as the optimal trophic distance (proposed in Wang and Or, 2014) are closely related to the relative abundance of both species.

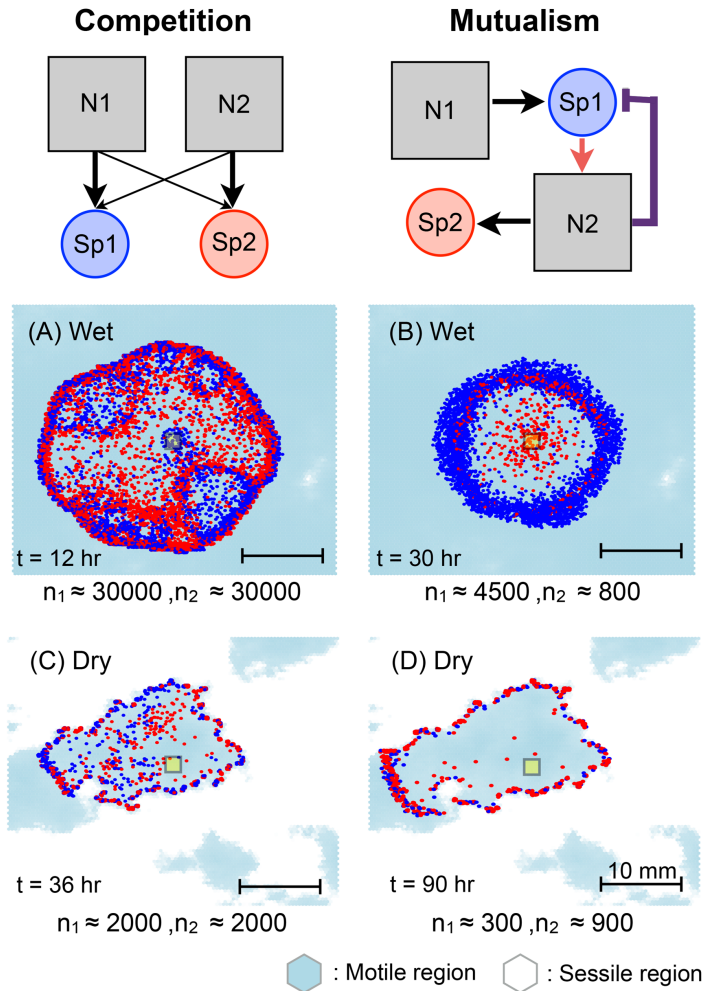


FIGURE 3.2: Examples of spatial patterns arising from different microbial consortia on rough surfaces for different hydration conditions. On the top figures, schematics of trophic interactions are given (competition and mutualism). Two example interactions are simulated for wet case ($\psi_m = -0.5 \text{ kPa}$) and dry case ($\psi_m = -3.6 \text{ kPa}$). At $t = 0$ well-mixed two populations (50 each) are inoculated at the centre (marked as a yellow square) of the roughness domain ($\bar{\Phi} = 0.4$, and $D = 1.2$). Light blue indicates the distribution of aqueous habitats and blue and red dots indicate species 1 and 2, respectively. n_i denotes the population of species i in the figure at the given time. The results show that different trophic interaction give a rise to different spatial organisations. For competitive interactions, we observe segregation between two species and altering the front line on the chemotactic band (A,C) while, for mutualistic interaction, the producer (Sp1) occupies the front line of the chemotactic band and the consumer (Sp2) follows (B,D). The spatial patterns are in qualitative agreement with the previous studies on model hydrated surfaces (Wang and Or, 2014).

3.3.2 Hydration effects on microbial diversity and onset of coexistence

A core question in contemporary environmental microbiology pertains to the origins and mechanisms that promote the unparalleled diversity found in soil. Using the rough surface patch model (RSPM) and the IBM enabled a systematic evaluation of variations in microbial community diversity with respect to hydration conditions and nutrient levels.

In Fig. 3.3A, the time evolution of normalised Shannon index (evenness, as the total richness remains constant) is given for three hydration conditions (shown in different colours) and two inoculation schemes (shown in different line types). For the “mixed” inoculation scenario, a balanced mixture of the 50 species was introduced to the surface at 4 locations, whereas for the “random” scenario, the same number of individuals were randomly distributed across the simulation domain. Results suggest that the system exhibits higher diversity/evenness when the domain is drier ($\psi_m = -3.6$ kPa) as a result of the interplay among shortened dispersal range, degree of aqueous habitat fragmentation, and decrease of nutrient flux owing to thinning water film thickness. In addition, random inoculation over the entire domain shows higher diversity (dashed lines), compared to the well-mixed population inoculation (solid lines) at the same hydration condition since the roughness of the surface allows slow-growing species to colonise a certain patch in long term by sheltering them from the competition with fast-growing species. Fig. 3.3D shows representative examples of microbial colony distribution for four different cases. When $\psi_m = -2.0$ kPa (relatively wet case with locally connected aqueous habitats), one can see the strongest competitor or the fastest growing species (with the lowest K_s and the highest μ_{\max} ; marked as orange circles) shows the highest abundance over the domain when well-mixed populations are inoculated. On the other hand, for the random inoculation, patchy distributions of various species are observed.

A biophysical index for the onset of coexistence has been proposed by (Wang and Or, 2012) based on the ratio of the microbial generation length (the distance traversed by a bacterial cell along the surface during one generation - from cell division to the next) to the effective linear size of the connected aqueous cluster. This metric is expected to vary with soil hydration conditions and surface properties that affect film thickness and microbial growth rates facilitated by diffusion (Wang and Or, 2012; Wang and Or, 2014). The index links the soil hydration conditions with micro-scale aqueous habitats fragmentation. The fragmentation of habitats inhibits microbial dispersion and growth rates of microbial populations cohabiting soil surfaces, thus highly promoting microbial coexistence. Following previous studies (Wang and Or, 2012), we have adopted the coexistence index (CI) for the rough surface patch model. We measured the CI at a state where nutrient concentration limits microbial growth of all species (on average). In other words, for a closed system with a certain amount of nutrients (i.e., no nutrient flux from outside of the domain), the population reaches a stationary state limited by nutrients. Fig. 3.3B depicts the relative abundance rank with the CI for different hydration conditions showing clearly that the population gradually becomes more even as the surfaces dries and connected aqueous habitats become smaller and more fragmented as expected from theory (Wang and Or, 2012). The significant part of the current work is the wide coverage of the Monod parameters. For the wet case, one

can observe that the CI of all the species (regardless of their relative abundance) lie below the unity (blue lines for $\psi_m = -0.5$ kPa). It means that the dispersal rate of all species is short compared to the range of interaction (via diffusion and uptake of the nutrient at the same/connected aqueous habitat). Even at $\psi_m = -3.6$ kPa, some species still exhibits the low coexistence index while some species with high CI (larger than unity, implying coexistence).

3.3.3 Surface roughness (texture) effects on microbial diversity

In the previous section, we have shown effects of hydration conditions on microbial diversity in soils (represented as rough surface domain). The result explicitly supports the ecological theory of non-competitive diversity pattern induced by spatial isolations owing to the low connectivity (Tiedje et al., 2001). Previous studies have shown that soil bacterial diversity is highly affected by particle size distribution and its relation to the fraction of fine particles in soil such as silt or clay (Sessitsch et al., 2001; Ranjard et al., 2000). Furthermore, in terms of microbial community structure in soil, it has been shown that the similarities of the communities both within and between habitats are strongly determined by soil texture rather than vegetation type or drainage conditions (Kim et al., 2013). The work of Carson et al., 2010 compared the changes in microbial diversity of two soil textures (sand (100%) and sand (90%)+silt-clay (10%)) under different matric potentials. They have measured the water filled pore space (WFPS) as an indicator of the pore connectivity and have shown that bacterial diversity is strongly correlated with WFPS for two cases with different soil textures. We have compared our model and their experiments to see the effect of soil texture on microbial diversity in soils for various hydration conditions (Fig. 3.4). For the simulated results, we have chosen different fractal dimensions to represent two different soil textures; $D = 1.35$ for sand $D = 1.65$ for 10% silty-clay (Tyler and Wheatcraft, 1992) and the surface porosity was similar for both (i.e. $\bar{\Phi} = 0.4$). We have used the same species distribution as presented in previous section; 50 species were inoculated at randomly distributed locations and the normalised Shannon index was calculated when the population sizes reach at the stationary state limited by nutrients. The results show that the model was capable of capturing the observed trends in population evenness (expressed as normalised Shannon Index) as a function of soil hydration status. The effect of surface roughness becomes important at matric potential values higher (wetter) than about $\psi_m = -3.0$ kPa. Sandy surface (smooth) supports the lower evenness compared to the silty-clay (rough) surfaces. These results could be interpreted that presence of larger pores or surface regions filled with water provide advantage to more fit species with higher growth rate and lower population evenness. At the same time, rough surface with higher fraction of small obstacles (the contribution of silt-clay sized particles) would reduce the interaction degree by increasing tortuosity of the microbial dispersal pathways (see Fig. 2.2 to compare the landscapes of the domains with different fractal dimensions), which results in higher evenness in the silty-clay domain even under wet conditions.

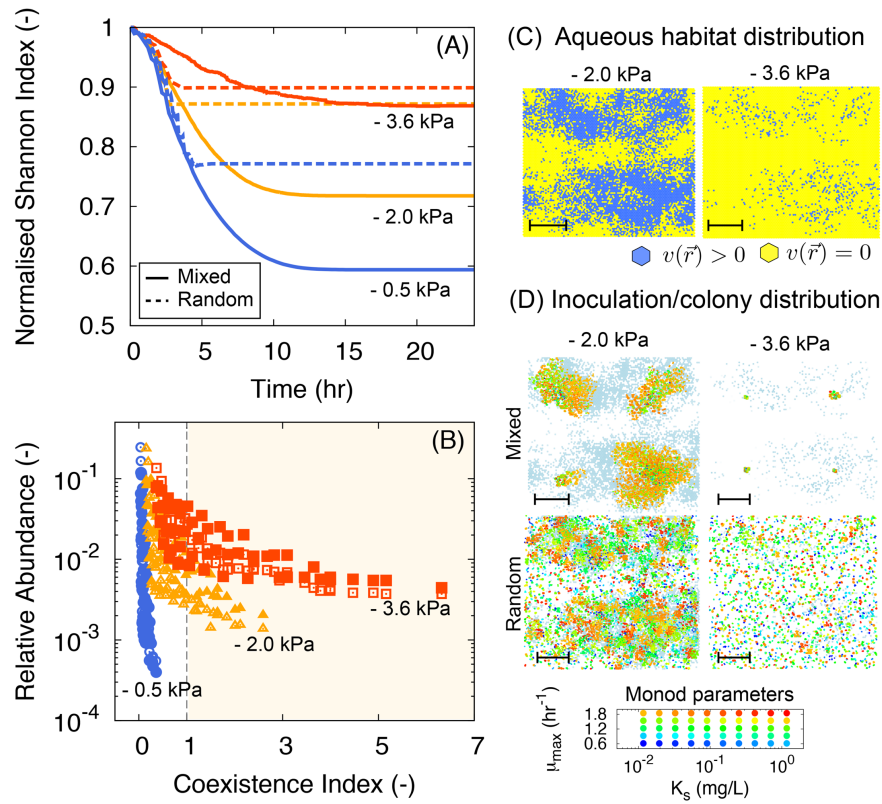


FIGURE 3.3: Microbial population diversity and coexistence index (CI) analysis of rough surface patch model ($D = 1.35$ and $\Phi = 0.4$, as an example case of sand) for a range of hydration conditions and associated aqueous phase connectivity. (A) Time evolution of normalised Shannon Index on the nutrient limited surface at different values of matric potential considering a population with 50 different species (differentiated by their Monod growth parameters). (B) Relative abundance rank is plotted with the coexistence index following Wang and Or, 2012 when the population sizes reach to the steady state with nutrient limited condition (at $t = 24$ hr). Different line colours indicate hydration conditions of the surface, $\psi_m = -0.5$ kPa in blue (wet), $\psi_m = -2.0$ kPa in yellow (intermediate), and $\psi_m = -3.6$ kPa in red (dry). For each hydration condition, we tested two different inoculation schemes; (1) well-mixed population inoculations (shown in solid lines and empty symbols), and (2) random inoculation for the entire domain (shown in dashed lines and filled symbols). An example of aqueous habitat distribution is given for two different matric potential in Fig. 3.3C. Typical microbial colony distributions for four different cases (wet-dry; mixed-random) at $t = 18$ hr are shown in Fig. 3.3D. White-grey-blue scale on the background show the the microbial swimming speed field (representing aqueous habitats) and circles in various colours at each patch represent the relative population sizes and colours indicate different species with different growth patterns according to the Monod Parameters, K_s and μ_{max} , shown in the graph below. The scale bars indicate 10 mm. Results are obtained under the competitive interaction over a single limiting nutrient among 50 different species. As the system desiccates, the microbial diversity (Shannon Index) becomes higher. It implies that species evenness is higher when system is dry and the coexistence index becomes larger than unity (marked as yellow region in Fig. 3.3B). Random inoculation of microbial cells exhibits higher diversity indices suggesting that pre-colonisation of slow-growing species derives benefits from a fragmented aqueous habitat.

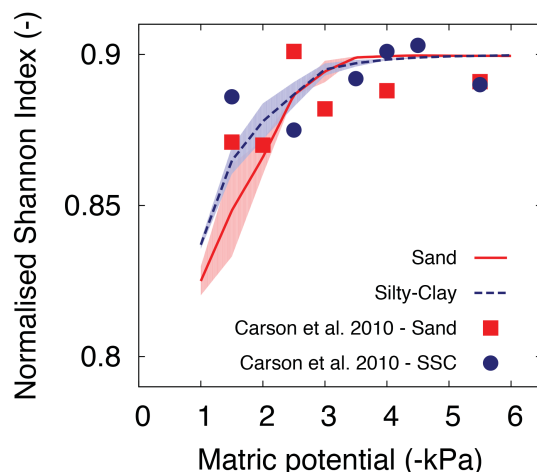


FIGURE 3.4: **Roughness effects on microbial population diversity for different hydration conditions.** Normalised Shannon index (population evenness) is calculated for two domains representing different soil textures. Different fractal dimensions are assigned for sand ($D = 1.35$) and sand+silty-clay (SSC) ($D = 1.65$). Simulated results are shown in red solid line and blue dashed line for sandy surface and sand (90%)+silty-clay (10%), respectively. The values were calculated from three different rough surface domains with same roughness parameters and the shaded areas represent 1 s.t.d. Model predictions of normalised Shannon index agree with the experimental data of Carson et al., 2010 and show a decrease in microbial population evenness as the domain becomes wet (less negative matric potential values).

The experimental data were obtained from an indigenous bacterial community in field soil that undoubtedly contained a diverse array of substrates and complex trophic interactions. Although the simulated results from RSPM assumes the simplest case of competitive interaction, the model provides the comparable range of evenness degree and its changes in different hydration conditions, thus confirming previous findings (e.g., Figure 3.3) that as a soil becomes wetter, species with better fitness characteristics may express their physiological advantages and become dominant as a result of enabled motility, aqueous habitat connectedness, and higher nutrient transport. Conversely, when the soil dries, less interactions between species are expected (due to the disabled motility-attached to the surface), which will allow species with lower fitness to inhabit locally without competing with others with higher fitness.

3.3.4 Microbial diversity dynamics during a hydration event

Not only in the static hydration conditions, the model was also applied to capture the response of bacterial diversity after a hydration event. The result of IBM with sporulation and germination processes is compared with the data of Šťovíček et al., 2017. For a comparison, the model deduced water distribution at the pore scale (relevant for microbial life) from bulk soil properties which is measured and reported at soil representative volumes. In other words, the degree of microbial interaction are obtained as a function of matric potential or saturation degree (water contents). Spatial distribution of effective water thickness on the rough surface determines the substrate diffusion field and the microbial motility enabled by

flagellated movement in aqueous phase. Therefore, hydration conditions of the surface affect the dynamics of microbial populations and the of each soil patch over a wetting drying cycle by regulating amount of nutrient flux and microbial dispersal rate.

The rough surface domain (preserving the bulk sample property) was inoculated with a well-mixed population of 50 different microbial species initiated from the centre of the domain (Fig. 3.5A). The substrate concentration was set to be constant at the boundary of the domain, modelling the influx of nutrients into the system. Mimicking the water contents measured in the field, a wetting drying cycle was applied as a boundary condition of hydration. The time-dependent-hydration condition of the domain modifies the nutrient-diffusion fields and thus changes the carrying-capacity distribution over time. The obtained platform simulated the microbial activity during a hydration desiccation cycle and this enabled us to calculate relative abundance distributions and estimate the diversity indices (Used Monod parameters are shown in Fig. 3.5B and listed in Table A.3).

In Figure 3.5 depicts comparison of observations and model predictions. In general, diversity indices, especially richness, indicated a drop during the wetting event and a recovery during desiccation. This implies that the rise of dominant species during wetting that is driven from the competitive interaction among individuals change the microbial diversity significantly. The recovery of diversity reflects the effect of aqueous habitat fragmentation; as the degree of microbial interaction decrease and less competitive species could avoid aggressive adversaries.

3.4 Discussion

The new descriptions for the microbial growth and the growth rate dependent chemotaxis enable the model to be extended with multiple nutrients and multiple species. The advantage of RSPM is the physically based description for the habitat fragmentation and connectivity that maintain salient physical features of real hydrated surfaces. Mathematical models of competitive interactions among multiple species predict that consumer species cannot co-exist in excess of the number of limiting resources at equilibrium (MacArthur and Levins, 1964; Levins, 1968; Tilman, 1982). These models are often applied in non-spatial and homogeneous habitats for all species, in other words, the model describes essentially all-to-all interactions among individuals in well-mixed conditions. Some models show that spatial subdivision allows global coexistence of competitors (Tilman, 1982; Smith, 1993; Tilman, 1994; Fahrig, 2003; Miller et al., 2005). In such cases that have enough nutrients to support many species, multiple species can coexist globally due to spatial fragmentation. Since the surface patch model already includes the aqueous habitat connectivity locally and globally, it allows us to investigate the effect of hydration on connectivities of such habitats, and consequently coexistence of multiples species (non-competitive diversity pattern) at the scale of the domain.

By using the applicability of multiple species on rough surface, we have applied RSPM

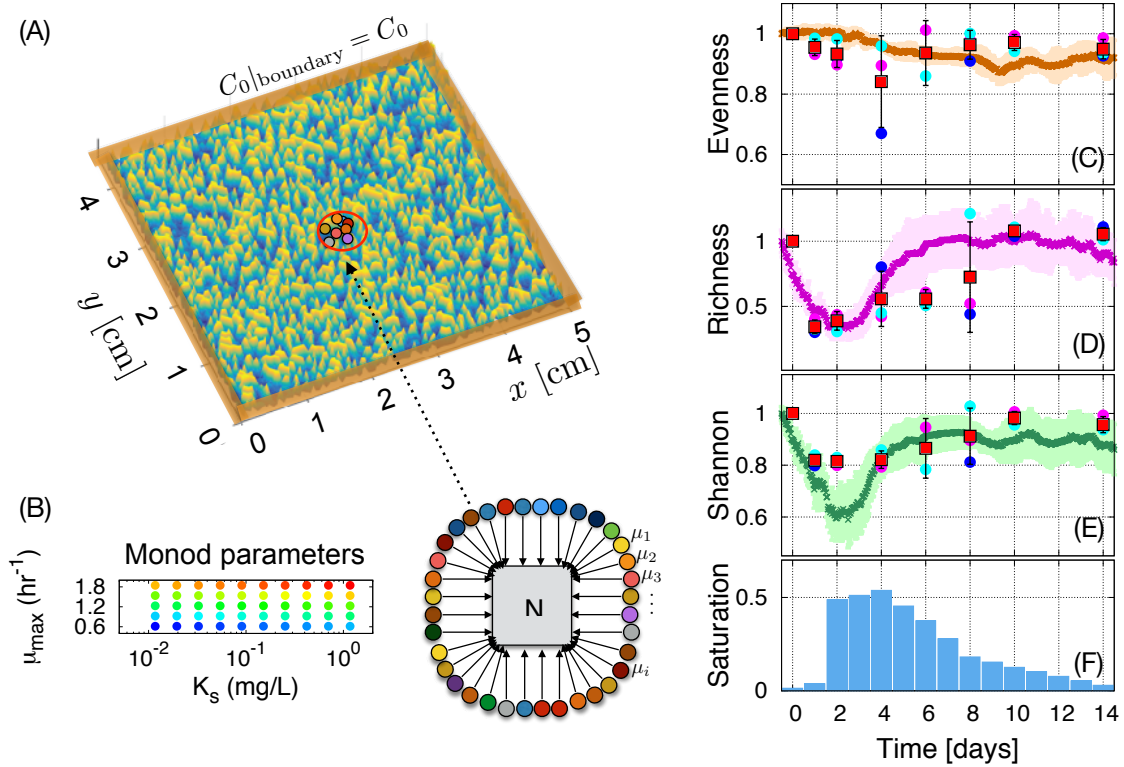


FIGURE 3.5: A wetting-drying cycle was applied to a rough-surface patch model (RSPM) to observe the effect of hydration on microbial diversity through community evenness, richness and Shannon indices. (A) A schematic of initial conditions and boundary conditions. Well-mixed populations of 50 species are inoculated in the middle of the domain. (B) The distribution of Monod parameters that are used in the simulations are given. The uniformly distributed maximum growth rates and the logarithmically distributed substrate affinities (half saturation constants for the limiting substrate). Relative changes in diversity indices, (C) evenness, (D) richness, and (E) Shannon diversity are plotted. The results are obtained from ten independent simulations under the same environmental conditions. Shaded area in simulation results indicates one standard deviation (STD) and averaged values of measurements (red squares) are presented with mean \pm STD, from three environmental replicates (shown in filled circles) in the field (Data from Št'ovíček et al., 2017). Especially, the Shannon diversity index decreased rapidly and dramatically after hydration and then recovered with desiccation. (F) The observed water contents (Data from Št'ovíček et al., 2017) were mapped to the saturation degree and these were used in the model as dynamic boundary condition.

to examine spontaneous emergence of the spatial organisation of two species on rough surfaces. The result has shown that different trophic interactions can give rise to different spatial organisation patterns of microbial communities. The model highlights the interplay between nutrient availability through diffusion and microbial chemotactic behaviour. Especially, the spatial organisation exhibits different patterns, such as double or single travelling band, patchy distribution, and alignment along the aqueous habitats, that can be controlled by surface roughness or hydration conditions. We explored the narrow range of the hydration conditions (that enables the flagella movements; see Fig. 2.4) since we only considered the motile microorganisms and their organisation through their chemotactic behaviour. The model can be extended by including sessile microorganisms or different types of cell motions (such as gliding, shoving) and localised nutrient sources to mimic natural environments.

A systematic evaluation of microbial diversity on rough surfaces has been explored with the RSPM-IBM model. The results elucidate the close relation between hydrated surface properties and microbial cell interactions. Although previous studies have provided the relations between the availability of water and microbial diversity (Torsvik and Øvreås, 2002; Bhatnagar and Bhatnagar, 2005; Bachar et al., 2010), the present model provides the physical link between water content (a bulk soil variable) and water film thickness (where microbial activity and trophic interactions occur). Prior models of IBM implemented in pore-networks have provided an approach to quantify the microbial interaction at micro-scale by using ordinary percolation theory on regular networks (Wang and Or, 2012; Ebrahimi and Or, 2014; Wang and Or, 2014). These studies have shown that pore-connectivity at micro-scale plays a pivotal role by regulating substrate diffusion rate, microbial dispersal length, and optimal trophic distance between different species. In this study, we extended these approaches on networks by using percolation processes on self-affine hydrated rough surface similar to those characterising soil grain surfaces. It allows us to track the connectivity at micro-scale and implement it at larger scales. In other words, the model considers cell-level interactions via effective water film thickness (that affects individual cell development and interactions with other cells in close proximity), which is obtained from the roughness of the domain and pore size distribution. The RSPM formulation enable consideration of soil texture effects (via roughness characteristics) on microbial diversity under varying hydration conditions. The model can be also applied to support experimental results of field observations by varying the boundary conditions of nutrient field, low-carbon surface soils/low-carbon saturated surface to examine different soil communities. The model is expected to show that the saturated subsurface soil communities possesses low Operational Taxonomic Unit (OTU) diversity and low evenness due to competitive interaction, spatial isolation explains diversity patterns in the low carbon surface soils (Zhou et al., 2002).

Since the up-scalable model allows the examination of the dynamics of microbial life over month long time scales, survival strategies can be investigated by including dormancy or sporulation in IBM procedure (Bär et al., 2002). Water availability during prolonged desiccation affects microbial communities, since the access to nutrients becomes more limited due to thinner water films, the nutrient flux reduces and the motility and metabolic activities

cannot be supported (Stark and Firestone, 1995). When long-term desiccations and sporadic wetting events are considered in the simulation, survival strategies in the model can be necessary (Jones and Lennon, 2010; Lennon and Jones, 2011). Another application could be to use the model to capture the dynamics of communities forming desert crusts (Paerl, Pinckney, and Steppe, 2000; Warren-Rhodes et al., 2007; Stal, 2012; Rajeev et al., 2013), where vertical gradients of water, temperature and light govern population dynamics and spatial distribution.

In summary, we developed a rough surface patch model to describe microbial life in soils with a possibility of upscaling spatially to cm scales and temporally to the scale of months. The model possesses high applicability, quantifying spatial-organisation of multiple species on hydrated rough surfaces and measuring microbial diversity in soil under hydration cycles over months, and examining the survival strategies during prolonged desiccation. From the model predictions and comparisons with other models and experiments, we have shown the necessity of describing microbial life in soils at pore-scale and thus the importance of scalability from at pore-scale to soil representative volumes. The model serves as a bridge connecting the spatial complexity of hydrated rough soil surfaces and the motile microbial community activity based on aqueous habitat connectivity. It can be a beneficial tool to answer the questions in soil microbial ecology for the extremely high biodiversity observed at all scales, in particular, the physical composition of soil surfaces would explain the effect of abiotic factors on microbial interactions and their evolution in terms of water and nutrient availability.

References

- Adler, J (1973). "A method for measuring chemotaxis and use of the method to determine optimum conditions for chemotaxis by *Escherichia coli*". In: *Journal of General Microbiology* 74.1, pp. 77–91.
- Adler, Julius (1966). "Chemotaxis in bacteria". In: *Science* 153.737, pp. 708–716.
- Bachar, Ami et al. (2010). "Soil microbial abundance and diversity along a low precipitation gradient". In: *Microbial Ecology* 60.2, pp. 453–461.
- Bär, M et al. (2002). "Modelling the survival of bacteria in drylands: the advantage of being dormant". In: *Proceedings of the Royal Society of London. Series B: Biological Sciences* 269.1494, pp. 937–942.
- Bhatnagar, Ashish and Monica Bhatnagar (2005). "Microbial diversity in desert ecosystems". In: *Current Science* 89.1, pp. 91–100.
- Carson, Jennifer K et al. (2010). "Low pore connectivity increases bacterial diversity in soil". In: *Applied and Environmental Microbiology* 76.12, pp. 3936–3942.
- Colwell, Robert K (2009). "Biodiversity: concepts, patterns, and measurement". In: *The Princeton Guide to Ecology*, pp. 257–263.
- Dai, Jing et al. (2013). "Charting microbial phenotypes in multiplex nanoliter batch bioreactors". In: *Analytical chemistry* 85.12, pp. 5892–5899.
- Ebrahimi, Ali N and Dani Or (2014). "Microbial dispersal in unsaturated porous media: Characteristics of motile bacterial cell motions in unsaturated angular pore networks". In: *Water Resources Research* 50.9, pp. 7406–7429.
- Fahrig, Lenore (2003). "Effects of habitat fragmentation on biodiversity". In: *Annual Review of Ecology, Evolution, and Systematics*, pp. 487–515.
- Jones, Stuart E and Jay T Lennon (2010). "Dormancy contributes to the maintenance of microbial diversity". In: *Proceedings of the National Academy of Sciences* 107.13, pp. 5881–5886.
- Jost, Lou (2006). "Entropy and diversity". In: *Oikos* 113.2, pp. 363–375.
- (2010). "The relation between evenness and diversity". In: *Diversity* 2.2, pp. 207–232.
- Keller, Evelyn F and Lee A Segel (1971). "Traveling bands of chemotactic bacteria: a theoretical analysis". In: *Journal of Theoretical Biology* 30.2, pp. 235–248.
- Kim, Mincheol et al. (2013). "Structure of soil bacterial communities in relation to environmental variables in a semi-arid region of Mongolia". In: *Journal of Arid Environments* 89, pp. 38–44.
- Kim, Minsu and Dani Or (2016). "Individual-based model of microbial life on hydrated rough soil surfaces". In: *PLoS ONE* 11.1, e0147394.
- Kreft, Jan-Ulrich, Ginger Booth, and Julian WT Wimpenny (1998). "BacSim, a simulator for individual-based modelling of bacterial colony growth". In: *Microbiology* 144.12, pp. 3275–3287.
- Leblanc, Raymond and Gerald M Lefebvre (1984). "A stochastic model of bacterial spore germination". In: *Bulletin of mathematical biology* 46.3, pp. 447–460.
- Lennon, Jay T and Stuart E Jones (2011). "Microbial seed banks: The ecological and evolutionary implications of dormancy". In: *Nature Reviews Microbiology* 9.2, pp. 119–130.

- Levins, Richard (1968). *Evolution in changing environments: Some theoretical explorations*. (No. 2). Princeton University Press.
- Losick, Richard, Philip Youngman, and Patrick J Piggot (1986). "Genetics of endospore formation in *Bacillus subtilis*". In: *Annual Review of Genetics* 20.1, pp. 625–669.
- MacArthur, Robert and Richard Levins (1964). "Competition, habitat selection, and character displacement in a patchy environment". In: *Proceedings of the National Academy of Sciences of the United States of America* 51.6, p. 1207.
- Miller, Thomas E et al. (2005). "A critical review of twenty years use of the resource ratio theory". In: *The American Naturalist* 165.4, pp. 439–448.
- Monod, Jacques (1942). "Recherches sur la croissance des cultures bacteriennes". In: *Hermann and Cie, Paris*.
- (1949). "The growth of bacterial cultures". In: *Annual Reviews in Microbiology* 3.1, pp. 371–394.
- Narula, Jatin et al. (2012). "Ultrasensitivity of the *Bacillus subtilis* sporulation decision". In: *Proceedings of the National Academy of Sciences* 109.50, E3513–E3522.
- Paerl, Hans W, James L Pinckney, and Timothy F Steppe (2000). "Cyanobacterial–bacterial mat consortia: Examining the functional unit of microbial survival and growth in extreme environments". In: *Environmental Microbiology* 2.1, pp. 11–26.
- Pielou, ECJ (1966). "The measurement of diversity in different types of biological collections". In: *Journal of theoretical biology* 13, pp. 131–144.
- Rajeev, Lara et al. (2013). "Dynamic cyanobacterial response to hydration and dehydration in a desert biological soil crust". In: *The ISME Journal* 7.11, pp. 2178–2191.
- Ranjard, L et al. (2000). "Heterogeneous cell density and genetic structure of bacterial pools associated with various soil microenvironments as determined by enumeration and DNA fingerprinting approach (RISA)". In: *Microbial Ecology* 39.4, pp. 263–272.
- Schultz, Daniel et al. (2009). "Deciding fate in adverse times: sporulation and competence in *Bacillus subtilis*". In: *Proceedings of the National Academy of Sciences* 106.50, pp. 21027–21034.
- Senn, Heinrich et al. (1994). "The growth of *Escherichia coli* in glucose-limited chemostat cultures: A re-examination of the kinetics". In: *Biochimica et Biophysica Acta (BBA)-General Subjects* 1201.3, pp. 424–436.
- Sessitsch, Angela et al. (2001). "Microbial population structures in soil particle size fractions of a long-term fertilizer field experiment". In: *Applied and Environmental Microbiology* 67.9, pp. 4215–4224.
- Smith, Val H (1993). "Implications of resource-ratio theory for microbial ecology". In: *Advances in Microbial Ecology*. Springer, pp. 1–37.
- Stal, Lucas J (2012). "Cyanobacterial mats and stromatolites". In: *Ecology of Cyanobacteria II*. Ed. by Brian A Whitton. Springer, pp. 65–125.
- Stark, John M and Mary K Firestone (1995). "Mechanisms for soil moisture effects on activity of nitrifying bacteria". In: *Applied and Environmental Microbiology* 61.1, pp. 218–221.
- Šťovíček, Adam et al. (2017). "Microbial community response to hydration-desiccation cycles in desert soil". In: *Scientific Reports* 7.45735.

- Tiedje, JM et al. (2001). "Soil teeming with life: new frontiers for soil science." In: *Sustainable Management of Soil Organic Matter*, pp. 393–425.
- Tilman, David (1982). *Resource Competition and Community Structure*. Princeton University Press Princeton, NJ.
- (1994). "Competition and biodiversity in spatially structured habitats". In: *Ecology* 75.1, pp. 2–16.
- Torsvik, Vigdis and Lise Øvreås (2002). "Microbial diversity and function in soil: From genes to ecosystems". In: *Current Opinion in Microbiology* 5.3, pp. 240–245.
- Tuomisto, Hanna (2012). "An updated consumer's guide to evenness and related indices". In: *Oikos* 121.8, pp. 1203–1218.
- Tyler, Scott W and Stephen W Wheatcraft (1992). "Fractal scaling of soil particle-size distributions: Analysis and limitations". In: *Soil Science Society of America Journal* 56.2, pp. 362–369.
- Wang, Gang and Dani Or (2012). "A Hydration-Based Biophysical Index for the Onset of Soil Microbial Coexistence". In: *Scientific Reports* 2.
- (2014). "Trophic interactions induce spatial self-organization of microbial consortia on rough surfaces". In: *Scientific Reports* 4.
- Warren-Rhodes, Kimberley A et al. (2007). "Ecology and spatial pattern of cyanobacterial community island patches in the Atacama Desert, Chile". In: *Journal of Geophysical Research* 112.G4, G04S15.
- Zeleney, VV, AHC Van Bruggen, and AM Semenov (2005). "Modeling wave-like dynamics of oligotrophic and copiotrophic bacteria along wheat roots in response to nutrient input from a growing root tip". In: *Ecological Modelling* 188.2, pp. 404–417.
- Zhou, Jizhong et al. (2002). "Spatial and resource factors influencing high microbial diversity in soil". In: *Applied and Environmental Microbiology* 68.1, pp. 326–334.

Chapter 4

Microbial Community Response to Hydration-Desiccation Cycles in Desert Soil¹

4.1 Introduction

Natural and highly dynamic variations in soil hydration conditions shape life in arid soil. Especially, soil microbial life is critically dependent on the amount and availability of water in pores and liquid films on surfaces (Or et al., 2007; Young et al., 2008) as aqueous phase configuration determines nutrient diffusion and microbial dispersion ranges (Dechesne, Or, and Smets, 2008; Dechesne et al., 2010; Vos et al., 2013). Furthermore, the temporal dynamics of water configuration within soil matrix due to rainfall, drainage, and evapotranspiration affect microbial community composition and function (Kieft, Soroker, and Firestone, 1987; Belnap et al., 2005; Huxman et al., 2004), most critically in water limited desert soil (Angel et al., 2013; Blazewicz, Schwartz, and Firestone, 2014).

More than 35% of the Earth's terrestrial surfaces are permanently or seasonally arid (Peel, Finlayson, and McMahon, 2007) where water is replenished by infrequent rainfall. Soil water is the main limiting resource for soil primary and secondary production and thus variable precipitation pulses in arid ecosystems boost massive vegetative growth (Noy-Meir, 1973; Noy-Meir, 1974). These bursts of primary productivity and the subsequent increase of plant biomass and diversity in deserts are well documented (Ogle and Reynolds, 2004); but how do soil communities of microorganisms respond to the sudden availability of water?

The effects of episodic wetting of arid soil on the diversity, size and function of microbial communities remain unclear. Early studies suggested that rainfall entails an increase in biomass and enhanced microbial activity (Kieft, Soroker, and Firestone, 1987; Belnap et al., 2005; Vishnevetsky and Steinberger, 1997) similar to that which occurs with macro-organisms. The carbon source for the microbial propagation was postulated to be either a portion of microbial biomass that died under dry conditions (Bottner, 1985) or large amount of microbial biomass that perishes during early stages of wetting due to osmotic shock (Kieft, Soroker, and Firestone, 1987; Bottner, 1985), in contrast, it was also suggested that the carbon originates from osmolytes released by cells during desiccation (Fierer and

¹This chapter is based on the publication of Šťovíček et al., 2017.

Schimel, 2003). Regardless of its origin, the microbial remnants would provide nutrients to the rain-activated communities, hence triggering CO₂ pulse and boosting new biomass (Bottner, 1985).

More recent studies that applied the tremendous advent of DNA analyses, have challenged these assumptions suggesting that the soil microbial response to wetting is independent of biomass (Fierer and Schimel, 2003; Barnard, Osborne, and Firestone, 2013; Angel et al., 2013). In conjunction with a stable biomass, a massive release of CO₂ was documented after abrupt wetting of desert soils and has been suggested to result from an increase in microbial metabolic activity (Huxman et al., 2004; Fierer and Schimel, 2003). This increase in activity could enhance microbial diversity, due to the positive correlation between microbial productivity and the length of the microbial food chains (Kaunzinger and Morin, 1998) or due to increased bacteriophage activity that keeps copiotrophs at bay and support diverse microbial communities (Bohannan and Lenski, 2000).

The response of microbial communities to hydration and desiccation could reflect changes induced by their varying environment. Concurrent changes in habitat connectivity (Dechesne et al., 2010; Treves et al., 2003), and temporal dynamics of nutrients diffusion or microbial dispersion ranges and pathways (Wang and Or, 2010). Increase in microbial dispersal rates and ranges could either increase richness by migration that could sustain and enhance the population, or decrease richness by diminishing local refuges that served competitively weaker taxa (Cadotte and Fukami, 2005).

Most studies on soil wetting effects on microbial diversity, to date, have concentrated on the hydration events following long droughts, often ignoring the role of subsequent desiccation (Placella, Brodie, and Firestone, 2012; Blazewicz, Schwartz, and Firestone, 2014; Barnard, Osborne, and Firestone, 2015). The few studies that examined the effects of soil water on residing microbial communities and the gradual drying that follows a rain event suggested that initial microbial diversity would eventually re-establish (Clark et al., 2009; Placella, Brodie, and Firestone, 2012; Bell et al., 2014). However, the patterns and dynamics of arid soil microbial communities during a hydration-desiccation cycle have not been previously studied systematically. Furthermore, the impact of rapid wetting on microbial community characteristics through a shift from oxic to anoxic condition has rarely been quantified. We predicted that water pulse following a long drought would modify the soil microbial habitats invoking changes in the microbial community composition. However, we inferred that the overall diversity would remain constant as adapted members of the microbial community would quickly occupy newly emerging niches.

The study describes the temporal dynamics of desert soil microbial diversity and community composition monitored in the field before, during, and after a rain event. Furthermore, a mechanistic model was developed to simulate changes in aqueous habitats and microbial community composition following the wetting and drying event including the onset of anoxic conditions.

4.2 Methods and Materials

4.2.1 Soil-sampling scheme

The field survey was performed in the morning, by sampling barren patches at the long-term ecological research (LTER) station of Avdat (30° 47' N, 34° 46' E, 600-700 m elevation), situated in the central Negev desert, Israel. The sampling sites were selected as replicate fields with comparable soil physico-chemical parameters and vegetation coverage (Olsvig-Whittaker et al., 2012). The average mean annual precipitation is ≈ 90 mm, distributed through several unpredictable rain events during the winter months. The annual potential evaporation is ≈ 2600 mm (Kidron and Zohar, 2010). The soil in the sampling site is wind deposited loess Kidron, Zohar, and Starinsky, 2014 with maximum water holding capacity of 16% (w/w) Doyle et al., 2006. Soil samples were collected before, during and after the first major rain event (≈ 35 mm of rain) in the winter of 2012/13 (Appendix B.1). We note that the rain event was isolated and was not preceded or exceeded by minor rain events within four weeks of the recorded event.

Soil chemical analyses followed standard methods Sparks, Helmke, and Page, 1996 as elaborated in the supplementary data (See Appendix B.2). Changes in soil chemical composition and their effect on bacterial diversity were evaluated using linear models (See Appendix B.3).

Approximately 1 kg soil was sampled between 9 and 10 am from the top 5 cm of the soil profile after discarding the soil crust, using an ethanol-cleaned scoop. At each time point, three composite samples, consisting of eight randomly selected subsamples, were collected from adjacent 40 \times 25 m plots (max. distance 20 m), providing three biological replicates. The soil samples were collected into sterile bags, transported to the laboratory and kept at 4 °C until processing (within no more than 4 h of sampling). Soil was homogenised by sieving through autoclave-sterilised sieve (2 mm pore grid size) as previously described (Angel, 2012). Samples for RNA extraction were collected and stored at -80 °C and the rest of the sample was dried at 65 °C in preparation for the chemical analysis.

4.2.2 RNA extraction and reverse transcription

The RNA profile of bacterial community was followed due to previously reported DNA recalcitrance in soil environment (Carini et al., 2016), especially in response to changes in water content (Angel et al., 2013). Total nucleic acids were extracted with phenol/chlorophorm at the pH 7 according to the protocol published by Angel, 2012. Complementary DNA was generated by reverse transcription, using ImProm-II reverse Transcription System (Promega, Madison, WI). The cDNA used for Illumina sequencing was generated using 50 - 100 ng of the template RNA to ensure a sufficient amount of DNA material for sequencing. In contrast, sequences used for qPCR were generated from 1 ng RNA to ensure precision of the back calculation.

4.2.3 Quantitative PCR (qPCR)

Total nucleic acids were extracted from the soil samples as previously described (Angel, 2012). The extract was purified by MasterPure RNA Purification Kit (Epicentre, Madison, WI). The DNA was degraded by DNase I supplied with the kit and the RNA samples were stored at -80 °C for further analysis. All qPCR reactions were performed in an iCycler thermocycler equipped with a MyiQ detection system (Bio-Rad, Munich, Germany). Data were processed using CFX Manager 3.0 software (Bio-Rad). Standards containing a known number of copies of the target gene, 16S rRNA from *Escherichia coli*, were serially diluted to calibrate each qPCR. The universal primers S-D-Bact-0341-a-S-171 and S-Bact-0515-a-S-19 (Table B.1) were used for amplification. Each qPCR contained the following mixture: 10 μ l SYBR Absolute Blue qPCR Rox Mix (Thermo Scientific, Waltham, MA), 1 μ l of 400 nM of each primer (Metabion, Rehovot, Israel), 5 μ l template cDNA and 3 μ l molecular-grade water (HyLab, Rehovot, Israel). Abundance estimation was performed under the following conditions: 95 °C for 15 min, followed by 35 cycles of 95 °C for 10 s, 60 °C for 15 s and extension at 72 °C for 30 s.

4.2.4 Taxonomic analysis

The microbial 16S rRNA units were sequenced with MiSeq (Illumina, San Diego, CA), using primers S*-Univ-0515-a-S-19 and S-D-Bact-0787-b-A-20 targeting the V3 and V4 region of the gene (Table B.1). The resulting reads were clustered into operational taxonomical units (OTUs) that corresponded to 90% of the rRNA difference using the Open reference picking pipeline, combining clustering against a database (Silva 111) with de novo clustering of yet unknown taxa, provided by the QIIME package (Caporaso et al., 2010). OTUs were identified and analysed, using the Silva 111 dataset (Quast et al., 2013) and sequences that were not present in the database were clustered de novo (see Appendix B.5). OTU counts in different samples were adjusted equal depth of sequencing (in our case 7955 sequences).

4.2.5 Non-metric multidimensional scaling

To evaluate the grouping of different communities, we performed a nonmetric multidimensional scaling (NMDS) transformation using the vegan package (Oksanen et al., 2016; McMurdie and Holmes, 2013). The solution was reached after 5 iterations with the final stress equal to 0.055 (indicative that the transformation is a good representation of the dataset).

4.2.6 Modelling microbial growth on hydrated surfaces

To assess the trends and soil microbial community dynamics in response to hydration desiccation cycles, we employed a mechanistic model comprised of three major components: representation of the physical soil environment and water and gas configurations, quantification of microbial community functioning at the cell level, and the resulting biophysical interactions during changes in hydration. We have modified previously developed rough

surface patch model (RSPM) to represent the physical environment in soil profile that mimics effects of hydration on water films and spatio-temporal changes in nutrient diffusion fields and oxygen inputs from gas phase to liquid phase that support growth of microorganisms (Kim and Or, 2016). Microbial activities of community members were represented by the Individual-Based Model (IBM) that considers a simple metabolism, motility, chemotactic behaviour and trophic interactions among individuals (See Appendix C).

The physical domain mimicking soil profile was generated and was inoculated with populations of 40 different virtual microbial taxa. In the model, we considered only 40 taxa to represent population dynamics and their dispersal within the domain (far less than the richness in real soil). The dissolved oxygen concentration was assigned from the partial pressure of the oxygen in the atmosphere (20.09%). Its input to the liquid phase is calculated following Henry's law and diffuses through the domain from the top of the domain. The concentration of other primary substrate, we assume in this study as the carbon source (e.g. glucose), was fixed at the top boundary of the domain to represent diffusive influx of nutrients into the system. The measured water contents in the field were mapped to the matric potential as a boundary condition of hydration to determine the physical configuration of water and gas in soil matrix. (For the details of its physical, chemical, and environmental conditions that are used as boundary conditions, see Appendix C). This time-dependent-hydration condition imposed on the domain modifies the nutrient-diffusion field and gas-liquid configuration and thus changes the carrying-capacity distribution over time. The obtained platform simulated the dynamics of the 40 microbial populations during the wetting-drying cycle and this enabled us to calculate the relative abundance dynamics and estimate the Shannon index.

To simplify the representation of a diverse microbial community, firstly, we designed microbial taxa with two distinctive groups, aerobically growing cells and anaerobically growing cells (20 taxa for each group in this work). Here, we assume that the majority of community members are heterotrophic organisms utilising the available carbon source for their metabolism. The growth functions for these two groups are given by different Monod parameters according to:

$$\mu_i^{ae}(\vec{r}) = \mu_{\max,i} \min\left[\frac{C_C(\vec{r})}{K_{S,i}^C + C_C(\vec{r})}, \frac{C_O(\vec{r})}{K_S^O + C_O(\vec{r})}\right] \quad (4.1)$$

$$\mu_i^{an}(\vec{r}) = \mu_{\max,i} \min\left[\frac{C_C(\vec{r})}{K_{S,i}^C + C_C(\vec{r})}, \frac{K_I^O}{K_I^O + C_O(\vec{r})}\right] \quad (4.2)$$

where μ_i^{ae} and μ_i^{an} are growth functions of aerobes and anaerobes, respectively. Two groups differentiate with the growth response to the local oxygen concentration, $C_O(\vec{r})$, assigned with the half-saturation constant, K_S^O , for aerobes and the inhibition constant, K_I^O , for anaerobes. We note that we did not consider the variation of bacterial response to oxygen and only obligate aerobes and obligate anaerobes are included in the model for the simplicity (Morris and Schmidt, 2013). $C_C(\vec{r})$ is the local concentration of the carbon source and differences between virtual taxa are assigned with the maximum growth rate and Monod half-saturation on carbon source, $\{\mu_{\max,i}, K_{S,i}^C\}$. These values were drawn from a wide range

of reported literature values of aerobically and anaerobically growing cells (Pirt, 1965; Heijnen, 1999; Stouthamer, 2012). However, we note that higher maximum growth rates of anaerobes were assumed to compensate the strong inhibition term of oxygen in the model. The range of Monod parameters that used in the current modelling work are reported in Table C.2 in Appendix C. Differences in assigned Monod parameters implied different nutrient-consumption patterns and ecological strategies, spanning the range from “pseudo-copiotrophic” to “pseudo-oligotrophic”, during the hydration cycle (Zelenev, Van Bruggen, and Semenov, 2005). Other properties, such as cell size, shape, motility, chemotactic sensitivity, and optimal temperature for growth were assumed to be equal for all taxa. The substrate yields and maintenance rates were assumed to be different between aerobic taxa group and anaerobic taxa group considering that high costs of anaerobic activity (Pirt, 1965; Stouthamer, 2012).

The simplicity gained by pre-assigned Monod parameters enabled definitive tracking of the dynamics of relative abundance and microbial diversity. To avoid loss of taxa during the hydration desiccation cycles (due to the smallness of the community size that could be practically modelled), we tagged the cells at starvation condition (negative growth rate, costs for maintenance exceed growth related costs) as potentially active cells so it contributes to the diversity index dynamics.

4.2.7 Measuring microbial diversity

We selected the observed OTUs, $N_s(t)$, as the species-richness estimator $R(t)$, and the Pielou’s evenness index as an estimator of population evenness $E_P(t)$ (Pielou, 1966).

$$R(t) = N_s(t), \quad (4.3)$$

$$E_P(t) = -\frac{1}{\ln R(t)} \sum_{i=1}^{N_s(t)} p_i(t) \ln p_i(t). \quad (4.4)$$

where $p_i(t)$ is the relative abundance or the probability that a certain individual belongs to species i at time t . The Shannon Index is the non-normalised form of Pielou’s index estimating the total-diversity;

$$H(t) = -\sum_{i=1}^{N_s(t)} p_i(t) \ln p_i(t). \quad (4.5)$$

To compare field observations with and model predictions we used relative changes of the Shannon index, $\tilde{H}(t)$ by dividing the data sets by the Shannon index at the onset of the rain event, $t = 0$;

$$\tilde{H}(t) = \frac{H(t)}{H(0)}. \quad (4.6)$$

4.3 Results

4.3.1 Community composition changes during a rainfall event: Field observations

The cumulative rainfall during the field study reached $\sim 35\text{mm}$ in the course of two days (IMS, 2014). The water content of the soil collected before the rain event (September 2012) was about 1 % (g/g) which is equivalent to matric potential of -10MPa (calculated according to Castelblanco et al, 2012 Castelblanco et al., 2012). During two rainy days, the soil water content increased to 17 % (g/g) (Appendix B.1) with total rainfall depths of $\sim 16\text{ mm}$ and $\sim 19\text{ mm}$ for the first and second consecutive rainy days, respectively. This water content is equivalent to a matric potential of -10kPa and a degree of saturation ~ 0.6 suggesting the soil reached its water holding capacity. Observations have shown a gradual desiccation of the soil over time after the rain. Detailed chemical analysis of the soil solution did not reveal significant changes except in the total ammonia and total nitrate (see Appendix B.2). The amount of total nitrate increased right after the rain and gradually decreased as soil desiccated while the amount of total ammonia exhibited complementary behaviour with nitrate.

We applied qPCR analysis on extracted ribosomal RNA showing that the total abundance of microbial ribosomes was stable over the wetting-drying cycle. We quantified the abundance of microbial ribosomes throughout the wetting and desiccation period in all our soil samples (see Appendix B.6). No significant changes in the total ribosomal count was detected except in the first sample taken during severe desiccation, which showed an order of magnitude decrease in ribosomal count. While the total abundance remained stable, the relative abundance exhibited dynamic changes following the rainfall event (Fig. 4.1A). Observed is that several taxa became dominant for the first few days after the rainfall (*Enterobacteriales*, *Clostridiales*, *Lactobacillales* and *Bacteroidales*). Subsequently, these dominant classes slowly declined in the ensuing soil desiccation. Some of these, specifically *Clostridiales*, *Lactobacillales* and *Bacteroidales* are known to include many anaerobic species (Sumbali and Mehrotra, 2009) implying that some niches in the saturated desert soil have become anaerobic. Importantly, the pre-rainfall community composition was recovered within six to seven days as the soil water content dropped below 10 % (g/g).

The changes in the relative abundances of soil microbial taxa reflect drastic and rapid changes in microbial community composition. To track the shift in the microbial communities during the wetting and drying cycle, we performed a non-metric multidimensional scaling (Fig. 4.2B). Three distinct communities emerged: one (orange squares) consisting of a microbial community in desiccated desert soil (low hydration conditions), a second (blue triangles) clustering the communities in very wet soil (the saturation degree is about $0.5\sim 0.6$, denoted as high hydration conditions), and a third (green circles) banding together a community during the gradual desiccation (denoted as medium hydration conditions). Moreover, soil communities were grouped according to time of sampling: samples collected during low hydration conditions (time zero, days 1, 8, 10 and 14), high hydration (days 2, 4 and 6) and intermediate hydration conditions (days 6 and 8), formed separate clusters,

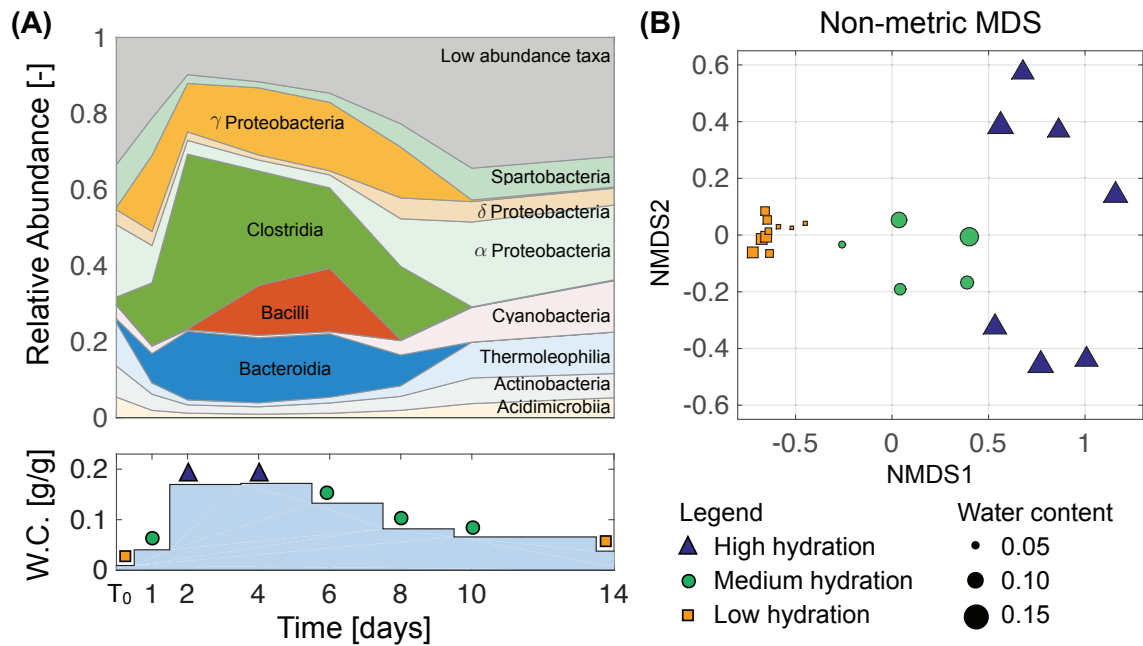


FIGURE 4.1: **Microbial community response to a hydration cycle.** (A) The dynamics of relative abundance of soil microbial classes during the field observations. Each time point is an average of three biological replicates. Time zero is an average of three samples taken from fully desiccated soil during the summer of 2012. (B) Non-metric Multidimensional Scaling based on the soil rRNA sequencing (MiSeq) dataset. The size of the symbol corresponds to the water content measured in the soil at the time of sampling.

quantitatively. This implies that the main component of the community before the rain event and after the desiccation was not affected.

4.3.2 Community diversity metrics during a rainfall event: Field observations

The variations in relative abundance were translated to changes in soil microbial diversity. Fig. 4.2 depicts the dynamics of field measured microbial diversity during the wetting-drying event in terms of richness, observed OTU, and evenness, Pielous's evenness. In Fig. 4.2A, the richness index indicated a statistically significant drop during the rain event (days 1 and 2) and initial stages of desiccation (days 4 and 6) (per group $t < -11.80$, per group $p < 1.8 \times 10^{-10}$, Appendix B.8). Similarly, we observed a slight decrease in evenness, but unlike changes in richness, the evenness index displayed gradual but statistically significant changes (field observation $F = 77.8$, $p = 3.015 \times 10^{-6}$, Appendix B.8) and steady recovery during the hydration cycle (Fig. 4.2B). In the field, we monitored three adjacent plots concomitantly; minute differences in their desiccation rates instigated observable differences in the community (Fig. 4.2C). For example, the soil in plot 3 (marked as yellow in the figure) dried relatively faster than in plots 1 and 2, possibly leading to earlier onset of changes in microbial diversity in the plot.

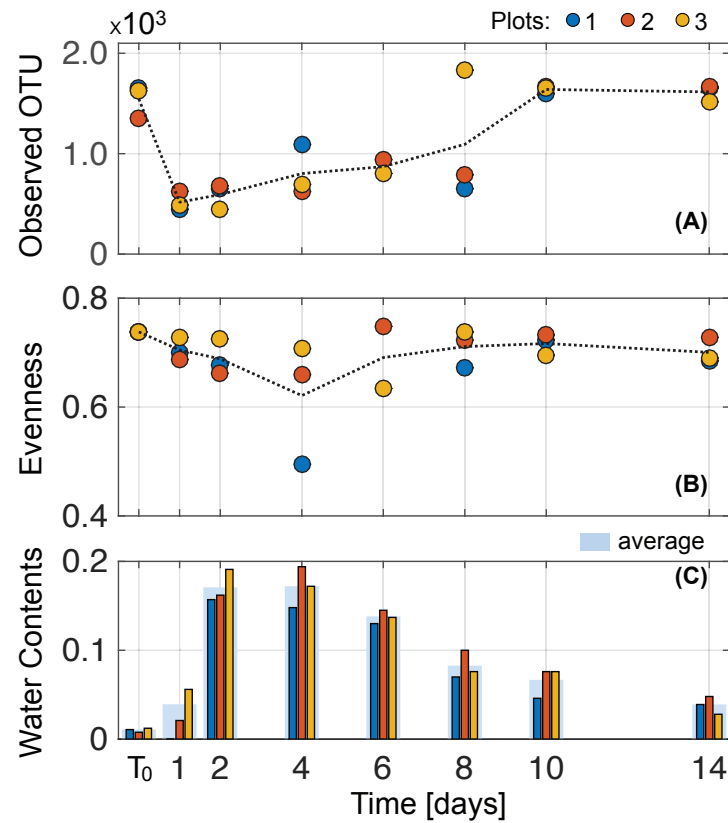


FIGURE 4.2: **Microbial diversity dynamics during a hydration cycle.** Richness and evenness of soil bacterial populations sampled in three adjacent plots during a wetting-drying cycle. Population richness was expressed as the number of observed species (A) and population evenness is displayed using Pielou's evenness index (or Shannon's evenness) (B). The trend line is the averaged value of the data. The measured gravimetric water content of each plot (in corresponding colours) and the averaged values are given in (C).

4.3.3 Microbial community dynamics during a rainfall event: model predictions

We applied a mechanistic model for microbial populations' dynamics during changes in soil wetness (induced by the rainfall event). The model results were in qualitative agreement with field observations in terms of microbial diversity and the community composition changes. Fig. 4.3 depicts the predicted effect of hydration dynamics on the soil microbial community. After soil wetting, the relative abundance of various taxa exhibited a dynamic response. Fig. 4.3A shows the rise of anaerobic classes (marked with strong colours) from day 2 to day 7, replacing aerobic classes that were prevalent in the dry soil. The model results show the sharp decrease of anaerobes at between day 6 and day 7 as the soil became aerated again. While drying, air penetrates through the profile and shifts most of the domain back from anoxic to oxic conditions (corresponding to a water content of 0.1 [g/g]). Furthermore, in Fig. 4.3B, the relative changes in Shannon index was chosen as the key diversity index for a comparison with the field observations. The decrease in diversity indicates the rises of dominant taxa during wetting. This is driven by competitive interactions among individuals over a common substrate, in this case the carbon source. The connected aqueous habitats and the increased dispersal of cells allowed intense competition for the substrate thereby causing the changes in diversity. The recovery of diversity reflects the role of aqueous habitat fragmentation. As the degree of connectivity in the aqueous phase decreased, microbial interactions are spatially limited (Wang and Or, 2012). Essentially, the observed dynamics of community composition and diversity are the outcome of simultaneous effects of the competition over dissolved substrates and the temporary dominance of anaerobic taxa due the transition from oxic to anoxic conditions in some parts of the wet soil.

4.4 Discussion

Several studies have followed soil microbial communities *in situ* measuring their diversity and community composition following wetting events (Treves et al., 2003; Zhou et al., 2002; Carson et al., 2010). The findings generally support higher microbial diversity (or coexistence degree) under drier conditions where the aqueous-phase is largely fragmented and dispersion is limited. In previous studies, hydration conditions were under controlled laboratory experiments (Fierer and Schimel, 2003; Placella, Brodie, and Firestone, 2012; Angel et al., 2013; Blazewicz, Schwartz, and Firestone, 2014), and in the field following the first rainfall after a prolonged draught (Placella, Brodie, and Firestone, 2012; Barnard, Osborne, and Firestone, 2013; Barnard, Osborne, and Firestone, 2015). In contrast with such a step-change in hydration conditions, the dynamics of soil microbial diversity during a cycle of wetting and gradual desiccation received little attention. Here, we provide a detailed account of microbial response to wetting and subsequent drying in desert soil in the field and using a mechanistic model.

We quantified soil microbial community composition in desert before, during, and after a major rain event. Microbial community dynamics deduced from field observations were compared with results of the mechanistic model that simulated substrate diffusion and growth of multi-taxa microbial communities on idealised hydrated soil profile. The

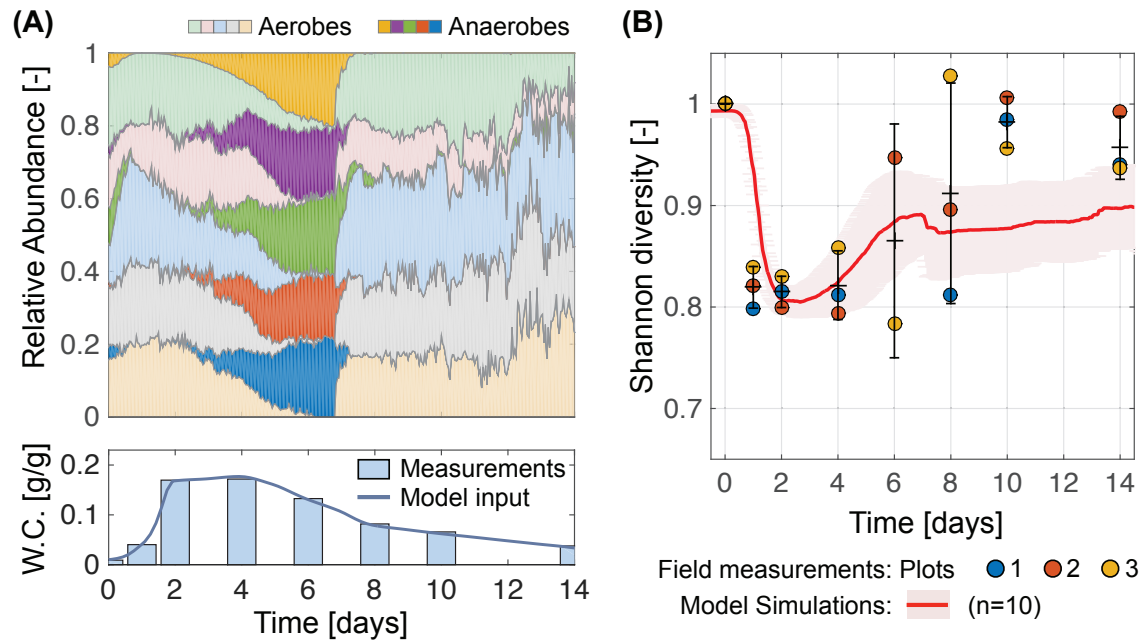


FIGURE 4.3: **Model prediction: effect of hydration dynamics on the soil microbial community.** A wetting-drying cycle was applied to the modified rough-surface patch model (RSPM) to observe its effect on bacterial diversity and the community composition. (A) The relative abundance dynamics of modelled bacterial classes are depicted. In the simulations, 40 virtual taxa (20 taxa growing aerobically and other 20 taxa growing anaerobically) were inoculated. For this figure, the virtual taxa were classified to 10 classes (5 aerobic groups shown in light colours and 5 anaerobic groups shown in dark colours) and the relative abundance dynamics of 10 independent simulations were averaged. (B) Shannon index of the simulated bacterial populations were compared with the field measurements suggesting that in both the diversity decreased rapidly after wetting and then recovered with drying. For this comparison, the field measurements and the simulation results were rescaled with the value at day 0 (dry soil) indicating the relative changes. Results from 10 individual simulations (with different inoculation of microbial cells and different soil structures with same pore size distribution and porosity) are averaged (red line) and shaded area (in pink) indicates the standard deviation (s.t.d.). Averaged values of measurements are presented with $\text{mean} \pm \text{s.t.d.}$ (black solid lines) calculated from three environmental replicates in 3 adjacent plots.

field observations and modelling results yield similar temporal dynamics of microbial diversity and community composition during hydration-desiccation cycles. The results show a significant change in composition together with a decrease in soil microbial diversity upon wetting, and gradual recovery as the soil dries to pre-rainfall levels (Figures 4.1, 4.2, and 4.3). The model focuses on the putative role of aqueous phase connectivity. Following soil wetting, the increased connectivity of habitats facilitates higher rates of substrate diffusion and larger ranges of cell dispersion as key mechanisms for the observed loss of diversity during wetting (Wang and Or, 2012; Kim and Or, 2016). Furthermore, the detailed account of water configuration dynamics in the soil profile and associated oxygen diffusion suggest the possibility of establishing anoxic conditions following wetting that may last a day or two within the soil volume.

We have shown that microbial community composition and diversity co-vary during wetting, and subsequently recover to pre-wetting levels as the soil desiccates (Figures 4.1 and 4.2). Notably, the extensive changes in diversity were not reflected in the abundance of active microorganisms (Appendix B.6), this is in agreement with previous studies that show no changes in soil bacterial abundance with hydration following a long drought (Barnard, Osborne, and Firestone, 2013; Angel et al., 2013; Blazewicz, Schwartz, and Firestone, 2014). The soil community composition was significantly altered after a large rainfall event (Fig. 4.1). Some of the observed changes under field conditions could have resulted from dispersal and establishment of other migrated taxa during desiccation. Yet, in the model such dispersal processes were minor, and the resulting diversity patterns were similar to field observations (Fig. 4.3). Moreover, the nMDS suggest that the community composition had returned to pre-rainfall composition (Fig. 4.1B). This supports that immigration effect during and after wetting is questionable. We thus conclude that although dispersal and migration could contribute to changes in community composition, they are probably not the main factors in this complex ecosystem.

A factor that may have contributed to the changes in microbial community composition was the formation of anoxic regions in the soil following the rainfall (Tiedje et al., 1984; Skopp, Jawson, and Doran, 1990). In other words, the high hydration conditions near the soil surface and the stimulation of biological activity limited oxygen diffusion and promoted favourable conditions for anaerobic organisms (Figures 4.1 and 4.3A). Such episodic increase in anaerobic taxa with the onset of anoxic conditions has been shown in previous studies (Lozupone and Knight, 2007) and their occurrence was coincidental to increase fluxes of carbon and nitrogen (Tiedje et al., 1984; Torsvik and Øvreås, 2008; Standing and Killham, 2006). The carbon flux is introduced with precipitation from the carbon fixing soil crust in this system (Austin et al., 2004). This results in an increase of available organic carbon in the top soil profile during days 1-3 (Appendix B.2). This was represented in the model by the substrate entering to the system given as the constant concentration boundary condition on the top of the domain. Mass flux, however, is elevated during wetting due to greater water film thickness (See Fig. C.1 in Appendix C). Heterotrophic organisms utilise this fixed carbon source for their activity. Since metabolism in anoxic environments requires different terminal electron acceptors, nitrate respiration is expected. The soil nitrate pool increases

during dry periods and this will be available for anaerobes together with carbon sources right after the wetting (Austin et al., 2004). Changes in total nitrate (Appendix B.2) support the postulated increase in anaerobic activity (Austin et al., 2004). On the other hand, total ammonia shows a complementary behaviour to nitrate (Appendix B.2) owing to the suppressed aerobic activity as aerobic metabolism requires ammonia as the nitrogen source. We note that it is not clear where the ammonia flux comes from. It could be either nitrogen fixing bacteria on the crust or a deposited source at the surface introduced by the rainfall event. Although nitrogen dynamics were not considered explicitly in the model, the observed community dynamics match with the predictions. This implies that the sampled area might be mostly carbon limited during the wetting-drying cycle as the model assumed.

The generally dry and aerated arid soil conditions suggest that such dominance is limited to narrow windows of hydration conditions after major rain events and before the soil dries. Within this narrow activity window in the field, the community richness has markedly decreased (Fig. 4.2A) and the diversity patterns were consistent in both the field and the model (Figures 4.2 and 4.3B). The rise of putative anaerobic taxa replacing aerobic taxa in the dry soil does not necessarily explain the decrease in diversity as it could have temporally increased richness during the transition from oxic to anoxic or vice versa. This suggests that oxygen depletion might not be the main driver for the observed decrease in diversity.

A full representation of microbial diversity found in soil is beyond the computational capacity of most models. Predicting microbial responses from dynamic hydration conditions in soil might be even more challenging. The model attempts to minimise the variability of physiological differences among taxa and to highlight the effect of physical and chemical processes in soil during wetting and drying. Dividing microbial taxa in soil community to only two groups, obligate aerobes and obligate anaerobes, is somewhat arbitrary, yet imposing the field-measured hydration values yielded a reasonable time scale for anoxic dominance. The sharp transition in community composition in the model predictions (Fig. 4.3A) reflects on immediate inhibition of anaerobic activity following the gas phase percolation (increase in oxygen concentration). In reality one expects a more gradual response afforded by soil heterogeneity and a range of microbial responses to the presence of oxygen. For example, including facultative anaerobes or aerotolerant anaerobes might form groups which persist through out the wetting-drying cycle and smoothen the transition.

The model distinguishes microbes according to the response to O₂ presence, as well as a substrate utilisation through Monod parameters (specific growth rate and affinity to the carbon source), while other morphological and physiological characteristics were assumed to be identical. Each combination of parameters defined a “taxon” and was counted in the diversity metrics. The choice for the parameter range can change the intensity of diversity response in the model, yet the impact is relatively small and the selected values cover the realistic range (Heijnen, 1999). While the model predicts the response in Shannon index by tracking the microbial populations, the observed decrease in richness was not met. This is because of the dominance of rare members in the real community indicating that other survival strategies may exist besides the growth functions (i.e. facultative anaerobes,

aerotolerant anaerobes, or microaerophiles). Furthermore, the diurnal changes in the soil temperature were also included in the model of microbial activity, but its contribution were not significant, since the variation of the soil temperature keep within the range of 2 – 5°C (See Fig. C.2 in Appendix C).

Despite numerous simplifying assumptions of taxon numbers and their interactions, the model qualitatively reproduces the community dynamics observed in the field (Figures 4.2 and 4.3). In contrast with our initial hypothesis we noted drastic changes in both the diversity and the composition of soil microbial communities after soil wetting. The interplay between the sudden increase in nutrient fluxes, rapid dispersion and stronger competition over the dissolved carbon source was important for the diversity dynamics. The enhanced connectivity during wetting resulted in the reduction of diversity with small effects on nutrient-consumption patterns while altering the composition from the aerobes-dominated to anaerobes-dominated community. The remarkable recovery of diversity and composition with the onset of dry conditions illustrates the resilience of the microbial communities in desert soils following major rain events. The field results together with the model simulations point to the centrality of the configuration of water and gas in soil shaping cell dispersion and nutrient diffusion and thus in microbial community diversity and composition in a highly dynamic soil environment.

References

- Angel, Roey (2012). "Total Nucleic Acid Extraction from Soil". In: *Protoc. Exch.*
- Angel, Roey et al. (2013). "Active and total prokaryotic communities in dryland soils". In: *FEMS microbiology ecology* 86.1, pp. 130–138.
- Austin, Amy T et al. (2004). "Water pulses and biogeochemical cycles in arid and semiarid ecosystems". In: *Oecologia* 141.2, pp. 221–235.
- Barnard, Romain L, Catherine A Osborne, and Mary K Firestone (2013). "Responses of soil bacterial and fungal communities to extreme desiccation and rewetting". In: *The ISME Journal* 7.11, pp. 2229–2241.
- (2015). "Changing precipitation pattern alters soil microbial community response to wet-up under a Mediterranean-type climate". In: *The ISME Journal* 9.4, pp. 946–957.
- Bell, Colin W et al. (2014). "Soil microbial and nutrient responses to 7 years of seasonally altered precipitation in a Chihuahuan Desert grassland." In: *Glob. Chang. Biol.* 20.5, pp. 1657–73. ISSN: 1365-2486.
- Belnap, Jayne et al. (2005). "Linkages between microbial and hydrologic processes in arid and semiarid watersheds". In: *Ecology* 86.2, pp. 298–307.
- Blazewicz, Steven J, Egbert Schwartz, and Mary K Firestone (2014). "Growth and death of bacteria and fungi underlie rainfall-induced carbon dioxide pulses from seasonally dried soil". In: *Ecology* 95.5, pp. 1162–1172.
- Bohannan, Brendan J M and Richard E Lenski (2000). "Linking genetic change to community evolution: insights from studies of bacteria and bacteriophage". In: *Ecol. Lett.* 3, pp. 362–377.
- Bottner, P (1985). "Response of microbial biomass to alternate moist and dry conditions in a soil incubated with ¹⁴C- and ¹⁵N-labelled plant material". In: *Soil Biol. Biochem.* 17.3, pp. 329–337. ISSN: 00380717.
- Cadotte, Marc W and Tadashi Fukami (2005). "Dispersal, spatial scale, and species diversity in a hierarchically structured experimental landscape". In: *Ecology Letters* 8.5, pp. 548–557.
- Caporaso, J Gregory et al. (2010). "QIIME allows analysis of high-throughput community sequencing data." In: *Nat. Methods* 7.5, pp. 335–336. ISSN: 1548-7091.
- Carini, Paul et al. (2016). "Relic DNA is abundant in soil and obscures estimates of soil microbial diversity". In: *Nature Microbiology* 2, p. 16242.
- Carson, Jennifer K et al. (2010). "Low pore connectivity increases bacterial diversity in soil". In: *Applied and Environmental Microbiology* 76.12, pp. 3936–3942.
- Castelblanco, JA Muñoz et al. (2012). "The water retention properties of a natural unsaturated loess from Northern France". In: *Geotechnique* 62.2, pp. 95–106.
- Clark, Jeb S et al. (2009). "Soil microbial community response to drought and precipitation variability in the Chihuahuan Desert." In: *Microb. Ecol.* 57.2, pp. 248–60. ISSN: 0095-3628.
- Dechesne, Arnaud, Dani Or, and Barth F Smets (2008). "Limited diffusive fluxes of substrate facilitate coexistence of two competing bacterial strains". In: *FEMS Microbiology Ecology* 64.1, pp. 1–8.

- Dechesne, Arnaud et al. (2010). "Hydration-controlled bacterial motility and dispersal on surfaces". In: *Proceedings of the National Academy of Sciences* 107.32, pp. 14369–14372.
- Doyle, Jack et al. (2006). "Cellulase dynamics in a desert soil". In: *Soil Biology and Biochemistry* 38.2, pp. 371–376.
- Fierer, Noah and Joshua P Schimel (2003). "A proposed mechanism for the pulse in carbon dioxide production commonly observed following the rapid rewetting of a dry soil". In: *Soil Science Society of America Journal* 67.3, pp. 798–805.
- Heijnen, Joseph J (1999). "Bioenergetics of microbial growth". In: *Encyclopedia of Bioprocess Technology*.
- Huxman, Travis E et al. (2004). "Precipitation pulses and carbon fluxes in semiarid and arid ecosystems." In: *Oecologia* 141.2, pp. 254–68. ISSN: 0029-8549.
- IMS (2014). *Israel Meteorological Service*. URL: <http://data.gov.il/ims>.
- Kaunzinger, Christina M. K. and Peter J. Morin (1998). "Productivity controls food-chain properties in microbial communities". en. In: *Nature* 395.6701, pp. 495–497. ISSN: 0028-0836.
- Kidron, Giora J and Motti Zohar (2010). "Spatial evaporation patterns within a small drainage basin in the Negev Desert". In: *Journal of hydrology* 380.3-4, pp. 376–385.
- Kidron, Giora J, Motti Zohar, and Abraham Starinsky (2014). "Spatial distribution of dust deposition within a small drainage basin: Implications for loess deposits in the Negev Desert". In: *Sedimentology* 61.7, pp. 1908–1922.
- Kieft, Thomas L., Edith Soroaker, and Mary K Firestone (1987). "Microbial biomass response to a rapid increase in water potential when dry soil is wetted". In: *Soil Biol. Biochem.* 19.2, pp. 119–126.
- Kim, Minsu and Dani Or (2016). "Individual-based model of microbial life on hydrated rough soil surfaces". In: *PLoS ONE* 11.1, e0147394.
- Lozupone, Catherine A and Rob Knight (2007). "Global patterns in bacterial diversity". In: *Proceedings of the National Academy of Sciences* 104.27, pp. 11436–11440.
- McMurdie, Paul J and Susan Holmes (2013). "phyloseq: an R package for reproducible interactive analysis and graphics of microbiome census data." In: *PLoS One* 8.4, e61217. ISSN: 1932-6203.
- Morris, Rachel L and Thomas M Schmidt (2013). "Shallow breathing: bacterial life at low O₂". In: *Nature Reviews Microbiology* 11.3, pp. 205–212.
- Noy-Meir, Immanuel (1973). "Desert ecosystems: environment and producers". In: *Annu. Rev. Ecol. Syst.* 4.1973, pp. 25–51.
- (1974). "Desert ecosystems: higher trophic levels". In: *Annu. Rev. Ecol. Syst.* 5.1974, pp. 195–214.
- Ogle, Kiona and James F Reynolds (2004). "Plant responses to precipitation in desert ecosystems: integrating functional types, pulses, thresholds, and delays." In: *Oecologia* 141.2, pp. 282–94. ISSN: 0029-8549.
- Oksanen, J et al. (2016). "vegan: community ecology package. R package version 2.0–7. 2013". In: URL <http://CRAN.R-project.org/package=vegan>.

- Olsvig-Whittaker, Linda et al. (2012). "Patterns in habitat type, species richness and community composition at Avdat LTER, Israel". In: *Journal of Landscape Ecology* 5.3, pp. 5–23.
- Or, Dani. et al. (2007). "Physical constraints affecting bacterial habitats and activity in unsaturated porous media—a review". In: *Advances in Water Resources* 30.6, pp. 1505–1527.
- Peel, M C, B L Finlayson, and T A McMahon (2007). "Updated world map of the Köppen-Geiger climate classification". In: *Hydrol. Earth Syst. Sci.*
- Pielou, ECJ (1966). "The measurement of diversity in different types of biological collections". In: *Journal of theoretical biology* 13, pp. 131–144.
- Pirt, SJ (1965). "The maintenance energy of bacteria in growing cultures". In: *Proceedings of the Royal Society of London B: Biological Sciences* 163.991, pp. 224–231.
- Placella, Sarah A, Eoin L Brodie, and Mary K Firestone (2012). "Rainfall-induced carbon dioxide pulses result from sequential resuscitation of phylogenetically clustered microbial groups". In: *Proceedings of the National Academy of Sciences* 109.27, pp. 10931–10936.
- Quast, Christian et al. (2013). "The SILVA ribosomal RNA gene database project: improved data processing and web-based tools." In: *Nucleic Acids Res.* 41, pp. D590–6. ISSN: 1362-4962.
- Skopp, J, MD Jawson, and JW Doran (1990). "Steady-state aerobic microbial activity as a function of soil water content". In: *Soil Science Society of America Journal* 54.6, pp. 1619–1625.
- Sparks, Donald L, PA Helmke, and AL Page (1996). *Methods of soil analysis: Chemical methods*. Tech. rep. SSSA.
- Standing, Dominic and Ken Killham (2006). "The Soil Environment". In: *Modern Soil Microbiology*. Ed. by Jan Dirk van Elsas, Jansson JK, and Trevors JT. 2nd. CRC Press, Taylor and Francis, Boca Raton, FL, pp. 1–22.
- Stouthamer, Adriaan Hendrik (2012). *Quantitative aspects of growth and metabolism of microorganisms*. Springer Science & Business Media.
- Šťovíček, Adam et al. (2017). "Microbial community response to hydration-desiccation cycles in desert soil". In: *Scientific Reports* 7.45735.
- Sumbali, Geeta and RS Mehrotra (2009). *Principles of microbiology*. Tata McGraw-Hill.
- Tiedje, JM et al. (1984). "Anaerobic processes in soil". In: *Plant and Soil* 76.1-3, pp. 197–212.
- Torsvik, Vigdis and Lise Øvreås (2008). "Microbial diversity, life strategies, and adaptation to life in extreme soils". In: *Microbiology of Extreme Soils*. Springer, pp. 15–43.
- Treves, DS et al. (2003). "A two-species test of the hypothesis that spatial isolation influences microbial diversity in soil". In: *Microbial Ecology* 45.1, pp. 20–28.
- Vishnevetsky, S and Y Steinberger (1997). "Bacterial and fungal dynamics and their contribution to microbial biomass in desert soil". In: *J. Arid Environ.* 37.1, pp. 83–90. ISSN: 01401963.
- Vos, Michiel et al. (2013). "Micro-scale determinants of bacterial diversity in soil". In: *FEMS Microbiology Reviews* 37.6, pp. 936–954.

- Wang, Gang. and Dani. Or (2010). "Aqueous films limit bacterial cell motility and colony expansion on partially saturated rough surfaces". In: *Environmental Microbiology* 12.5, pp. 1363–1373.
- Wang, Gang and Dani Or (2012). "Hydration dynamics promote bacterial coexistence on rough surfaces". In: *The ISME Journal* 7.2, pp. 395–404.
- Young, I.M. et al. (2008). "Microbial distribution in soils: Physics and scaling". In: *Advances in Agronomy* 100, pp. 81–121.
- Zelenev, VV, AHC Van Bruggen, and AM Semenov (2005). "Modeling wave-like dynamics of oligotrophic and copiotrophic bacteria along wheat roots in response to nutrient input from a growing root tip". In: *Ecological Modelling* 188.2, pp. 404–417.
- Zhou, Jizhong et al. (2002). "Spatial and resource factors influencing high microbial diversity in soil". In: *Applied and Environmental Microbiology* 68.1, pp. 326–334.

Chapter 5

Hydration Status and Diurnal Trophic Interactions Shape Microbial Community Function in Desert Biocrusts¹

5.1 Introduction

Large tracks of arid lands are often covered by thin biological soil crusts (hereafter, biocrusts) that, in the absence of significant vegetation cover, play an important role in arid ecosystems. Biocrusts serve as biodiversity “hotspots” (Belnap, Weber, and Büdel, 2016) and act as ecosystem engineers to promote rehabilitation of eroded soils in arid lands (Bowker, 2007). The photoautotrophs inhabiting biocrusts support rich and diverse food webs and provide the main source of organic carbon covering over 70 % of arid land surface area (about 30 % of all terrestrial surfaces; Belnap and Lange, 2003; Mager, 2010). Biocrust microbial activity produces extracellular organic exudates that alter the immediate environment by supporting a stable structure, altering water retention and transport properties of the biocrusts (Mazor et al., 1996; Belnap and Lange, 2003; Belnap, 2003; Rodríguez-Caballero et al., 2015). The resulting modification of local hydrological processes such as infiltration-runoff and water storage (Chamizo et al., 2012) enhances the capability of other organisms to cope with water scarcity (Chamizo et al., 2016; Faist et al., 2017). Furthermore, this water-regulating function of biocrusts also protects the soil surface against wind and water erosion (Belnap and Gillette, 1998; Warren, 2001).

Evidence suggests that biocrusts are locally and globally important component of the ecosystem in terms of biogeochemical fluxes; arid land biocrusts affect global cycles of carbon and nitrogen (Weber, Büdel, and Belnap, 2016). Biocrusts regulate carbon dioxide efflux through soil by fixing ~ 0.6 Pg of carbon per year, which is about 9 % of the net primary productivity of this ecosystem (Sancho et al., 2016; Elbert et al., 2012). Their contribution to nitrogen fixation from the atmosphere is even more significant, evaluated as about 26 Tg per year, corresponding to about 40 % of the global terrestrial biological nitrogen fixation (Elbert et al., 2012; Ciais et al., 2014). Although biocrust contribution to terrestrial nitrogen fixation

¹This chapter is based on the publication of Kim and Or, 2017.

is considerably high, arid land ecosystems remain largely nitrogen-limited due to the substantial losses of nitrogen gas caused by abiotic (temperature, pH) and biotic (nitrification, denitrification) processes (Peterjohn and Schlesinger, 1990; McCalley and Sparks, 2009). The global emission of reactive nitrogen (such as NO, HONO) from biocrusts has been estimated at about 20 % of the globally emitted reactive nitrogen compounds from natural soils (Weber et al., 2015).

Biocrusts are sensitive and highly vulnerable systems to anthropogenic and natural disturbances, leading to the erosion of the invaluable microbial community (Kuske et al., 2012). Natural recovery of biocrusts is a slow process (multi decades) (Weber et al., 2016), and the recovery rates may vary widely depending on precipitation, soil texture, or carbon content (Weber et al., 2016). The recovery stage follows a general successional pattern beginning with surface soil colonisation by mobile cyanobacteria such as *Microcoleus vaginatus* (Büdel et al., 2009; Zaady et al., 2010). The settlement of photoautotrophic organisms is followed by other phototrophic, heterotrophic and chemoautotrophic microorganisms, algae, fungi, mosses, and lichens etc (Pepe-Rannek et al., 2016). Most established biocrusts consist of microscopic and macroscopic organisms within the top few centimetres of the soil surface (e.g., around 5 mm thick for cyanobacterial crusts and up to 5 cm thick for moss crusts). A typical biocrust community consists of hundreds of species, representing different levels of trophic interactions that enable an entire arid land ecosystem to function systematically (Bowker, Maestre, and Escolar, 2010; Bowker, Soliveres, and Maestre, 2010).

The composition and structure of a biocrust are determined by several environmental factors. At a local scale, soil properties such as texture, nutrient level, and pH, are the main determinants (Bowker et al., 2016). At a global or regional scale, the characteristics of a biocrust community differ with climatic regions (from cold to warm deserts), soil type, and crust age since last disturbance (Garcia-Pichel et al., 2013; Bowker et al., 2016). Regional climatic variables such as the amount of precipitation or the potential evapotranspiration influences the biomass of cyanobacteria and other photoautotrophs, as a consequence, define the community composition (Isichei, 1990; Hagemann et al., 2015; Barnard, Osborne, and Firestone, 2015). Studies have shown that cyanobacterial crust distribution and their activity are highly correlated with periods between rain events and soil water availability rather than precipitation amount of a single rain event (Lange, 2003; Cable and Huxman, 2004; Büdel et al., 2009). Thus, the response of microbial activity to wetting events, such as precipitation, is a crucial factor in the ecology of biocrusts.

Notwithstanding the importance of these ecosystems, quantitative studies using mathematical or computational approaches are scarce and interrelations among biological, physical, and chemical processes that underlie this sensitive ecosystem remain unclear. Statistical analyses have been served as the main means to deduce impacts of various environmental factors on observed biocrust response in majority of field and laboratory studies (Barger et al., 2006; Grote et al., 2010; Bowker, Maestre, and Escolar, 2010; Castillo-Monroy et al., 2011; Maestre et al., 2013). Process-based models have been also developed for biocrusts of lichens and mosses (Porada et al., 2013; Porada et al., 2014; Porada et al., 2016; Porada et al., 2017). These works estimate their contribution to the carbon uptake and nitrous oxide emissions

at global scale under various climatic conditions.

This study reports a mechanistic model for the early stages of biocrust formation and key biophysical and chemical processes. We construct a representation of hydrological processes within a biocrust and trophic interactions among key members of biocrust microbial community. The model includes a detailed account of the physical domain available for microbial life (simple rough surfaces) and the consequences of different hydration conditions on connectivity and transport of nutrients, gas, temperature, and light. The model also considers dynamic chemical processes. The key ingredient in biocrust functioning is the highly dynamic and spatially self-organising microbial community. For simplicity, we considered four microbial groups: photoautotrophs (primarily cyanobacteria), aerobic heterotrophs, anaerobic heterotrophs (denitrifiers), and chemoautotrophs (Garcia-Pichel and Belnap, 2002; Johnson et al., 2005; Johnson, Neuer, and Garcia-Pichel, 2007; Abed et al., 2010; Abed et al., 2013; Rocha et al., 2015), to consider their role in carbon and nitrogen cycling. Table 5.1 summaries the model in terms of processes, variables, parameters, and simulated results in this work.

The organisation of this paper is as follows: We first introduce the key physical and chemical processes in the mechanistic model. Next, the biochemical feedback of microbial activity and its spatial organisation is investigated. The results of this model are compared with data obtained from laboratory experiments. Finally, we provide new insights into the ecological functions of unsaturated soil structures in established biocrusts in arid regions.

5.2 A mechanistic model of desert biocrusts

The study was motivated by interest in biocrusts as a model ecosystem supporting multi-species microbial community that interact at a limited spatial extent under large environmental gradients (Bowker et al., 2014). We employ individual based modelling of microbial processes in the presence of sharp environmental gradients in resources and conditions. The model addresses first the physical domain and its dynamics characteristics that vary with hydration conditions. Chemical and biological processes are then introduced into the physical domain (associated primarily with the aqueous phase and its distribution).

5.2.1 The biocrust physical domain

We use a modified rough surface patch model (Šťovíček et al., 2017; Kim and Or, 2016) to represent the top millimetres to centimetres of soil where most biocrusts develop (see Fig. 5.1a). For the physical domain, we consider a vertical cross-section of a biocrust that considers rough soil grains and the gas pathways between grains (described in 2-D but in a simplified fashion including 3-D features in a spatial element). Geometrically-explicit features of the rough surface (pyramid-shaped depressions of different sizes) are averaged according to a probability distribution of the pore sizes (representing roughness decorating soil grains). For the size distribution, we assign three parameters, local porosity ϕ , surface roughness porosity Φ , and fractal dimension D (Šťovíček et al., 2017; Kim and Or, 2016).

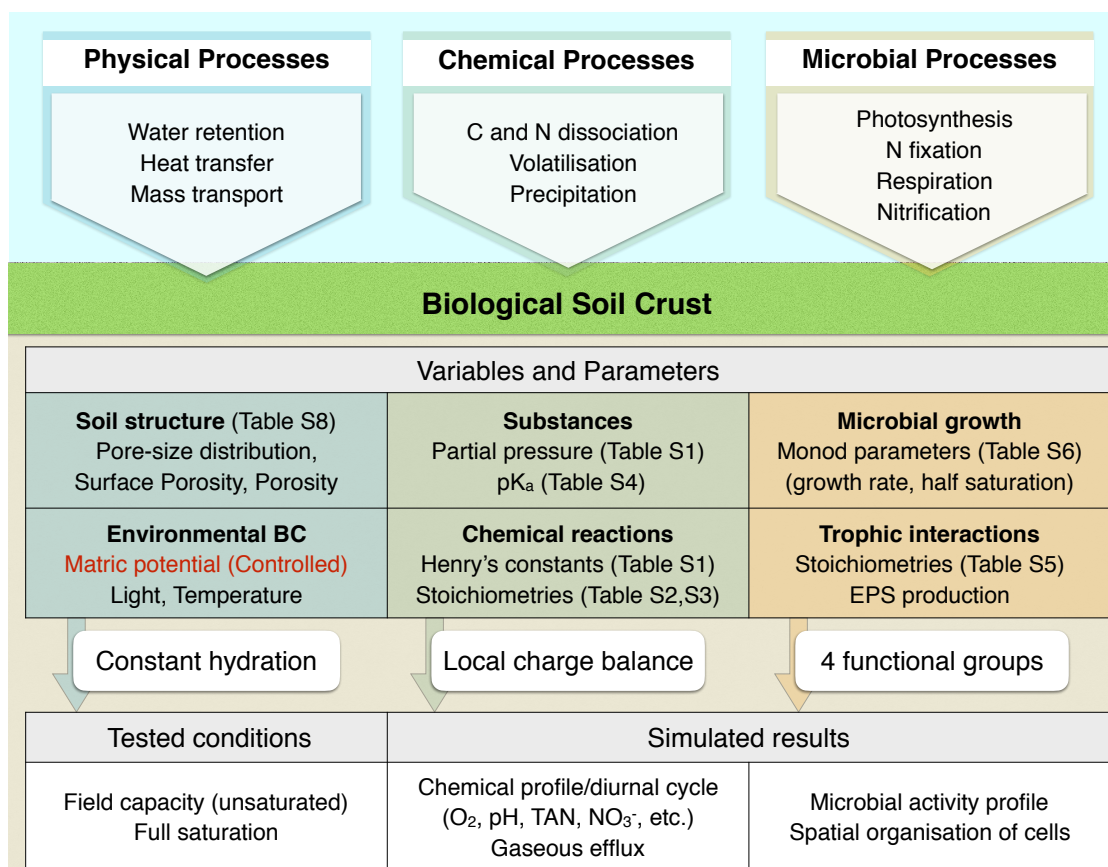


TABLE 5.1: **A summary of the desert biocrust model (DBM).** The DBM includes various physical, chemical, and microbial processes occurring within biocrusts. Variables and parameters used in modelling are listed and the main assumptions for each process are summarised. In this work, we focused on how hydration conditions under diurnal cycles shape chemical and biological profiles within desert biocrusts.

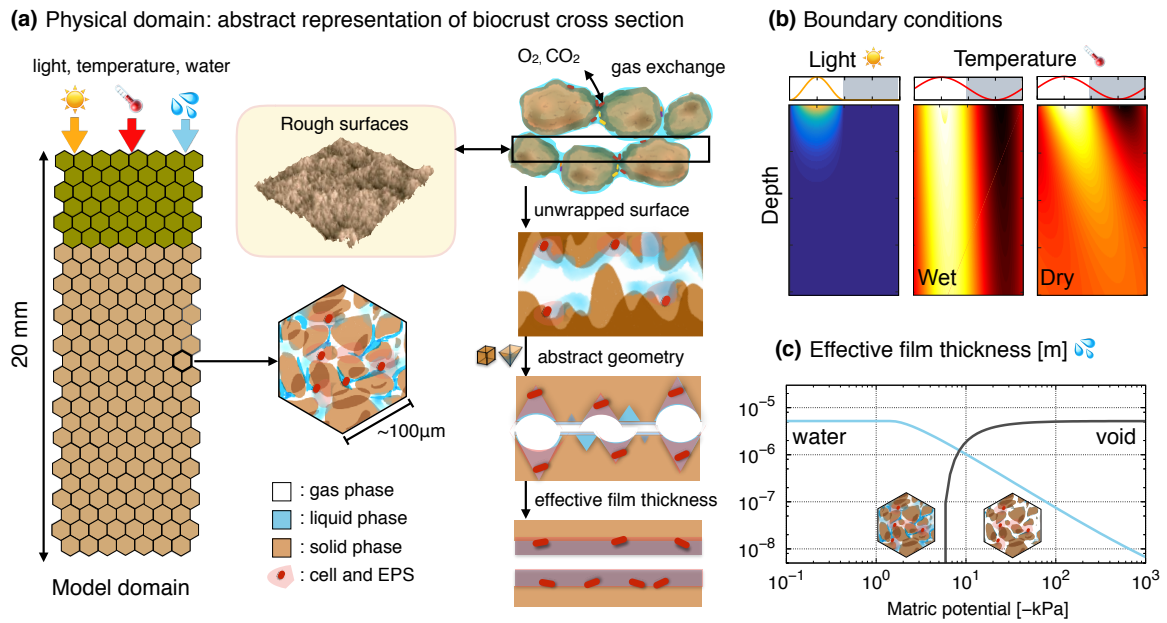


FIGURE 5.1: A schematic of the physical domain and environmental conditions of the desert biocrust model (DBM). (a) A cross section of the physical domain of desert soil is modelled up to 20 mm and most microbial activities occur at the uppermost 5 mm, indicating “biocrust”, the region of interest in this work (marked in green). The domain is comprised of hexagonal patches with different physical properties to represent the heterogeneity of soil (mimicking soil pores and rough surfaces) with the pre-assigned mean values (See Table D.7 in Appendix D). We note that physical properties of the domain were assigned to be statistically the same for biocrust and below-crust regions. The rough surface is simplified with abstract geometries to calculate the effective film thicknesses of the surface on a patch scale. To represent interference of the liquid phase with respect to gas diffusion, we consider two rough soil surfaces (cross sections) facing each other as described previously (Kim and Or, 2016; Št’ovíček et al., 2017). (b) Spatio-temporal variations in light intensity and temperature as boundary conditions (wet and dry) during a diurnal cycle. Surface boundary conditions of temperature changes in accordance with light irradiance during the same period of a day. Unlike light penetration, the temperature profile depends on hydration conditions (thermal diffusivity is controlled by the matric potential). Under wetter conditions, thermal diffusivity is higher. (c) The effective thicknesses of water film and void space are determined as a function of matric potential.

This abstract representation of the physical domain permits physically-based calculation of the amount of water held within the rough surface for given matric potential (our standard hydration metric). The water films then determine the diffusion rates and pathways of nutrients, microbial dispersion rates and ranges, connectivity, and the complementary spaces for gas diffusion. While the representation of microbial life is assigned to the two-dimensional rough surface, the inference of gas phase within the cross-section is applied into the model by considering two rough surfaces facing each other (see Fig. 5.1a). This approach allows us to extend the surface model to the vertical cross-section model and to include gas diffusion and mass transfer between liquid and gas phases as a function of matric potential by using effective film thickness (Fig. 5.1c) without the complexity of 3-D modelling of the pore space in the biocrust (Kim and Or, 2016; Št’ovíček et al., 2017).

We represent a section through the biocrust by a spatially distributed soil properties assigning key parameters $\{\phi, \Phi, D\}$ to individual patches (representing soil grains or small aggregates). This domain represents a strong heterogeneity of soil structure including regions with low or high porosities. For simplicity, we assume in this study that the matric potential is constant for the entire biocrust. Hence, the water distribution in the model biocrust including phase connectivity and related properties were predetermined for a simulation. Although evaporation or drainage processes following (rare) rainfall events can generate hydraulic gradients across the biocrust, these effects can be neglected given the small domain size (< 10 mm).

5.2.2 Environmental boundary conditions

The model includes three essential environmental variables that shape microbial community in desert soil: water, light, and temperature. For simplicity, we prescribe the hydration status of the biocrust, this status determines the configurations of the liquid and gas phases (that, in turn, determines the respective diffusion coefficients). The extension to dynamic hydration conditions is relatively simple considering infiltration, redistribution and soil evaporation (these processes are functions of the crust properties and are representable analytically or numerically). Temperature and light are applied as time-dependent boundary conditions to the top of the crust domain to mimic diel cycles.

Light irradiance on the surface

Light determines the photosynthetic activity of the phototrophs (e.g., cyanobacteria) within the biocrust (Berner and Evenari, 1978; Davies et al., 2013). To represent light penetration and diurnal day-night cycle, we express irradiance, $I(z; t)$, as a function of depth z and time t ,

$$I(z; t) = \begin{cases} \frac{I_0}{2} (1 - \cos(\omega t + \phi_I)) e^{-z/\delta_p} & \text{day} \\ 0 & \text{night} \end{cases} \quad (5.1)$$

where I_0 is maximum irradiance (at midday on the biocrust surface). Incident irradiance at the surface is given by the period $P \equiv \frac{2\pi}{\omega}$ (24 hours) and $\phi_I = 0$ (with $t = 0$ at sunrise, 6AM). δ_p is the light characteristic penetration depth. The values of I_0 and δ_p regulate the activity and spatial location for an optimised growth of phototrophs in the model. The sinusoidal function with I_0 and ω can be changed with respect to the specific location of the biocrust and the season of the year (and even the local aspect and slope of the surface). The value of δ_p varies from about 10^{-4} to 10^{-3} m depending on the amount of mineral or soil texture (grain size distribution) (Garcia-Pichel and Bebout, 1996). In this work, we chose a maximum irradiance of $I_0 = 500 \mu \text{ mol.m}^{-2}.\text{s}^{-1}$ corresponding to the light intensity of overcast sky (assuming that a biocrust shows activity when it is wet, i.e. during rainy days). The calculations consider a constant light penetration depth of 0.2 mm (Garcia-Pichel and Belnap, 1996), and only vertical penetration is considered in the current work. The resulting distribution of irradiance in the model is depicted in Fig. 5.1b.

Temperature dynamics

The profile of soil temperature varies with time and space following a periodic function coupled with light incidence. We consider ambient temperature as a sinusoidal function for the surface boundary condition (Phillips et al., 2011):

$$T(z = 0, t) = \bar{T} + A_0 \sin(\omega t + \phi_T) \quad (5.2)$$

where \bar{T} is the average temperature on surface and A_0 is the diurnal amplitude. The period $P \equiv \frac{2\pi}{\omega}$ is assumed to be one day and the phase is set to be 0, so the maximum temperature corresponds to the maximum of light intensity (midday). Considering a homogenous domain with uniform hydration status, an analytical solution for a 1D heat equation with sinusoidal temperature boundary condition (Equation (2)) yields a dynamic description of diurnal soil temperature profile (similar solution is obtained for seasonal profiles).

$$T(z, t) = \bar{T} + A_0 e^{-\frac{z}{d}} \sin\left(\omega t + \phi_T - \frac{z}{d}\right) \quad (5.3)$$

where d is a characteristic damping depth of the domain given by $d = \sqrt{\frac{P\alpha}{\pi}}$ where $\alpha \equiv \frac{\lambda}{c_v}$ is thermal diffusivity (for details, see Appendix D: Text D.1). Thermal diffusivity is a function of hydration conditions. i.e., conductivity increases with wetness. Soil temperature distribution over depth during a diurnal cycle for wet and dry conditions is illustrated Fig. 5.1b.

5.2.3 Biocrust biogeochemical processes: mass transfer/inorganic C and N partitioning

The chemical environment of soil is strongly influenced by its microbial activity (especially at the main biocrust region). For example, the pH of biocrust is altered diurnally due to microbial respiration (release of protons and bicarbonates) and photosynthesis, with CO_2 removal significantly modifying pore water pH. These, in turn, affect nutrient availability and mobility, CO_2 dissolution rates, and solubilisation of soil minerals (Belnap, Prasse, and Harper, 2002). The model includes certain essential chemical processes; diffusion, gas-liquid phase partitioning, and acid-base dissociation, that affect microbial activity within typical biocrusts.

Gas diffusion with the biocrust

Unsaturated conditions dominate microbial life in desert biocrusts and support unhindered gas diffusion most of the time. Gas diffusion coefficient is in the order of $10^{-6} \text{ m}^2 \cdot \text{s}^{-1}$, which is about 10^4 times greater than that in aqueous phase. The largely aerated biocrust, the partial pressures of soil gas near surface equilibrate with the atmospheric level almost instantly (it takes a few seconds to aerate soil at depth of a few millimetres). In contrast, when the soil surface becomes especially wet, the aqueous phase configuration may temporarily hinder gas diffusion and delay such instantaneous partial pressure equilibration. Thus, an understanding of water configuration within the domain is necessary. In unsaturated soils, water

is held on the rough soil surface due to the capillary force (given by Young-Laplace equation) and absorbed waterfilm (van der Waals force). The abstract model (Fig. 5.1a) provides a means for calculating the proportion of water held at the given hydration conditions from preassigned soil properties. This yields the degree of saturation after normalisation with the volume of void space and local gas/water content (proportion of gas/water) of each spatial element (a patch). We used these local properties for gas phase invasion probability and local diffusion coefficients. When a patch at location \vec{r} is connected to the atmosphere (invasion percolation), constant boundary conditions at the gas phase are assigned in respect of atmospheric mixing ratio of each gaseous element instead of resolving gas diffusion at near surface (assuming instant equilibration).

Mass transfer between gas and liquid

The mass transfer rate across the gas-liquid interface can be determined by using Fick's law and the film model.

$$\frac{\Delta C^l}{\Delta t} = -\frac{A_{lv}}{d_{\text{tot}}} \left(\frac{D_g}{1-\Theta} - \frac{D_l}{\Theta} \right) (C^l - C^g) \equiv -k_{l \leftrightarrow g} (C^l - C^g), \quad (5.4)$$

where C^l and C^g are substrate concentration in liquid and gas phases, respectively; A_{lv} $\text{m}^2 \cdot \text{m}^{-3}$ is the specific liquid-vapour interfacial area; d_{tot} is the effective thickness of soil pore space; D_l and D_g are diffusion coefficients for liquid and gas phases; Θ is the degree of saturation; and $k_{l \leftrightarrow g}$ is the net mass transfer rate across the interface, which is a function of hydration conditions.

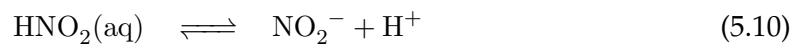
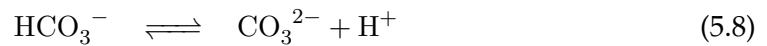
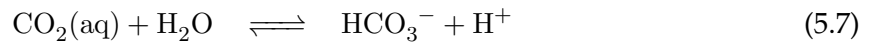
The proposed model allows us to calculate the specific liquid-vapour interfacial area and the effective thickness of void space (Kim and Or, 2016). For instance, the model estimates that $A_{lv} \approx 10^5 \text{ m}^2 \cdot \text{m}^{-3}$ and $d_{\text{tot}} \approx 10^{-5} \text{ m}$ at $\Theta = 0.5$ (half saturation). These values are consistent with other studies that have used a preassigned water retention curve (Zand-Parsa and Sepaskhah, 2004). Considering that gas diffusion coefficient is in the order of $10^{-6} \text{ m}^2 \cdot \text{s}^{-1}$, the net mass transfer rate between two phases is $\sim 10^4 \text{ s}^{-1}$ in aerated soils. This implies that the concentration at liquid phase also equilibrates almost instantly to the concentration at gas phase. Even when the soil is nearly saturated, the rate is $\sim 1 - 10 \text{ s}^{-1}$ ($\Theta \rightarrow 1, \theta \approx \theta_s$) (For comparison, studies on waste water treatment used the rate of $\approx 6.9 \times 10^{-5} \text{ s}^{-1}$ (Buhr and Miller, 1983; Yang, 2011).). Thus, mass transfer between gas and liquid in unsaturated soils is assumed to be rapid, and the concentration at each phase is always at equilibrium following Henry's law.

$$C^{l*} = H_{cc}(T) C^{g*} \quad (5.5)$$

where $H_{cc}(T)$ is a dimensionless Henry's constant at temperature T ; $H_{cc} = H_{cc}^S e^{-\frac{\Delta_{\text{soln}} H}{R} \left(\frac{1}{T} - \frac{1}{T^S} \right)}$ where $\Delta_{\text{soln}} H$ is the enthalpy of solution, R is the gas constant, and S refers to the standard condition ($T^S = 298.15 \text{ K}$) (Sander, 1999).

Dissociation of chemical substances

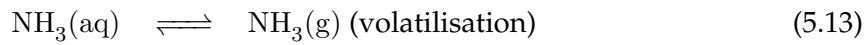
To evaluate available CO_2 in soil-biocrust water, one must consider the open-system behaviours of CO_2 and the different species of dissolved inorganic carbon (DIC), carbonic acid (H_2CO_3), bicarbonate (HCO_3^-), and carbonate (CO_3^{2-}). The relative amounts of such DIC species can be determined by the concentration of protons, pH of the solution. Considering that most desert soils are alkaline (Bresler, McNeal, and Carter, 2012) (implying the predominant DIC species to be bicarbonate), the determination of the amount of dissolved CO_2 in soil is essential to the growth and functioning of autotrophs and to distinguishing between abiotic and biotic processes for CO_2 efflux estimation. Assuming that other chemical species are inert, the model includes the following geochemical reactions focusing on carbon and nitrogen dynamics in soil:



Some mathematical models have introduced pH estimation for systems with phototrophs under light-dark cycles, such as algal ponds (Buhr and Miller, 1983; Yang, 2011; Gomez, Höffner, and Barton, 2014) and phototrophic biofilms (Wolf, Picioreanu, and Loosdrecht, 2007). The algal pond models invoke solution equilibrium and charge neutrality and employ differential algebraic equations to estimate pH, while the phototrophic biofilm models consider acid-base reactions with rate equations by proposing near-equilibrium kinetics. The unsaturated conditions in desert biocrusts with large air-liquid interfacial areas and high mass transfer rates require a special treatment. We adopted a similar approach of kinetics with charge balance (Wolf, Picioreanu, and Loosdrecht, 2007). In addition, the range of geochemical reactions were extended by including nitrous acid (HONO) and nitrous oxide (N_2O) to investigate nitrogen-related gas emissions from biocrusts. In this work, calcium is considered enabling evaluation of biogenic precipitation of calcium carbonate in biocrust formation. All the kinetics are based on the local concentration of each substrate in pore water with an assumption of water activity 1.

The equilibrium gas phase concentrations of O_2 , CO_2 , NH_3 , N_2O , and HONO are considered in the model according to Henry's law. Considered reactions for gas and liquid phase

partitioning and precipitation are listed below:



Values and detailed kinetic equations used in the model are summarised in Appendix D: Text D.2.

5.2.4 Microbial community in desert biocrust ecosystem

Advances in molecular taxonomic techniques and DNA sequencing have greatly expanded our knowledge on microbial community structure and diversity in biocrusts. These data generally delineate the interplay between multi-level trophic interactions (Bowker et al., 2011; Rocha et al., 2015; Pepe-Rannek et al., 2016) and surrounding environmental conditions (Caruso et al., 2011). Biocrusts host a complex community of diverse autotrophs and heterotrophs (hundreds of species including about 20 generic or subgeneric taxa of cyanobacteria) (Bowker, Maestre, and Escobar, 2010; Bowker, Soliveres, and Maestre, 2010; Garcia-Pichel et al., 2013). Considering biocrusts as independent and self-sufficient ecosystems, the intrinsic diversity found in this system should not come as a surprise. The incorporation of natural microbial diversity found in biocrusts is beyond the present capabilities of most models. Hence, we opted for a representation of the main microbial actors for modelling of associated biogeochemical cycles in a cyanobacterial crust.

Microbial community and trophic interactions

Four functional microbial groups are represented in the *in silico* microbial model of a desert biocrust: diazotrophic photoautotrophs (that are able to fix atmospheric carbon and nitrogen), aerobic heterotrophs, anaerobic heterotrophs (denitrifiers, strictly anaerobes using NO_3^- as a terminal electron acceptor), and chemoautotrophs (nitrifiers). These groups are chosen to elucidate the interlinked functionality of C/N cycling in a biocrust microbial community. Thus, we considered the following substrates in the soil solution that support microbial activity: oxygen (O_2), dissolved inorganic carbon, DIC, ($\text{CO}_2/\text{HCO}_3^-$), ammonium (NH_4^+), oxidised nitrogen species (NO_3^- , NO_2^-), and organic carbon (CH_2O , as an elementary form of polyglucose). Here, phototrophically produced CH_2O is assumed to be the primary carbon source available, which can be transformed into extracellular polymeric substances (EPS) depending on environmental conditions. Other chemical species, Ca^{2+} , CO_3^{2-} , N_2O , NH_3 , and HNO_2 , are included for the study of chemical reactions but are not directly utilised by these microbial species.

The four microbial groups interact based on prescribed stoichiometric relations (see Appendix D: Table D.5). These stoichiometric relations require the photoautotrophs to be classified into four subgroups (Wolf, Piciooreanu, and Loosdrecht, 2007), using one inorganic carbon source and one inorganic nitrogen source during photosynthesis (i.e. $\text{CO}_2 + \text{NH}_4^+$, $\text{HCO}_3^- + \text{NH}_4^+$, $\text{CO}_2 + \text{NO}_3^-$, and $\text{HCO}_3^- + \text{NO}_3^-$). Aerobic heterotrophs use CH_2O as an electron donor, O_2 as an electron acceptor, and NH_4^+ as a nitrogen source. Anaerobic heterotrophs (denitrifiers) use CH_2O as an electron donor, NO_3^- as an electron acceptor as well as a nitrogen source. As obligate anaerobes, their growth is inhibited by the presence of oxygen. Chemoautotrophs are described in two subgroups, considering two oxidation processes, firstly, of ammonia to nitrite by ammonia oxidising bacteria (AOB) and, secondly, of nitrite to nitrate by nitrite-oxidising bacteria (NOB).

By using Monod-type kinetics with limiting substrates, the growth rate of species i , with a limiting factor j can be written as;

$$\mu_i = \mu_{\max,i} \min[f_i^1, f_i^2, \dots, f_i^j], \quad (5.17)$$

where $\mu_{\max,i}$ is the maximum growth rate of species i and Monod factors are of two types, $f_i^j = \frac{C_j}{K_{S,i}^j + C_j}$ (when nutrient j is a substrate for the growth) or $f_i^j = \frac{K_{i,i}^j}{K_{i,i}^j + C_j}$ (when nutrient j is an inhibitor of growth) (For details, see Fig. 5.2 and see Appendix D: Table D.7).

The proposed model describes the various roles of phototrophs (i.e., cyanobacteria) within its growth dynamics by including the activity switch between photosynthesis and dark respiration, regulation of C/N ratio via N_2 fixation by heterocysts, and production of EPS. By means of adapting their growth stoichiometry to the local environment, phototrophs in the model control the primary productivity of the entire system depending on the time of the day (photosynthesis, dark respiration), nutrient availability (unbalanced C/N ratio), and hydration conditions (EPS production). A detailed description of the activity of phototrophs is provided in Appendix D: Text D.3.3.

To evaluate stoichiometries of heterotrophs and nitrifiers, microbial metabolic reactions are explicitly considered using the MBT-Tool (Metabolism based on Thermodynamics) (Araujo, Gras, and Ginovart, 2016). Details of stoichiometry for microbial growth in the model can be found in Appendix D: Table D.5. A graphical summary of microbial growth and trophic interactions is given in Fig. 5.2

Temperature-dependent microbial growth

Desert environments are often characterised by large diurnal temperature fluctuations (especially in hot deserts), which influence microbial activity. To consider these thermal effects, a temperature-dependent growth model using Arrhenius equation is included in the model. Although temperature adaptation and growth adjustments may vary among microbial species, we opted for a simple representation where all species are assumed to follow the same optimal temperature. The maximal growth rate for a cell at temperature T is scaled

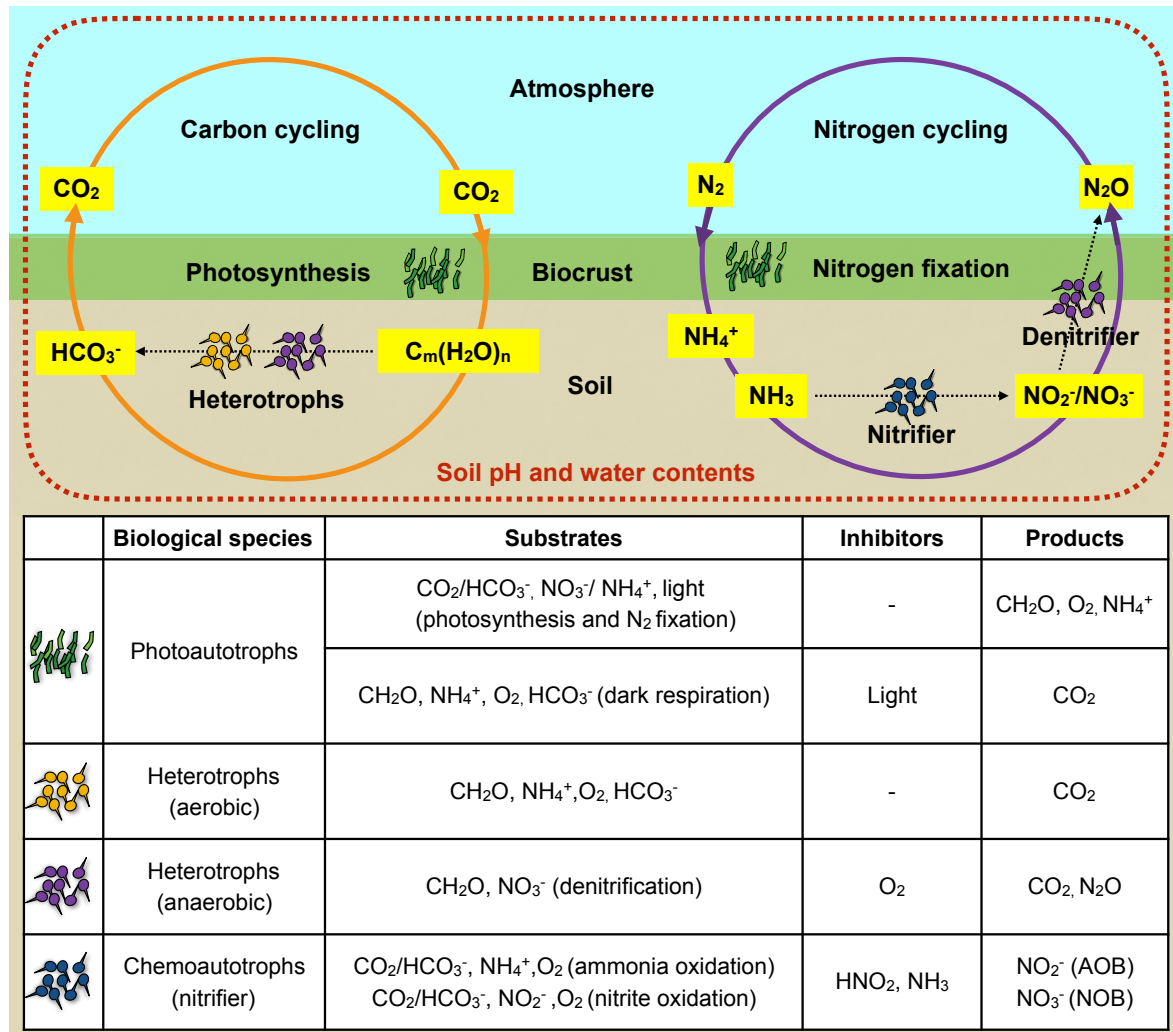


FIGURE 5.2: **Key microbial functional groups and biogeochemical interactions within the desert biocrust model.** The biocrust is considered an ecological unit in which four groups of biological species to describe carbon and nitrogen cycling. The introduced chemical and biological species in conjunction with the chemical processes determine the dynamics of the local pH of soil pore-water and gaseous efflux at the top of the domain. The growth rate of each species is determined from Equation (17). For details of stoichiometry, rate expressions, and Monod parameters, see Appendix D: Text D.4.

as follows (Schoolfield, Sharpe, and Magnuson, 1981):

$$f_T = \left[\frac{\frac{T}{T^S} e^{\frac{\Delta H^S}{R} \left(\frac{1}{T^S} - \frac{1}{T} \right)}}{1 + e^{\frac{\Delta H^L}{R} \left(\frac{1}{T_L} - \frac{1}{T} \right)} + e^{\frac{\Delta H^H}{R} \left(\frac{1}{T_H} - \frac{1}{T} \right)}} \right], \quad (5.18)$$

where T^S is reference temperature ($25^\circ\text{C} = 298\text{K}$) and ΔH^S (cal.mol^{-1}) is activation enthalpy of the reaction. In this model, two inactivation regimes are considered, one of low temperature, denoted by L , and other of high temperature, denoted by H . Parameters included for enthalpies and inactivation regimes are given in Appendix D: Table A.2.

pH feedback

Our model considers the spatial and temporal variations in pH values that could locally affect microbial activity. Unlike the narrow range of high pH regulating the activity of autotrophs (often limited by dissolved organic carbon), the activity of heterotrophs in the presence of dark respirations likely lowers pH when other substrates are not limited. Furthermore, nitrate accumulation can result in acidification of the soil domain when denitrification is absent. Considering that high acidity and alkalinity profoundly affects microbial growth through substrate binding and catalyse reactions, the feedback of microbial growth to local pH change is included in the model. The microbial feedback on biocrust pH can vary based on types of enzymes, number of ionisable groups, and organisms under consideration. In this work, a non-competitive inhibition model in a form of Monod function is employed (Tan, Wang, and Marshall, 1998):

$$f_{pH} = \frac{K_{pH}}{K_{pH} + [H]} \quad (5.19)$$

where K_{pH} is inhibition constant that deactivates microbial growth at very low pH (in this work, microbial activity ceases at pH below 5, $K_{pH} = 10^{-5}$ [M]). Usually, K_{pH} is a function of binding energy although it is implemented as a constant in our model for simplicity. Unlike other pH-dependent growth models, the inhibition term for hydroxyl ions is not included since the resulting high pH will regulate DIC and its partitioning will limit microbial growth without any inhibition terms (lack of protons for activity).

Microbial growth rates

A key objective of our model is to determine the spatial organisation of microbial community based on local gradients in conditions and resources. Several biocrust physico-chemical properties and environmental conditions determine the microbial growth rate following the diel cycles of light, temperature, and feedback of pH. As a result, the growth rate of individual cell i , Equation (17), is explicitly expressed as

$$\mu_i(\vec{r}, t) = \mu_{\max, i} f_T(\vec{r}, t) f_{pH}(\vec{r}, t) \min[f_i^1(\vec{r}, t), f_i^2(\vec{r}, t), \dots]. \quad (5.20)$$

Here, substrates are described within their minimum function (mass limitation of electron donors/acceptors) unlike pH and temperature correction terms. We assume that f_T indicates the optimal temperature of enzymes, and f_{pH} indicates the costs of osmosis of protons; therefore, they act on the maximum growth rate directly.

5.2.5 Microbial EPS production

The importance of EPS for microbial life in natural environments has been discussed in many review articles (Or, Phutane, and Dechesne, 2007; Flemming and Wingender, 2010; More et al., 2014). Especially, in arid or semi-arid environments, the role of EPS secreted by cyanobacteria is crucial for microbial communities surviving within (and below) biocrusts (De Philippis and Vincenzini, 1998; Pereira et al., 2009; Mager and Thomas, 2011; Rossi et al., 2012; Colica et al., 2014; Rossi and De Philippis, 2015). The synthesis of EPS contributes to the stability of soil structure and hydrated microenvironments in soil, making it a key ingredient of biocrust formation. EPS also functions as a nutrient storage by immobilising nutrients (dust trapping or glycosidic bonds) and as a protective shield from adverse environments, such as UV radiation, antibiotic substances, and invasion of viruses. In this work, we focus on two key aspects of EPS in biocrusts: modification of diffusion process of substrates and its role as a nutrient reservoir (increase in soil C) (Or, Phutane, and Dechesne, 2007; Pereira et al., 2009; Mager and Thomas, 2011). The complete range of EPS effects on soil hydrology, such as swelling of hydrated gel, owing to its chemical composition and physical structure, are not considered in this study.

EPS production and transport properties

EPS production by cyanobacteria in drylands varies with soil type, climatic conditions, hydration status and other resources (Hu et al., 2002). Estimation of production rates and amounts remain challenging. It is generally accepted that EPS synthesis in cyanobacterial soil crusts is affected by changes in moisture availability and nitrogen level (Mager and Thomas, 2011). We thus coupled photosynthesis and N_2 fixation in the biocrust model. This approach allows to compute the net production of carbohydrates using dynamic stoichiometry. A certain proportion of carbohydrate produced is assumed to be transformed into EPS depending on the local hydration conditions (for details, see Appendix D: Text A.2).

The fraction of EPS produced from photosynthetically fixed carbon is defined by the binding of extracellular carbohydrate residues to the polymeric matrix. The binding probability is written as a function of EPS concentration C_{EPS} and saturation degree of water Θ in the model:

$$f_p(C, \Theta) = \frac{1}{e^{-\frac{C_{EPS} - C_{EPS}^*}{C_{EPS}^* \Theta}} + 1} \quad (5.21)$$

where C_{EPS}^* is the gelation point for EPS as a polymeric substance. The function describes that residual carbohydrate will not bind to the polymeric substances as soon as EPS is in a form of weak gel (reaching C_{EPS}^*). The degree of polymer binding is regulated by the

saturation degree. For example, when the domain is wet, EPS hydrolysis will lower the binding probability of newly produced residual carbohydrates.

Many studies have suggested different physical models to describe the diffusion coefficient in EPS (Masaro and Zhu, 1999). For our biocrust model, we adopted a simple diffusion model in gels proposed by (Phillies, 1987).

$$D = D_0 e^{-\alpha_d c^\nu} \quad (5.22)$$

where α_d and ν are scaling parameters that differ from substance to substance. It is shown that α_d depends on the diffusant's molecular weight (in g.L⁻¹) and $\nu \sim 0.5$ for a high-molecular-weight diffusant (macromolecules). Diffusion of carbohydrates and EPS is governed by this equation in the model.

5.2.6 Diffusion reaction equation at the biocrust scale

Microbial activity and resource consumption are expressed as a set of diffusion reaction equations within the biocrust domain.

$$\frac{\partial C_j(\vec{r}, t)}{\partial t} = \nabla \cdot (D_j(\vec{r}, t) \nabla C_j(\vec{r}, t)) - \frac{1}{V_w(\vec{r}, t)} \sum_{i=1}^{N(\vec{r})} \frac{\mu_i(\vec{r})}{Y_{\text{net}_j^i}} b_i(t) + S_j(\vec{r}, t), \quad (5.23)$$

where $C_j(\vec{r}, t)$ is the local concentration of substrate j , $D_j(\vec{r}, t)$ is the local diffusion coefficient (including modification by EPS), and $V_w(\vec{r}, t)$ is the amount of water in a given patch at position \vec{r} and time t . The second term on the right-hand side is the reaction term to calculate the total substrate consumption/production in the patch. $N(\vec{r})$ is the total number of individual cells at \vec{r} , $Y_{\text{net}_j^i}$ is the net yield of species i on substrate j , $b_i(t)$ is the biomass, and $\mu_i(\vec{r})$ is the growth rate described in Equation (20). The last term $S_j(\vec{r}, t)$ is the source or sink term of substrate j with respect to the mass transfer between gas and liquid phases and charge compensation from principles of solution equilibrium and charge neutrality. These chemical processes are very fast compared to microbial reaction and diffusion processes. Thus, we implemented these terms as dynamic boundary conditions (keeping gaseous element solubility and local charge neutrality during one time step). For individual cells, the growth dynamics is written as:

$$\frac{db_i(t)}{dt} = [\mu_i(\vec{r}, t) - m_i] b_i(t) \quad (5.24)$$

where $\mu_i(\vec{r}, t)$ is growth rate, from Equation (20), and m_i is maintenance rate of cell i . Cell growth, division, locomotion, and death are described using the Individual Based Modelling (Kim and Or, 2016; Kreft, Booth, and Wimpenny, 1998).

5.2.7 Evaluation of the proposed mechanistic Desert Biocrust Model (DBM)

A pioneering study on microbial community within desert biocrusts (Garcia-Pichel et al., 2003) has suggested a vertical stratification of microbial community members where abundance (biomass) and composition (functional groups) vary with depth of the biocrust. Observations by Garcia-Pichel et al., 2003 demonstrated the stratification as a result of vertical gradients in physico-chemical conditions such as light, oxygen, pH, and other nutrients. Vertical profiles of N_2 fixation and potential NH_4^+ oxidation rates (Johnson et al., 2005), chemical profiles (total ammonium, nitrate) of soil solutions within active biocrusts (Johnson, Neuer, and Garcia-Pichel, 2007), and profiling of oxygen concentration after wetting (Abed et al., 2014) have been investigated as well. Recently, the effect of physical conditions on cyanobacterial activity was examined using X-ray microtomography (Raanan et al., 2015). These experimental data on microprofiles within biocrusts can be used for a comparison between measurements and numerical simulations of chemical/biological components within saturated crusts. For the comparisons in a spatial context, the DBM quantifies the biological activity as a product of local growth rate, μ_i , and biomass, b_i , of cells with a unit of $\mu \text{ g}_{\text{cell}} \cdot \text{g}_{\text{soil}}^{-1} \cdot \text{h}^{-1}$:

$$A_i(\vec{r}, t) = \mu_i(\vec{r}, t) b_i(\vec{r}, t). \quad (5.25)$$

This activity measure is suitable to indicate the active pathways for the upregulation of functional genes (i.e., spatial distribution of gene activity). From this activity distribution, it is possible to calculate the rates of microbial processes, such as carbon fixation, ammonia oxidation, denitrification, etc, by simply multiplying the yields from the stoichiometry of each species.

In contrast with the generally dry state of biocrust, most of the detailed studies reported above were conducted using saturated biocrusts (a state that rarely occurs in the field). Data on unsaturated biocrusts are hindered due to the technical difficulty in using microsensors (Pedersen, Smets, and Dechesne, 2015) and molecular analysis of microbial activity (Carini et al., 2016). Consequently, we are left with the undesired option of using detailed data from saturated biocrusts for model evaluation. The primary aim of this study is to establish confidence in the DBM for these rare conditions and extend the predictions to the more common case of unsaturated biocrusts.

The DBM was evaluated with respect to diurnal dynamics and results are compared to experimental studies that measured certain traits (e.g., gaseous efflux) such as the studies of Thomas, Hoon, and Linton, 2008; Rajeev et al., 2013; Darrouzet-Nardi et al., 2015; Weber et al., 2015. In this work, we focus on carbon dioxide efflux under fully saturated conditions (Rajeev et al., 2013). Although the gaseous fluxes are usually considered direct indicators of microbial activity, quantitatively speaking, these macroscopic measures emerged from all possible biological, chemical, and physical interactions combined.

5.2.8 Physical domain and boundary conditions for nutrients

For a prescribed matric potential (constant hydration conditions), the corresponding water film thickness, aqueous habitat connectivity, diffusion properties, and specific surface area

are obtained locally at patch scale (about $100 \mu\text{m}$) from preassigned surface properties and local porosity of each patch (a spatial element that determines local patch property). We selected parameters that mimic the property of loamy sand ($\bar{\phi} = 0.4$, $\bar{\Phi} = 0.6$, $D = 2.65$). By applying $m \times n$ patches, the domain describes a thin strip of a biocrust with periodic boundary conditions in the horizontal direction.

For boundary conditions of chemical substances, gaseous elements and dissolved elements are treated differently. Oxygen, carbon dioxide, ammonia, nitrous oxide, and nitrous acid in gas phase are assigned based on the atmospheric composition from literature (see Appendix D: Table D.1). The mixing ratios of atmospheric components are kept constant at the top of the domain during simulations assuming zero diffusive boundary layer and maximised gas exchange between atmosphere and biocrusts. These gaseous compounds are transferred to liquid phase by their own solubility based on Henry's law (Sander, 1999). DIC, ammonia, and nitrous acid are partitioned with the principle of local charge neutrality at obtained pH values.

Model evaluation is based on the following components: We first present steady state distribution of geochemical variables within the biocrust domain. Next, we present quasi-steady distribution of microbial functional groups within the biocrust under field capacity (relatively wet conditions). We then compare model results for saturated conditions where sample experimental data are available.

5.3 Results

5.3.1 Steady state of geochemical traits within the biocrust (no biological activity)

The abiotic exchanges that affect local distributions of geochemical environments and traits are evaluated first. A steady state of chemical domain is calculated in the absence of biological activity. We consider a biocrust following wetting at field capacity (corresponding to water saturation of 0.6 for the entire domain) assuming that this condition describes wetted crusts after drainage (in contrast to a fully saturated crust with saturation degree 1). We focus on traits such as diffusion, gas-liquid partitioning, and acid-base calculation without microbial activity. The spatial variations in phase distributions within the simulation domain (vertical cross-section of biocrust) and related attributes are depicted in Fig. 5.3. The results suggest that these relative wet conditions may disrupt gas phase connectivity to the atmosphere. Gas diffusion through the biocrust is determined by the connectedness of gas phase according to percolation theory. For certain values of local gas content (below 0.2), the gas phase becomes disconnected, affecting O_2 distribution. This implies that gas volumes not connected to the atmosphere may exist in isolated pockets within the soil domain. Thus, the local concentration of dissolved oxygen varies according to this atmospheric source and spatial heterogeneity (Fig. 5.3c). This also shows a correlation between gas phase configuration and spatial heterogeneity of pore water pH; the higher the local gas content, the lower the pH values (activity of protons). This indicates that a higher mass transfer rate from gas

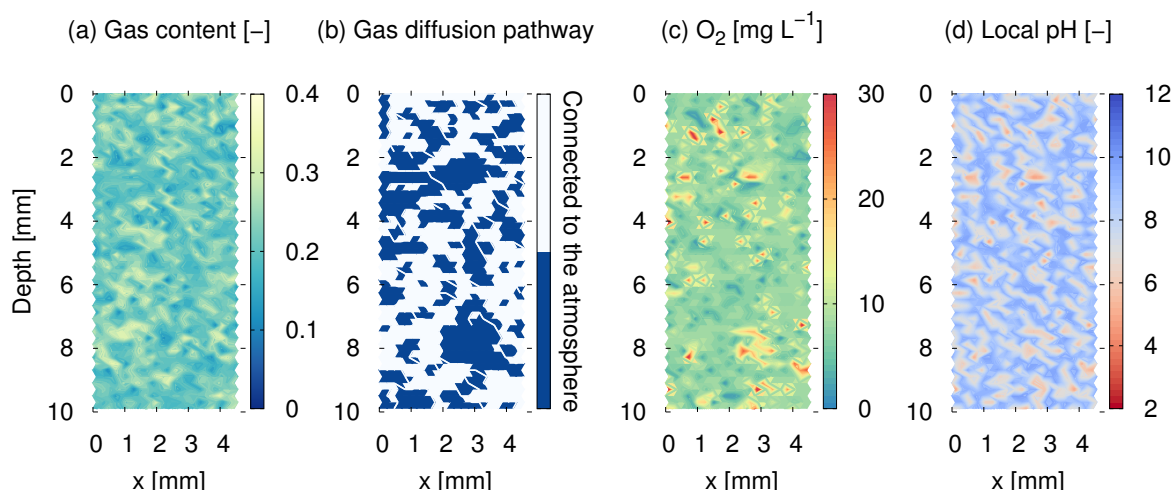


FIGURE 5.3: Aqueous-phase distribution affects diffusion pathways and geochemical conditions (no biological activity) A typical simulation result of a steady-state soil biocrust (up to 10 mm of depth) when biological activities are absent at standard ambient temperature ($T = 25^\circ\text{C}$). (a) A pre-assigned soil structure determines the local gas content and configuration of water at field capacity (the aqueous phase is complementary in these pore spaces). (b) The unsaturated soil permits the gas phase to penetrate over the biocrust depth along pathways (marked in blue) not blocked by the aqueous phase (marked in blue). The process is described by invasion percolation in this study. When the gas phase is connected to the atmosphere, partial pressures of gaseous compounds equilibrate to the atmospheric level as boundary conditions. Gas- and liquid-phase configurations determine the distribution of chemical species in the liquid phase, (c) The distribution of dissolved oxygen concentration, and (d) localised soil porewater pH.

to aqueous phase yields acidity since the dissolution of CO_2 is very fast in unsaturated soils (large surface areas and thin water films). On the other hand, patches with high water content and limited gas phase penetration show higher pH (around 8-9) as the model mimics alkaline soils with high cation content (about $10 \mu\text{g.g}^{-1}$ calcium and same amount of other non-reactive cation as shown in (Johnson et al., 2005)). This implies that volume-averaged pH may not be representative of local soil pore water/waterfilm pH in unsaturated soil, thereby affecting microbial activity locally and giving rise to processes not definable by average values.

5.3.2 Microbial activity effects on the biocrust chemical environment

The four microbial groups are introduced into the simulation domain (representing a cross-section in desert biocrust) and allowed the system to stabilise under diurnal cycles. Phototrophs were initially inoculated in the domain in an exponentially decaying manner over the biocrust depth to reflect a natural organisation under light penetration, while other groups were inoculated uniformly in the domain. Only phototrophs were inoculated differently to reduce the computational time as phototrophs only thrives up to the depth where light penetrates. This well-mixed inoculation pattern assures that the spatial organisation of microbial populations within the crust was not affected by initial conditions. The initial population sizes were the same for all functional groups, about 4000 cells, for the entire domain.

After about five consecutive days (diurnal cycles), the total population/spatial distribution of microbial groups reached a quasi-steady state.

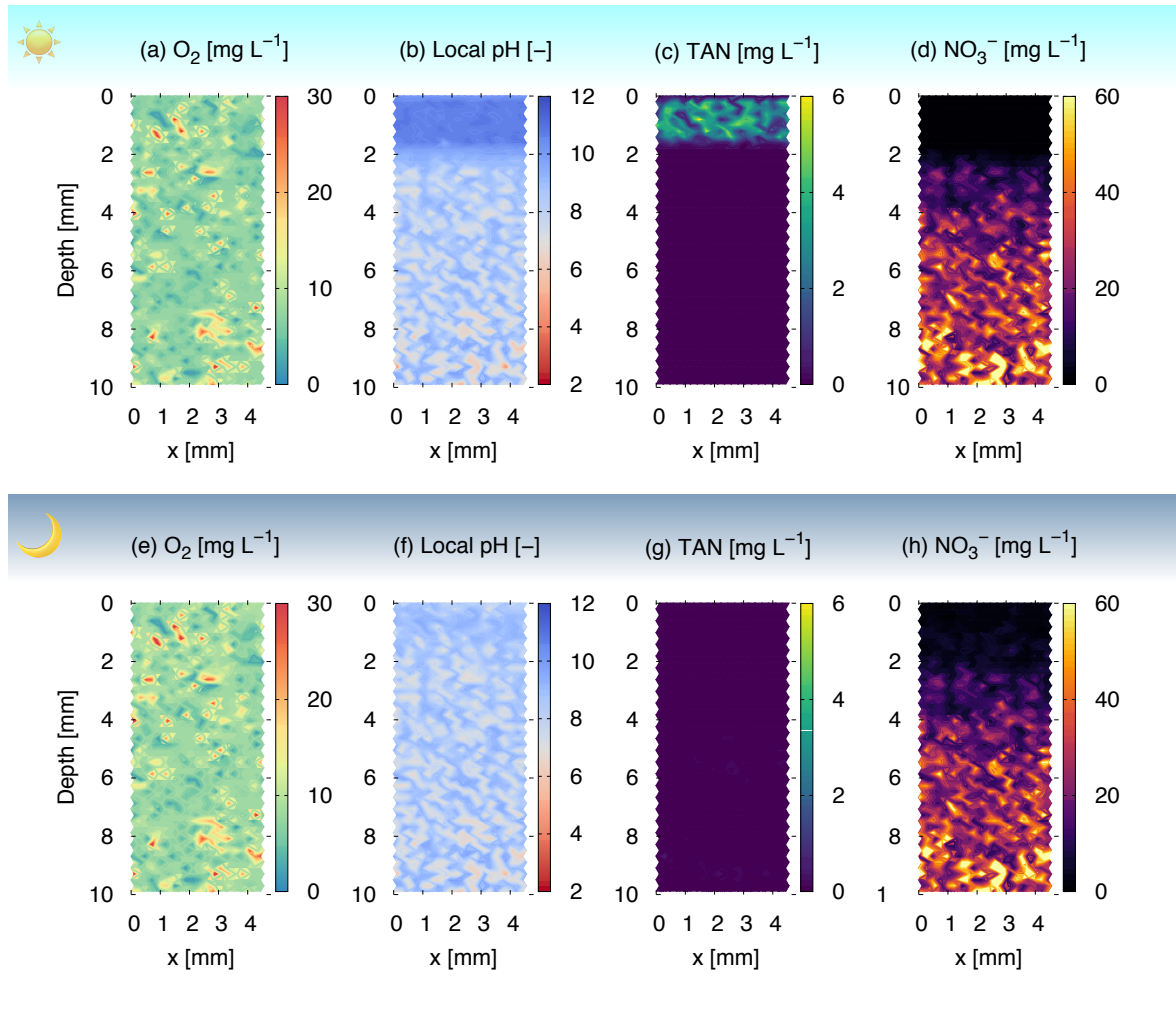


FIGURE 5.4: **Diurnal distributions of chemical constituents in the desert biocrust.** A typical result of simulated chemical profile within biocrusts at midday (top panel) and at midnight (bottom panel) at field capacity (wet but unsaturated). (a, e) The profile of dissolved oxygen is relatively stable during the day and night cycle. This implies that gas transport from the atmosphere is fast enough to override the consumption and production of the microbial community. (b, f) The profile of pH changes in contrast to that of oxygen. During the day, the top of the crust (within 2 mm) exhibits strong alkalisation, marked as blue in the figure. During the night, pH at the top goes back to a similar level as below 2 mm. (c, g) Total ammonia nitrogen (TAN) increases during the day on the top of the crust due to microbial production (N_2 fixation) and decreases during the night through microbial consumption. (d, h) Nitrate distribution shows a tendency of cumulation below 4-5 mm without clear diurnal patterns.

Noticeable changes in the resulting chemical environments occurred due to microbial activities even though physical environments and hydration conditions were assumed to be constant (held at relatively wet conditions corresponding to field capacity). Fig. 5.4 depicts four spatially distributed chemical attributes, namely dissolved oxygen, pH, total ammonia nitrogen, and nitrate, for midday (top panel) and midnight (bottom panel). The chemical profiles delineate the diurnal cycles of microbial activity across the soil domain. For instance, the alkalisation of top crust (2 mm) was clearly shown together with the production

of ammonium. This implies phototrophic activity fixes inorganic carbon as well as produces ammonium to fix N_2 using heterocysts. However, the oxygen profile was relatively stable compared to other chemical substances although photosynthesis and dark respiration could introduce changes in the local concentration of dissolved oxygen. This is due to the unsaturated conditions on the top crust, where gas transfer rates override the net reaction rate of oxygen within the profile. In addition, the nitrate profile exhibits the tendency of cumulation below 4-5 mm, implying that inhibited denitrification occurred under unsaturated conditions. The diurnal patterns of nitrate were not clear unlike the profile under saturated biocrusts (See Fig. S4 in Text 6). In general, regardless of differences among various chemical species and diurnal cycles, the strong spatial heterogeneity was still significant within the domain shaped by gas-liquid configuration.

5.3.3 Vertical stratification of microbial functional groups

The dynamics of the biocrust chemical environments are not only due to general microbial activity, but specifically due to trophic interactions within the biocrust community (due to different substrate use by microbial groups). A typical simulation result of the DBM is given in Fig. 5.5 to represent the activities and interactions among biocrust microbiota under two distinctive phases: (1) during daytime with active photosynthesis (a-d), (2) during nighttime with dark respiration (e-h). Results show emergence of vertical stratification of each microbial process within the thin biocrust (10 mm). The biocrust community is highly active above 4 mm and only some aerobic activities appeared very sparse and low below 4 mm. The spatial pattern is driven by trophic interactions among groups, by the chemical environments, and resource gradient since the non-phototrophic cells were uniformly inoculated over the entire domain. We note that, while activity and growth rates were in diel cycles, the spatial pattern become relatively steady and migration is not observed although cell motility is enabled (each population reached its local carrying capacity). The patterns can be analysed as follows: The phototrophs as primary producers (green in Fig. 5.5) perform intense photosynthesis at the biocrust's top following the distribution of light. The produced oxygen and carbohydrates combined with N_2 fixation benefit aerobic heterotrophs (yellow in Fig. 5.5) that exhibit high activity 2 mm below the surface. This strong cooperation between phototrophs and aerobic heterotrophs support high population on the top of the crust. Although a close proximity (mixing) between phototrophs and aerobes is expected, their activities are segregated due to the strong alkalisation during photosynthesis and intense competition over ammonium with AOB (marked in dark blue). A weak activity of anaerobic bacteria is also found together with aerobes at a similar depth due to the need of organic carbon for their activity. Local anoxic conditions support their growth in certain regions (purple in Fig. 5.5a and e) due to the consumption of oxygen by other organisms, heterotrophs, and nitrifiers. Below 3 mm, anaerobic activity is not found because the oxygen consumption by aerobic organisms is too low to create local anoxic conditions. Chemoautotrophs appear sparse over the depth and AOB and NOB (light blue) stay in proxy as they are in a mutualistic relation. AOB shows high activity within 2 mm during daytime, benefiting from ammonium fixed by heterocysts of phototrophs and inorganic carbon produced by

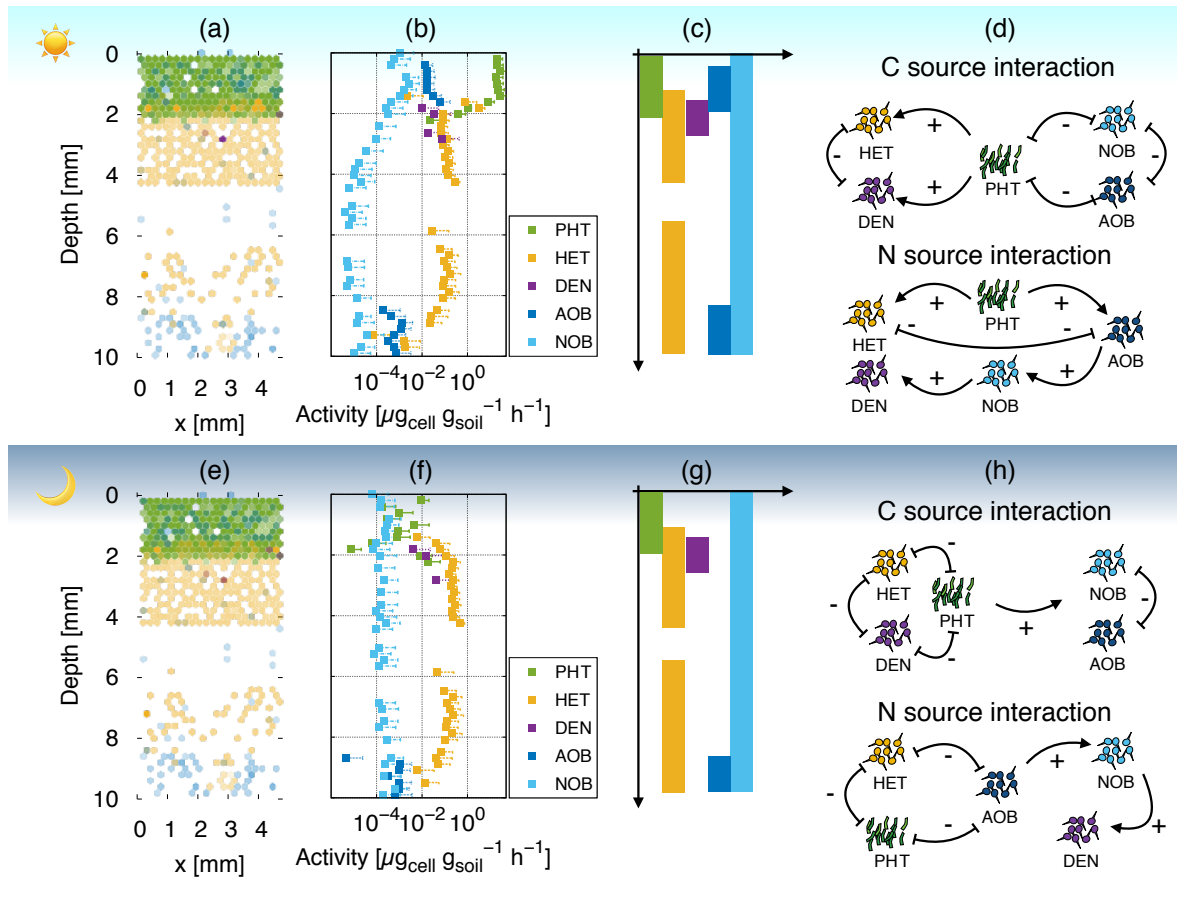


FIGURE 5.5: Diurnal shifts in microbial activity and spatial distributions in desert biocrusts A typical result of simulated biological activity profiles within wet biocrusts at midday (top panel) and at midnight (bottom panel) at field capacity. Local microbial activity is expressed in $\mu\text{g}_{\text{cell}} \cdot \text{g}_{\text{soil}}^{-1} \cdot \text{h}^{-1}$ (product of local biomass and growth rate per gram of soil). (a, e) Spatial distribution of microbial activity is given. Five colours (green, yellow, purple, dark blue, and light blue) represent the microbial groups (photoautotrophs (PH), aerobic heterotrophs (HET), anaerobic heterotrophs (DEN), ammonia oxidisers (AOB), and nitrite oxidisers (NOB), respectively). Higher activity is shown with stronger colours. Vertical distribution of microbial activity at midday (b) and at midnight (f). Local activities are averaged (only with patches where the activity occurs) with respect to the horizontal direction. Only upper standard deviations (+1 SD) are shown considering the log scale plot. (c, g) The spatial extent of the activity of each functional microbial group within the biocrust is represented by a bar (of the assigned colours above). (d, h) Phototrophic activity changes during the day and night, resulting in distinctive trophic interaction patterns over carbon and nitrogen sources. (+) and (−) indicate mutualistic and competitive interactions, respectively.

heterotrophs. Its growth is mainly limited by inorganic carbon used during photosynthesis. The activity of NOB is also high at the top crust due to nitrite production by AOB.

Generally, during daytime, the activity of phototrophs enhances other microbial activity by fixing inorganic carbon and nitrogen (Fig. 5.5d). During nighttime, phototrophs switch their activity to dark respiration. Dark respiration by phototrophs drives an intense competition for organic carbon and ammonium among individuals at the top of the domain. As the input of fixed carbon and nitrogen is absent, the depletion of ammonium at the top crust lowers the activity of most organisms (Fig. 5.4g). However, NOB shows slightly higher activity during night at below 3 mm, suggesting that, during daytime, they are outcompeted

by other organisms owing to their high yield and low growth rate.

5.3.4 Fully saturated biocrusts: comparing model predictions with observations

Despite the focus of the desert biocrust model (DBM) on unsaturated conditions in desert systems, we had to rely on definitive experimental data from saturated biocrusts to evaluate details of model performance (Garcia-Pichel and Belnap, 1996; Johnson, Neuer, and Garcia-Pichel, 2007; Abed et al., 2013; Rajeev et al., 2013; Raanan et al., 2015). The simulation domain was saturated by simply applying near zero matric potential and filling up all surface pores with water. Using the fully saturated domain with stable microbial community distribution, the model biocrust was then exposed to diurnal cycles of radiation and temperature.

The spatial distribution of microbial activity within a fully saturated biocrust is given in Fig. 5.6. Ten independent simulations were averaged to obtain the possible distribution of microbial processes. The potential activity of anaerobes peaks below 2 mm (in contrast to other aerobic organisms) due to the formation of an anoxic region (Appendix D: Fig. D.4 in Text D.6). At the top, microbial distribution is clearly stratified as phototrophs-nitrifiers-aerobic heterotrophs-denitrifiers. Unlike unsaturated biocrusts, the vertical stratification is accentuated largely because of a strong oxygen gradient profile driven by photosynthesis.

The spatio-temporal behaviour of oxygen and pH profiles predicted by the model are compared with available dataset in Fig. 5.7. Simulation results are in quantitative agreement with reported data from experiments on various types of cyanobacterial crusts (e.g. light crusts and dark crusts) from several locations (Garcia-Pichel and Belnap, 1996; Johnson, Neuer, and Garcia-Pichel, 2007; Abed et al., 2013; Rajeev et al., 2013; Raanan et al., 2015). A common finding with respect to the oxygen profile is its supersaturation within a top few millimetres and the formation of an anoxic region below. While the model was able to capture the dynamics of dissolved oxygen, pH dynamics showed large deviations between model and data, especially during nighttime. Chemical environments of other substrates during daytime and nighttime are given in Appendix D: Fig. D.4 in Text D.6

5.3.5 Diurnal cycles of gaseous efflux from saturated biocrusts

In addition to comparing processes within the crust (Fig. 5.6, 5.7), we simulated gas efflux from the saturated biocrust and compared with the measurements of Rajeev et al., 2013. Fig. 5.8 depicts the efflux of three gas compounds of carbon and nitrogen, namely CO₂, NH₃, and N₂O. We represent uptake by negative gas efflux and positive sign for emissions. The diel cycles of CO₂ efflux are plotted together with experimental data tracking the net carbon exchange between the biocrust and the atmosphere (Fig. 5.8a). Within the biocrust, carbon fixation and respiration occur simultaneously; the net CO₂ efflux indicates a balance between respiration (release) and photosynthesis (uptake). Simulation results are in a qualitative agreement with experimental data, except the steep transitions after sunrise and gradual changes after sunset that are not captured properly. We attribute this to the simplified model (using Monod functions) of the onset of photosynthesis and dark respiration.

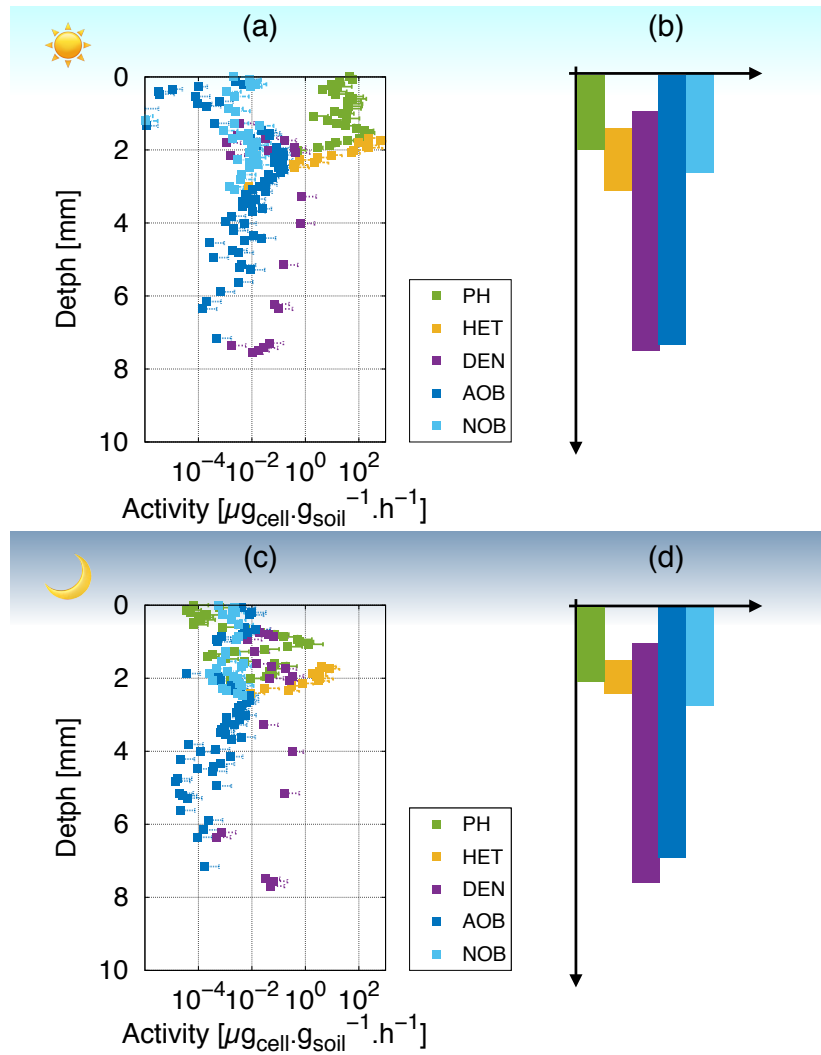


FIGURE 5.6: **Diurnal variations in microbial activity within saturated biocrusts.** Simulated microbial activity profiles and vertical stratification at midday (a) and midnight (c). The spatial distribution of microbial activity is averaged with respect to the horizontal direction for 10 independent simulations. (only upper standard deviations (+1 S.D) are shown considering the log scale) (b,d) Based on the vertical distribution of microbial community members, the depth containing the activity of each microbial group within the biocrust is marked by the bars (with respective colour coding).

Next we evaluate the daily patterns of ammonia volatilisation to represent nitrogen abiotic losses. The results in Fig. 5.8b show that ammonia volatilisation occurs mainly during daytime as the top of the biocrust turns alkaline (pH above 10). The total ammonia loss due to volatilisation was estimated to be about $500 \text{ nmol} \cdot \text{m}^{-2} \cdot \text{day}^{-1}$, similar to reported values, $540 \sim 1000 \text{ nmol} \cdot \text{m}^{-2} \cdot \text{day}^{-1}$, from intact biocrusts in Colorado plateau (Evans and Johansen, 1999; Barger et al., 2016). We then evaluate N_2O release from the biocrust (indicative of denitrification), the results in Fig. 5.8c show that immediately after wetting N_2O flux is high. We attribute this rapid release to accumulation of NO_3^- during unsaturated conditions. After 2 days, nitrate is exhausted and denitrification relies on the activity of NOB. Finally, we also considered the potential release of NO_2^- from the soil solution in the form of nitrous acid HONO. Results show, however, no such release in agreement with the observations

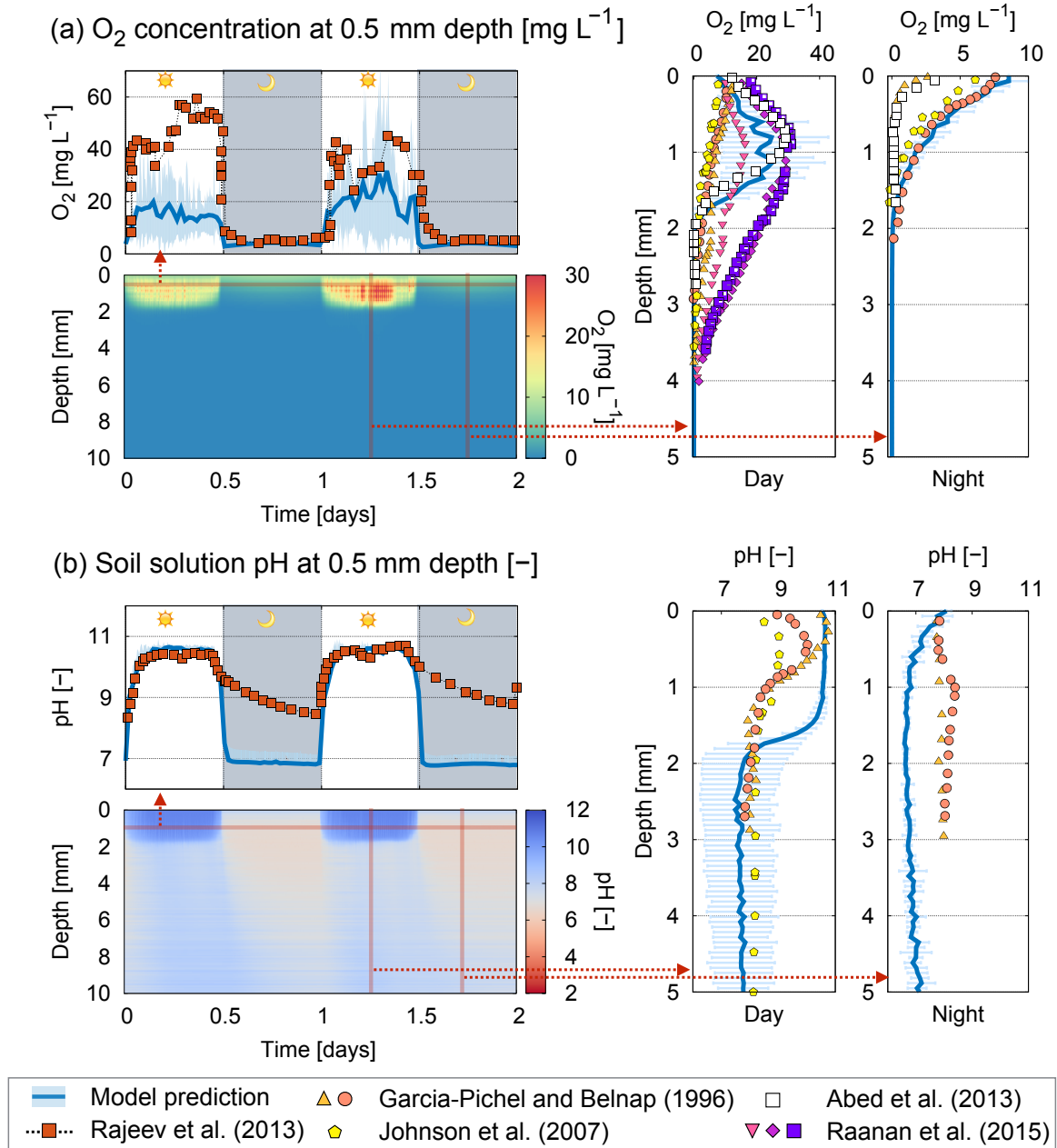


FIGURE 5.7: **Oxygen and pH profiles within saturated biocrusts.** Spatio-temporal dynamics of the (a) oxygen profile and (b) pH profile of modelled biocrusts (fully saturated) under diurnal cycles. The horizontal average of profiles is taken and 10 independent simulations are averaged to see the general dynamics of various biocrusts. For comparisons, 500 μm of depth is chosen to represent the temporal behaviour of the top crust. Depth-averaged profiles at midday and midnight are used to compare with experimental measurements of biocrust response under light and dark conditions.

of Weber et al., 2015 (Not presented in this paper).

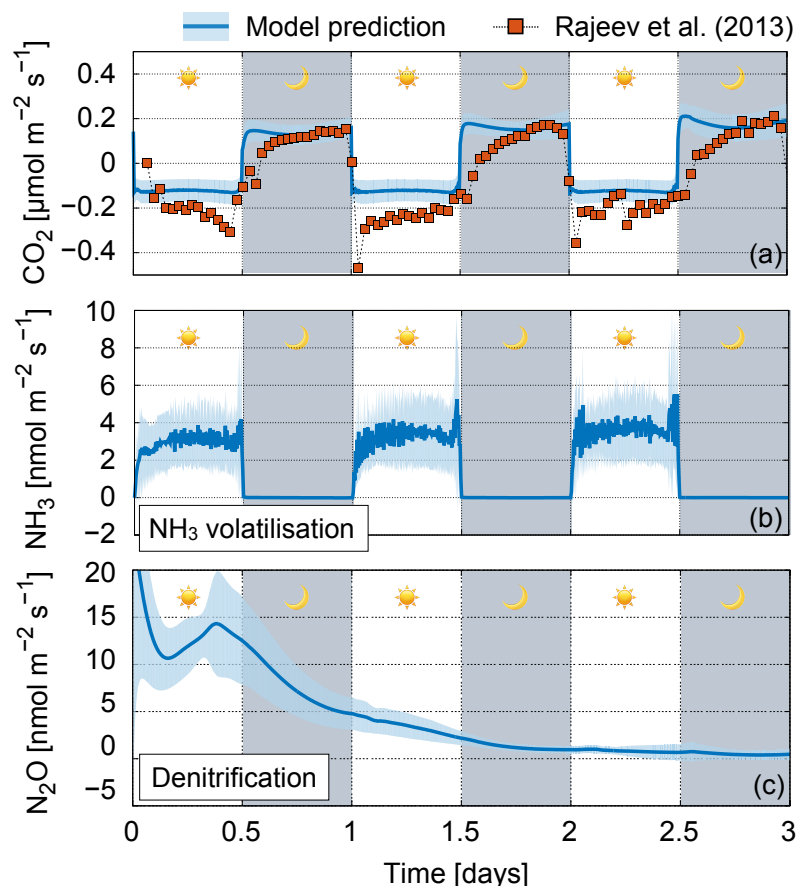


FIGURE 5.8: **Gas effluxes from saturated biocrusts.** Gaseous efflux from saturated biocrusts is concomitantly obtained with chemical profiles and microbial activity from 10 independent simulations of the model. (a) CO_2 efflux shows diel cycles of uptake (during daytime) and release (during nighttime). The averaged CO_2 efflux dynamics are compared with an observation (red squares from Rajeev et al., 2013). (b) NH_3 efflux dynamics show volatilisation of ammonia gas mainly caused by alkalisation of the top crust during daytime, resulting in a net volatilisation rate of about $500 \text{ nmol.m}^{-2}\text{day}^{-1}$. (c) N_2O efflux is also calculated as an indicator of denitrification. The highest denitrification rate is observed during the first 1-2 days.

5.4 Discussion

5.4.1 Spatial and temporal variations in local pH within unsaturated biocrusts

Soil pH has been recognised as a significant predictor of microbial community composition and diversity (Fierer and Jackson, 2006; Lauber et al., 2009). Furthermore, for alkaline or saline soils (typical desert soils), abiotic contributions to gaseous efflux may account for up to 40 % of total CO_2 emissions (Ma et al., 2013). Thus, to separate biotic and abiotic contributions for gaseous efflux, reliable estimates of pH are needed. Especially, it is more crucial when the main producer of the system, phototrophic microorganisms, depends on the accessibility of inorganic C and N. The proposed desert biocrust model (DBM) offers a distinct advantage in this respect, namely the localised (pore scale) representation of pH that integrates physico-chemical interactions and microbial activity. Simulated pH profile dynamics within wet biocrusts presented above (Fig. 5.7) have confirmed that the activity

of photoautotrophs alters local pH by depleting DIC during a diel cycle (consistent with observations).

Results by the DBM suggest strong spatial variations of local pH within the unsaturated biocrust although the overall (spatially averaged) soil pH indicates an alkaline soil (Fig. 5.3). In practice, however, the spatial distribution of local soil pH is difficult to measure and often requires the use of microelectrodes (Pedersen, Smets, and Dechesne, 2015). Moreover, it has been argued that the use of microsensors is limited to near-saturated soils (McIntyre, 1966). The modelled spatial variations in local acidity are consistent with uptake kinetics of nitrous acid in the gas phase on a wetted wall film (Hirokawa, Kato, and Mafuné, 2008). Model results suggest that pH in thin water films may be lower than in the bulk liquid due to the resistance of mass transfer from the gas to the bulk liquid phase (we use the term “bulk” to represent large water-filled pores within the biocrust). As liquid surface on the wall corresponded to acidity at thin water film in the model, this result may support model predictions and the importance of soil water configuration in shaping local pH within unsaturated soils.

The strong correlation between soil moisture retention and soil pH and their role in defining the microbial community structure (Lauber et al., 2009) might be attributed to local pH distribution in unsaturated soil. We speculate that the high abundance of *Acidobacteria* (at phylum level), known to grow well at acidic culture (pH 3.5-6.5) as aerobic heterotrophs (Pankratov et al., 2008), in most soils (Jones et al., 2009; Lauber et al., 2009) might offer another evidence of the importance of localised acidity in unsaturated soils. We note that such acidity related phylum was also found in biocrust communities (Steven, Belnap, Kuske, et al., 2013).

5.4.2 Microbial community stratification within biocrusts

Spatial segregation along vertical gradients is a well-known feature of microbial communities in aquatic biofilms, microbial mats, and endolithic communities (Schramm et al., 2000; Paerl, Pinckney, and Steppe, 2000). Similar to the Winogradsky column, these microbial stratifications are driven by the distribution of electron acceptors/donors. Since the most favourable electron acceptor for aerobic organisms is oxygen, the low solubility of oxygen and the limited diffusion of dissolved oxygen play a pivotal role in the emergence of spatial stratification. The stratification within biocrusts is also observed in terms of biomass of oxygenic phototrophs, aerobic copiotrophs (Garcia-Pichel et al., 2003), and community composition analysis based on 16S rRNA sequencing (Steven, Belnap, Kuske, et al., 2013). The simulated results of our biocrust model agree with observations exhibiting vertical stratifications of the biocrust community (Fig. 5.5 and 5.6).

The DBM captures the key physico-chemical conditions essential for vertical stratifications. The steep gradient of oxygen on top of the fully saturated biocrust (Fig. 5.7, Appendix D: Fig. D.4 in Text D.6) is caused by limited mass transfer from the atmosphere and rapid consumption of oxygen. During nighttime, depletion of oxygen (below few millimetres) is expected naturally because of limited amount of oxygen input. The oxygen produced

by phototrophs during daytime is immediately depleted by aerobic organisms in the domain. Clearly, such formation of anoxic region within the crust benefits anaerobic activity a few mm (Fig. 5.6). The creation of supersaturation closer to the surface also indicates slower diffusion than net production/consumption of oxygen. Experiments on biocrusts immersed in water indicated effervescing of (presumably) oxygen at surface (Rajeev et al., 2013). This proves that the net production of oxygen is higher than diffusion of dissolved oxygen.

The vertical segregation of different microbial groups also indicates diffusion of organic carbon and nitrogen diffusing from the photoautotrophs and become available to other microbial members, especially, stratification among aerobic organisms. The dominance of nitrite oxidising bacteria (NOB) at the top 2 mm is largely due to ammonia volatilisation. The alkalisation of the top crust during daytime increases ammonia volatilisation, which is not beneficial for aerobic heterotrophs and ammonia oxidising bacteria (AOB). Therefore, their activity retreats deeper to around 2 mm, allowing NOB to appear at the top surface. Below the location of NOB, we find AOB and aerobic heterotrophs. Although the model has a simple assumption on microbial groups utilising various substrates in a specific trophic landscape assumed for this study (Fig. 5.5d, h), a similar pattern of segregation is expected within real biocrusts in field.

For aerated unsaturated biocrusts, the results in Fig. 5.4a and e show that the high oxygen transfer rate to soil water overrides net reaction, and thus a strong gradient of oxygen is not observed in unsaturated cases (Appendix D: Fig. D.4a in Text D.6). Therefore, the aqueous phase configuration within unsaturated biocrusts (also possibly extending to general unsaturated soils) shapes microbial activity unlike in aquatic, microbial mats and similar saturated systems. This stable oxygen profile of unsaturated biocrusts is due to the mass transfer between gas and liquid which is assumed to be very rapid in the model (instant equilibration by Henry's law, see section 2.3.2). However, real biocrusts in natural fields, the exchange of gases with the atmosphere can be constrained even under unsaturated conditions (at a certain range) because of a dense layer of EPS and a finer soil texture of uppermost part within biocrusts. These factors can retard the mass transfer by decreasing interfacial area at a relatively wet conditions (finer soil texture) and by sustaining thick water film thickness owing to the presence of EPS. The current model allows to assign a finer soil texture on the biocrusts domain by using a low porosity or a high fractal dimension on the uppermost part. For the biocrusts loaded with dense EPS layer, the model can be improved by relating the local EPS amount with the water film thickness at a given matric potential.

5.4.3 Complex trophic interactions of microbial community within biocrusts

The biocrust community exhibits highly dynamic and complex trophic interactions, such as commensalism surrounding organic carbon utilisation between phototrophs and heterotrophs, competition over nitrogen sources between aerobic heterotrophs and AOB, cooperation between NOB and anaerobic denitrifiers, etc. Temporally, diel patterns of trophic interactions (orchestrated by phototrophs) drive the shift in activity distribution of microbial activity as it has been shown from Namib desert soil (Gunnigle et al., 2017). Spatially,

these complex trophic interactions take place within thin biocrusts and yield emergent spatial distribution of microbial groups as depicted in Fig. 5.5. The remarkable concentration of such interactions within a few mm and the stratification of the activities of the various functional groups highlight the ecological sophistication and versatility of such fine-tuned desert ecosystems. Remarkably, opportunistic life forms are harboured within such biocrusts for example, the presence of anaerobic heterotrophs that are present at low numbers suggesting presence of local anoxic conditions even under mild unsaturated conditions (Ebrahimi and Or, 2015) and their rapid response to episodic wetting events (Šťovíček et al., 2017).

5.4.4 Gaseous efflux from desert biocrusts

Motivated by availability of definitive data, the DBM was applied to simulating diurnal changes in gas efflux from saturated biocrusts. The results were in good agreement with measured CO₂ efflux (Fig. 5.8). The model represents diurnal cycles of other gas fluxes that may be sensitive to pH such as ammonia volatilisation, HONO emission, etc. Details of the geochemical environment shed light on the important role of local conditions (pH) on soil/biocrust microbial activity. For example, the activity of AOB in alkaline soils can be suppressed during daytime on the top crust as strong alkalisation leads to a loss of nitrogen compound. On the other hand, NOB in acidic soils should experience the opposite, as the soil becomes more acidic, HONO emission would lead to nitrogen loss.

To realistically describe microbial life within unsaturated biocrusts or dry soils, the inclusion of gas phase interactions is necessary. Most experiments on biocrusts were conducted under saturated conditions (presumably to induce significant and measurable response), however, these responses occur during narrow climatic windows with high precipitation (Garcia-Pichel and Belnap, 1996; Garcia-Pichel and Belnap, 2002; Johnson, Neuer, and Garcia-Pichel, 2007). Although we have shown gaseous efflux from saturated soils to compare with experimental results, the DBM is capable of quantifying gaseous efflux from unsaturated biocrusts by tracking gas and water distribution.

5.4.5 Assumptions and limitations of the desert biocrust model (DBM)

The proposed DBM makes numerous simplifications pertaining to the life and functions of a complex microbial community in biocrusts in arid and semi-arid regions. Regarding the key physical processes, we built a physical domain that contains small subregions represented as patches. A patch is a subsection within a small vertical cross-section in the biocrust that represents soil surfaces with different properties that retain waterfilms and transport nutrients and gas. This enables consideration of spatial heterogeneity within a vertical two-dimensional cross-section across a biocrust, however, lateral variations in biocrust properties in space are not considered here.

Key geochemical processes that are dominant in desert soils (and biocrusts) are considered in this model. For simplicity, we consider calcium as a buffer together with other non-diffusing background cations (assuming uniformly distributed non-reactive cations as

a setpoint of pH). The effects of saline soil (also a common property of desert soils) on dissociation constants and its influence on soil pH are not considered. We also did not include the effect of EPS (as organic matter) on the top of the biocrust. The role of EPS as a gate for matter flux on desert soil surface, interaction between pH alteration by microbial activity, and changes in physical properties of soil (relation between EPS swelling ratio and pH) can be the next goal for a mechanistic model of biocrusts. Other important aspects regarding chemical processes include modifying the diffusion equation. In the current model, the possibility of electrokinetic flow is not included. A more detailed description of electromigration can be included by modifying the diffusion equation for ionic particles by using the Nernst Planck equation. However, as the input of carbon dioxide to the thin water film is faster than the aqueous diffusion of ionic particles, the occurrence of local pH variation owing to the configuration of gas phase is still expected in unsaturated soil.

By far, the most simplified component in this model is the biological one related to microbial processes. The DBM represents a system containing an astonishing level of diversity with a small number of microbial functional groups. The interactions among these community members are regulated by simple stoichiometric relations that control microbial growth. Monod parameters are mostly taken from models for activated sludge (a system far removed from life in desert biocrusts) (Henze, 2000). Considering that a desert is a water-, carbon-, and nitrogen-limited system with abiotic stresses, the values of these parameters are likely to be different from those governing life in sludge systems. We note however, that the proposed Monod growth parameters are affected by local environmental conditions, such as temperature, pH, and substrate concentrations. Yet, an understanding of half-saturation constants and ratios between growth rates among different microbial groups would be necessary for establishing quantitative predictions by the DBM for real systems.

The members of the biocrust consortia were selected focusing on C and N cycling and characteristics of arid environments. Recently, the role of heterotrophic diazotrophs, anaerobic ammonium oxidisers, and nitrate-reducing bacteria within biocrusts has been studied. Including these members might alter some of expected rates that we presented in this study. Comparisons between crust models with their presence and absence can be one of the future applications. Furthermore, as the model describes a hydrated porous medium, the fully saturated domain is easily applicable to describe the microbial community of sediments or microbial mats. However, when it comes to modelling such systems, other groups such as anaerobic phototrophs, sulfate/iron-reducing bacteria, or methanogens might need to be considered together with the proposed community of C/N cycling. This might be beneficial for a mechanistic understanding of the biogeochemistry of such systems.

The DBM can be further used to predict the gaseous efflux dynamics of wetting-drying cycles and C and N turnover rates during hydration events. As hydration events in arid and semi-arid areas are scarce, a mechanistic understanding of biocrust response to hydration would benefit to estimate its contribution to global biogeochemical cycles. For instance, high N loss via NO_3^- leaching, NH_3 volatilisation, and HONO emissions can be investigated with respect to N cycling in such environment. Furthermore, short term perturbations of hydration conditions on biocrusts can be also another application of the model, such as

short wet-up cycles or rapid evaporation at high temperatures. Physical roles of biocrusts on hydrological processes can also influence on C and N cycling in arid area. For instance, changes in infiltration properties and wind and water erosion are not considered in the current work on microbial communities in biocrust. However, at larger scale, these physical changes in the domain can be further extended.

5.5 Summary and conclusions

In this study we develop a mechanistic model of desert biocrust microbial community under strong vertical resource gradients prevailing in surfaces of arid landscapes. The desert biocrust model (DBM) combines a detailed account of soil hydration for different soil properties, individual based description of microbial life, and chemical processes that affect the trophic interactions among the microbial groups as an ecologically functioning unit. Although simplified (as much as possible) it elucidates the role of soil structure in shaping gaseous/aqueous diffusion and substrate fluxes at the atmosphere-soil interface crucial for microbial activity occurring therein.

Model results show the distribution and composition of microbial functional groups over vertical gradients of light, temperature, and substrates across a model biocrust. Furthermore, geochemical and physical processes of mass transfer at the gas-liquid interfacial area in soil matrix and kinetics for inorganic carbon and nitrogen fractionation underline the importance of modelling unsaturated soil that significantly deviates from other environments such as aquatic systems or saturated soils. Especially, the modified chemical environment displays the feedback of microbial activity from photosynthesis to CO₂ efflux from biocrusts. The local pH of soil water as a cumulative measure of local ionic species concentrations determines the availability of inorganic carbon and nitrogen or other minerals for microorganisms by controlling the solubility of chemical compounds and their degree of protonation. Although the model does not include individual differences of optimal pH for microbial activity, its results based on acid-base equilibrium predict the spatially and temporally organised activity of all functional groups. This self organisation indicates one of the reasons why biocrusts can host high abundance and diversity of microorganisms even under very harsh conditions like deserts. The DBM provides a means for systematic and climatic-driven evaluation of the critical role of microorganisms in desert ecosystems. The model offers predictive capabilities (within the limitations of the assumptions) for biocrust responses to climate change and their contribution to large scale carbon and nitrogen cycles.

References

- Abed, Raeid MM et al. (2010). "Bacterial diversity, pigments and nitrogen fixation of biological desert crusts from the Sultanate of Oman". In: *FEMS Microbiology Ecology* 72.3, pp. 418–428.
- Abed, Raeid MM et al. (2013). "High rates of denitrification and nitrous oxide emission in arid biological soil crusts from the Sultanate of Oman". In: *The ISME Journal* 7.9, pp. 1862–1875.
- Abed, Raeid MM et al. (2014). "Rapid Recovery of Cyanobacterial Pigments in Desiccated Biological Soil Crusts following Addition of Water". In: *PLoS ONE* 9 (11).e112372.
- Araujo, Pablo Granda, Anna Gras, and Marta Ginovart (2016). "MbT-Tool: An open-access tool based on Thermodynamic Electron Equivalents Model to obtain microbial-metabolic reactions to be used in biotechnological process". In: *Computational and Structural Biotechnology Journal* 14, pp. 325–332.
- Barger, Nichole N et al. (2006). "Impacts of biological soil crust disturbance and composition on C and N loss from water erosion". In: *Biogeochemistry* 77.2, pp. 247–263.
- Barger, Nichole N et al. (2016). "Patterns and controls on nitrogen cycling of biological soil crusts". In: *Biological Soil Crusts: An Organizing Principle in Drylands*. Springer, pp. 257–285.
- Barnard, Romain L, Catherine A Osborne, and Mary K Firestone (2015). "Changing precipitation pattern alters soil microbial community response to wet-up under a Mediterranean-type climate". In: *The ISME Journal* 9.4, pp. 946–957.
- Belnap, Jayne (2003). "Biological soil crusts in deserts: A short review of their role in soil fertility, stabilization, and water relations". In: *Algological Studies* 109.1, pp. 113–126.
- Belnap, Jayne and Dale A Gillette (1998). "Vulnerability of desert biological soil crusts to wind erosion: The influences of crust development, soil texture, and disturbance". In: *Journal of Arid Environments* 39.2, pp. 133–142.
- Belnap, Jayne and Otto L Lange, eds. (2003). *Biological Soil Crusts: Structure, Function, and Management*. Springer.
- Belnap, Jayne, Rüdiger Prasse, and Kimball T Harper (2002). "Influence of biological soil crusts on soil environments and vascular plants". In: *Biological Soil Crusts: Structure, Function, and Management*. Springer, pp. 281–300.
- Belnap, Jayne, Bettina Weber, and Burkhard Büdel (2016). "Biological Soil Crusts as an Organizing Principle in Drylands". In: *Biological Soil Crusts: An Organizing Principle in Drylands*. Springer, pp. 3–13.
- Berner, T and M Evenari (1978). "The influence of temperature and light penetration on the abundance of the hypolithic algae in the Negev Desert of Israel". In: *Oecologia* 33.2, pp. 255–260.
- Bowker, Matthew A (2007). "Biological soil crust rehabilitation in theory and practice: An underexploited opportunity". In: *Restoration Ecology* 15.1, pp. 13–23.

- Bowker, Matthew A, Fernando T Maestre, and Cristina Escolar (2010). "Biological crusts as a model system for examining the biodiversity–ecosystem function relationship in soils". In: *Soil Biology and Biochemistry* 42.3, pp. 405–417.
- Bowker, Matthew A, Santiago Soliveres, and Fernando T Maestre (2010). "Competition increases with abiotic stress and regulates the diversity of biological soil crusts". In: *Journal of Ecology* 98.3, pp. 551–560.
- Bowker, Matthew A et al. (2011). "Functional profiles reveal unique ecological roles of various biological soil crust organisms". In: *Functional Ecology* 25.4, pp. 787–795.
- Bowker, Matthew A et al. (2014). "Biological soil crusts (biocrusts) as a model system in community, landscape and ecosystem ecology". In: *Biodiversity and Conservation* 23.7, pp. 1619–1637.
- Bowker, Matthew A et al. (2016). "Controls on distribution patterns of biological soil crusts at micro to global scales". In: *Biological Soil Crusts: An Organizing Principle in Drylands*. Springer, pp. 173–197.
- Bresler, Eshel, Brian L McNeal, and David L Carter (2012). *Saline and sodic soils: principles-dynamics-modeling*. Vol. 10. Springer Science & Business Media.
- Büdel, Burkhard et al. (2009). "Southern African biological soil crusts are ubiquitous and highly diverse in drylands, being restricted by rainfall frequency". In: *Microbial Ecology* 57.2, pp. 229–247.
- Buhr, HO and SB Miller (1983). "A dynamic model of the high-rate algal-bacterial wastewater treatment pond". In: *Water Research* 17.1, pp. 29–37.
- Cable, Jessica M and Travis E Huxman (2004). "Precipitation pulse size effects on Sonoran Desert soil microbial crusts". In: *Oecologia* 141.2, pp. 317–324.
- Carini, Paul et al. (2016). "Relic DNA is abundant in soil and obscures estimates of soil microbial diversity". In: *Nature Microbiology* 2, p. 16242.
- Caruso, Tancredi et al. (2011). "Stochastic and deterministic processes interact in the assembly of desert microbial communities on a global scale". In: *The ISME Journal* 5.9, pp. 1406–1413.
- Castillo-Monroy, Andrea P et al. (2011). "Relationships between biological soil crusts, bacterial diversity and abundance, and ecosystem functioning: Insights from a semi-arid Mediterranean environment". In: *Journal of Vegetation Science* 22.1, pp. 165–174.
- Chamizo, Sonia et al. (2012). "Runoff at contrasting scales in a semiarid ecosystem: A complex balance between biological soil crust features and rainfall characteristics". In: *Journal of Hydrology* 452, pp. 130–138.
- Chamizo, Sonia et al. (2016). "The role of biocrusts in arid land hydrology". In: *Biological soil crusts: An organizing principle in drylands*. Springer, pp. 321–346.
- Ciais, Philippe et al. (2014). "Carbon and other biogeochemical cycles". In: *Climate change 2013: the physical science basis. Contribution of Working Group I to the Fifth Assessment Report of the Intergovernmental Panel on Climate Change*. Cambridge University Press, pp. 465–570.

- Colica, Giovanni et al. (2014). "Microbial secreted exopolysaccharides affect the hydrological behavior of induced biological soil crusts in desert sandy soils". In: *Soil Biology and Biochemistry* 68, pp. 62–70.
- Darrouzet-Nardi, Anthony et al. (2015). "Observations of net soil exchange of CO₂ in a dryland show experimental warming increases carbon losses in biocrust soils". In: *Biogeochemistry* 126.3, pp. 363–378.
- Davies, Lawrence O et al. (2013). "Light structures phototroph, bacterial and fungal communities at the soil surface". In: *PLoS ONE* 8.7, e69048.
- De Philippis, Roberto and Massimo Vincenzini (1998). "Exocellular polysaccharides from cyanobacteria and their possible applications". In: *FEMS Microbiology Reviews* 22.3, pp. 151–175.
- Ebrahimi, Ali and Dani Or (2015). "Hydration and diffusion processes shape microbial community organization and function in model soil aggregates". In: *Water Resources Research*.
- Elbert, Wolfgang et al. (2012). "Contribution of cryptogamic covers to the global cycles of carbon and nitrogen". In: *Nature Geoscience* 5.7, pp. 459–462.
- Evans, RD and JR Johansen (1999). "Microbiotic crusts and ecosystem processes". In: *Critical Reviews in Plant Sciences* 18.2, pp. 183–225.
- Faist, Akasha M et al. (2017). "Biological soil crust and disturbance controls on surface hydrology in a semi-arid ecosystem". In: *Ecosphere* 8.3.
- Fierer, Noah and Robert B Jackson (2006). "The diversity and biogeography of soil bacterial communities". In: *Proceedings of the National Academy of Sciences* 103.3, pp. 626–631.
- Flemming, Hans-Curt and Jost Wingender (2010). "The biofilm matrix". In: *Nature Reviews Microbiology* 8.9, pp. 623–633.
- Garcia-Pichel, Ferran and Brad M Bebout (1996). "Penetration of ultraviolet radiation into shallow water sediments: High exposure for photosynthetic communities". In: *Marine Ecology Progress Series. Oldendorf* 131.1, pp. 257–262.
- Garcia-Pichel, Ferran and Jayne Belnap (1996). "Microenvironments and Microscale Productivity of Cyanobacterial Desert Crusts¹". In: *Journal of Phycology* 32.5, pp. 774–782.
- (2002). "Small-scale environments and distribution of biological soil crusts". In: *Biological Soil Crusts : Structure, Function, and Management*. Springer, pp. 193–201.
- Garcia-Pichel, Ferran et al. (2003). "Small-scale vertical distribution of bacterial biomass and diversity in biological soil crusts from arid lands in the Colorado Plateau". In: *Microbial Ecology* 46.3, pp. 312–321.
- Garcia-Pichel, Ferran et al. (2013). "Temperature drives the continental-scale distribution of key microbes in topsoil communities". In: *Science* 340.6140, pp. 1574–1577.
- Gomez, Jose A, Kai Höffner, and Paul I Barton (2014). "DFBALab: A fast and reliable MATLAB code for dynamic flux balance analysis". In: *BMC Bioinformatics* 15.1, p. 1.
- Grote, Edmund E et al. (2010). "Carbon exchange in biological soil crust communities under differential temperatures and soil water contents: implications for global change". In: *Global Change Biology* 16.10, pp. 2763–2774.
- Gunnigle, Eoin et al. (2017). "Diel-scale temporal dynamics recorded for bacterial groups in Namib Desert soil". In: *Scientific Reports* 7, p. 40189.

- Hagemann, Martin et al. (2015). "Cyanobacterial diversity in biological soil crusts along a precipitation gradient, Northwest Negev Desert, Israel". In: *Microbial Ecology* 70.1, pp. 219–230.
- Henze, Mogens (2000). *Activated Sludge Models ASM1, ASM2, ASM2d and ASM3*. Vol. 9. IWA Publishing.
- Hirokawa, Jun, Takehiro Kato, and Fumitaka Mafuné (2008). "Uptake of gas-phase nitrous acid by pH-controlled aqueous solution studied by a wetted wall flow tube". In: *The Journal of Physical Chemistry A* 112.47, pp. 12143–12150.
- Hu, Chunxiang et al. (2002). "Effect of desert soil algae on the stabilization of fine sands". In: *Journal of Applied Phycology* 14.4, pp. 281–292.
- Isichei, Augustine O (1990). "The role of algae and cyanobacteria in arid lands. A review". In: *Arid Land Research and Management* 4.1, pp. 1–17.
- Johnson, Shannon L, Susanne Neuer, and Ferran Garcia-Pichel (2007). "Export of nitrogenous compounds due to incomplete cycling within biological soil crusts of arid lands". In: *Environmental Microbiology* 9.3, pp. 680–689.
- Johnson, Shannon L et al. (2005). "Relevance of ammonium oxidation within biological soil crust communities". In: *Environmental Microbiology* 7.1, pp. 1–12.
- Jones, Ryan T et al. (2009). "A comprehensive survey of soil acidobacterial diversity using pyrosequencing and clone library analyses". In: *The ISME Journal* 3.4, pp. 442–453.
- Kim, Minsu and Dani Or (2016). "Individual-based model of microbial life on hydrated rough soil surfaces". In: *PLoS ONE* 11.1, e0147394.
- (2017). "Hydration status and diurnal trophic interactions shape microbial community function in desert biocrusts". In: *Biogeosciences* 14.23, pp. 5403–5424.
- Kreft, Jan-Ulrich, Ginger Booth, and Julian WT Wimpenny (1998). "BacSim, a simulator for individual-based modelling of bacterial colony growth". In: *Microbiology* 144.12, pp. 3275–3287.
- Kuske, Cheryl R et al. (2012). "Response and resilience of soil biocrust bacterial communities to chronic physical disturbance in arid shrublands". In: *The ISME Journal* 6.4, pp. 886–897.
- Lange, Otto L (2003). "Photosynthesis of soil-crust biota as dependent on environmental factors". In: *Biological Soil Crusts: Structure, Function, and Management*. Springer, pp. 217–240.
- Lauber, Christian L et al. (2009). "Pyrosequencing-based assessment of soil pH as a predictor of soil bacterial community structure at the continental scale". In: *Applied and Environmental Microbiology* 75.15, pp. 5111–5120.
- Ma, Jie et al. (2013). "An inorganic CO₂ diffusion and dissolution process explains negative CO₂ fluxes in saline/alkaline soils". In: *Scientific Reports* 3.
- Maestre, Fernando T et al. (2013). "Changes in biocrust cover drive carbon cycle responses to climate change in drylands". In: *Global change biology* 19.12, pp. 3835–3847.
- Mager, Denise M (2010). "Carbohydrates in cyanobacterial soil crusts as a source of carbon in the southwest Kalahari, Botswana". In: *Soil Biology and Biochemistry* 42.2, pp. 313–318.

- Mager, DM and AD Thomas (2011). "Extracellular polysaccharides from cyanobacterial soil crusts: A review of their role in dryland soil processes". In: *Journal of Arid Environments* 75.2, pp. 91–97.
- Masaro, L and XX Zhu (1999). "Physical models of diffusion for polymer solutions, gels and solids". In: *Progress in Polymer Science* 24.5, pp. 731–775.
- Mazor, Gideon et al. (1996). "The role of cyanobacterial exopolysaccharides in structuring desert microbial crusts". In: *FEMS Microbiology Ecology* 21.2, pp. 121–130.
- McCalley, Carmody K and Jed P Sparks (2009). "Abiotic gas formation drives nitrogen loss from a desert ecosystem". In: *Science* 326.5954, pp. 837–840.
- McIntyre, DS (1966). "Characterizing soil aeration with a platinum microelectrode. II. Response under controlled soil physical conditions". In: *Soil Research* 4.2, pp. 103–113.
- More, TT et al. (2014). "Extracellular polymeric substances of bacteria and their potential environmental applications". In: *Journal of Environmental Management* 144, pp. 1–25.
- Or, Dani, Sachin Phutane, and Arnaud Dechesne (2007). "Extracellular polymeric substances affecting pore-scale hydrologic conditions for bacterial activity in unsaturated soils". In: *Vadose Zone Journal* 6.2, pp. 298–305.
- Paerl, Hans W, James L Pinckney, and Timothy F Steppe (2000). "Cyanobacterial–bacterial mat consortia: Examining the functional unit of microbial survival and growth in extreme environments". In: *Environmental Microbiology* 2.1, pp. 11–26.
- Pankratov, Timofei A et al. (2008). "Substrate-induced growth and isolation of Acidobacteria from acidic Sphagnum peat". In: *The ISME Journal* 2.5, pp. 551–560.
- Pedersen, Lasse L, Barth F Smets, and Arnaud Dechesne (2015). "Measuring biogeochemical heterogeneity at the micro scale in soils and sediments". In: *Soil Biology and Biochemistry* 90, pp. 122–138.
- Pepe-Ranney, Charles et al. (2016). "Non-cyanobacterial diazotrophs mediate dinitrogen fixation in biological soil crusts during early crust formation". In: *The ISME Journal* 10.2, pp. 287–298.
- Pereira, Sara et al. (2009). "Complexity of cyanobacterial exopolysaccharides: Composition, structures, inducing factors and putative genes involved in their biosynthesis and assembly". In: *FEMS Microbiology Reviews* 33.5, pp. 917–941.
- Peterjohn, William T and William H Schlesinger (1990). "Nitrogen loss from deserts in the southwestern United States". In: *Biogeochemistry* 10.1, pp. 67–79.
- Phillies, George DJ (1987). "Dynamics of polymers in concentrated solutions: The universal scaling equation derived". In: *Macromolecules* 20.3, pp. 558–564.
- Phillips, Claire L et al. (2011). "Interpreting diel hysteresis between soil respiration and temperature". In: *Global Change Biology* 17.1, pp. 515–527.
- Porada, Philipp et al. (2013). "Estimating global carbon uptake by lichens and bryophytes with a process-based model". In: *Biogeosciences* 10, pp. 6989–6989.
- Porada, Philipp et al. (2014). "Estimating impacts of lichens and bryophytes on global biogeochemical cycles". In: *Global Biogeochemical Cycles* 28.2, pp. 71–85.
- Porada, Philipp et al. (2016). "High potential for weathering and climate effects of non-vascular vegetation in the Late Ordovician". In: *Nature communications* 7.

- Porada, Philipp et al. (2017). "Estimating global nitrous oxide emissions by lichens and bryophytes with a process-based productivity model". In: *Biogeosciences* 14.6, pp. 1593–1602.
- Raanan, Hagai et al. (2015). "Three-dimensional structure and cyanobacterial activity within a desert biological soil crust". In: *Environmental Microbiology*.
- Rajeev, Lara et al. (2013). "Dynamic cyanobacterial response to hydration and dehydration in a desert biological soil crust". In: *The ISME Journal* 7.11, pp. 2178–2191.
- Rocha, Ulisses Nunes da et al. (2015). "Isolation of a significant fraction of non-phototroph diversity from a desert Biological Soil Crust". In: *Frontiers in Microbiology* 6.
- Rodríguez-Caballero, Emilio et al. (2015). "Swelling of biocrusts upon wetting induces changes in surface micro-topography". In: *Soil Biology and Biochemistry* 82, pp. 107–111.
- Rossi, Federico and Roberto De Philippis (2015). "Role of cyanobacterial exopolysaccharides in phototrophic biofilms and in complex microbial mats". In: *Life* 5.2, pp. 1218–1238.
- Rossi, Federico et al. (2012). "Characteristics and role of the exocellular polysaccharides produced by five cyanobacteria isolated from phototrophic biofilms growing on stone monuments". In: *Biofouling* 28.2, pp. 215–224.
- Sancho, Leopoldo G et al. (2016). "Carbon Budgets of Biological Soil Crusts at Micro-, Meso-, and Global Scales". In: *Biological Soil Crusts: An Organizing Principle in Drylands*. Springer, pp. 287–304.
- Sander, Rolf (1999). *Compilation of Henry's law constants for inorganic and organic species of potential importance in environmental chemistry*.
- Schoolfield, RM, PJH Sharpe, and CE Magnuson (1981). "Non-linear regression of biological temperature-dependent rate models based on absolute reaction-rate theory". In: *Journal of Theoretical Biology* 88.4, pp. 719–731.
- Schramm, Andreas et al. (2000). "Microenvironments and distribution of nitrifying bacteria in a membrane-bound biofilm". In: *Environmental Microbiology* 2.6, pp. 680–686.
- Steven, Blaire, Jayne Belnap, Cheryl R Kuske, et al. (2013). "Dryland soil microbial communities display spatial biogeographic patterns associated with soil depth and soil parent material". In: *FEMS Microbiology Ecology* 86.1, pp. 101–113.
- Šťovíček, Adam et al. (2017). "Microbial community response to hydration-desiccation cycles in desert soil". In: *Scientific Reports* 7.45735.
- Tan, Yunhu, Zhi-Xin Wang, and Kevin C Marshall (1998). "Modeling pH effects on microbial growth: A statistical thermodynamic approach". In: *Biotechnology and Bioengineering* 59.6, pp. 724–731.
- Thomas, Andrew D, Steve R Hoon, and Patricia E Linton (2008). "Carbon dioxide fluxes from cyanobacteria crusted soils in the Kalahari". In: *Applied Soil Ecology* 39.3, pp. 254–263.
- Warren, SD (2001). "Synopsis: Influence of biological soil crusts on arid land hydrology and soil stability". In: *Biological Soil Crusts: Structure, Function, and Management*. Springer, pp. 349–360.
- Weber, Bettina, Burkhard Büdel, and Jayne Belnap, eds. (2016). *Biological Soil Crusts: An Organizing Principle in Drylands*. Springer.

- Weber, Bettina et al. (2015). "Biological soil crusts accelerate the nitrogen cycle through large NO and HONO emissions in drylands". In: *Proceedings of the National Academy of Sciences* 112.50, pp. 15384–15389.
- Weber, Bettina et al. (2016). "Natural recovery of biological soil crusts after disturbance". In: *Biological Soil Crusts: An Organizing Principle in Drylands*. Springer, pp. 479–498.
- Wolf, Gundula, Cristian Picioreanu, and Mark van Loosdrecht (2007). "Kinetic modeling of phototrophic biofilms: The PHOBIA model". In: *Biotechnology and Bioengineering* 97.5, pp. 1064–1079.
- Yang, Aidong (2011). "Modeling and evaluation of CO₂ supply and utilization in algal ponds". In: *Industrial & Engineering Chemistry Research* 50.19, pp. 11181–11192.
- Zaady, Eli et al. (2010). "Inferring biological soil crust successional stage using combined PLFA, DGGE, physical and biophysiological analyses". In: *Soil Biology and Biochemistry* 42.5, pp. 842–849.
- Zand-Parsa, Sh and AR Sepaskhah (2004). "Soil hydraulic conductivity function based on specific liquid–vapor interfacial area around the soil particles". In: *Geoderma* 119.1, pp. 143–157.

Chapter 6

The Role of Localised pH on HONO and NH₃ Emissions from Drying Soils and Biocrusts

6.1 Introduction

Biological soil crusts (hereafter biocrusts) are dense cryptogamic communities developed on soil surfaces (mostly < 10 mm thick) in arid and semi-arid regions, and are estimated to cover about 12% of terrestrial surfaces (Rodriguez-Caballero et al., 2018). Biocrust communities constitute of photoautotrophs, such as cyanobacteria, algae, lichens, and mosses, and other heterotrophic microorganisms (Belnap and Lange, 2003; Weber, Büdel, and Belnap, 2016). Biocrusts are considered pioneers of dryland ecosystems due to their role as producers of fixed carbon and nitrogen and as exporters of these fixed nutrients to their surroundings and thus increase fertility of initially barren dryland soils and promote conditions for ecosystem evolution (Pointing and Belnap, 2012).

A prominent characteristic of this live cover, that overlays many dryland surfaces, is its contribution to nitrogen cycling at regional and global scales. Estimates suggest that diazotrophs in biocrusts fix about 24.4 (3.1 – 45.6) Tg of N per year globally, representing 40 to 85% of terrestrial biological N₂ fixation (Rodriguez-Caballero et al., 2018). However, the fate of this large input of fixed N by biocrusts remains unclear. In desert soils, soil N accretion rates are generally low, only 10% of fixed N being retained, (Peterjohn and Schlesinger, 1990), with N loss occurring multiple pathways such as dissolution and transport with infiltrating in soil water, gaseous emissions, and erosional processes (Barger et al., 2016).

Gaseous emissions of fixed N are considered the primary loss pathway, accounting for about 77% of total N inputs according to some estimates (Peterjohn and Schlesinger, 1990). A suite of nitrogen oxides can be released as byproducts of biological activity in biocrusts, including by nitrification (Johnson et al., 2005; Johnson, Neuer, and Garcia-Pichel, 2007; Strauss, Day, and Garcia-Pichel, 2012) and denitrification (Abed et al., 2013). The sources of abiotic emissions are often chemical reactions mediated by solar radiation and soil moisture (McCalley and Sparks, 2009) or by local acidity caused by mineral substrates on soil surfaces (Donaldson, Bish, and Raff, 2014; Kebede et al., 2016). The form of emitted N

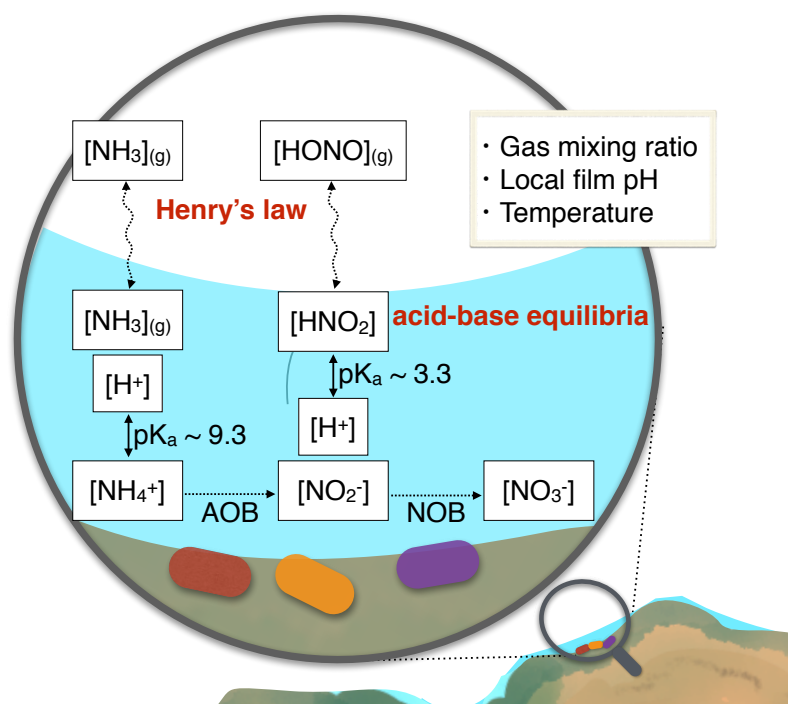


FIGURE 6.1: A schematic of HONO and NH₃ emissions caused by biotic and abiotic factors in an unsaturated soil/desert biocrust. Nitrification performed by ammonia oxidising bacteria (AOB) and nitrite oxidising bacteria (NOB) increases or reduces the gas emissions of NH₃ and HONO directly by altering the concentrations of their protonated forms within thin water film. Increase in concentration during a course of desiccation causes outgassing and precipitation of these compounds depending on the solubility determined by the partial pressure (the mixing ratio) of the compound in soil air, local film pH, and temperature.

gases from biocrusts include greenhouse gases and reactive trace gases, such as nitrous oxide (N₂O) (Abed et al., 2013; Lenhart et al., 2015), nitric oxide (NO) (Barger et al., 2005; McCalley and Sparks, 2008; McCalley and Sparks, 2009; Weber et al., 2015), nitrous acid (HONO) (Weber et al., 2015; Meusel et al., 2018), and ammonia (NH₃) (Barger, 2003; McCalley and Sparks, 2008; McCalley and Sparks, 2009). This study focuses on HONO and NH₃ emissions, both known to be affected by air-soil exchange as driven by coupled biotic and abiotic processes in desert biocrusts.

HONO and NH₃ are important atmospheric trace gases, and their emissions from biocrusts (and from soils in general) play a crucial role for atmospheric pollution at regional to global scales. NH₃ is the primary alkaline gas that regulates rain acidity, it also affects formation of clouds and aerosols (Behera et al., 2013). HONO is a daytime source of hydroxyl (OH) radical and nitric oxide (NO) that regulate the oxidative capacity of the atmosphere. These two soil nitrogen compounds are tightly coupled in terms of nitrification (biotic process) and share their pH dependency on emission in gaseous form (an abiotic process) (Fig. 6.1). During the biologically driven nitrification, ammonia oxidisers including bacteria and archaea (in this model, these oxidisers are simply represented as AOB) transform the fixed inorganic N, ammonium (NH₄⁺), to nitrite (NO₂⁻) where NO₂⁻ is transformed to nitrate (NO₃⁻) by nitrite oxidising bacteria (NOB). Biologically available NH₄⁺ for AOB depends

on the input of fixed N and pH of soil water. At high pH, NH_4^+ can be emitted as NH_3 gas ($\text{pK}_a \sim 9.3$) where this volatilisation may suppress AOB activity. Furthermore, AOB release an intermediate product of nitrification, NO_2^- , which has been suggested as a major source of HONO emissions from soils (Su et al., 2011; Oswald et al., 2013; Scharko et al., 2015). An essential step for such emissions, is the protonation of NO_2^- , forming HONO. Since the acid-base dissociation constant of HONO is $\text{pK}_a \sim 3.3$, soils with low pH and high NO_2^- levels are expected to release a substantial amount of HONO (Su et al., 2011). However, in contrast with the expectation that HONO emissions are promoted in acidic soils, evidence suggests that significant fluxes of HONO are emitted from neutral or alkaline soils (above $\text{pH} \sim 5$) and from desert biocrusts (Oswald et al., 2013; Weber et al., 2015). Moreover, the temporal patterns of HONO emissions are similar characteristics across different soil types and cyanobacteria-dominated biocrusts, exhibiting emissions with a well-defined peak at a certain “optimal” water content. Studies have proposed that AOB activity could be responsible for such distinct pattern of HONO emissions (Oswald et al., 2013). Scharko et al., 2015 combined flux chamber with genomic approaches to conclude that HONO emissions were related to the abundance of ammonia oxidisers within neutral or alkaline soils (that exhibit high nitrification rates). Their genomic analysis has also shown the presence of active NOB that are supposed to complete the nitrification process.

These consistent observations raise several questions: First, the observations of simultaneous HONO and NH_3 emissions from a soil or biocrust appears to be in contradiction with the high levels of NH_4^+ and NO_2^- and bulk soil pH in equilibrium. Second, if NOB are active in a soil, the production of NO_2^- by AOB as the direct source for HONO emission must be reconciled due to the expectation of NO_2^- consumption by NOB. Finally, a characteristic feature of HONO emissions in drying soils (and biocrusts) is the strong moisture dependency irrespective of nitrifiers’ activity. The dependency on soil hydration conditions motivated us to have a closer look at how changes in soil chemistry caused by hydration dynamics affect microbial activity? and how soil pH is affected by surface drying?

To address these questions we focused on soil hydration dynamics at the microbial scale. Surprisingly, effect of hydration dynamics at the microscale have been largely ignored although it is a ubiquitous process in surface soils. We employ a mechanistic model for the interactions between soil properties, microbial activity, and physicochemical processes across water-air interfaces within drying soils. We focus on the roles of hydration dynamics and spatial heterogeneity of soil surfaces in modifying pH related gaseous emissions. We first address biotic-abiotic processes occurring within drying soils and then expand the picture to thin desert biocrusts.

6.2 Results and Discussion

6.2.1 Soil hydration represented by water contents and water film thickness distributions

The quantitative description of soil gaseous exchanges is strongly dependent on the representation of the soil aqueous phase and air-water interfaces. Macroscopically, soil hydration is characterised by water contents and matric potentials, these interdependent variables modifying gas diffusivity and thus gaseous fluxes from soil. However, the macroscopic representation does not provide resolved geometrical information on the distribution of soil aqueous phase that is shaped by complex pores and surfaces at scales relevant to microbial life (submillimetre scales) (Grundmann et al., 2001; Nunan et al., 2003). In this study, we use the water film thickness retained by rough soil surfaces to represent soil hydration status at the microscale (as the primary interface for gas uptake and emissions). The volume of the liquid film controls local concentrations of substances, thereby determining amounts of matter exchange between gas and bare mineral surfaces.

We implemented a previously developed rough surface model (Kim and Or, 2016; Šťovíček et al., 2017; Kim and Or, 2017) that links macroscopic soil water content to aqueous film thickness at different matric potential values. We define a physical domain representing a vertical cross-section of a desert biocrust comprised of soil grain surfaces (rough solid patches) each retaining water based on own roughness and ambient matric potential. The effective film thickness reflects the combined effects of adsorption and capillarity encapsulated in the definition of soil matric potential (energy state of soil water). The spatial heterogeneity of pores and surface roughness yields a distribution of water film thickness that contributes to the macroscopic water content (for model details see Appendix E, Fig. E.3). The model shows that, as the soil water content varies from about $0.3 \text{ m}^3 \cdot \text{m}^{-3}$ (total porosity) to about $0.01 \text{ m}^3 \cdot \text{m}^{-3}$ (residual water content) during desiccation, the effective water film thickness varies by orders of magnitude from about 10^{-5} m at saturation to about 10^{-8} m (Fig. 6.2a, Tuller and Or, 2005). Even under moderately dry conditions, a thin water film on soil surfaces serves as the gas-liquid interface.

6.2.2 Time scales of physicochemical processes in unsaturated soils

Changes in the distribution of aqueous film thickness during soil desiccation affect the time scales of various processes (Fig. 6.2b). Here we focus primarily on physical and chemical processes within and across the gas-liquid interface. Near saturation, water fills the soil pores and hinders gas percolation and exchange, whereas nutrient diffusion and chemical processes become similar to aquatic systems. However, during soil desiccation, the air percolates through empty soil pores and facilitates exchange of gaseous compounds to and from the residual water film on the rough soil grains. The large surface area of the thin water film allows instant equilibration of mass transfer; thus, dissolved gases follow Henry's equilibria. Diffusivity of other compounds through the aqueous phase becomes reduced under unsaturated conditions owing to lower connectivity and higher tortuosity (Moldrup

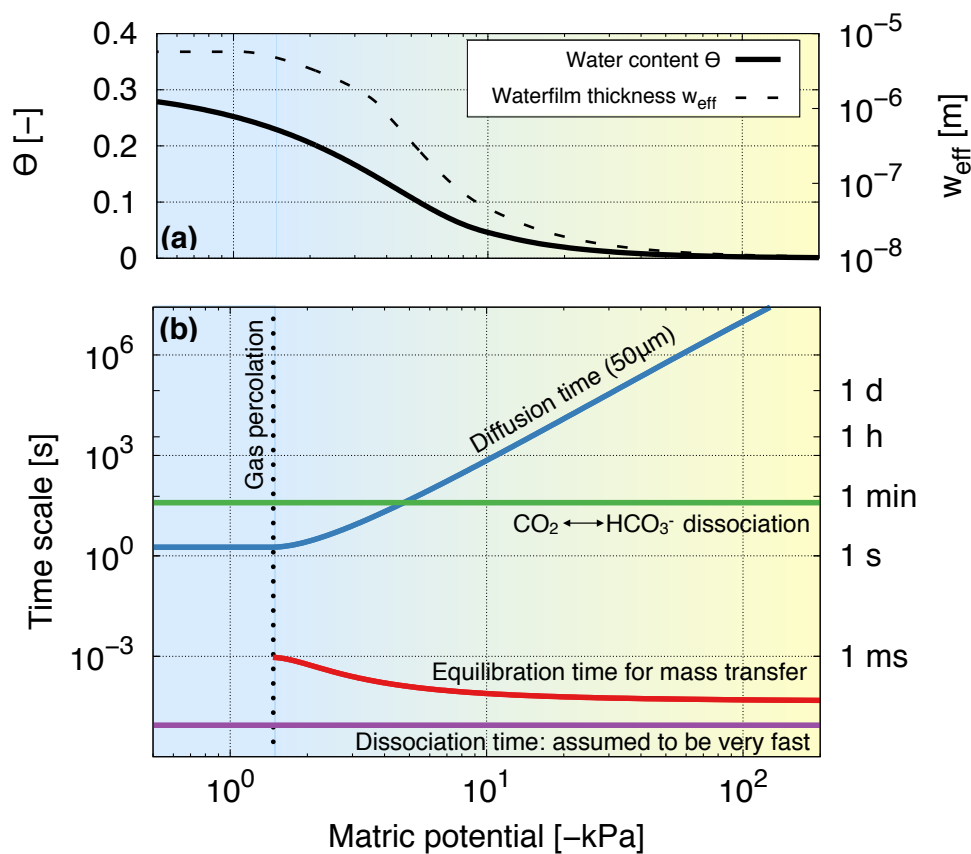


FIGURE 6.2: **Changes in abiotic conditions while drying soils in the model.** (a) A typical model calculation of water content (black solid line) and effective water film thickness (black dashed line) as a function of matric potential (blue-yellow gradient represents relative wetness). (b) A comparison of characteristic time scales for physico-chemical processes relevant for local pH determination in aqueous films for a range of hydration conditions (expressed as matric potential).

et al., 2003). Chemical processes, such as acid-base dissociation or hydrolysis, are relatively fast compared with other processes. Under moderately dry conditions, the water film is sufficiently thick to permit high water activity and dissociation processes are assumed to instantly equilibrate. Consequently, lateral solute diffusion through the water film becomes limiting relative to gaseous exchanges in unsaturated soils. In Fig. 6.2b, the timescale of diffusion in the aqueous phase is estimated from $t \sim 2l/D_{\text{eff}}$ where l is characteristic diffusion distance (we use here $50\mu\text{m}$ a representative local scale considering average inter-cell distances in soil is in the order of 10^{-5} m (Raynaud and Nunan, 2014)) and D_{eff} is the effective diffusivity of a solute at the given matric potential. This suggests that the productions and/or consumptions of dissolved compounds would be localised under unsaturated conditions because of the slow diffusion. Hence, distribution of soil minerals and biological entities become decisive and yield strong spatial heterogeneity in chemical conditions.

6.2.3 Mean soil pH vs. local aqueous film pH

Soil pH is considered a primary attribute for soil microbial activity and community structure (Fierer and Jackson, 2006; Lauber et al., 2009). Additionally, soil pH has been used to describe the chemical dissociation for estimating pH-dependent gas emissions (Su et al., 2011). However, local variations in pH and spatial heterogeneity in chemical status of aqueous films under unsaturated conditions would greatly affect microbial processes especially in dense desert biocrusts. While the soil or biocrust are drying, the resulting changes in the aqueous phase configuration (i.e., film thickness in this study) and gas phase percolation jointly shape concentrations of dissolved gaseous compounds as determined by mixing ratios of inorganic carbon and nitrogen (i.e. CO₂, NH₃, HONO etc.) based on Henry's law at local scale. The pH distribution under unsaturated conditions can be deduced from acid-base equilibria and charge balance (See Appendix E for details). The spatial heterogeneity of pH within drying soils is affected by air-soil exchange and diffusion without considering biological activity. Additionally, the distribution of soil minerals, such as iron, aluminium (hydr)oxides or calcite, would contribute to spatial heterogeneity (Donaldson, Bish, and Raff, 2014) and the resulting soil pH. We note that the reactivity of these minerals is also affected by hydration dynamics that determines the dissolution of gaseous compounds (mainly CO₂). In the model, we consider a finite amount of exchangeable Ca²⁺ is included as a representative (calcite forming) mineral to mimic calcareous desert soils where most of biocrusts develop. Ca²⁺ precipitation regulates the upper bound of local pH where a finite buffering capacity could be easily exceeded in shrinking aqueous volumes during soil drying.

An additional source of spatial variation in pH is the distribution of chemical ions in aqueous phase, such as the highly soluble NO₃⁻, that may be independent of gas phase constraints and strongly affects local pH. We suggest that non-uniform distribution of sources and sinks and its limited diffusion causes local imbalance in free cations and anions. This, thus, results in strong heterogeneity of pH under unsaturated conditions that cannot be captured with bulk soil pH (see Appendix E).

6.2.4 Spatially resolved pH measurements of drying soils

Evaporative water loss in soils increases concentrations of chemical compounds and precipitation of salts. These changes influence acid-base dissociations that are kinetically rapid and highly depending on pH of aqueous solutions. For systems with limited buffering capacity pH is likely to vary during soil desiccation. Surprisingly, such a local and dynamic aspect has been missing in studies that often consider a constant bulk soil pH value irrespective of hydration conditions. To examine the dynamic and local nature of soil pH during drying, we conducted a series of proof of concept tests by measuring the pH of buffer solutions and wet quartz sand (sterilised) under two wet-dry cycles (Fig. 6.3). The pH values and map were obtained from planar pH optodes (Blossfeld et al., 2010; PreSens) and simultaneously verified using independent microelectrodes (Amman, 1988; Unisense). Optode measurements showed a consistent (albeit mild) decrease in pH (about 0.2-0.3 units) during drying confirming that the evaporative water removal alters the pH in the remaining water films. The microelectrode revealed a more drastic drop of pH of about 1 pH unit. This could indicate that the buffering capacities of the solution and that of sand pore water was exceeded in the small volume of remaining water film. The differences in the magnitude of pH values measured by the optodes and electrodes may also reflect on the nature of the measurement itself (highly localised with the electrodes and more diffused with the optodes). The optodes not only allowed for observations to dry conditions (drier than possible with the electrodes), but they also provided a spatial distribution of pH values. We have used different textures of sands and modified the levels of $p\text{CO}_2$ levels in the air (Fig. 6.4). In these measurements, the sample of sterilised quartz sand was deliberately laid out with two distinctive regions with fine and coarse textures to highlight non-uniform pH dynamics during drying. This nested behaviour in pH decrease in the entire region highlighted relations between local pH and soil texture. This relation persisted under different $p\text{CO}_2$ levels in the air suggesting a potential role of soil microscale structure affecting local pH dynamics (as also demonstrated by the vertical gradient of pH during drying Appendix E Fig. E.4). Furthermore, increasing $p\text{CO}_2$ levels increased the concentrations of carbonic acid and lowered the pH of the entire domain.

These results, should be interpreted with caution because the responses of the optode and electrodes were designed primarily for wet conditions, hence we trust results from intermediate hydration conditions where the optode remains fully hydrated (while film diffusion becomes limited). These limitations notwithstanding, these preliminary measurements demonstrate how local pH varies during soil desiccation

6.2.5 Predicting emissions dynamics from drying biocrusts

We now expand the discussion from drying sterile soil to the surface layer hosting a biocrust with interacting bacterial communities by employing a mechanistic biocrust model (Kim and Or, 2017) to gain insights into pH-dependent gas emissions from biocrusts. For comparisons of model predications with measurements, we considered a wetting-drying event

applied to model biocrust under darkness (hence no photosynthesis) mimicking reported lab experiments (Weber et al., 2015; Maier et al., 2018; Meusel et al., 2018)

Fig. 6.5 depicts simulated dynamics of drying biocrusts. During the 24 hours of simulated drying (Fig. 6.5a), the net biogenic production rate of soil NO_2^- was negative during drying due to the consumption rates by NOB exceeding production rates by AOB (Fig. 6.5b).

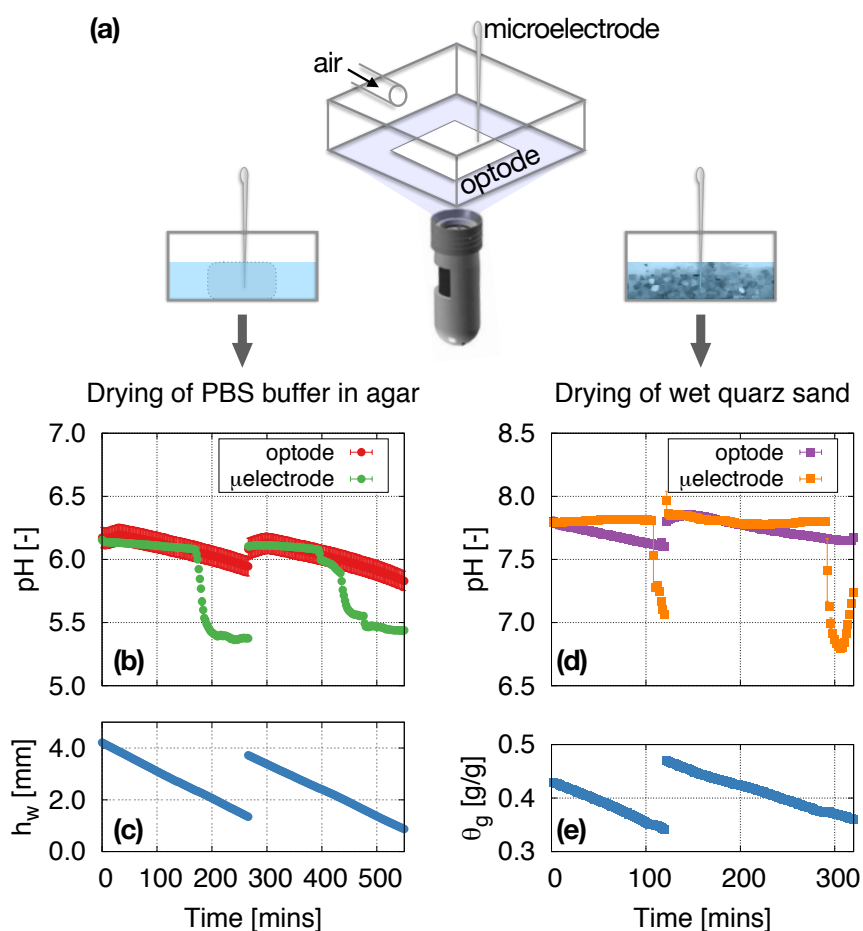


FIGURE 6.3: Changes in pH under wet-dry cycles are monitored with a planar optode and a microelectrode. Figure 3. Laboratory measurements of pH dynamics under two wet-dry cycles monitored using a planar pH optode (pH sensor SF-HP5-OIW, PreSens GmbH, Rosensburg, Germany) and a pH microelectrode (PH-200C, Unisense, Aarhus, Denmark). (a) An illustration of the measurement cuvette and experimental setup. The optode imaging sensor was mounted at the bottom of the glass cuvette and the microelectrode was installed from the top, upright. A small glass cuvette (20 mm × 20 mm × 20 mm) filled with an agar block saturated with phosphate buffer saline (PBS pH = 6.1, 0.1M) (left) or wet quartz sand (right) while monitoring pH variations during drying. Sample desiccation was controlled by airflow rate (relative humidity 20%) into the cube and hydration status of the sample was monitored simultaneously by weighing the cuvette. (b) pH changes in drying agar monitored with the optode (red circles) and the microelectrode (green circles). (c) The amount of water in the cube was measured in weight and the value was translated to equivalent water depth of the agar cube (maximal value was 4 mm). (d) pH changes during drying of wet quartz sand monitored with the optode (purple squares) and an microelectrode (orange squares). (e) variations in the hydration status of the sand expressed as gravimetric water contents (weight of water/weight of wet sand [g/g]).

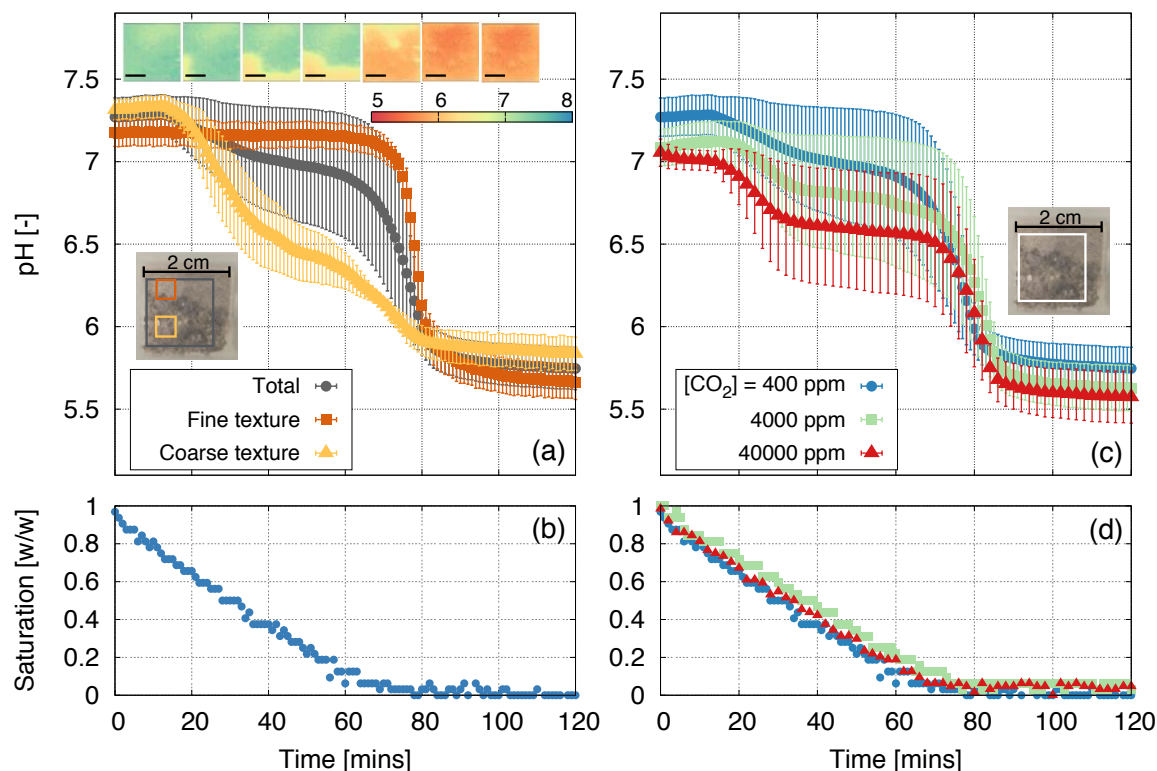


FIGURE 6.4: **Direct measurement of pH localisation and dynamics during desiccation of quartz sand of different textures under different atmospheric $p\text{CO}_2$ levels.** (a) A top view of gamma-ray sterilised quartz sand with fine (0.08–0.2 mm, red box in the inset) and coarse (0.7–3 mm, yellow box in the inset) domains; optode measured pH values for different regions are shown by symbols with error bars; the dynamics of spatial pH maps during pH transition are given as inset figures at 20 min intervals (the scale bar indicates 5 mm) (b) The saturation dynamics during evaporation defined as the amount of water in the sample relative to the amount of deionised water applied for saturating the sample). (c) The variations in spatially averaged pH of the same sterilised quartz during drying for different levels of $p\text{CO}_2$ in the measurement cuvette. (d) saturation dynamics during desiccation for experiments conducted under different $p\text{CO}_2$ levels.

Consequently, microbial activity (combining AOB and NOB) together, did not provide a direct source for HONO emissions (the system acted as a sink of HONO via Henry's law). The strong variations in local pH resulted from the joint effects of microbial activity and desiccation (Fig. 6.5c). Under wet conditions (high saturation), most of the domain is alkaline (and the bulk soil pH is near 7), thus high levels of NH_3 volatilisation occurred at the soil surface (marked by a positive NH_3 flux in Fig. 6.5d). The emission of NH_3 increased following desaturation and invasion of gas phase through the biocrust (marked by gas percolation degree in Fig. 6.5a). These reflect an impediment to gas emissions under high saturation irrespective of local chemical conditions. Furthermore, simulations show a decrease in aqueous film pH during drying similar to observations (Figures 6.3 and 6.4). The resulting spatial variations in local pH span a range of pK_a values for HONO with an increase in emission rates (Fig. 6.5c, d, f). The local acidification of the water film drives the HONO release and NH_3 absorption. Following the complete desiccation of the biocrust with the cessation of biological activity and high local acidification, HONO efflux proceeds

abiotically as outgassing by Henry's law and volatilisation (Fig. 6.5d).

We attribute this local acidification during drying to nitrification that results in accumulation of NO₃⁻ while water is removed by evaporation (Fig. 6.5e, f). To examine these effects of hydration conditions and local nitrate accumulation on aqueous film pH, we systematically calculated local pH as a function of nitrate amounts and matric potentials (Fig. 6.5g). In this calculation, we ignore diffusion within the film and across aqueous patches and consider evaporative concentrations and instantaneous equilibration of gas-liquid partitioning at local scale only (the size of a connected liquid patch is of the order of 100 μm²). Result suggests that the local amount of NO₃⁻ is the primary determinant of local pH during evaporative water loss. While other inorganic carbon and nitrogen components are constrained by their protonated forms of gaseous compounds (NH₃ + H⁺ ⇌ NH₄⁺, HONO ⇌ NO₂⁻ + H⁺, etc.), NO₃⁻ remains in the water film due to its high solubility in water (in the range of ~10-1000 g/L) and it can be protonated to nitric acid (HNO₃) only under extremely acidic conditions (pK_a ~ -1.4). For moderately dry conditions on the soil surface (in the order of kPa), the amount of nitrate is an important variable in determining local pH. This implies that the localised sources or sinks of NO₃⁻ within unsaturated soils under limited diffusion can provide strong heterogeneity in pH covering the pK_a values for HONO and NH₃. Interestingly, the emitted amounts of HONO from soils are shown to be strongly correlated with high nitrification rate (Scharko et al., 2015) or contents of NO₃⁻ and NO₂⁻ (Meusel et al., 2018), which however was not observed by Weber et al., 2015. This could support our hypothesis of local acidification caused by NO₃⁻ accumulation.

6.2.6 HONO and NH₃ emissions under different desiccation rates and atmospheric ammonia levels

Measuring local pH heterogeneity under unsaturated conditions and separating abiotic and biotic effects experimentally remain a challenge. We thus use the model to systematically evaluate HONO emissions under a range of conditions including different drying rates and atmospheric NH₃ levels. Desiccation rates regulate the optimal time window for HONO and NH₃ emissions (Fig. 6.6a, b, c) through their joint dependency on water contents and pH. Simulations suggest the NH₃ emissions occur before HONO emissions during drying. Additionally, the absorption of NH₃ to water film can be expected at peak of HONO emissions illustrating the interrelation between these two gases that are mediated by local pH in the aqueous phase. The mixing ratios of these gases in the air also affect magnitudes of HONO emission and NH₃ absorption during drying (Appendix E). Increasing NH₃ levels increases the maximum emission flux of HONO by promoting AOB activity with higher nitrification rates (See Fig. 6.6 and Fig. E.3 in Appendix E). The water content dependency of gaseous emission is illustrated by plotting the simulated emissions as a function of hydration conditions (presented with percent of water holding capacity) (Fig. 6.6d, e). In Fig. 6.6d we compare model simulations with HONO emission rates determined in laboratory studies of cyanobacterial biocrusts (without higher organisms such as moss or lichens) (Weber et al., 2015; Maier et al., 2018; Meusel et al., 2018). We also provide concurrent simulated NH₃ emissions (Fig. 6.6e) in the absence of data. The comparison shows that the model captures

the salient features of biocrust HONO emissions, with the characteristic single peak at “optimal” water content (for different drying rates and atmospheric NH_3 levels). We note that the peak HONO emissions does not occur at the same water content for all conditions (although the range is narrow 10 to 25% of WHC). The results suggest that the desiccation rate affects the shape of the HONO emission peak, and these drying patterns reflect the properties of the biocrust and external driving forces (evaporation rate). For instance, lichen- and bryophyte-dominated biocrusts emit smaller amounts of HONO over a wider range of water contents (Weber et al., 2015; Maier et al., 2018) and it may be owing to its higher water-holding capacity that would delay desiccation process. The level of atmospheric NH_3 determines the magnitude of the HONO peak emissions and these can be related to the population size and activity of diazotrophs and nitrifiers inhabiting the biocrust.

6.3 Methods and Materials

6.3.1 The desert biocrust mathematical model

The desert biocrust model (DBM) (Kim and Or, 2017) is a mechanistic model that links the aqueous state with geochemical processes and biological activity in pioneer desert biocrusts (no lichens and mosses). The DBM considers diffusion-reaction, mass transfer at gas/liquid interface, and chemical processes like C and N dissociation, volatilisation, and precipitation, whereas microbial processes are described by an individual based representation of cells. The biocrust microbial community consists of four functional groups; photoautotrophs, aerobic heterotrophs, denitrifiers (anaerobic heterotrophs), and chemoautotrophs (nitrifiers; AOB and NOB). The cycles of carbon and nitrogen are performed only by microorganisms (no higher organisms) and thus representing cyanobacteria dominated biocrusts. For fully saturated biocrusts, the model has been tested extensively and found to agree with multiple lab experiments in terms of dynamics of oxygen and pH profile, and CO_2 efflux from biocrust under day-night cycles (Kim and Or, 2017). This study extends the previous work by exposing the microbial community to dynamic hydration conditions (wet-dry). In other words, we have used the distribution and abundances of microorganisms obtained at full saturation as initial conditions for the subsequent desiccation and rewetting cycles. In this study, the atmospheric level of HONO was kept constant as 1 ppb in agreement with field measurements for semiarid pine forest (Su et al., 2011). The mixing ratio of NH_3 was used as a control parameter for the simulations of Fig. 6.6 and Fig. E.3 in Appendix E. We varied the atmospheric level of NH_3 from 0.1 ppb to 20 ppb (representing typical values in the range of 1 to 10 ppb depending on the time of the day, season, and regions). Detailed description is provided in Kim and Or (2017) and in the supplementary information for this study.

Detailed descriptions are provided in Kim and Or, 2017 and Appendix E.

6.3.2 Experimental setup for localised pH

We have used a planar pH optode sensor (PreSens GmbH, Rosensburg, Germany) and a PH-200C microelectrode (Unisense, Aarhus, Denmark) that were installed in a cubic glass

sample holder ($20 \times 20 \times 20$ mm). The cubic sample holder (Fig. 6.3) was filled with (1) 2% agar saturated with phosphate buffered saline (PBS) solution (pH = 6.1, 0.1M) (2) sterilised quartz sand (gamma ray) with grain size in the range of 0.08~3 mm initially saturated with deionised water. The sample holder was equipped with an inlet for supply of constant gas flow to the sample. The composition of air in the sample was controlled by injecting mixture of air and carbon dioxide (CO₂). For mixing the gas in situ, we used a rotameter (product code: FL-2AB-04SA; OMEGA Engineering, Manchester, UK). For airflow we maintained a constant relative humidity of 20% and a fixed rate of 1 L.min⁻¹ using a dew point generator (LI-610; LI-COR, Lincoln, USA). The hydration status of the sample (evaporative mass loss) was monitored by logging the sample weight during drying. For details of the experimental procedures and additional measurements, see Appendix E.

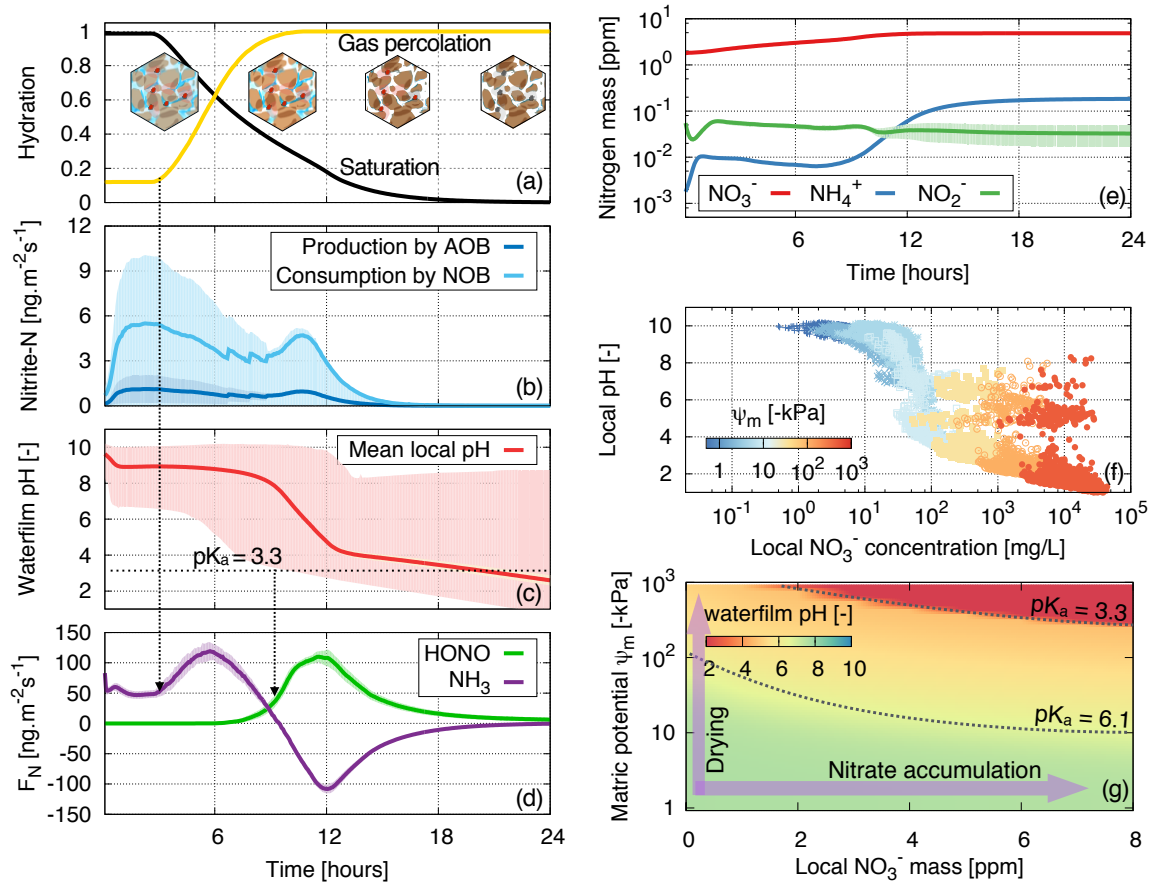


FIGURE 6.5: **Dynamic processes during biocrust desiccation as predicted by the desert biocrusts model (DBM).** The results were obtained from 8 different simulations with identical boundary conditions using numerical biocrusts. (a) Changes in saturation and increase in gas percolation during 24 h drying (the insets schematically depict aqueous phase configurations during drying). (b) Simulated production and consumption of NO_2^- by microorganisms; NO_2^- consumption by NOB (light blue) exceeds the production by AOB (dark blue). Solid lines are the averaged values and shaded areas indicate 1 std for all simulations. (c) Mean local pH (red line) where spatial heterogeneity of local pH spans a wide range of pH values (shaded area indicates from minimum to the maximum). (d) The dynamics of HONO (green) and NH_3 (purple) emissions from the model biocrust with positive and negative flux values indicate emission or uptake from the domain, respectively. (e) Simulated variations in inorganic nitrogen compounds with NO_3^- (red), NH_4^+ (blue), and NO_2^- , (green) during drying (values are given in ppm with the unit $\text{g}/\text{g}_{\text{soil}}$) (f) Simulated local concentrations of NO_3^- in the aqueous phase plotted against local pH at 4 hours intervals ($t = 0, 4, \dots, 24$) during drying (the colour bar corresponds to mean matric potential and the values are taken from a typical simulation). (g) The relationship between local aqueous film pH as a function of hydration state (expressed as matric potential) and the amount of NO_3^- .

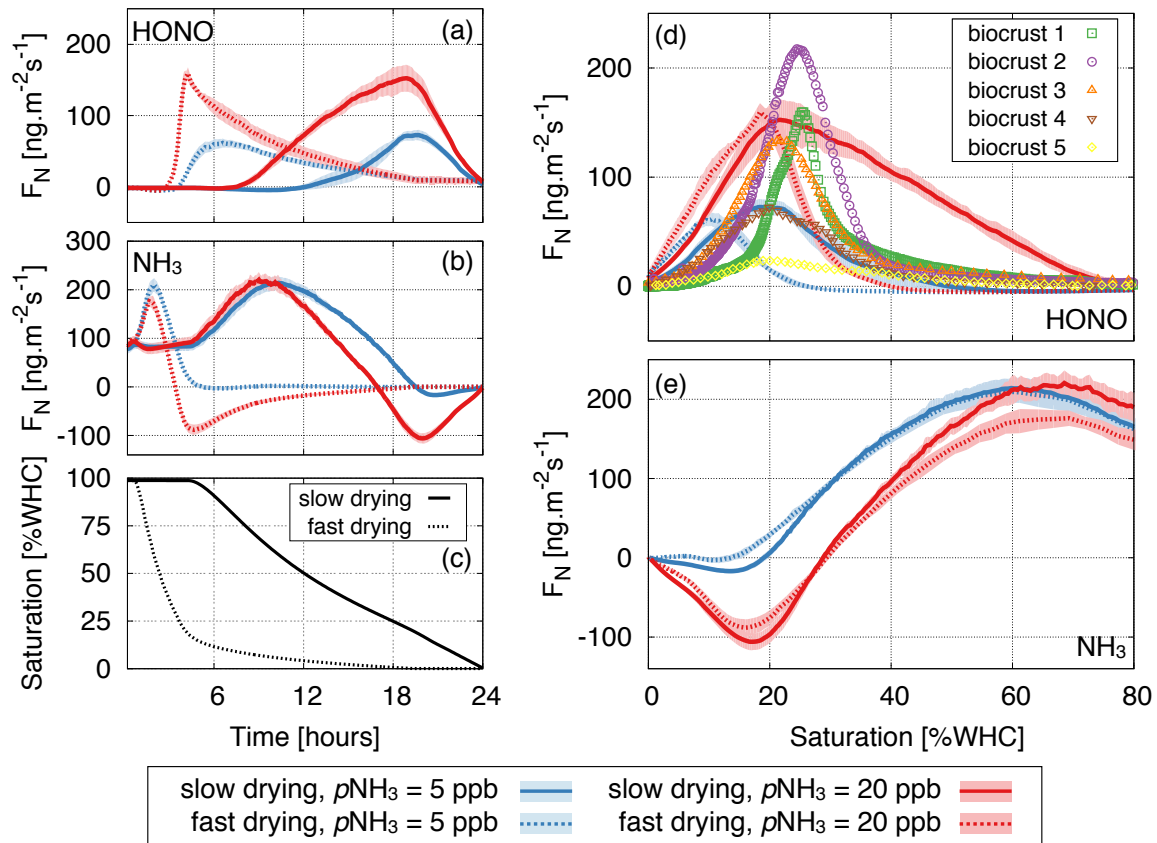


FIGURE 6.6: **HONO and NH_3 gaseous emissions during biocrust drying.** HONO and NH_3 gaseous emissions during biocrust drying as functions of time (left column) and soil hydration conditions (right, expressed in percent of water holding capacity). Simulations of different conditions in drying patterns (Solid lines: slow drying, Dashed lines: fast drying), and atmospheric NH_3 levels (low: 5 ppb given in blue, high: 20 ppb given in red) are presented. The simulation results of (a) HONO and (b) NH_3 emissions during (c) 24 hours of drying at two rates. (d) measured (symbols) and simulated (lines) HONO emissions with measurements from several biocrusts, biocrust 1 (light crust in South Africa, Weber et al., 2015), biocrust 2 (dark crust in South Africa, Weber et al., 2015), biocrust 3 (cyanobacteria-dominated crust in South Africa, Maier et al., 2018), biocrust 4 (light crust in Cyprus, Meusel et al., 2018), and biocrust 5 (dark crust in Cyprus, Meusel et al., 2018). (e) Simulated emissions of NH_3 from the same drying biocrusts are plotted (no data for comparison).

References

- Abed, Raeid MM et al. (2013). "High rates of denitrification and nitrous oxide emission in arid biological soil crusts from the Sultanate of Oman". In: *The ISME Journal* 7.9, pp. 1862–1875.
- Amman, Daniel (1988). *Ion-selective micro-electrodes*. Springer Berlin.
- Barger, Nichole N (2003). "Biogeochemical Cycling and N Dynamics of Biological Soil Crusts in Semi-arid Ecosystem". PhD thesis. Colorado State University.
- Barger, Nichole N et al. (2005). "NO gas loss from biologically crusted soils in Canyonlands National Park, Utah". In: *Biogeochemistry* 75.3, pp. 373–391.
- Barger, Nichole N et al. (2016). "Patterns and controls on nitrogen cycling of biological soil crusts". In: *Biological Soil Crusts: An Organizing Principle in Drylands*. Springer, pp. 257–285.
- Behera, Sailesh N et al. (2013). "Ammonia in the atmosphere: a review on emission sources, atmospheric chemistry and deposition on terrestrial bodies". In: *Environmental Science and Pollution Research* 20.11, pp. 8092–8131.
- Belnap, Jayne and Otto L Lange, eds. (2003). *Biological Soil Crusts: Structure, Function, and Management*. Springer.
- Blossfeld, Stephan et al. (2010). "Rhizosphere pH dynamics in trace-metal-contaminated soils, monitored with planar pH optodes". In: *Plant and soil* 330.1-2, pp. 173–184.
- Donaldson, Melissa A, David L Bish, and Jonathan D Raff (2014). "Soil surface acidity plays a determining role in the atmospheric-terrestrial exchange of nitrous acid". In: *Proceedings of the National Academy of Sciences* 111.52, pp. 18472–18477.
- Fierer, Noah and Robert B Jackson (2006). "The diversity and biogeography of soil bacterial communities". In: *Proceedings of the National Academy of Sciences* 103.3, pp. 626–631.
- Grundmann, GL et al. (2001). "Spatial modeling of nitrifier microhabitats in soil". In: *Soil Science Society of America Journal* 65.6, pp. 1709–1716.
- Johnson, Shannon L, Susanne Neuer, and Ferran Garcia-Pichel (2007). "Export of nitrogenous compounds due to incomplete cycling within biological soil crusts of arid lands". In: *Environmental Microbiology* 9.3, pp. 680–689.
- Johnson, Shannon L et al. (2005). "Relevance of ammonium oxidation within biological soil crust communities". In: *Environmental Microbiology* 7.1, pp. 1–12.
- Kebede, Mulu A et al. (2016). "The Role of Iron-Bearing Minerals in NO₂ to HONO Conversion on Soil Surfaces". In: *Environmental Science & Technology* 50.16, pp. 8649–8660.
- Kim, Minsu and Dani Or (2016). "Individual-based model of microbial life on hydrated rough soil surfaces". In: *PLoS ONE* 11.1, e0147394.
- (2017). "Hydration status and diurnal trophic interactions shape microbial community function in desert biocrusts". In: *Biogeosciences* 14.23, pp. 5403–5424.
- Lauber, Christian L et al. (2009). "Pyrosequencing-based assessment of soil pH as a predictor of soil bacterial community structure at the continental scale". In: *Applied and Environmental Microbiology* 75.15, pp. 5111–5120.

- Lenhart, Katharina et al. (2015). "Nitrous oxide and methane emissions from cryptogamic covers". In: *Global change biology* 21.10, pp. 3889–3900.
- Maier, Stefanie et al. (2018). "Photoautotrophic organisms control microbial abundance, diversity, and physiology in different types of biological soil crusts". In: *The ISME journal* 12, pp. 1032–1046.
- McCalley, Carmody K and Jed P Sparks (2008). "Controls over nitric oxide and ammonia emissions from Mojave Desert soils". In: *Oecologia* 156.4, pp. 871–881.
- (2009). "Abiotic gas formation drives nitrogen loss from a desert ecosystem". In: *Science* 326.5954, pp. 837–840.
- Meusel, Hannah et al. (2018). "Emission of nitrous acid from soil and biological soil crusts represents an important source of HONO in the remote atmosphere in Cyprus". In: *Atmospheric Chemistry and Physics* 18.2, pp. 799–813.
- Moldrup, P. et al. (2003). "Modeling diffusion and reaction in soils: X. A unifying model for solute and gas diffusivity in unsaturated soil". In: *Soil Science* 168.5, pp. 321–337.
- Nunan, N. et al. (2003). "Spatial distribution of bacterial communities and their relationships with the micro-architecture of soil". In: *FEMS Microbiology Ecology* 44.2, pp. 203–215.
- Oswald, R et al. (2013). "HONO emissions from soil bacteria as a major source of atmospheric reactive nitrogen". In: *Science* 341.6151, pp. 1233–1235.
- Peterjohn, William T and William H Schlesinger (1990). "Nitrogen loss from deserts in the southwestern United States". In: *Biogeochemistry* 10.1, pp. 67–79.
- Pointing, Stephen B and Jayne Belnap (2012). "Microbial colonization and controls in dryland systems". In: *Nature Reviews Microbiology*.
- Raynaud, Xavier and Naoise Nunan (2014). "Spatial ecology of bacteria at the microscale in soil". In: *PloS one* 9.1.
- Rodriguez-Caballero, Emilio et al. (2018). "Dryland photoautotrophic soil surface communities endangered by global change". In: *Nature Geoscience* 11.3, p. 185.
- Scharko, Nicole K et al. (2015). "Combined flux chamber and genomics approach links nitrous acid emissions to ammonia oxidizing bacteria and archaea in urban and agricultural soil". In: *Environmental Science & Technology* 49.23, pp. 13825–13834.
- Šťovíček, Adam et al. (2017). "Microbial community response to hydration-desiccation cycles in desert soil". In: *Scientific Reports* 7.45735.
- Strauss, Sarah L, Thomas A Day, and Ferran Garcia-Pichel (2012). "Nitrogen cycling in desert biological soil crusts across biogeographic regions in the Southwestern United States". In: *Biogeochemistry* 108.1–3, pp. 171–182.
- Su, Hang et al. (2011). "Soil nitrite as a source of atmospheric HONO and OH radicals". In: *Science* 333.6049, pp. 1616–1618.
- Tuller, Markus and Dani Or (2005). "Water films and scaling of soil characteristic curves at low water contents". In: *Water Resources Research* 41.9.
- Weber, Bettina, Burkhard Büdel, and Jayne Belnap, eds. (2016). *Biological Soil Crusts: An Organizing Principle in Drylands*. Springer.

-
- Weber, Bettina et al. (2015). "Biological soil crusts accelerate the nitrogen cycle through large NO and HONO emissions in drylands". In: *Proceedings of the National Academy of Sciences* 112.50, pp. 15384–15389.

Chapter 7

Conclusions and outlook

In this PhD thesis, a framework of modelling microbial life in unsaturated soils is introduced. The model combines an abstract representation of rough surfaces/cross-section of vertical soils, namely the rough surface patch model (RSPM), with the individual based model (IBM) of microbial cells inhabiting in the physical domain. The model was further developed to a mechanistic model of biological soil crusts in deserts (the desert biocrusts model, DBM). The proposed models attempt to include a detailed description of microhydrology for different soil properties, which influence the intra and interspecies interaction of microbial communities under dynamic hydration conditions. Furthermore, some of chemical processes are also considered in the model to predict the local changes of chemical status (such as pH), that are modified by microbial activity, and to estimate the efflux of various gases. The main conclusions are summarised here and outlook for future research is presented.

7.1 Summary and concluding remarks

1. Bridging the gap between microbial processes and representative soil volumes (Chapters 2 and 3)

The RSPM was proposed to describe microbial life in soils with a possibility of upscaling, spatially to centimetre scales and temporally to the scale of months (Kim and Or, 2016). The main advantage of this model is to connect the hydration condition at macroscale (at representative soil volume scale) to the microscale that are relevant for the microorganisms inhabiting on soil surfaces. In the model, the physical domain, abstract hydrated-soil-surfaces, is discretised with hexagonal patches with roughness parameters. These roughness parameters represent a size distribution of water retaining surface geometries, surface pores and smooth surfaces. The spatial variation of roughness collectively yields a simple mathematical representation of different soil types and their hydration conditions, such as water contents at a given matric potential. Meanwhile, the retained water within a patch provides effective water film thickness and patch connectivity that jointly determine microbial dispersion rates and diffusion of substrates in aqueous phase. Several illustrative examples of microbial trophic interactions and population dynamics are provided in Chapter 2 and 3 demonstrating its applicability to a wide range of topics in soil microbiology.

2. Understanding responses of microbial community in desert soils to wetting-drying cycles (Chapter 4)

The RSPM was extended to describe a cross-section of vertical soil domain. This extended model of vertical soil domain allows to include gas phase, which plays a pivotal role for shaping microbial activity during wetting-drying cycles by altering transport properties of gaseous compounds (e.g. O_2 , CO_2 , etc.). Using the extended RSPM, the time-dependent-hydration conditions were imposed on the domain with multiple species including aerobic and anaerobic heterotrophs. Confirming the field observation, the simulation results capture the drastic changes in both the diversity and the composition of soil microbial communities after soil wetting. The enhanced hydraulic connectivity leads to increase in nutrient flux, rapid dispersion, and stronger competition within the connected aqueous habitats, thus decrease in diversity. Meanwhile, the microbial composition is altered from the aerobes-dominated to anaerobes-dominate community with small effects on the consumption patterns of carbon source (the limiting nutrient) (Šťovíček et al., 2017).

3. Providing a generalised model of biological soil crusts and its functioning under different hydrated conditions (Chapter 5)

Following up the extended RSPM of a cross-section of vertical soil domain, a mechanistic model of desert biological soil crusts (biocrusts), the DBM, is proposed (Kim and Or, 2017). The model links the biophysical and chemical processes that shape the functioning of microbial community in biocrusts. The community includes four functional groups mainly for carbon and nitrogen cycling; diazotrophic photoautotrophs, aerobic heterotrophs, anaerobic heterotrophs (denitrifiers), and chemoautotrophs (nitrifiers, ammonia oxidising bacteria, nitrite oxidising bacteria). These members of the community interact trophically and respond dynamically to cycles of hydration, light, and temperature, representing an ecologically functioning unit. The spatial organisation of these functional groups, the vertical stratification, emerged from their trophic interactions under the steep gradients of various nutrient sources within a few mm thick biocrusts. This indicates one of reasons why biocrusts can host a high abundance and diversity of microorganisms under very harsh conditions like deserts. One of the key features of the model was to capture the dynamics of chemical conditions, that are modified by microbial activity. For instance, the supersaturation of oxygen and the alkalisation occurring on the top of saturated biocrusts in a spatio-temporal context of diurnal cycles are captured with the mathematical model for the first time to the extent of our knowledge.

4. Predicting reactive gaseous emissions from soils/biocrusts by disentangling biotic-abiotic factors under hydration dynamics (Chapter 6)

The DBM was applied to dynamic hydration conditions. This work attempts to provide mechanistic understanding of interaction between biotic and abiotic processes that are tightly coupled under dynamic conditions, such as drying after wetting events (Kim and Or, 2018).

Especially, pH-dependent emissions of reactive trace gases, HONO and NH_3 , were examined and their fluxes were estimated under varying environmental conditions. The localisation of pH in unsaturated soils/biocrusts was suggested to be the main cause for the emission of these gases. The localised acidification of water films was tested in laboratory measurements and results supports the onset of such localisation even in the absence of biological activities in sterilised soils. With support of the simple measurements, the modelling results showed that activity of nitrifiers, AOB and NOB together, was shown to be the source of such local acidification, by producing environmentally mobile NO_3^- together with H^+ , that keeps the charge neutrality of local water films. The findings resolve the paradox of significant emissions of HONO from globally ubiquitous biological soil crusts and alkaline soils – the culprit is the localised acidification driven by evaporative desiccation and nonuniform activity of nitrification within drying biocrusts, which can extend to general soils that are exposed to frequent wet-dry cycles.

To sum up, this thesis provides a modelling framework of microbial life in unsaturated soils under hydration dynamics and spatial gradients. The abstract representation of soil rough surfaces and pore spaces provide a link between macroscopic and microscopic measures of soil hydration. The water film thickness distribution connects the discrepancy between the scale of observation (centimetric) and the scale relevant to microbial life (sub-millimetric). The mechanistic model combining physical, chemical, and biological processes elucidates the importance of microscale processes, which cannot be captured with bulk measurements, in determining globally relevant biogeochemical processes.

7.2 Outlook for future research

The modelling framework presented in this thesis has opened a number of research lines that can be explored in the future. Here are some examples of possible topics that can be investigated with the present model and other applications with some modification.

1. Exploring roles of hydration events in shaping microbial communities in deserts

Non-rainfall water inputs to soils, such as dew, vapour, and fog are important to many ecosystems (Wang, Kaseke, and Seely, 2017), particularly hyper-arid, arid, and semi-arid regions where rainfall events are infrequent and scarce (Makhalanyane et al., 2015). Biological soil crusts and hypolithic communities in resource-limited deserts are shown to be strongly shaped by such non-rainfall hydration events ranging from microbial composition, diversity, and functioning to biocrust types (Cáceres et al., 2007; Azúa-Bustos et al., 2011; Kidron, Herrnsstadt, and Barzilay, 2002; Warren-Rhodes et al., 2013). The model capability of handling unsaturated conditions can benefit to understand roles of such non-rainfall events for the livings under harsh conditions in deserts. For instance, integrating physical models of dew formation to the current model may delineate the time-window for the cyanobacterial (and other microbial) activities during early morning hours (Agam and Berliner, 2006; Gunnigle et al., 2017; Chamizo et al., 2016) and this may offer the evaluation of potential net

CO₂ uptake by biocrusts, that absorb dew/fog moisture, during dry seasons, which is often neglected in regional and global models. Furthermore, such modelling exercise can offer quantitative analyses of a positive feedback that enhances harvesting of non-rainfall water input to the desert ecosystem.

2. Application of the desert biocrust model to other ecosystems

The modified RSPM essentially represents a hydrated porous medium. Therefore, the model can be applicable with ease to the fully saturated domain, like sediments or microbial mats, with some modification of community members. In the DBM, the microbial community was “designed” specifically for the carbon and nitrogen cycling performed by desert biocrusts. If other saturated systems are under consideration, anaerobic phototrophs, surface-iron-reducing bacteria, or methanogens, could be introduced in the community to investigate their interaction and distribution. This would be beneficial for a mechanistic understanding of biogeochemistry of such systems. Furthermore, hydrogen-generating photosynthetic bacteria within microbial mat (Burow et al., 2012) can be an interesting topic for an extended version of the current model in the future to predict the emission of hydration gas as renewable energy sources.

3. Disentangling abiotic, biotic factors to estimate biogeochemical cycles

Microbial activity occurring within soil is often strongly coupled with other abiotic factors. Especially, when it comes to estimating CO₂ release/adsorption from/to soils, separating contributions of biotic and abiotic factors from laboratory or fields measurements is challenging. This is the reason why many studies of soil respiration often remain descriptive with a phenomenological expression (such as the Q_{10} value). The mechanistic model of soils would allow us to separate the abiotic contribution from soil “respiration”, which highly depends on temperature, soil moisture, and soil minerals in concert. By resolving heat transfer and mass transfer between gas and liquid in soils, efflux of CO₂ from soils without biological activity can be estimated. Fig. 7.1 shows an example calculation of CO₂ emission contributed by only abiotic factor, diurnal cycles of temperature and soil wetting-drying event. The results can benefit the long-term measurement by automated CO₂ flux chambers (Darrouzet-Nardi et al., 2015) to connect the microbial activity within biocrusts by subtracting the contribution of abiotic factors, degassing. For instance, the active CO₂ uptake by biocrusts can be predicted right after sunrise within moderately dry biocrusts, which can be easily dismissed when the total flux is considered. As previously mentioned, such active uptake during early evenings may indicate the role of dew formation during the measurement circumstances. Such approach would provide a comprehensive look at CO₂ exchange between biocrust soils (or general soils) and the atmosphere that has a high impact on climate dynamics.

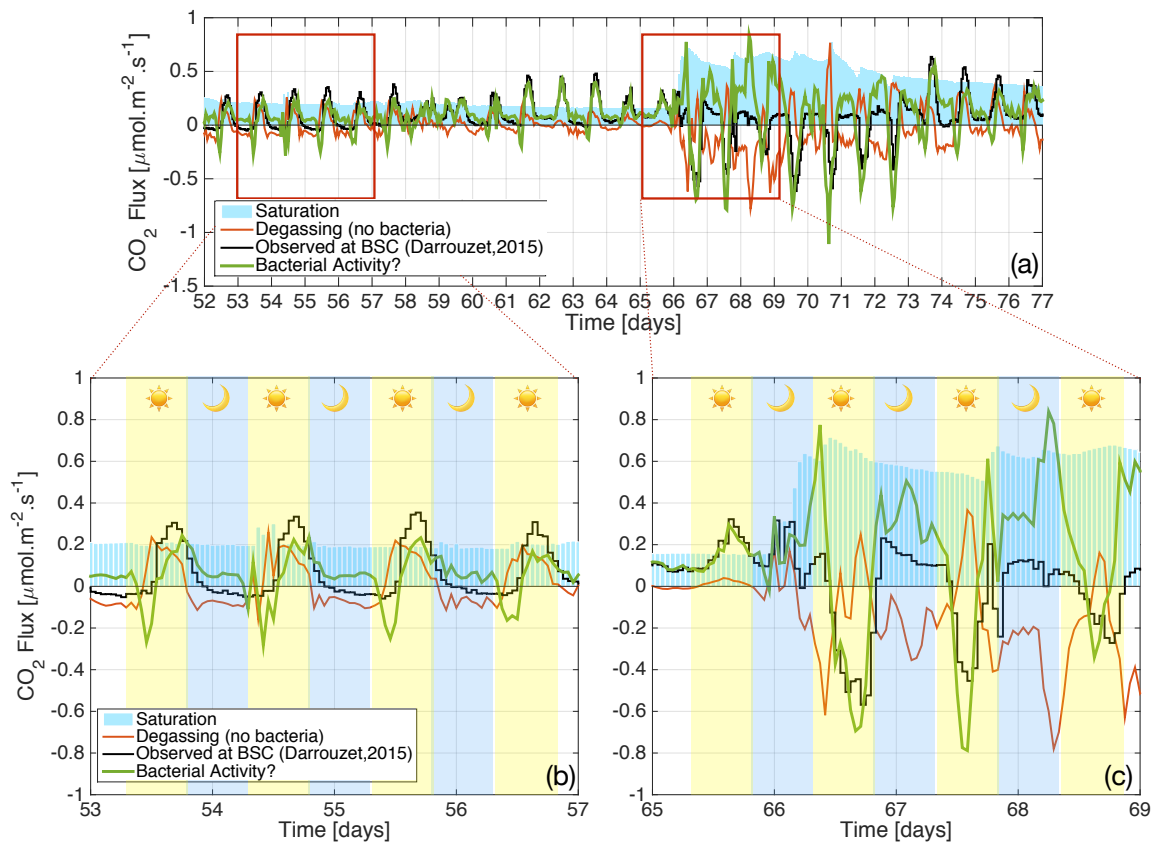


FIGURE 7.1: Separating abiotic contributions from CO₂ efflux measured from biological crusts. The long-term measurement of CO₂ efflux from biocrusts on the Colorado Plateau, USA (Darrouzet-Nardi et al., 2015) is analysed as an example of the model application to estimate contributions of biotic and abiotic factors. By using the reported data of soil hydration and temperature, the abiotic contribution, mainly degassing by Henry's law, is estimated. (a) Example calculations of CO₂ emissions driven only by temperature and hydration are given for the duration of 25 days. By subtracting the calculated abiotic contribution (red lines) from observed CO₂ flux (black lines), the possible contribution by biological activity can be estimated (green lines). The blue bars indicate the saturation of the soil at 5cm depth. (b) The calculation is provided for selected 5 consecutive days under dry conditions. The results suggest that active uptake of CO₂ by phototrophs within biocrusts right after sunrise which is not captured in the total flux of CO₂. (c) The calculation is provided for selected 5 consecutive days under wet conditions after rainfalls. The results suggest the augmented biological activity, photosynthesis during daytime and dark-respiration during nighttime, under wet conditions.

4. The exploration of climatic conditions for the global model

Biocrusts have been shown to play a role in global biogeochemical cycles and climate change would likely reduce its coverage on Earth's terrestrial surfaces, thus affect microbial contribution to N cycling (Rodriguez-Caballero et al., 2018). The proposed desert biocrust model provides a prediction of N loss via gaseous pathways including the concurrent emissions of HONO and NH₃ during desiccation which was not predicted in global models. Some improvement of the current model, in terms of computational capacity to speed up calculations, could allow us to make a new estimate of N cycles at the global scale by combining

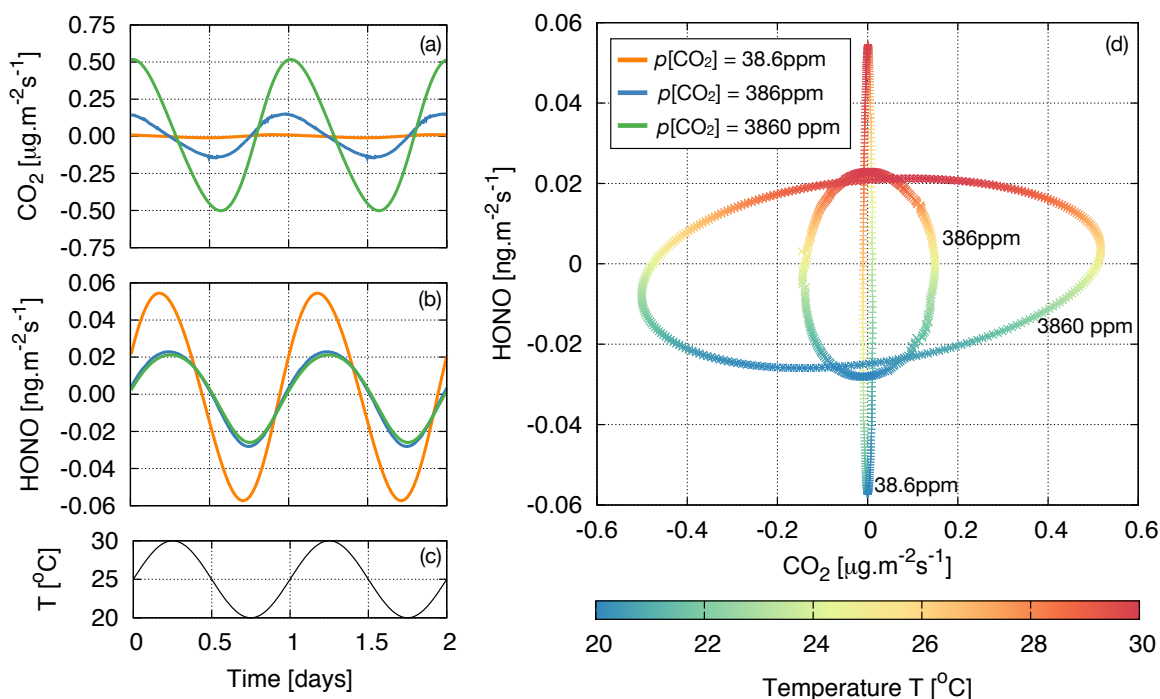


FIGURE 7.2: **Diurnal dynamics of CO₂ and HONO** An example calculation of CO₂ (a) and HONO (b) emissions and absorption from hydrated surface under diurnal cycles of temperature (c) (a sinusoidal function is assumed in a range of $25 \pm 5^{\circ}\text{C}$). (d) changes in partial pressure of CO₂ affects the gaseous emissions of HONO and CO₂. The result shows the strong coupling between two gaseous compounds caused only by temperature cycles in the absence of biological activity.

global dataset of rainfall, atmospheric composition and dry depositions of inorganic N. Furthermore, other higher organisms of biocrusts with algae, moss, and lichens can be included to make a full picture although the model of their physiological factors may require new approach in terms of their consumption patterns for inorganic C and N.

5. Generalised model of microbial life at surface-air interface

In spite of the fact that the DBM has been developed to describe the microbial life in soil and biocrusts, the model can also serve microbial activity on any hydrated surfaces and its interaction with surrounding air. Since microbial communities present almost every surfaces and they are able to emit/absorb gaseous compounds, there is no doubt in investigating their roles in influencing the composition of atmosphere, thus climate change at regional scale. In this context, an endeavour to generalise the model of microbial life at surfaces should be beneficial. For instance, as we have shown in Chapter 6, using the generalised surface model would allow to capture the feedback of microbial and chemical processes on atmospheric composition of CO₂ and other trace reactive gases under varying environmental conditions.

Fig. 7.2 provides an example calculation of gaseous emission of CO₂ and HONO from a hydrated surface under diurnal cycles of temperature. This figure shows the strongly

coupled behaviour of these two trace gases. Formally, Henry's law and the charge balance principle on the local water film of hydrated surfaces cause this coupling. This effect leads to diurnal cycles of HONO efflux, that were shown independent from the presence of biological activity but solely regulated by temperature changes. This simulation results demonstrate that a diurnal cycle of temperature causing the abiotic release of CO₂ may be sufficient to achieve the acid-displacement process at local scale, which was proposed to be a nocturnal loss and daytime source of HONO (VandenBoer et al., 2014; VandenBoer et al., 2015). Therefore, temperature cycles and tight coupling between CO₂ and ceHONO through hydrated surfaces might be necessary in models of atmospheric pollutant dynamics to allow for identification of the missing daytime source of HONO (Michoud et al., 2014; Laufs et al., 2017). Furthermore, the results suggest the potential surface HONO reservoir in daily lives and in numerous environments including agricultural, urban and vegetated regions.

Considering that the consumption (sinks) of CO₂ would affect HONO emission caused by acid-displacement, in depth investigation on the role of surface colonising communities, like vegetation, green leaves, or cryptogamic covers including bryophytes (comprising liverworts and mosses) and lichens, can provide a meaningful estimate for the oxidative capacity of regional air, that is mainly controlled by HONO (see Fig. 7.3). The knowledge of biological processes (physiology, community interaction, etc.) occurring on surfaces as sinks and sources of trace gases and their coverage can be combined with physical models at mesoscale that integrates dispersion of pollutant in complex structured-environment (such as buildings) (Oetl, 2015). Such integrated model would allow us to examine the roles of urban landscapes inhabited by urban microbes (King, 2014) and the relation between their activity and quality of ambient air.

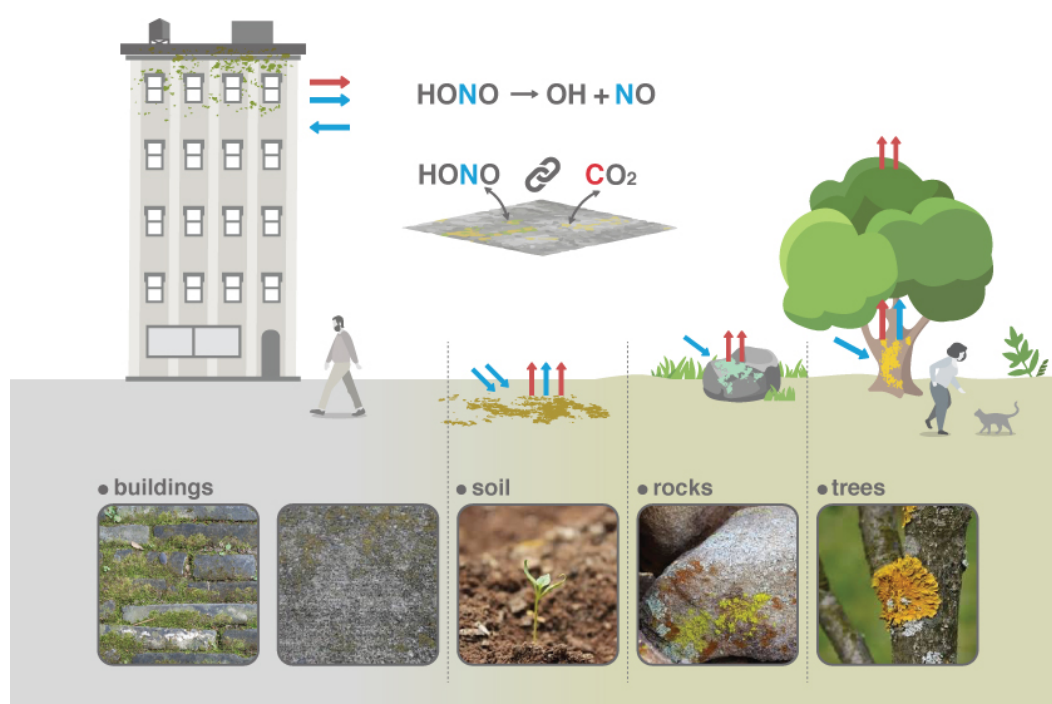


FIGURE 7.3: Interplay between CO_2 and HONO on microbially mediated surfaces The model can be further extended to a generalised surface model to quantify emissions/depositions of carbon and nitrogen gases from/to surfaces that are colonised by organisms (ubiquitous in our surroundings, from buildings to soils, rocks and trees). Especially, trace gas emissions caused by these surface communities can be of general interest. The tight coupling of CO_2 and HONO emissions will manifest the importance of small organisms in our daily lives for regional air quality.

References

- Agam, N and PR Berliner (2006). "Dew formation and water vapor adsorption in semi-arid environments—a review". In: *Journal of Arid Environments* 65.4, pp. 572–590.
- Azúa-Bustos, Armando et al. (2011). "Hypolithic cyanobacteria supported mainly by fog in the coastal range of the Atacama Desert". In: *Microbial Ecology* 61.3, pp. 568–581.
- Burow, Luke C et al. (2012). "Hydrogen production in photosynthetic microbial mats in the Elkhorn Slough estuary, Monterey Bay". In: *The ISME journal* 6.4, p. 863.
- Cáceres, Luis et al. (2007). "Relative humidity patterns and fog water precipitation in the Atacama Desert and biological implications". In: *Journal of Geophysical Research: Biogeosciences* 112.G4.
- Chamizo, Sonia et al. (2016). "The role of biocrusts in arid land hydrology". In: *Biological soil crusts: An organizing principle in drylands*. Springer, pp. 321–346.
- Darrouzet-Nardi, Anthony et al. (2015). "Observations of net soil exchange of CO₂ in a dry-land show experimental warming increases carbon losses in biocrust soils". In: *Biogeochemistry* 126.3, pp. 363–378.
- Gunnigle, Eoin et al. (2017). "Diel-scale temporal dynamics recorded for bacterial groups in Namib Desert soil". In: *Scientific Reports* 7, p. 40189.
- Kidron, Giora J, Ilana Herrnschmidt, and Eldad Barzilay (2002). "The role of dew as a moisture source for sand microbiotic crusts in the Negev Desert, Israel". In: *Journal of Arid Environments* 52.4, pp. 517–533.
- Kim, Minsu and Dani Or (2016). "Individual-based model of microbial life on hydrated rough soil surfaces". In: *PLoS ONE* 11.1, e0147394.
- (2017). "Hydration status and diurnal trophic interactions shape microbial community function in desert biocrusts". In: *Biogeosciences* 14.23, pp. 5403–5424.
- (2018). "The role of localised pH on HONO and NH₃ emissions from drying soils and desert biocrusts". In: *in review*.
- King, Gary M (2014). "Urban microbiomes and urban ecology: How do microbes in the built environment affect human sustainability in cities?" In: *Journal of Microbiology* 52.9, pp. 721–728.
- Laufs, Sebastian et al. (2017). "Diurnal fluxes of HONO above a crop rotation". In: *Atmospheric Chemistry and Physics* 17.11, p. 6907.
- Makhalanyane, Thulani P et al. (2015). "Microbial ecology of hot desert edaphic systems". In: *FEMS Microbiology Reviews* 39.2, pp. 203–221.
- Michoud, Vincent et al. (2014). "Study of the unknown HONO daytime source at a European suburban site during the MEGAPOLI summer and winter field campaigns". In: *Atmospheric Chemistry and Physics* 14.6, pp. 2805–2822.
- Oettl, D (2015). "A multiscale modelling methodology applicable for regulatory purposes taking into account effects of complex terrain and buildings on pollutant dispersion: a case study for an inner Alpine basin". In: *Environmental Science and Pollution Research* 22.22, pp. 17860–17875.

- Rodriguez-Caballero, Emilio et al. (2018). "Dryland photoautotrophic soil surface communities endangered by global change". In: *Nature Geoscience* 11.3, p. 185.
- Šťovíček, Adam et al. (2017). "Microbial community response to hydration-desiccation cycles in desert soil". In: *Scientific Reports* 7.45735.
- VandenBoer, TC et al. (2014). "Evidence for a nitrous acid (HONO) reservoir at the ground surface in Bakersfield, CA, during CalNex 2010". In: *Journal of Geophysical Research: Atmospheres* 119.14, pp. 9093–9106.
- VandenBoer, Trevor C et al. (2015). "Nocturnal loss and daytime source of nitrous acid through reactive uptake and displacement". In: *Nature Geoscience* 8.1, pp. 55–60.
- Wang, Lixin, Kudzai F Kaseke, and Mary K Seely (2017). "Effects of non-rainfall water inputs on ecosystem functions". In: *Wiley Interdisciplinary Reviews: Water* 4.1, e1179.
- Warren-Rhodes, Kimberley A et al. (2013). "Physical ecology of hypolithic communities in the central Namib Desert: the role of fog, rain, rock habitat, and light". In: *Journal of geophysical research: biogeosciences* 118.4, pp. 1451–1460.

Appendix A

Individual-Based Model of Microbial Life on Hydrated Rough Soil Surfaces

The rough surface patch model (RSPM) is a model for patchy hydrated surfaces defined with distributions of available water which sustains microbial life. The two-dimensional patchy domain representation helps to simplify complex soil structure and still captures not only aqueous phase configuration but also nutrient transport and microbial activities.

A.1 A patch

A patch represents a certain area on the surface and is assumed to be a uniform domain with several representative measures (i.e. homogeneous inside). Embracing the surface pore size distribution and its scale invariance property, the roughness of each patch is defined and can be rewritten as multi-scale percolation systems or pore-solid-fractal (PSF) model (Neimark, 1989; Perrier, Bird, and Rieu, 1999; Perrier et al., 2003). Roughness of each patch is characterised with a fractal dimension D for the pore-size distribution and the surface porosity Φ . When the size distribution of surface pore volume follows a power-law with a fractal dimension D (i.e. $N(r) \sim r^{-D}$), the probability that a point on the surface belongs to an angular pore with size X in the interval $[r, r + \delta r]$ can be written as

$$\Pr[r \leq X \leq r + \delta r] = \Phi \int_r^{r+\delta r} \mathcal{N}(X) dX \sim \Phi r^{-D} \delta r, \quad (\text{A.1})$$

where $\mathcal{N}(r)$ is the probability density function of surface pore size r

$$\mathcal{N}(r) = \frac{1}{A} r^{-(D+1)}. \quad (\text{A.2})$$

A is the normalising constant of the distribution, $A = \int_{r_{\min}}^{r_{\max}} \mathcal{N}(r) dr$. r_{\min} and r_{\max} are length-scale cutoffs: r_{\min} is set to be 10^{-7} m to represent the minimum size of physical elements on the rough surface (related to the size of clay particle) and r_{\max} is given 10^{-3} m indicating the maximum size of elements. These cutoffs are necessary for the model not only to avoid the divergence problem but also to describe the rarity of the large-scale structure and the minimum size of roughness scale. Eq. (A.1) shows the surface porosity, Φ , is the proportion of angular pores on the smooth surface and the fractal dimension, D , indicates the relative effects of large-scale pore structure.

A.2 The effective water film thickness and the degree of saturation

The aim of the new model is to calculate representative measures to describe hydration status of soil rough surface, such as effective water film thickness and saturation degree. Unlike usual approaches in fractal models, this model includes corner effects of angular pores. In PSF model and Brooks-Corey model, corner effects of pores are ignored in calculations of water retention properties (Perrier, Bird, and Rieu, 1999; Bird, Perrier, and Rieu, 2000; Kewen et al., 2004; Ghanbarian-Alavijeh, Millán, and Huang, 2011). In these models, each pore gets completely desaturated after the critical matric potential with an assumption that shape of pores are spheres. It can be a reasonable approach to achieve water retention property of bulk soils in terms of quantitative measures. In reality, however, pores possess angular shapes rather than spheres. Angular shapes enable soil surface to hold substantial amounts of water and it enhances the hydraulic connectivity at the low saturation (Ransohoff and Radke, 1988; Or and Tuller, 2000).

Let's assume that we have a small surface domain with size αl_p^2 , which corresponds to a patch in the model. l_p is the length scale of the patch and α is the shape factor; for square patch, $\alpha = 1$; for triangular patch, $\alpha = \frac{\sqrt{3}}{4}$. This surface might be smooth or rough. A completely smooth surface is a domain without any surface pores and roughness (i.e. $\Phi = 0$). To build a rough surface, we assume that there are two different states on the surface, angular voids (pores) and smooth surface (solids). Starting with a completely smooth surface without any voids, we build pore or solid sections in different sizes following a size distribution, $\mathcal{N}(r)$. The fractions p , s , and f (where $p + s + f = 1$) of the total area correspond to the proportion of pores, solids, and undetermined or fractal, respectively, by borrowing the concept of fractal sections in the multi-scale percolation systems Neimark, 1989. Here, we keep the state, undetermined or fractal, to include sub-structures at all scales. The surface porosity can be calculated as $\Phi \equiv \frac{p}{p+s}$ in the continuum limit without the lower cutoff (i.e. $r_{\min} \rightarrow 0$). Accordingly, the number density of pores and solids of size r can be written

$$\mathcal{N}_p(r) = N_p^0 \frac{p}{f} \mathcal{N}(r) \sim \Phi \mathcal{N}(r), \quad (\text{A.3})$$

$$\mathcal{N}_s(r) = N_s^0 \frac{s}{f} \mathcal{N}(r) \sim (1 - \Phi) \mathcal{N}(r), \quad (\text{A.4})$$

where N_p^0 and N_s^0 are normalising constants. Here, we made an assumption that mass fractal dimension and the pore fractal dimension are the same.

We obtain the amount of water held in a single pore with the size r from two distinctive physical processes, 1) capillary water at corners obtained from the Young-Laplace equation, 2) absorbed water on the surface due to van der Waals interactions. For a simple representation of angular pore, we assume that a pore element with size r is a square pyramid with the height H and the base r . For generalising the model, H can be another variable which can be a function of r or constant in the model. The shape of pores can be also different kinds of polyhedrons, such as cubes or tetrahedrons, or can be irregular. In our model, we simply choose a square pyramid to reflect the real geometry of surface roughness and to simplify calculations. For solid elements, it is assumed to be a completely smooth surface

so only absorbed water film would exist on the solid fraction. When a matric potential, ψ_m , is given as an environmental condition, the radius of meniscus curvature would be $R_\mu(\psi_m) = -\frac{\sigma}{\psi_m}$ where σ is surface tension of water. The absorbed water film thickness would be $h_\mu(\psi_m) = \left(\frac{A_{svl}}{6\pi\psi_m}\right)^{1/3}$ where A_{svl} is Hamaker constant. The matric potential determines the critical pore size, $r_c(\psi_m) = 2(R_\mu(\psi_m) + h_\mu(\psi_m))$, to get a pore desaturated. In other words, pores with size smaller than $r_c(\psi_m)$ would be saturated and pores with sizes above the critical value would be desaturated, with some capillary water remaining due to corner effects. For a pore with size r and height H , the amount of water which is held by capillarity is

$$\mathcal{V}(r, \psi_m) = \begin{cases} \mathcal{V}(r, \psi_m)^s = \frac{1}{3}Hr^2 & \text{where } r \leq r_c(\psi_m) \\ \mathcal{V}(r, \psi_m)^d = \frac{1}{3}Hr^2\Theta_r(r, \psi_m) & \text{where } r \geq r_c(\psi_m) \end{cases}, \quad (\text{A.5})$$

where Θ_r is the saturation degree of an individual pore with size r ,

$$\Theta_r(r, \psi_m) = \left(\frac{r_c}{r}\right)^3 + 3(4 - \pi) \left(\frac{R_\mu}{r}\right)^2 \left(1 - \frac{r_c}{r}\right) + 6 \left(\frac{h_\mu}{r}\right) \left(1 - \frac{r_c^2}{r^2}\right). \quad (\text{A.6})$$

The expected value of the total amount of water in the domain can be calculated following the probability distribution, Eq. (A.2),

$$\bar{\mathcal{V}}(\psi_m) = \int_{r_{\min}}^{r_{\max}} [p\mathcal{V}(r, \psi_m) + sh_\mu r^2] \mathcal{N}(r) dr. \quad (\text{A.7})$$

Expected surface area of the patch is

$$\bar{\mathcal{A}} = \int_{r_{\min}}^{r_{\max}} (p + s)r^2 \mathcal{N}(r) dr. \quad (\text{A.8})$$

The effective water film thickness of each patch can be simply defined as $\bar{\mathcal{V}}(\psi_m)/\bar{\mathcal{A}}$

$$w_{\text{eff}}(\psi_m) = \frac{\bar{\mathcal{V}}(\psi_m)}{\bar{\mathcal{A}}} = \frac{\int_{r_{\min}}^{r_{\max}} [\Phi \mathcal{V}(r, \psi_m) + (1 - \Phi)h_\mu r^2] r^{-(D+1)} dr}{\int_{r_{\min}}^{r_{\max}} r^2 r^{-(D+1)} dr}. \quad (\text{A.9})$$

The expected saturation degree of a patch can be written

$$\Theta(\psi_m) = \frac{\int_{r_{\min}}^{r_{\max}} [\Phi \mathcal{V}(r, \psi_m) + (1 - \Phi)h_\mu r^2] r^{-(D+1)} dr}{\int_{r_{\min}}^{r_{\max}} [\Phi \frac{1}{3}r^2 H(r) + (1 - \Phi)h_\mu r^2] r^{-(D+1)} dr}. \quad (\text{A.10})$$

Eq. (A.9) and Eq. (A.10) show that the physical measures of the effective water film thickness and the saturation degree of each patch can be calculated solely by values Φ and D . When we consider the shape factor $H(r)$ is the same as r , extra parameters are only cutoff values, r_{\min} and r_{\max} .

In this work, we only consider the physical property of rough surface and its water-holding capacity. In the model, effects of surfactants (surface active agents) can be also included. The main property of surfactants is to lower the surface tension or to increase the

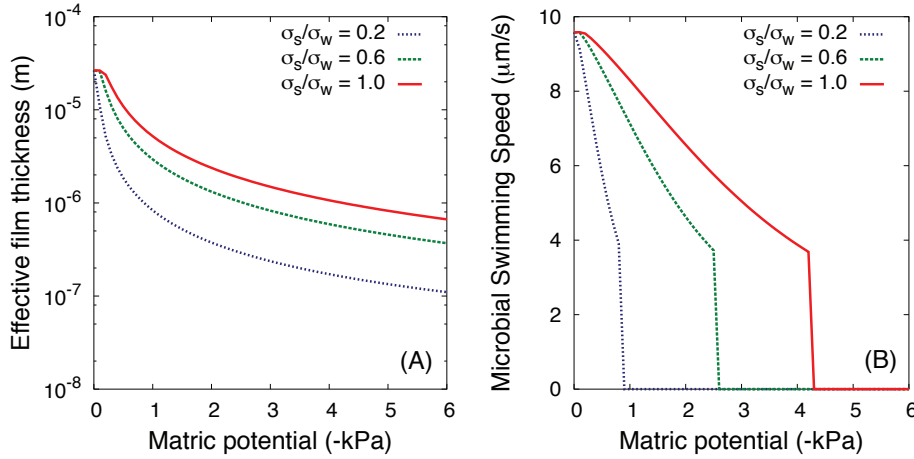


FIGURE A.1: **Effects of lowering surface tension on effective water film thickness and microbial swimming speed.** We have compared the effect of surface tension on effective water film thickness of the surface that affects microbial swimming velocity on a patch ($D = 1.8$ and $\Phi = 0.4$). The surface tension of water is $\sigma_w = 72\text{mM.m}^{-1}$ and the changed surface tension under the effect of surfactants is σ_s . Three different cases are given, $\sigma_s = 0.2\sigma_w$, $0.6\sigma_w$, and σ_w . (A) The effective water film thickness decreases when surface tension is lowered as a result of surfactant production at a given matric potential. (B) Microbial swimming speed is also slower when surfactants are produced by microorganisms.

contact angles (Christofi and Ivshina, 2002; Rockhold et al., 2002). For instance, Surfactin from *Bacillus subtilis* is known to change the surface tension of water from 72mM.m^{-1} to around 27mM.m^{-1} (Christofi and Ivshina, 2002). In Fig. A.1, effects of lowering surface tension on effective film thickness and microbial swimming speed are given. In the figure, we fixed the contact angle as 0° .

A.3 Connectivity of within patch aqueous habitats.

Notwithstanding the averaging associated with patch description, we seek to retain certain physical traits for a patch without detailed modelling of the patch roughness. Hence, the degree of aqueous habitat connectivity in a patch is described based on accessible surface pores (represented as films of certain thickness) that supports flagellated motility. The accessibility of an individual pore can be determined from the effective water film thickness of individual pore, $\bar{H}_{\text{eff}}(r, \psi_m)$. When it is larger than the size of microbial cell, $R \equiv 1\mu\text{m}$, this pore is accessible for microorganisms

$$\bar{H}_{\text{eff}}(r, \psi_m) = \frac{\mathcal{V}(r, \psi_m)}{r^2} = \frac{1}{3}H(r)\Theta_r(r, \psi_m) \geq R. \quad (\text{A.11})$$

When $H(r) = r$, the critical pore size, r_a^c , for the accessibility where $\bar{H}_{\text{eff}}(r_a^c, \psi_m) = R$, can be exactly calculated from a positive root of the quadratic equation by rearranging the

Eq. (A.11). The probability of occupation of the aqueous habitat area, a_H at ψ_m would be

$$p(\psi_m) = \frac{\bar{a}_H}{\mathcal{A}_p} = \frac{\int_{3R}^{r_a^c(\psi_m)} p \bar{H}_{\text{eff}}(r, \psi_m) r^2 \mathcal{N}(r) dr}{\int_{r_{\min}}^{r_{\max}} (p + s) \bar{H}_{\text{eff}}(r, \psi_m) r^2 \mathcal{N}(r) dr} = \Phi \frac{\int_{3R}^{r_a^c(\psi_m)} \mathcal{V}(r, \psi_m) \mathcal{N}(r) dr}{\int_{r_{\min}}^{r_{\max}} \mathcal{V}(r, \psi_m) \mathcal{N}(r) dr}. \quad (\text{A.12})$$

Here, we used total accessible area of the patch, \mathcal{A}_p , as the expected area in the patch. In addition, when $r_a^c(\psi_m) < 3R$, the numerator is assumed to be zero. We determine the local connectivity $\xi(\psi_m, \vec{r})$ of the patch at \vec{r} by using the occupation probability of aqueous habitats $p(\psi_m)$ and the global percolation probability $P(\psi_m)$ which is determined by the largest cluster of aqueous habitats at domain scale.

$$\xi(\psi_m, \vec{r}) = \begin{cases} P(\psi_m) & \text{if } p(\psi_m, \vec{r}) > p_c(\vec{r}) \\ p(\psi_m, \vec{r}) P(\psi_m) & \text{elsewhere} \end{cases},$$

where $p(\psi_m, \vec{r})$ as statistically averaged occupation probability of aqueous region in a patch and it is calculated as the expected value of the pore area where microbial motility is enabled. In the present work, we consider the percolation processes on the self-affine surface that have been analytically and numerically investigated (Isichenko, 1992; Schmittbuhl, Vilotte, and Roux, 1993; Du, Satik, and Yortsos, 1996; Sahimi, 1998). Previous studies have shown that the percolation threshold p_c on self-affine surface is dependent on Hurst's exponent H (roughness parameter) and p_c is a stochastic variable with a mean value (ensemble averaged) $\langle p_c \rangle(H)$ and a variance $\sigma(H)$ regardless of system sizes. The mean value of $\langle p_c \rangle(H)$ monotonically decreases with H such that $\langle p_c \rangle(H = 0) = 0.5$ and $\langle p_c \rangle(H = 1) = 0.386$ (Prakash et al., 1992). Thus, we draw a certain local percolation threshold value $p_c(\vec{r})$ for each patch (Schmittbuhl, Vilotte, and Roux, 1993). Eventually, these considerations are used to classify a patch with respect to flagellated motility as “motile” when film thickness is sufficient for motion, and the hydrated roughness is connected, otherwise a patch is declared “sessile” and not cell motion is allowed until hydration conditions change.

A.4 Diffusion process on rough surface patch model

In this section, we provide the method for the numerical calculation to obtain the flux of the nutrient at each site and the time evolution of the concentration field. According to Fick's law, the flux can be obtained as

$$\vec{J}(\vec{r}, t) = -D(\vec{r}) \nabla C(\vec{r}, t), \quad (\text{A.13})$$

where $\vec{J}(\vec{r}, t)$ is the flux due to the gradient of nutrient concentration $C(\vec{r}, t)$. $D(\vec{r})$ is the diffusion coefficient at \vec{r} . Macroscopically, the value would be determined based on the distribution of roughness elements. However, in terms of nutrient transport in the model, we already include spatial effects in the effective water film thickness, thus the diffusion coefficient at bulk water D_0 is used for the calculation. The rate of the nutrient change at

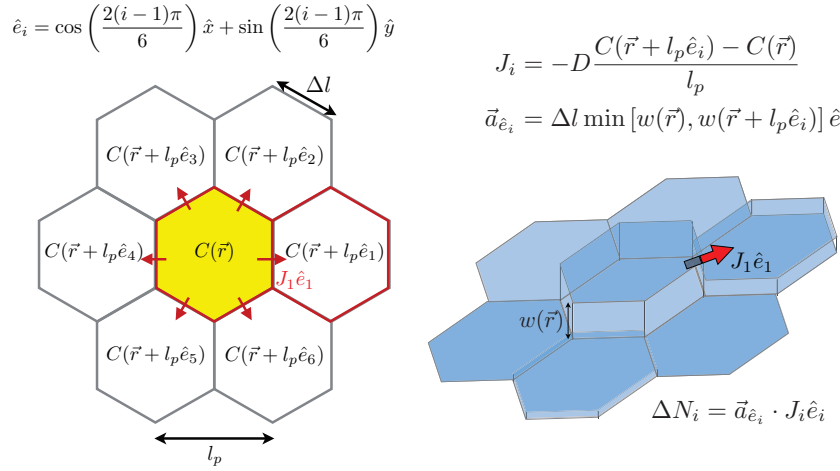


FIGURE A.2: **A schematic diagram of flux calculation.** A schematic diagram of the flux to/from patch at the position \vec{r} on the hexagonal lattice.

time t can be obtained from the divergence theorem,

$$\frac{dN(\vec{r}, t)}{dt} = \int_{\mathcal{V}} \nabla \cdot \vec{J}(\vec{r}, t) d\vec{r}, \quad (\text{A.14})$$

$$= \int_{\mathcal{A}} \vec{J}(\vec{r}, t) \cdot d\vec{a}, \quad (\text{A.15})$$

where $\mathcal{V}(\vec{r})$ indicates the patch at position \vec{r} and $d\vec{a}$ is the surface area that the nutrient moves in/out due to Fick's law.

In the numerical calculation, this integration has to be discretised. When the water film thickness at the given patch at position \vec{r} is given as $w(\vec{r})$, the cross section area that the nutrient moves can be assigned as

$$\vec{a}_{\hat{n}} = \Delta l w(\vec{r}) \hat{n}, \quad (\text{A.16})$$

where \hat{n} is the normal vector of the cross section area and Δl is a length of the edge and is related to the size of a patch. In our numerical simulation, we use the hexagonal lattice. The hexagonal lattice is better suited to describe microbial behaviour in a probabilistic model since all the neighbours are at the same distance. Fig. A.2 shows a detailed schematic diagram of the calculation for the flux of one element on the hexagonal lattice. The nearest neighbour vectors on a hexagonal lattice are denoted as \hat{e}_i where $i \in [1, \dots, 6]$. For example, the flux $\vec{J} \cdot \hat{e}_i$ denotes the flux from the current patch to the nearest neighbour \hat{e}_i . When the effective water film thickness is different to the neighbour, the minimum value of the film thicknesses of the adjacent pair would determine the cross sectional area,

$$\vec{a}_{\hat{e}_i} = \Delta l \min[w(\vec{r}), w(\vec{r} + l_p \hat{e}_i)] \hat{e}_i. \quad (\text{A.17})$$

Equation (A.15) as a discretised expression can be written as

$$\frac{\Delta N(\vec{r}, t)}{\Delta t} = \sum_{i=1}^6 \vec{J} \cdot \vec{a}_{\hat{e}_i}. \quad (\text{A.18})$$

This leads to the next time step,

$$N(t + \Delta t) = N(t) - \Delta N(t), \quad (\text{A.19})$$

$$C(t + \Delta t) = \frac{N(t + \Delta t)}{V}, \quad (\text{A.20})$$

where V is the volume of the given patch and the position vector \vec{r} is rewritten with indices of the lattice.

A.5 Microbial growth

A.5.1 Metabolism

On the soil rough surface domain, microbial activity is added by using individual based modelling (IBM) (Kreft, Booth, and Wimpenny, 1998). Microbial growth of an individual cell can be written as

$$\begin{aligned} \tilde{\mu} b = \frac{db}{dt} &= \left(\mu_{\max} \min\left[\left\{\frac{C_1}{K_s^1 + C_1}, \frac{C_2}{K_s^2 + C_2}, \dots\right\}\right] - m \right) b, \\ \tilde{\mu} &= \mu_{\max} \min\left[\left\{\frac{C_1}{K_s^1 + C_1}, \frac{C_2}{K_s^2 + C_2}, \dots\right\}\right] - m = \mu - m, \end{aligned} \quad (\text{A.21})$$

where b is the biomass of the cell and its net growth rate is denoted $\tilde{\mu}$. The net growth rate is comprised with two factors, anabolism and maintenance. Anabolism could be interpreted as conversion of nutrient to cell biomass with the rate μ which is a function of nutrient concentrations, C_i , and limited with the maximum specific growth rate μ_{\max} . Here, we used the min function from separate Monod growth terms to indicate the growth rate controlled by limiting nutrients. When the concentration of certain nutrient i satisfies the condition, $C_i \gg K_s^i$ for any time, this nutrient i does not restrict the growth rate of the microorganisms. Maintenance of a cell is simply given with a constant maintenance rate m .

Microbial growth rate can be determined by their substrates that can be used for growth. However, there are some substances that are toxic for cells so it inhibits their growth. For this case, the Eq. (A.21) can be extended as

$$\mu = \mu_{\max} \min\left[\left\{\frac{C_1}{K_s^1 + C_1}, \frac{C_2}{K_s^2 + C_2}, \dots\right\}\right] \min\left[\left\{\frac{K_I^1}{K_I^1 + C_1}, \frac{K_I^2}{K_I^2 + C_2}, \dots\right\}\right], \quad (\text{A.22})$$

where K_I^j is the inhibition coefficient with respect to the nutrient j . When a species excretes by-product of their growth with rate β , we reduce the growth rate of the specie with the factor of $1 - \beta$.

A.5.2 Cell division.

Cell division process is considered in IBM. The descriptive Danachie model is applied to estimate cell volume (Donachie and Robinson, 1987). The cell volume of an agent is given as $V = \rho b$ with cell density ρ . When the cell volume V becomes greater than the volume at division, $V_{d,\min}$, the cell produces two identical daughter cells in juxtaposition and the biomass of each daughter cell is given as a half of the biomass of their mother cell.

A.5.3 Death.

If an agent is under starvation condition ($\tilde{\mu} < 0$), the agent keeps shrinking and its biomass decreases due to maintenance. The agent dies if its biomass falls below a minimum value, ρV_{\min} . On death, biomass is converted back into substrate with a conversion rate $1/Y_{\max}$.

A.6 Swimming speed.

Bacterial flagella motility on a roughness network has been studied with regard to physical properties of pore geometries (Wang and Or, 2010; Long and Or, 2007). In these studies, the roughness network is modelled with nodes as reservoirs of nutrients and links as water channels between reservoirs. Since the physical shape of a pore is included in the model, the movement of a microorganism and its motility could embrace mechanical aspects of soil environment to microbes. The previous model successfully obtains thresholds of motility and velocity of bacteria in the channel by applying self propulsion, cell-wall interaction, and capillary pinning force

$$v(\psi_m) = v_0 \frac{F_M - F_\lambda(\psi_m) - F_c(\psi_m)}{F_M}, \quad (\text{A.23})$$

where v_0 is the velocity of a cell in bulk water and ψ_m is the matric potential that controls the effective water film thickness. F_M , F_λ , F_c are self propulsion, cell-surface interaction, and capillary pinning force, respectively. Self propulsion has the same value of viscous drag force so that the velocity of the microbes can be constant in bulk water. Cell-surface interaction and capillary force are functions of the effective water film thickness.

In the current work the rough surface is modelled by patches with macroscopic properties. All the microscopic structure of pore spaces are averaged and represented as a macroscopic variable, such as effective water film thickness and saturation degree for each patch. From the effective water film thickness, we calculate the swimming speed of microorganisms by adopting Eq. (A.23). The equation provides the maximum swimming speed of a cell under a certain hydration condition or roughness of the surface. When the system becomes rougher or dryer, the maximum velocity of microbes decreases.

A.7 Chemotactic Motion.

For the flagellated bacteria such as *E. coli*, the motion can be described as follows. A bacterium runs, moves forward linearly, with a constant velocity for a random length of time called the “running time”. Then it tumbles for a random length of time, the “tumbling time”, and chooses a new direction randomly and repeats the cycle. The average running time is about 1 sec in the absence of chemotaxis at bulk water, the average tumbling time is about one tenth of the running time, about 0.1 sec, and their distributions decay exponentially (Berg, 1990). Essentially, the tumbling selects a new direction, but the direction is chosen randomly because the size of bacteria is too small to detect the local gradient of attractants. However, the running length increases when the microbial cell runs in a favourable direction. In the absence of favourable directions, the movement of microbes can be described as a random walker. On the other hand, when the preference on direction exists due to chemotaxis, a biased random walk can be considered (Alt, 1980). Based on the experimental results and the theory of biased random walks, the effect of chemical attractants on individual cell paths has been studied (Ford and Lauffenburger, 1991; Rivero et al., 1989; Lovely and Dahlquist, 1975). The mean run time τ increases exponentially with the change in the number of receptor-attractant complexes N_b (Berg and Brown, 1972)

$$\tau = \tau_0 \exp \left(\sigma \frac{DN_b}{Dt} \right), \quad (\text{A.24})$$

where τ_0 is the mean run time in the absence of a chemical attractant and σ is the change in the mean run time of a bacterium per rate of change of bound receptors. This implies that the number of bound receptors defines the chemotactic potential. This model is known as the “receptor” model (Hillen and Painter, 2009). The total derivative of the number of bound receptors is

$$\frac{DN_b}{Dt} = \frac{\partial N_b}{\partial t} + \vec{\nabla} N_b. \quad (\text{A.25})$$

When we consider the case with only one attractant, a single homogeneous cell receptor density at equilibrium can be written as a Monod type of interaction,

$$N_b = \frac{N_T C}{K_d + C}, \quad (\text{A.26})$$

where C is the attractant concentration, K_d is the dissociation equilibrium constant, and N_T is the total number of cell receptors for the ligand. In this model, the attractant is simply a nutrient that microorganisms consume and the kinetic equation is described as a law of mass action at equilibrium (Monod equation). This implies that the dissociation constant K_d is assumed to be the same as half concentration constant K_s . Then the spatial derivation can be rewritten as

$$\vec{\nabla} N_b = \vec{\nabla} \left(\frac{N_T C}{K_s + C} \right) = \frac{N_T K_s}{(K_s + C)^2} \vec{\nabla} C. \quad (\text{A.27})$$

When we consider the trophic interaction with multiple nutrients, we have to consider the gradients of all nutrients. To simplify movement, the specific growth rate would be considered instead of concentrations of all the nutrients in the trophic interaction model. We assume that the microbial organisms would direct themselves towards the higher growth rate, as a result of chemotaxis towards necessary nutrients. Thus (A.27) can be further rewritten

$$\vec{\nabla} N_b = \frac{N_T K_s}{(K_s + C)^2} \vec{\nabla} C \approx \frac{N_T}{\mu_{\max}} \vec{\nabla} \mu, \quad (\text{A.28})$$

where $\mu = \mu_{\max} \min \left[\frac{C_1}{K_s^1 + C_1}, \frac{C_2}{K_s^2 + C_2} \right]$. So far, we have two assumptions on chemotactic movement :

(1) The chemotactic potential is defined by the number of bound receptors.

$$\phi_c(V) = N_b = \frac{N_T C}{K_d + C}. \quad (\text{A.29})$$

(2) When the chemotaxis is towards several nutrients that make growth of the cell by consumptions, the change of number of bound receptors can be interpreted with the expected specific growth rate (i.e. receptor binding model and the consumption of nutrients are the same kinetics).

$$\vec{\nabla} \phi_c(V) = \vec{\nabla} N_b = a \vec{\nabla} \mu, \quad (\text{A.30})$$

where a is the proportional constant.

Employing a quasi steady-state hypothesis, one can ignore the time derivative of the number of bound receptors. As a result, when the microbe runs towards the direction \hat{x} , the mean run time $\tau_{\hat{x}}$ would be

$$\tau_{\hat{x}} = \tau_0 \exp \left(\frac{\sigma N_T}{\mu_{\max}} \vec{\nabla} \mu \cdot \hat{x} \right). \quad (\text{A.31})$$

By combining with Alt's governing equations in the biased random walk model (Alt, 1980), σ can be described as

$$\sigma \equiv \frac{\chi_0}{2N_T v}, \quad (\text{A.32})$$

where v is the velocity of the microbe and χ_0 is the chemotactic sensitivity. The reciprocal of the mean run time can be assumed as a tumbling probability

$$p_{t:\hat{x}} = p_0 \exp \left(-\frac{\chi_0}{2v\mu_{\max}} \vec{\nabla} \mu \cdot \hat{x} \right), \quad (\text{A.33})$$

where p_0 is the normalisation constant. Eq. (A.33) describes the probability of tumbling when the microbe runs to the direction \hat{x} . After tumbling, the microbe runs in another direction \hat{x}' . The probability of the new direction is independent of the gradient of the apparent growth rate.

The model aims at up-scalability of microbial life at pore scale. Describing individual tumbling in large scale is unrealistic in terms of computational time. Thus, to simplify all the processes, we approach the distribution of microbial cells using a probability distribution with an assumption that the mean displacement after a certain time is determined based on

the running time distribution towards each direction. In a hexagonal lattice as a discretised case, there are six neighbours. The unit direction to each nearest neighbour can be written as \hat{e}_i where $i \in \{1, 2, \dots, 6\}$ and \hat{e}_7 is defined the origin, $\hat{e}_7 \equiv (0, 0)$. The probability to move towards the direction \hat{e}_i , $p_i(t)$, can be determined as

$$p_i(t) = \frac{w_i e^{(\alpha \vec{\nabla} \mu(t) \cdot \hat{e}_i)}}{\sum_{j=1}^7 w_j e^{\alpha \vec{\nabla} \mu(t) \cdot \hat{e}_j}}, \quad (\text{A.34})$$

where α is the factor for the chemotactic motion,

$$\alpha \equiv \frac{\chi_0}{2\mu_{\max} v(\psi_m)}. \quad (\text{A.35})$$

In the expression, $v(\psi_m)$ is the velocity of microbe at the given matrix potential ψ_m . In Eq. (A.34), the weight factor w_i is determined by effective water film thickness $d_i(\psi_m)$

$$w_i = \frac{d_i(\psi_m)}{\sum_{j=1}^7 d_j(\psi_m)}, \quad (\text{A.36})$$

where d_7 is the water film thickness of the current patch where the cell is. We assume that the flux of the nutrients from each neighbour will weigh the chemotactic movements. When the water film thicknesses of some neighbours are thinner than the size of microbial cell, $w < R$, we modify the weight factor as follows since the patch is physically non accessible for the cell

$$w'_i = \begin{cases} \frac{d_i(\psi_m)}{\sum_{j=1}^7 d_j(\psi_m)} & \text{if } d_i \geq R \\ 0 & \text{if } d_i < R \\ \frac{(\sum_{k, d_k < R} d_k(\psi_m)) + d_7}{\sum_{j=1}^7 d_j(\psi_m)} & \text{if } i = 7 \end{cases}.$$

By applying this weight factor, one can make the staying probability unity when the cell is trapped in the patch due to physical barriers. On the other hand, when the structure is homogeneous, the weight factor would be cancelled out and the distribution follows only the chemotactic probability. In addition, when the chemotactic sensitivity is very low, (i.e. $\alpha \rightarrow 0$), the system becomes a pure diffusion system without chemotaxis and the microbial cells move based on the distribution of water.

Based on the probability towards each direction, the expected displacement can be calculated

$$\langle \vec{X}(t) \rangle = \sum_{i=1}^6 v(\psi) \Delta t p_i(t) \hat{e}_i. \quad (\text{A.37})$$

Here, we do not use a continuous integration since the population size of patch and the migration rate between patch are our interest in the model. The expected displacement would be accumulated until it exceeds the patch size l_p with the tortuosity effect:

$$\left| \sum_{k=1}^n \vec{X}(k \Delta t) \right| > \tau(\psi_m) l_p, \quad (\text{A.38})$$

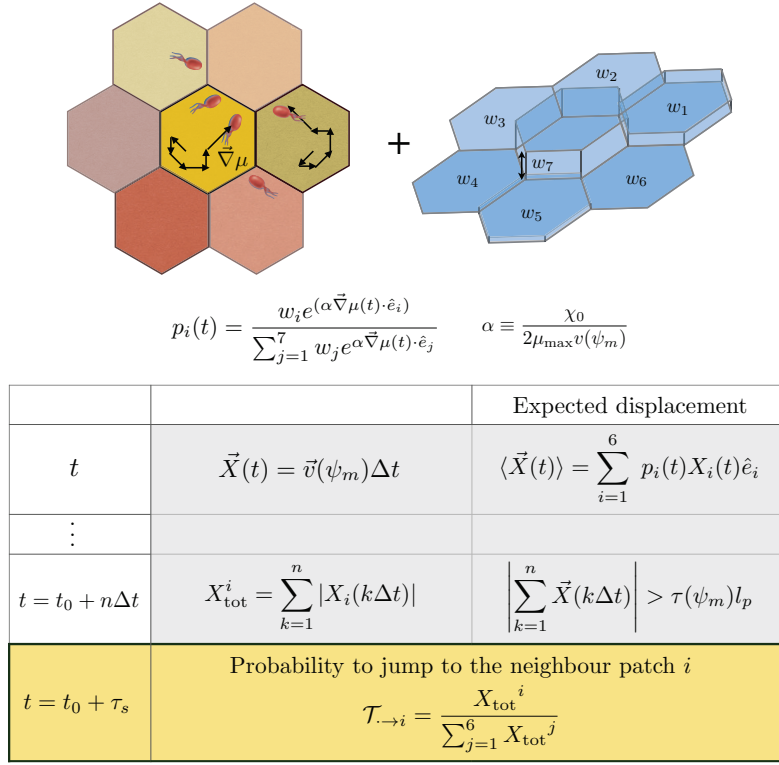


FIGURE A.3: **A diagram for microbial locomotion** A diagram for the numerical calculation of individual movement. The biased probability of movement is given as a function of the effective water film thickness and the chemotactic factor α . The displacement during Δt towards each direction is given as $|v(\psi_m)| \Delta t$. When the cumulative expected displacement exceeds the distance between patches, $\tau(\psi_m) l_p$, the microbes will move to the other patch based on the transition probability $\mathcal{T}_{\rightarrow i}$.

where $\tau(\psi_m)$ is the tortuosity of the patch defined from roughness and connectivity. This criterion is simply given as a step function of the staying probability and it forces the agent to move to the neighbour patch if the displacement exceeds the patch length. This part can be changed to a stochastic process by applying the probability to escape from the current patch, given as $p(t) = e^{-\langle X(t) \rangle / l_p}$. The probability to move to neighbouring patch i from the current patch is determined as

$$\mathcal{T}_{\rightarrow i} = \frac{X_{\text{tot}}^i}{\sum_{j=1}^6 X_{\text{tot}}^j}, \quad (\text{A.39})$$

where $X_{\text{tot}}^i = \sum_{k=1}^n |\vec{X}_i(k \Delta t)|$. As a result, we divide the time to stay at a given patch based on Eq. (A.38) and the population distribution to the neighbour patch based on Eq. (A.39). A diagram for the numerical calculation is given in Fig. A.3.

A.8 Parameters used for physical domain

TABLE A.1: Parameters for rough surface domain (Chapter 2 and 3)

Notations	Parameters	Units	Values
r_{\min}	minimum size of roughness element	m	10^{-7}
r_{\max}	maximum size of roughness element	m	$10^{-3,a}$
D	fractal dimension for pore size distribution	-	Vary ^b
$\bar{\Phi}$	mean surface porosity	-	Vary ^b
l_p	size of a patch	m	5×10^{-4}

Parameters used to generate roughness domain.

^a We have used 10^{-3} m for all simulations as the largest roughness domain except for the comparison with data of Tokunaga and Wan, 1997 to consider their sample size, 50×10^{-3} m.

^b Values of D and $\bar{\Phi}$ vary for different simulations and the values are chosen under considerations of experimental data to be compared (such as for Tuff rock (Fig. 2.3 in the main text), $D = 1.4$ and $\bar{\Phi} = 0.1$ are used as a single patch and for sandy soil (Fig. 3.4 in the main text) $D = 1.35$ and $\bar{\Phi} = 0.4$ are used). Used values are given in the caption of each figure.

A.9 Parameters used for IBM

TABLE A.2: Parameters for Individual Based Modelling (IBM)(Chapter 2 and 3)

Notation	Parameter	unit	value
μ_{\max}^i	specific growth rate	hr ⁻¹	Vary ^a
K_s^i	half-saturation constant	mg.L ⁻¹	Vary ^b
Y_{\max}	apparent yield	g.g ⁻¹	0.44 ^c
α_m	ratio for maintenance rate	-	0.0129
\bar{V}_B	median cell volume	fl	0.4
$V_{B,d}$	cell volume at division	fl	$2\bar{V}_B/1.433$
$V_{\min,d}$	minimal active cell volume	fl	$\bar{V}_B/5$
ρ	cell density (dry mass)	fg.fl ⁻¹	290
R	size of microbial cells	μm	1
D_0	nutrient diffusion coefficient	mm ² .hr ⁻¹	2.4
v_0	cell velocity at bulk water	mm.hr ⁻¹	50.4
χ_0	chemotactic sensitivity	mm ² .hr ⁻¹	180
β	by-product yield	g.g ⁻¹	0.8

Parameters used to simulate microorganisms. Most of parameters for individual cells are chosen from Kreft, Booth, and Wimpenny, 1998.

^a $\mu_{\max} = 1.23\text{hr}^{-1}$ is used for a single species and mutualistic trophic interaction. For the evaluation of microbial diversity, values are chosen uniformly spaced values in

$\mathcal{U}[0.5\mu_{\max}, 1.5\mu_{\max}]$.

^b $K_s = 1.17\text{mg.L}^{-1}$ is used for a single species. For the mutualistic trophic interaction, $K_{s,1} = K_{s,2} = K_{I,1} = 10^{-3}\text{mg.L}^{-1}$ are used. For the evaluation of microbial diversity, values are logarithmically spaced values in $\mathcal{U}[10^{-2}K_s, K_s]$.

^c μ_{\max} , K_s and Y_{\max} for the Fig. 3.2A and Fig. 3.2C in the main text (Competitive trophic interaction) were used differently following the work of Wang and Or, 2014.

A.10 Parameters used for diversity dynamics

Notations	Parameters	Units	Values
μ_{\max}^{i*}	specific growth rate	hr^{-1}	$0.6 \sim 1.8$
K_s^{i*}	half-saturation constant	fg.fl^{-1}	$0.001 \sim 1$
v_0	cell velocity at bulk water	mm.hr^{-1}	36
χ_0	chemotactic sensitivity	$\text{mm}^2.\text{hr}^{-1}$	18
C_0	initial concentration of nutrients	mg.L^{-1}	0.1
p_f	probability to fail sporulation	-	0.5
T_g	germination time	day	2

TABLE A.3: **Parameters for individual-based modelling (IBM) in diversity dynamics**

* μ_{\max} and K_s are different for each species. μ_{\max} are chosen uniformly spaced values in $\mathcal{U}[0.6, 1.8]$ and K_s are logarithmically spaced values in $\mathcal{U}[1.7 \times 10^{-3}, 1.7]$. Other properties of cells are the same as Table A.2.

References

- Alt, Wolfgang (1980). "Biased random walk models for chemotaxis and related diffusion approximations". In: *Journal of Mathematical Biology* 9.2, pp. 147–177.
- Berg, HC (1990). "Bacterial microprocessing". In: *Cold Spring Harbor symposia on quantitative biology*. Vol. 55. Cold Spring Harbor Laboratory Press, pp. 539–545.
- Berg, Howard C and Douglas A Brown (1972). "Chemotaxis in *Escherichia coli* analysed by three-dimensional tracking". In: *Nature* 239.5374, pp. 500–504.
- Bird, NRA, Edith Perrier, and Michel Rieu (2000). "The water retention function for a model of soil structure with pore and solid fractal distributions". In: *European Journal of Soil Science* 51.1, pp. 55–63.
- Christofi, N and IB Ivshina (2002). "Microbial surfactants and their use in field studies of soil remediation". In: *Journal of Applied Microbiology* 93.6, pp. 915–929.
- Donachie, WD and AC Robinson (1987). "Cell division: Parameter values and the process". In: *Escherichia coli and Salmonella typhimurium: Cellular and Molecular Biology*. Ed. by C Neidhardt et al. 1st. Vol. 2. Washington, DC: ASM Press, pp. 1578–1593.
- Du, C, C Satik, and YC Yortsos (1996). "Percolation in a fractional Brownian motion lattice". In: *AIChE Journal* 42.8, pp. 2392–2395.
- Ford, Roseanne M and Douglas A Lauffenburger (1991). "Measurement of bacterial random motility and chemotaxis coefficients: II. Application of single-cell-based mathematical model". In: *Biotechnology and Bioengineering* 37.7, pp. 661–672.
- Ghanbarian-Alavijeh, Behzad, Humberto Millán, and Guanhua Huang (2011). "A review of fractal, prefractal and pore-solid-fractal models for parameterizing the soil water retention curve". In: *Canadian Journal of Soil Science* 91.1, pp. 1–14.
- Hillen, Thomas and Kevin J Painter (2009). "A user's guide to PDE models for chemotaxis". In: *Journal of Mathematical Biology* 58.1-2, pp. 183–217.
- Isichenko, Michael B (1992). "Percolation, statistical topography, and transport in random media". In: *Reviews of Modern Physics* 64.4, p. 961.
- Kewen, Li et al. (2004). "Theoretical development of the Brooks-Corey capillary pressure model from fractal modeling of porous media". In: *Society of Petroleum Engineers*.
- Kreft, Jan-Ulrich, Ginger Booth, and Julian WT Wimpenny (1998). "BacSim, a simulator for individual-based modelling of bacterial colony growth". In: *Microbiology* 144.12, pp. 3275–3287.
- Long, Tao. and Dani. Or (2007). "Microbial growth on partially saturated rough surfaces: Simulations in idealized roughness networks". In: *Water Resources Research* 43.2, W02409.
- Lovely, Peter S and FW Dahlquist (1975). "Statistical measures of bacterial motility and chemotaxis". In: *Journal of Theoretical Biology* 50.2, pp. 477–496.
- Neimark, AV (1989). "Multiscale percolation systems". In: *Soviet Physics - Journal of Experimental and Theoretical Physics* 96.4, pp. 1386–1396.
- Or, Dani. and Markus Tuller (2000). "Flow in unsaturated fractured porous media: Hydraulic conductivity of rough surfaces". In: *Water Resources Research* 36.5, pp. 1165–1177.

- Perrier, Edith, Nigel Bird, and Michel Rieu (1999). "Generalizing the fractal model of soil structure: The pore–solid fractal approach". In: *Geoderma* 88.3, pp. 137–164.
- Perrier, EMA et al. (2003). "The PSF model of soil structure: A multiscale approach". In: *Scaling Methods in Soil Physics*, pp. 1–18.
- Prakash, Sona et al. (1992). "Structural and dynamical properties of long-range correlated percolation". In: *Physical Review A* 46.4, R1724.
- Ransohoff, TC and CJ Radke (1988). "Laminar flow of a wetting liquid along the corners of a predominantly gas-occupied noncircular pore". In: *Journal of Colloid and Interface Science* 121.2, pp. 392–401.
- Rivero, Mercedes A et al. (1989). "Transport models for chemotactic cell populations based on individual cell behavior". In: *Chemical Engineering Science* 44.12, pp. 2881–2897.
- Rockhold, Mark L et al. (2002). "Considerations for modeling bacterial-induced changes in hydraulic properties of variably saturated porous media". In: *Advances in Water Resources* 25.5, pp. 477–495.
- Sahimi, Muhammad (1998). "Non-linear and non-local transport processes in heterogeneous media: from long-range correlated percolation to fracture and materials breakdown". In: *Physics Reports* 306.4, pp. 213–395.
- Schmittbuhl, Jean, J-P Vilotte, and Stéphane Roux (1993). "Percolation through self-affine surfaces". In: *Journal of Physics A: Mathematical and General* 26.22, p. 6115.
- Tokunaga, Tetsu K and Jiamin Wan (1997). "Water film flow along fracture surfaces of porous rock". In: *Water Resources Research* 33.6, pp. 1287–1295.
- Wang, Gang. and Dani. Or (2010). "Aqueous films limit bacterial cell motility and colony expansion on partially saturated rough surfaces". In: *Environmental Microbiology* 12.5, pp. 1363–1373.
- Wang, Gang and Dani Or (2014). "Trophic interactions induce spatial self-organization of microbial consortia on rough surfaces". In: *Scientific Reports* 4.

Appendix B

Microbial Community Response to Hydration-Desiccation Cycles

B.1 Average water contents

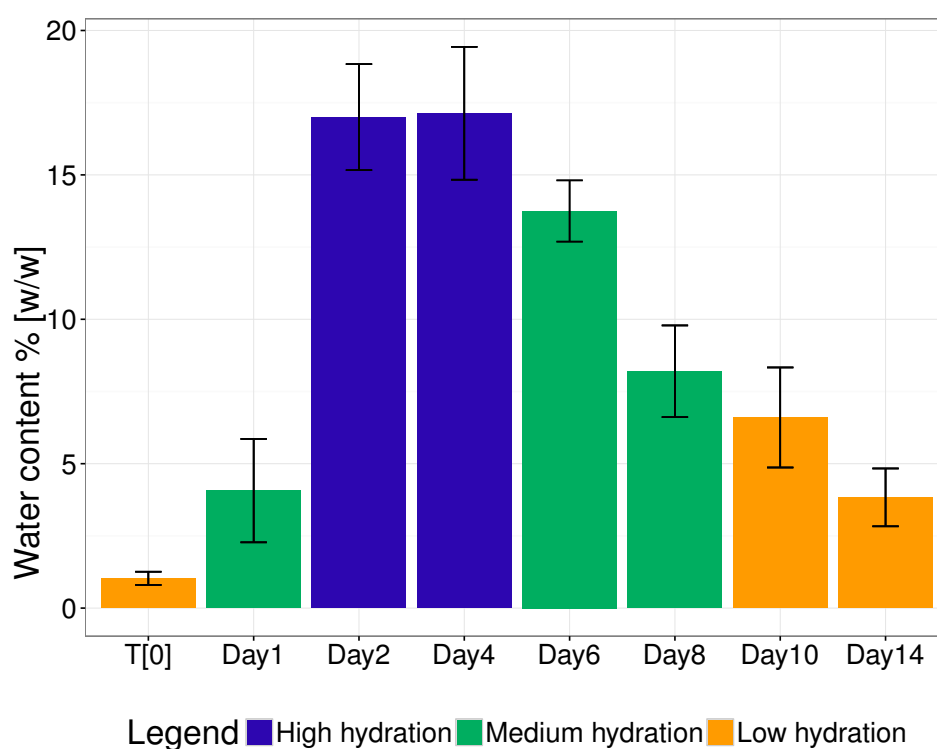


FIGURE B.1: **Average water contents.** Average water content as obtained gravimetrically during field measurements (N = 3).

B.2 Chemical analysis of the soil samples

About 500 g of the field-collected soil samples was chemically analyzed as previously described (Si et al., 2007). Values of pH and EC were measured in a saturated soil-paste extract. Phosphorus ions were extracted from the soil with $0.5 \text{ mol l}^{-1} \text{ NaHCO}_3$ (Olsen and Watanabe, 1957) and analysed colorimetrically in an auto analyzer (ASX-520 series, Quickchem 8500 series 2; Lachat instruments, Loveland, CO). Potassium was extracted by CaCl_2 and measured by flame atomic absorption spectrophotometry (Flame photometer M410; Sherwood Scientific, Cambridge, UK). Chloride in saturated soil paste extract was measured with a chloride meter (Chloride analyzer 926; Sherwood Scientific Ltd, Cambridge UK). Soil organic matter content was estimated by weight loss using the ignition method.

In the figure, electrical conductivity and chloride ions changed with the wetting front. Their concentration dropped from around 30 mg kg^{-1} to 10 mg kg^{-1} on days 2 to 4 and then steadily rose back to 30 mg kg^{-1} in tandem with the soil's desiccation (a,e). The soil pH was unchanged throughout the sampling period, mainly due to the desert soil's buffering capacity (c). Phosphorus and potassium ion concentrations in desert soil are usually correlated to plant litter (Cross and Schlesinger, 1999) and remained largely unchanged in the sampled barren soil (f,h). The amount of ammonium and nitrates in our samples followed previously reported patterns (Austin et al., 2004), with ammonia elevated during the wet period and lower in dry soil and nitrates accumulating in the dry soils and depleted during hydration (b,d). Lastly, the amount of total organic carbon was assessed throughout the sampling period; it increased on days 3 and 10 after hydration and in the early desiccation period (g).

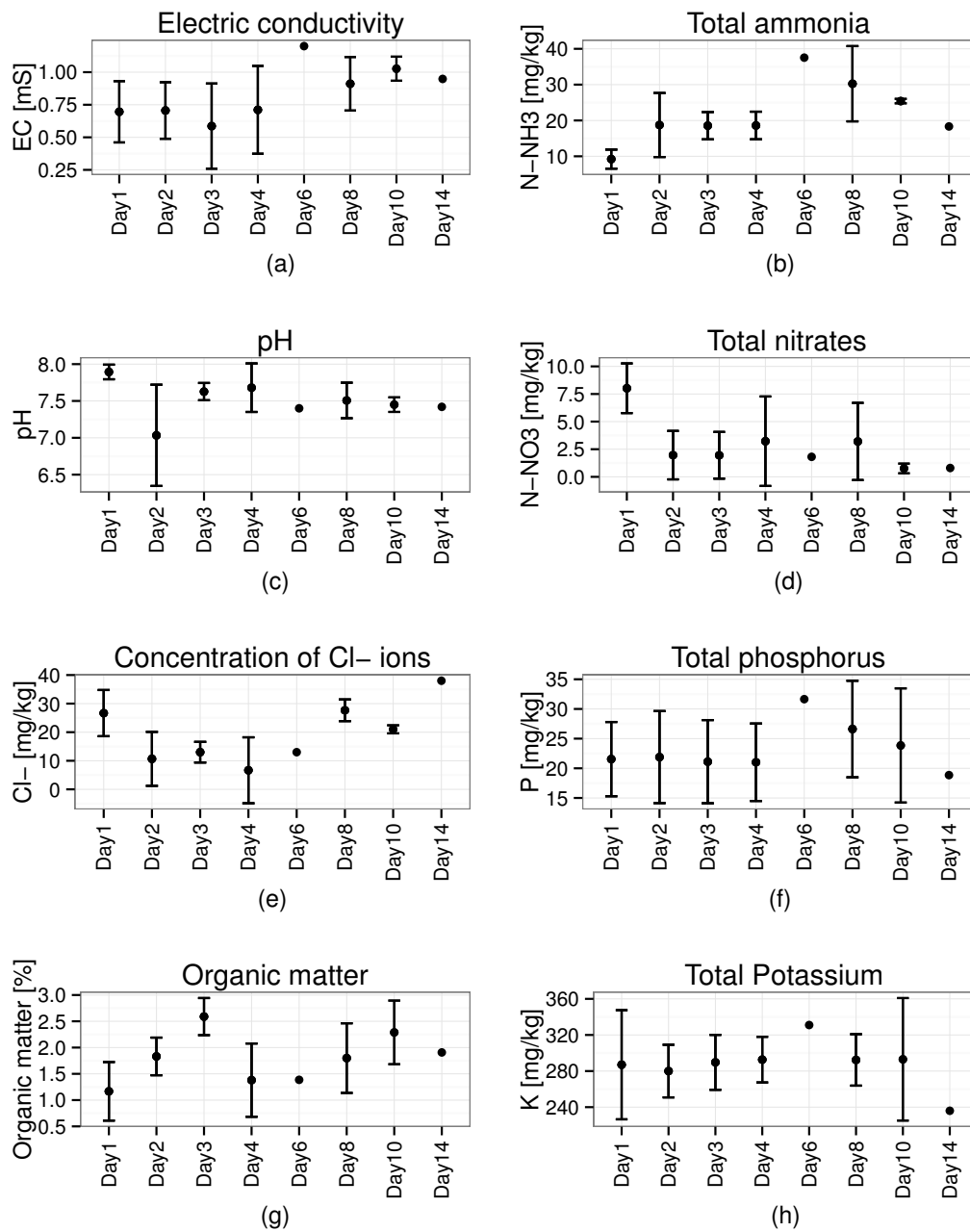


FIGURE B.2: Chemical analysis of the soil samples from the field.

B.3 Statistical analysis of the soil chemical composition

A null model was constructed first to evaluate the effect of field as an error term using linear mixed model (function `lmer` in R, package `lme4` v1.1-9) (Zeileis and Hothorn, 2002). Removing it did not influence the explanatory power of the model as measured by anova comparison (R, function `ANOVA` package `stats` v3.2.2). After removing temperature factor, the variance inflation factor (VIF) of all the samples dropped below the acceptable threshold of 5. Visual inspection of homoscedasticity, normality of residuals, Q-Q plot of residuals and residuals against predictors was inspected with the R `sjPlot` package function `sjp.lm` type "ma" (Lüdecke and Lüdecke, 2016). The model was subsequently reduced to contain

only water content, ammonia and chloride ions. The reduced model was not significantly different from the full model as tested with R, function anova. Final model collinearity was < 2 , residuals were normally distributed as tested with the Shapiro test (Richness: $W = 0.9516$, $p = 0.516$; Evenness: $W = 0.9716$, $p = 0.865$) (Rovston, 1982). Homoscedasticity of residuals was tested with the studentized Breuch Pagan test with R function bptest from the package lmtest v0.9-34 (Breusch and Pagan, 1979; Zeileis and Hothorn, 2002) (Richness: $BP = 5.967$, $df = 3$, $p = 0.11$; Evenness: $BP = 2.873$, $df = 3$, $p = 0.41$). All of the linear model assumptions were met.

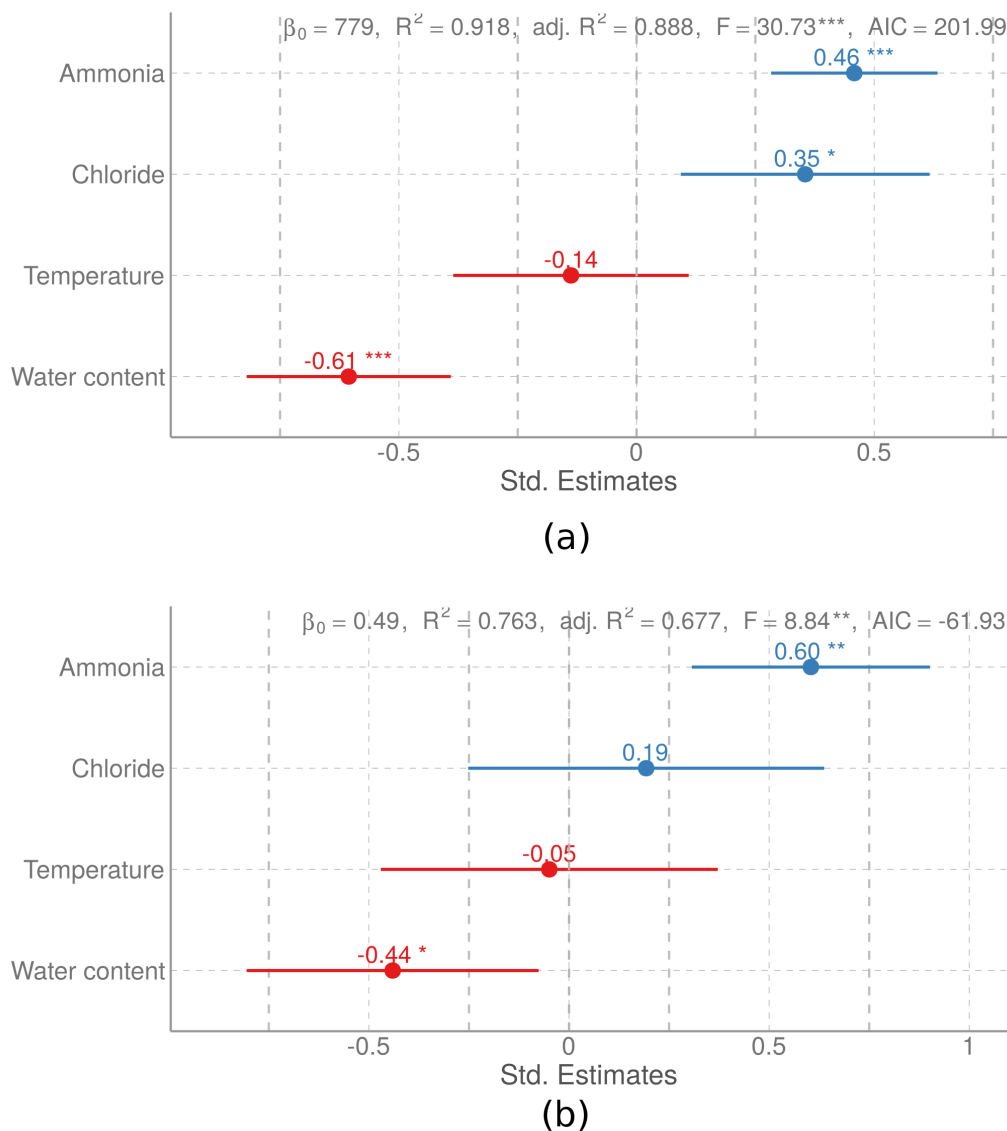


FIGURE B.3: **Linear model fit of chemical parameters.** Graphical representation of the results of the linear model fit of the chemical parameters to richness (a) and evenness (b) as explanatory variable.

B.4 Used primers

Analysis	Primers	Sequence (5' to 3')
Quantitative PCR	S-D-Bact-0341-b-S-17	CCTACGGGNGGCWGCAG
	S-D-Bact-0515-a-A-19	TTACCGCGGCTGCTGGCAC
T-RFLP	S-D-Bact-0341-b-S-17-FAM	CCTACGGGNGGCWGCAG-FAM
	S-D-Bact-0907-a-S-20	AAACTYAAARRAATTGACGG
Illumina sequencing	S*-Univ-0515-a-S-19	GTGCCAGCMGCCGCGGTAA
	S-D-Bact-0787-b-A-20	GGACTACHVGGGTWTCTAAT

TABLE B.1: **Primes Targeting 16S rRNA.** Primes targeting 16S rRNA gene used in this study (Klindworth et al., 2012)

B.5 MiSeq sequencing analysis

Sequencing files were analysed with the Qiime pipeline Caporaso et al., 2010. Barcodes and sequencing primers were removed in the sequencing facility. Samples were quality filtered to the phred score of 25. Subsequently the chimeric sequences were removed with the uchime algorithm (Edgar et al., 2011) using both a reference database (ChimeraSlayer reference database in the Broad Microbiome Utilities version microbiomeutil-r20110519) and de novo chimera detection. Approximately 30% of sequences were removed in this step. The remaining sequences were clustered with the **pick open reference otus** pipeline, using cluster algorithm against a Silva database v119 (Quast et al., 2013). The sequences were clustered on the 90% identity level. The resulting dataset was further analysed with the phyloseq package v1.12.2 in R (McMurdie and Holmes, 2013).

B.6 Average qPCR counts of rRNA units

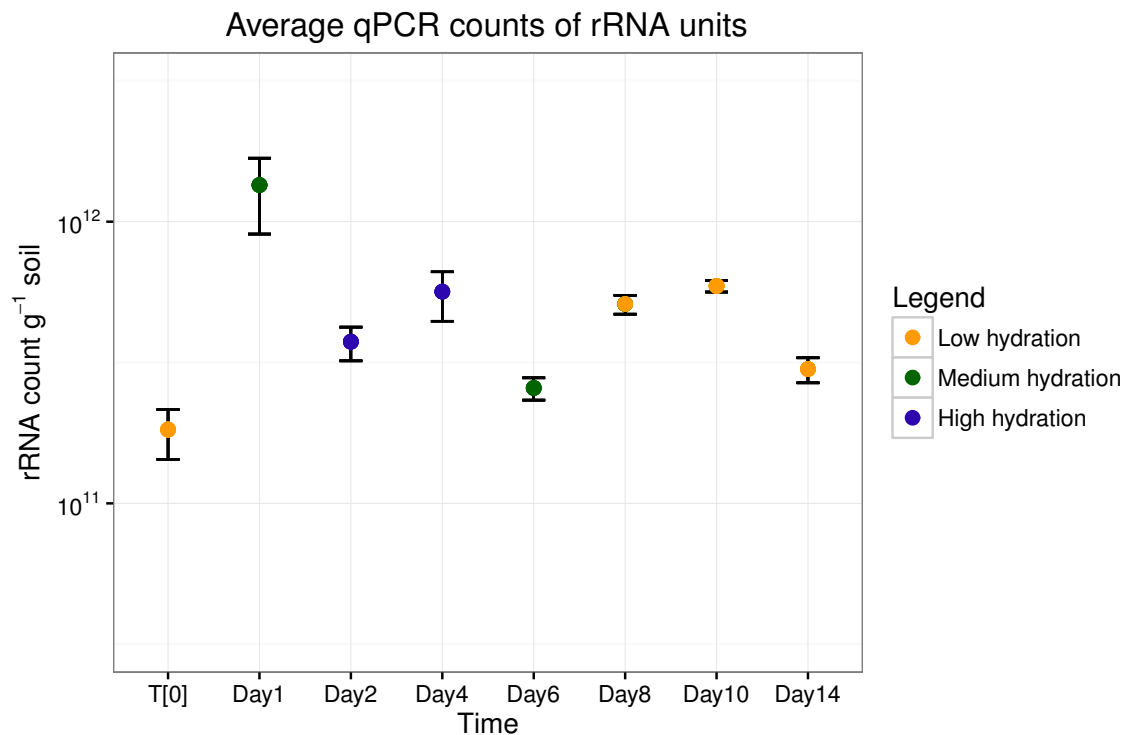


FIGURE B.4: **qPCR**. Total nucleic acids were extracted from the soil samples as previously described (Angel, 2012). The extract was purified by MasterPure RNA Purification Kit (Epicentre, Madison, WI). The DNA was degraded by DNase I supplied with the kit and the RNA samples were stored at -80°C for further analysis. Total bacterial rRNA unit quantification in the field measurements. Colour coding shows the different categories of samples with respect to community clustering (see Fig. 4.1 in the main text).

B.7 Analysis of similarity (ANOSIM) test.

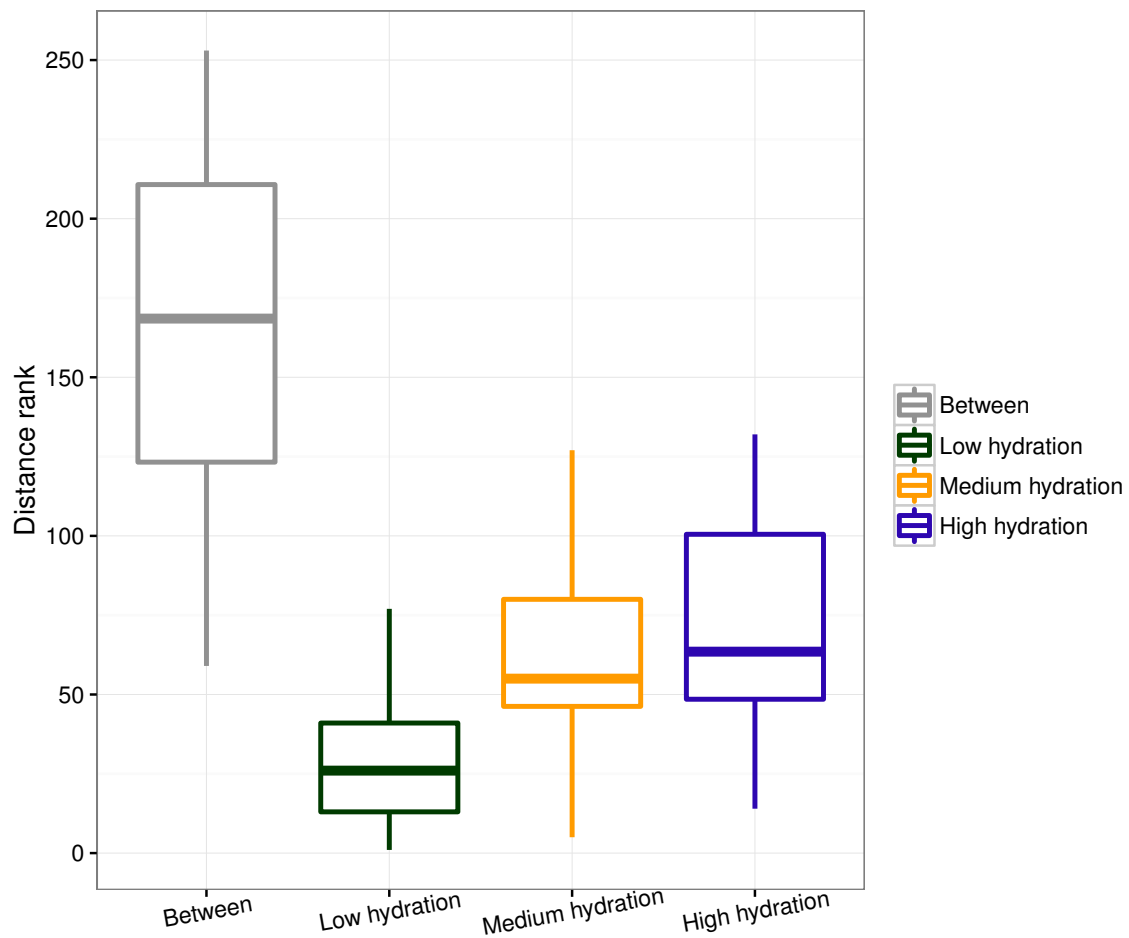


FIGURE B.5: **Analysis of similarity (ANOSIM) test.** Result indicating statistically significant difference between the four observed NMDS clusters in Fig. 4.1. Consequently, the resulting significant values of R and p support rejection of the null hypothesis that these were a result of a random process.

B.8 Richness and evenness per category

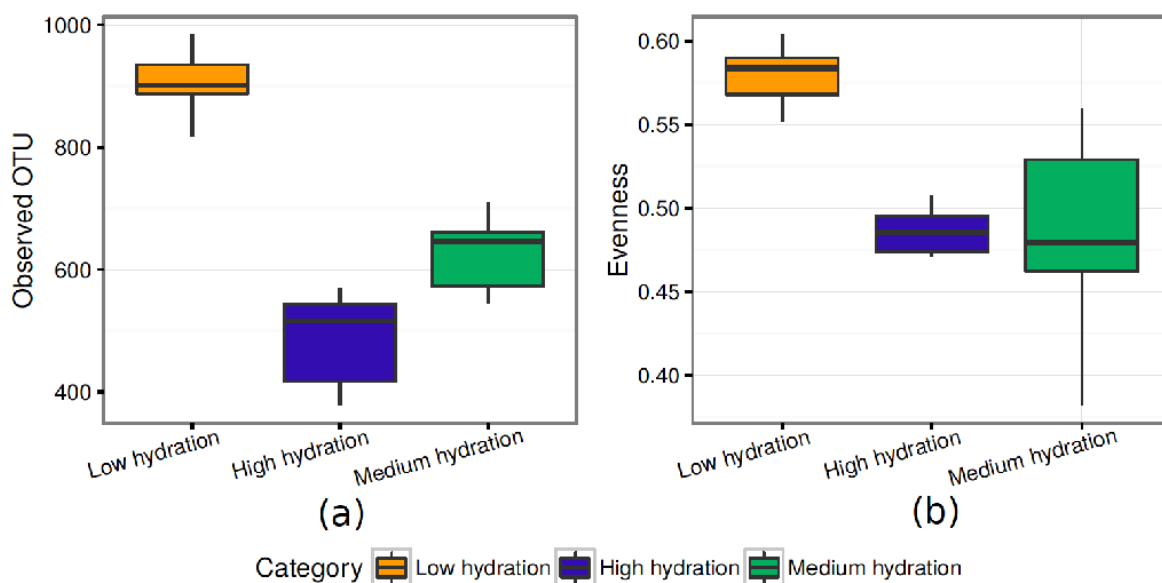


FIGURE B.6: **Comparison of the richness and evenness.** Comparison of the richness (a) and evenness (b) by the wetting categories. The Pielou evenness is normalised to compare between the sequencing and fingerprinting analyses. Boxed represent upper and lower quantile and the ticks display 5 and 95 quantile ($n \geq 5$).

References

- Angel, Roey (2012). "Total Nucleic Acid Extraction from Soil". In: *Protoc. Exch.*
- Austin, Amy T et al. (2004). "Water pulses and biogeochemical cycles in arid and semiarid ecosystems". In: *Oecologia* 141.2, pp. 221–235.
- Breusch, Trevor S and Adrian R Pagan (1979). "A simple test for heteroscedasticity and random coefficient variation". In: *Econometrica: Journal of the Econometric Society*, pp. 1287–1294.
- Caporaso, J Gregory et al. (2010). "QIIME allows analysis of high-throughput community sequencing data." In: *Nat. Methods* 7.5, pp. 335–336. ISSN: 1548-7091.
- Cross, Anne Fernald and William H Schlesinger (1999). "Plant regulation of soil nutrient distribution in the northern Chihuahuan Desert". In: *Plant Ecol.* 145. Balling 1988, pp. 11–25.
- Edgar, Robert C et al. (2011). "UCHIME improves sensitivity and speed of chimera detection". In: *Bioinformatics* 27.16, pp. 2194–2200.
- Klindworth, Anna et al. (2012). "Evaluation of general 16S ribosomal RNA gene PCR primers for classical and next-generation sequencing-based diversity studies". In: *Nucleic acids research*, gks808.
- Lüdecke, Daniel and Maintainer Daniel Lüdecke (2016). "Package 'sjPlot'". In: URL: <http://cran.r-project.org/package=sjmisc>.
- McMurdie, Paul J and Susan Holmes (2013). "phyloseq: an R package for reproducible interactive analysis and graphics of microbiome census data." In: *PLoS One* 8.4, e61217. ISSN: 1932-6203.
- Olsen, Sterling R. and Frank S. Watanabe (1957). "A Method to Determine a Phosphorus Adsorption Maximum of Soils as Measured by the Langmuir Isotherm1". en. In: *Soil Sci. Soc. Am. J.* 21.2, p. 144. ISSN: 0361-5995.
- Quast, Christian et al. (2013). "The SILVA ribosomal RNA gene database project: improved data processing and web-based tools." In: *Nucleic Acids Res.* 41, pp. D590–6. ISSN: 1362-4962.
- Rovston, P (1982). "Algorithm AS 181: The W Test for Normality". In: *Applied Statistics* 31, pp. 176–180.
- Si, BC et al. (2007). *Analysis of soil variability*.
- Zeileis, Achim and Torsten Hothorn (2002). "Diagnostic checking in regression relationships". In:

Appendix C

The Model of Microbial Life under Hydration-Desiccation Cycles

The rough surface patch model (RSPM) is employed and modified to generate physical domains (Kim and Or, 2016). In the RSPM, geometrical information of soil structure was averaged with a probability distribution of angular pore sizes and the effective water film thickness was introduced as an indicator of hydration condition that controls substrate diffusion, microbial dispersion rates, and aqueous habitat connectivity. In this study, we extended the probability based description from the rough surface domain to the soil profile domain to include gas phase and its diffusion during wetting. The domain for microorganisms is represented as a vertical section of the soil profile comprised with hexagonal patches (Fig. C.1A). Each patch (with a size $500\mu\text{m}$ in this work) is a spatial element of the domain that can be treated as a subdivided region with given soil properties, such as porosity ϕ , and a fractal dimension D for the pore-size distribution. These properties determine representative hydraulic measures essential for microbial life, such as effective water film-thickness, degree of saturation, effective void space volume, and connectivity of aqueous habitats. Locally pre-assigned properties yield spatial heterogeneity of water distribution in the domain at a given relative humidity.

C.1 Aqueous phase and gas phase in the physical domain

Following the RSPM, the same approach is used but extended by assuming the smooth surface region in RSPM as a cube and the surface pore as a square pyramid void (Fig. C.1A). It allows to calculate the local porosity ϕ of each patch (a small volume of bulk soil) to describe the soil type and roughness (described with the fractal dimension D and the surface porosity Φ) and its saturation degree at the given matric potential. The relation between the surface porosity in the RSPM and the total porosity of the soil profile in the modified RSPM can be written as following:

$$\phi = 1 - \frac{\int_{r_{\min}}^{r_{\max}} \left(\frac{2}{3}pH(r) + sr\right) r^2 \mathcal{N}(r) dr}{\int_{r_{\min}}^{r_{\max}} (pH(r) + sr) r^2 \mathcal{N}(r) dr} \quad (\text{C.1})$$

$$\equiv 1 - \frac{\int_{r_{\min}}^{r_{\max}} \left(\frac{2}{3}p + s\right) r^3 \mathcal{N}(r) dr}{\int_{r_{\min}}^{r_{\max}} (p + s) r^3 \mathcal{N}(r) dr} = 1 - \left\{ \frac{2}{3}\Phi + (1 - \Phi) \right\} = \frac{1}{3}\Phi, \quad (\text{C.2})$$

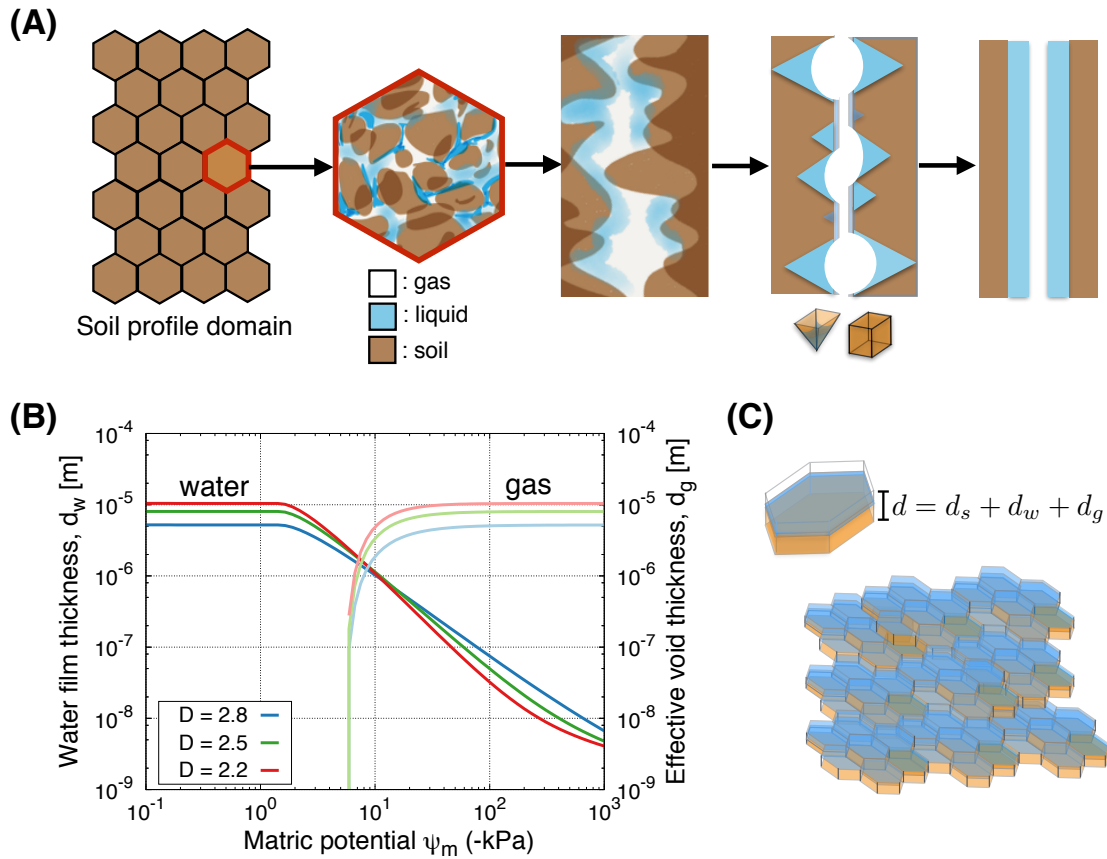


FIGURE C.1: **The abstract physical domain in the modified RSPM.** A schematic of the physical domain in the modified RSPM. (A) The roughness representation of a surface is extended to the vertical representation of three-dimensional soil profile including the gas phase (Kim and Or, 2016). A patch is a collection of roughness elements, cubic solid blocks and square pyramid voids. Using the effective medium assumption, effective thicknesses of each phase are determined. d_s , d_w , and d_g denote the effective thickness of solid, liquid, and gas phases, respectively. The porosity ϕ , the gas content ϵ , and the water content θ of each patch are converted from these effective thickness values. (B) Effective thicknesses for liquid and gas are calculated for three different fractal dimensions for pore size distribution. Strong coloured lines are water film thicknesses and corresponding pastel colours are for the void thicknesses. (C) For each patch, $d_s + d_w + d_g = d$ is given constant (calculated from the pre-assigned porosity) and the hydration condition and the thermal diffusivity are regulated by these effective thicknesses, d_w , d_e , and d_g . As a result, nutrients and heat diffusion between adjacent patches is a function of ψ_m , local relative humidity.

where r_{\min} and r_{\max} are the cutoff values for the pore size distribution, $H(r)$ is the height of the square pyramid pore with size r (Here, we assumed that the height of each square pyramid pore is the same as its base.), $\mathcal{N}(r) \sim r^{-D}$ is the probability density function of pore size r , p and s are the fraction of pore or solid elements in the space, respectively. We note that this relation could be different when different shape factors for solid and pore are assumed. The saturation degree at the given matric potential ψ_m can be obtained following RSPM.

$$\Theta(\psi_m) = \frac{\int_{r_{\min}}^{r_{\max}} [\Phi \mathcal{V}(r, \psi_m) + (1 - \Phi) h_\mu r^2] \mathcal{N}(r) dr}{\int_{r_{\min}}^{r_{\max}} [\Phi \frac{1}{3} r^2 H(r) + (1 - \Phi) h_\mu r^2] \mathcal{N}(r) dr}, \quad (\text{C.3})$$

where $\mathcal{V}(r, \psi_m)$ is the amount of water held in the pore with size r at the matric potential ψ_m due to the capillary force and the van der Waals force and h_μ is the absorbed water on the smooth surface (For the detailed explanation, see Kim and Or, 2016).

The total amounts of solid (soil grains), liquid (water held by capillarity and van der Waals force), and gas phases are mapped to the effective thicknesses to describe the transport properties between patches in the profile. Effective thicknesses of solid, liquid, and gas are d_s , d_w , and d_g , respectively:

$$d_s = (1 - \phi)d \quad (\text{C.4})$$

$$d_w(\psi_m) = \phi \Theta(\psi_m) d \quad (\text{C.5})$$

$$d_g(\psi_m) = \phi (1 - \Theta(\psi_m)) d \quad (\text{C.6})$$

where d is the total thickness of each patch for heat and solute transport and it can be calculated following equation:

$$d - d_s = \phi d = \frac{\int_{r_{\min}}^{r_{\max}} [\Phi \frac{1}{3} r^2 H(r) + (1 - \Phi) h_\mu r^2] \mathcal{N}(r) dr}{\int_{r_{\min}}^{r_{\max}} r^2 \mathcal{N}(r) dr}. \quad (\text{C.7})$$

In this research, the hydration condition (wetting and drying event) is controlled with the matric potential ψ_m mapped from the water contents ($\theta(\psi_m) \equiv \Theta(\psi_m)\phi$). The heterogeneity of the domain was achieved by assigning a set of $\{\Phi, D\}$ for an individual patch. To match the type of soil investigated in the field (Castelblanco et al., 2012), we assumed the fractal dimension of the pore-size distribution of loam soil 2.8 (corresponds to a fractional Brownian surface with the Hurst exponent $H = 0.2$) and the mean porosity to be $\bar{\phi} \approx 0.3$ (Tyler and Wheatcraft, 1992; Wang, Zhang, and Wang, 2005; Huang, Zhang, and Huang, 2006). This means that the probability that a point on the domain belongs to a pore with size X in the interval $[r, r + \delta r]$ is;

$$\text{Pr}[r \leq X \leq r + \delta r] \sim \bar{\Phi} r^{-(D-1)} \delta r. \quad (\text{C.8})$$

Parameters used to generate the physical domains for the simulations are given in Table C.1.

C.2 Parameters used to generate roughness domain for the modified RSPM.

Notations	Parameters	Units	Values
r_{\min}	minimum size of pores	m	10^{-7}
r_{\max}	maximum size of pores	m	5×10^{-4}
D	fractal dimension for pore size distribution	-	2.8
$\bar{\Phi}$	mean surface porosity	-	0.8
L_p	size of a patch	m	5×10^{-4}

TABLE C.1: **Parameters for the extended RSPM.** Parameters used to generate roughness domain for the extended RSPM

C.3 Diffusion processes through the profile

In the physical domain, we averaged microscopic details of the pore distribution and assumed that hydration conditions are represented with effective water film thickness and degree of saturation. The diffusion processes in this work is described as below to calculate local substrate concentration, $C(\vec{r}, t)$,

$$\frac{\partial C(\vec{r}, t)}{\partial t} = \nabla \cdot (D(\vec{r}) \nabla C(\vec{r}, t)) - \text{Sink terms} + \text{Source terms} \quad (\text{C.9})$$

where $D(\vec{r})$ is the apparent diffusion coefficient defined from the effective film thickness distribution of adjacent patches and the effective diffusion coefficient including tortuosity as a function of porosity and water contents. The net flux between two adjacent patches (for example, patch 1 and patch 2) due to diffusion is calculated as following:

$$\vec{J}_{1 \rightarrow 2} = - \frac{2D_{\text{eff}}(\vec{r}_1)D_{\text{eff}}(\vec{r}_2)}{D_{\text{eff}}(\vec{r}_1) + D_{\text{eff}}(\vec{r}_2)} \min[d_w(\vec{r}_1), d_w(\vec{r}_2)] \frac{C(\vec{r}_2) - C(\vec{r}_1)}{L_p}. \quad (\text{C.10})$$

To calculate the flux between heterogeneous medium, we have chosen the harmonic mean of diffusion coefficient and the minimum value of water film thicknesses between neighbouring patches (for the details, see Kim and Or, 2016). The effective diffusion coefficient of a patch is given following the Milington-Quirk tortuosity model (Milington and Quirk, 1961).

$$D_{\text{eff}}(\vec{r}) = D_0 \frac{\theta(\vec{r})^2}{\phi(\vec{r})^{4/3}} \quad (\text{C.11})$$

where D_0 is the diffusion coefficient of the substrate in bulk water and $\theta(\vec{r})$ and $\phi(\vec{r})$ are the water content and the porosity of the patch at \vec{r} . In Eq. (C.9), the second and third terms on r.h.s. indicate sink and source of substrates as reaction terms. Source terms are the mass transfer from the gas phase or the input of the source as boundary conditions and sink terms are the consumption by microorganisms.

Furthermore, we included dynamics of oxygen profile driven by diffusion in the gas phase and its input into the liquid phase as the dissolved oxygen. Aerobic bacteria are assumed to uptake the oxygen in the dissolved form (modelled as obligate aerobes) and anaerobic bacteria are inhibited by the local concentration of dissolved oxygen (modelled as obligate anaerobes). However, in the model, combining IBM and the gas diffusivity of oxygen through the soil profile is challenging as the time scales of these processes differ in order of magnitudes. For example, while the growth of a cell is in the order of hours, $\approx 10^3$ seconds, the gas diffusion through the domain (in this work, depth of 5 cm) is in the order of $\approx 10^{-2}$ seconds. Using the time scale of gas diffusion for all processes in the model is not plausible due to the computational time limit. Thus, we did not explicitly solve the gas diffusion for the oxygen source. Instead, we combined the Henry's law and percolation theory: Firstly, for the mass transfer between gas and liquid, Henry's law was applied;

$$C_O(\vec{r})^* = H_{cc}(T(\vec{r}))C_O^g(\vec{r})^* \quad (\text{C.12})$$

where $C_O(\vec{r})^*$ is the local concentration of dissolved oxygen in the liquid phase, $C_O^g(\vec{r})^*$ is the concentration of oxygen in the gas phase (converted from the partial pressure of the oxygen in the atmosphere) at equilibrium, and $H_{cc}(T(\vec{r}))$ is the dimensionless Henry's constant when temperature is given as T at the position \vec{r} . The temperature dependency of Henry's constant is described as $H_{cc} = H_{cc}^\Theta \exp\left(-\frac{\Delta_{\text{soln}}H}{R}\left(\frac{1}{T} - \frac{1}{T^\Theta}\right)\right)$ where $\Delta_{\text{soln}}H$ is the enthalpy of solution, R is the gas constant, T is absolute temperature, and Θ refers to standard condition ($T^\Theta = 298.15\text{K}$) (Sander, 1999). This assumption holds during entire simulations, as the soil matrix is characterised with large specific surface area and thin water film thickness (high mass transfer rate). Secondly, the invasive percolation of gas phase from the top of the domain through the profile is considered during the desiccation period. We assumed the gas percolation threshold based on the gas content of each patch. When the gas content of a patch exceeds a certain value (i.e. $\epsilon(\vec{r}) > \epsilon_c$. In this work we used $\epsilon_c = 0.243$ assuming the threshold of 3 dimensional body-centred cubic lattice (Sykes and Essam, 1964)), we assign the patch as a percolating patch.

C.4 Environmental conditions: temperature

The heat transport equation can be used to calculate the soil temperature profile $T(\vec{r}, t)$ (in the absence of fluid motion):

$$c_v(\vec{r})\frac{\partial T(\vec{r}, t)}{\partial t} = \nabla \cdot (\lambda(\vec{r})\nabla T(\vec{r}, t)) \quad (\text{C.13})$$

where $c_v(\vec{r})$ is the local heat capacity and $\lambda(\vec{r})$ is the local thermal conductivity at \vec{r} . From the local information of volume fractions and densities of solid, water, and gas, the soil volumetric heat capacity can be written:

$$c_v(\vec{r}) = \rho_s(1 - \phi(\vec{r}))c_s^s + \rho_w\theta(\vec{r})c_s^w + \rho_g\epsilon(\vec{r})c_s^g, \quad (\text{C.14})$$

where c_s is the specific heat capacity per unit mass, ρ is the density, and s, w , and g for each variables denote soil minerals, water, and gas. The volume fraction of each phase is given as $(1 - \phi)$, θ , ϵ for solid, liquid, and gas, respectively. In this equation, the proportion of organic matter (such as EPS, or microbial cells) are ignored for the thermal properties. Each volume fraction is determined by the hydration condition, therefore $c_v(\vec{r})$ varies following the water contents (Figure S4). The effective thermal conductivity at \vec{r} , $\lambda(\vec{r})$ is given as a harmonic mean of three conductivities, λ_s , λ_w , and λ_g from different phases.

$$\lambda(\vec{r}) = \left(\frac{1 - \phi(\vec{r})}{\lambda_s} + \frac{\theta(\vec{r})}{\lambda_w} + \frac{\epsilon(\vec{r})}{\lambda_g} \right)^{-1}. \quad (\text{C.15})$$

However, the thermal diffusivity in soil is also in the order of $\approx 10^{-6} \text{m}^2/\text{s}$, hence the coupling the microbial growth is not plausible. For the temperature, we solved the homogenous 1 dimensional domain (over the depth) at the varying hydration condition and applied the solution to the profile as boundary conditions. Considering that the soil crust (with 2mm thickness) was discarded and the sample was collected from top 5cm, we applied soil crust (fine soil structure with $D = 2.9$ and $\Phi = 0.9$) at the top 2mm and used Loess soil texture ($D = 2.8$ and $\Phi = 0.8$ same as the value we used in the main text) for the below crust. Boundary condition at the air-soil interface is assumed to be in the interfacial isothermal condition.

$$T(z = 0, t) = T_{\text{air}}(t) \quad (\text{C.16})$$

where $T_{\text{air}}(t)$ is assigned from the air temperature records of LTER where our field measurements were conducted. Considering the thermal damping depth of loess soil is around 10 cm, we modelled up to 15 cm with the zero heat flux boundary condition at the bottom of the domain. The calculated solution at the three selected depths are plotted in Fig. C.2. To sum up the mechanistic model for microbial populations in soil, a schematic of the model and its boundary conditions for hydration conditions, substrate and heat diffusion are given in Fig. C.3.

C.5 Individual based description of microbial growth on the heterogeneous domain

Microbial activity was added to the modified RSPM by using the IBM (Individual based model) (Kim and Or, 2016). The RSPM allows assigning local environmental conditions and the IBM examines cell-level response to it. Since the IBM is suitable for describing bacterial behaviour in heterogeneous and time-variant environment, combining these two models can be interpreted as an *in silico* experiment based on physical models. Each individual in the IBM represents microbial cell possessing intrinsic parameters that indicate its physiological characteristics, such as cell-size, specific growth rate, nutrient affinity, etc. The model tracks life history of each individual such as interactions with other cells and growth history at a single-cell point of view (see reviews by Ferrer, Prats, and López, 2008; Hellweger and Bucci, 2009). As an addition to previous IBM models, our model is spatially explicit and

includes motility of cells as they are able to actively explore the domain. The motility of a cell is regulated by the chemotactic response to substrate concentration and the swimming velocity on capillary surfaces. For its locomotion and net displacement, we used a biased random walk approach on the rough surface.

A reaction-diffusion equation was used in the model to obtain the nutrient distribution over time:

$$\frac{\partial C_j(\vec{r}, t)}{\partial t} = \nabla \cdot (D_j(\vec{r}, t) \nabla C_j(\vec{r}, t)) - \frac{1}{V_w(\vec{r}, t)} \sum_{i=1}^{N(\vec{r})} \frac{\mu_i(\vec{r})}{Y_{\max}^i} b_i(t) + S_j(\vec{r}), \quad (\text{C.17})$$

where $C_j(\vec{r}, t)$ is the local concentration of substrate j , $D_j(\vec{r}, t)$ is the local diffusion coefficient, and $V_w(\vec{r}, t)$ is the amount of water in a given patch at time t . The second term on the right-hand side is the reaction term calculating the total substrate consumption in the patch. $N(\vec{r})$ is the total number of individual cells at \vec{r} , Y_{\max}^i is the maximum growth yield of taxon i on the substrate j , $b_i(t)$ is the biomass, and $\mu_i(\vec{r})$ is the growth rate of cell i . The last term $S_j(\vec{r})$ is the source term of the substrate j .

Each cell consumes several chemical species that are obligatory for its growth, in this study oxygen and dissolved carbon following their physiological differences. We assign a growth rate of a taxon (or microbial species) i with multiple limiting substrates j by using Monod-type growth kinetics as a function of the substrate concentration field (Monod, 1942; Monod, 1949):

$$\mu_i(\vec{r}) = \mu_{\max, i} \min[f_i^1(\vec{r}), f_i^2(\vec{r}), \dots] \quad (\text{C.18})$$

where $f_i^j = \frac{C_j}{K_{S, i}^j + C_j}$ (when nutrient j is a substrate for the growth) or $f_i^j = \frac{K_{I, i}^j}{K_{I, i}^j + C_j}$ (when nutrient j is a inhibitor for the growth) and μ_{\max}^i , $K_S^i/K_{I, i}^j$ are the maximum growth rate

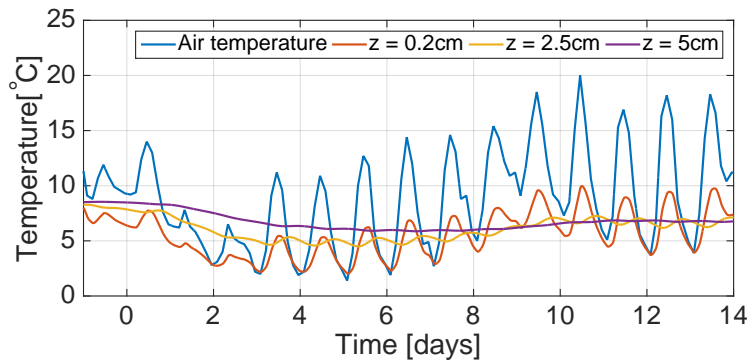


FIGURE C.2: **Dynamics of temperature profile** Calculated soil temperature profile from the air temperature records of LTER. Prediction of soil temperature profile during the field observation are plotted and the time corresponds to the time of field measurements in the main text. The blue line indicates the air temperature. The predicted soil temperature is given for depths, $z = 0.2$ (red), 2.5 (yellow), and 5 cm (purple). Only top 5 cm of the soil is sampled after discarding the soil crust with 2 mm thickness.

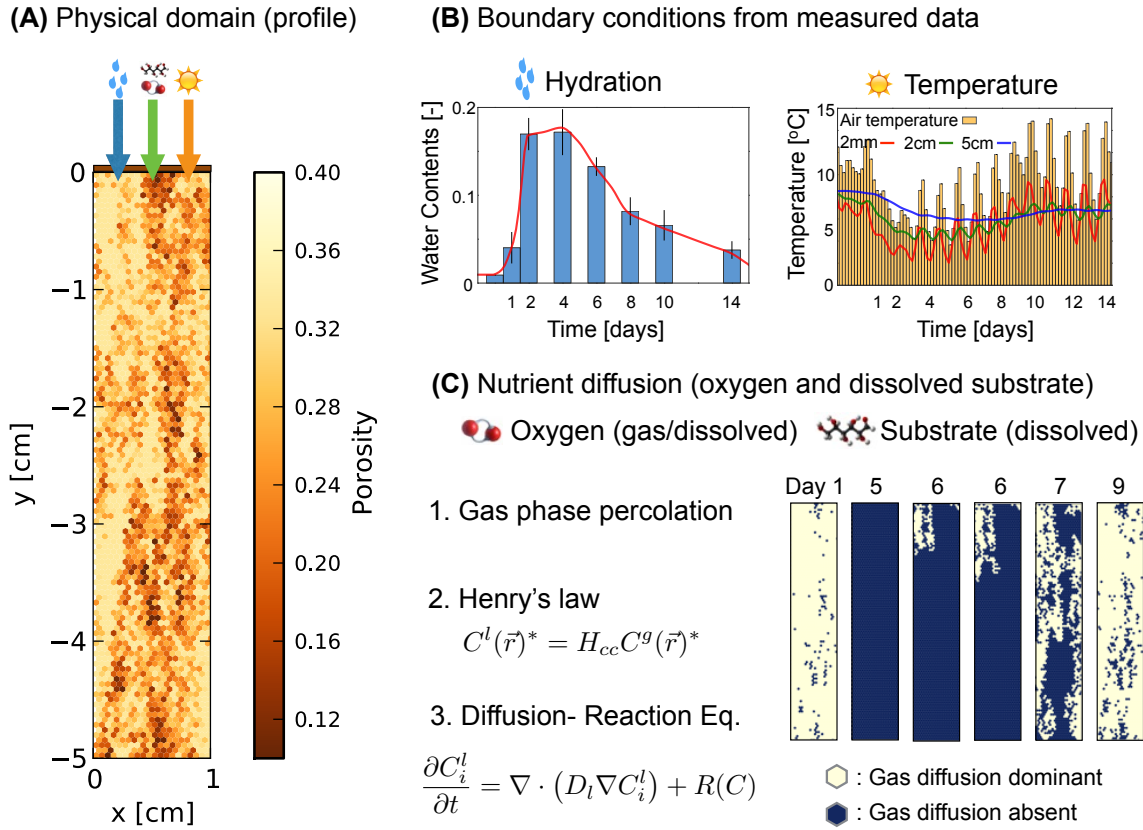


FIGURE C.3: A schematic of the soil profile domain. A schematic of the physical domain of the mechanistic model. (A) Physical domain is a soil profile with pre-assigned distribution of structural properties, such as porosity and fractal dimension (in this figure, fractal dimension $D = 2.8$ is used). The domain mimics the soil sample collected from the field (up to 5 cm depth from the surface). (B) Hydration and temperature conditions are used as dynamic boundary conditions through the entire simulations. For the hydration condition, measured gravimetric water contents (blue bars) were linearly interpolated (the red line) and mapped to the matric potential of the entire domain. By using the air temperature records of LTER, we calculated the soil temperature (combined with the hydration condition changes) over the profile. Orange bars are the record of air temperature, red, green, blue lines are the soil temperatures at depth 2mm, 2cm, and 5cm, respectively. (C) Dissolved nutrient distributions are solved with diffusion-reaction equations. Especially, the oxygen source in the profile (for aerobic cells) is the partition of gas and liquid phases and the model solves the input of dissolved oxygen from gas phase by combining gas percolation and Henry's law.

and half-saturation/inhibition constant of cell i , respectively. Specifically, in this study, we introduce two different groups of microorganisms, aerobically growing group and anaerobically growing group. Aerobes are simply assigned as a group that utilises oxygen and carbon source for growth. On the other hand, growth of anaerobes are inhibited by the presence of oxygen, meaning that only obligate anaerobes are considered. The growth rate of individual cell is calculated as following: For aerobic growth,

$$\mu_i^{ae}(\vec{r}) = \mu_{\max,i} \min\left[\frac{C_C(\vec{r})}{K_{S,i}^C + C_C(\vec{r})}, \frac{C_O(\vec{r})}{K_{S,i}^O + C_O(\vec{r})}\right] \quad (\text{C.19})$$

For anaerobic growth,

$$\mu_i^{an}(\vec{r}) = \mu_{\max,i} \min\left[\frac{C_C(\vec{r})}{K_{S,i}^C + C_C(\vec{r})}, \frac{K_{I,i}^O}{K_{I,i}^O + C_O(\vec{r})}\right] \quad (\text{C.20})$$

where $C_C(\vec{r})$ is the local concentration of the carbon source and $C_O(\vec{r})$ is the local concentration of the dissolved oxygen. We assumed that the individual growth rate at the pore scale is the same as the population growth rate in batch culture (Dai et al., 2013). Accordingly, the growth of an individual cell can be written as:

$$\frac{db_i(t)}{dt} = [\mu_i(\vec{r}) - m_i] b_i(t) \quad (\text{C.21})$$

where m_i is the maintenance rate of cell i .

Characteristics of multiple taxa were assigned before the inoculation on the RSPM. To avoid the complex definition of bacterial taxa, we defined different bacterial “taxa” based only on their nutrient-consumption patterns. Any other functional diversity or complex trophic interactions were not included in the model. The values used in the simulations are listed in Table C.2.

C.6 Temperature dependent microbial growth

In the model, we combined our growth model with a temperature dependent growth model using the Arrhenius equation (Schoolfield, Sharpe, and Magnuson, 1981) to see the effect of temperature in population dynamics. The level of adaptation to the temperature might vary among different organisms, however, we did not consider it and assumed that all microbial cells follow the same activation energy and the optimal temperature encapsulated in the maximum growth rate to reduce the complexity. The temperature dependency on the maximum growth rate of a cell at temperature T is assigned as following (Schoolfield, Sharpe, and Magnuson, 1981):

$$\tilde{\mu}_i(T) = \mu_{\max,i} \left[\frac{\frac{T}{T_\Theta} e^{\frac{\Delta H_\Theta}{R} \left(\frac{1}{T_\Theta} - \frac{1}{T} \right)}}{1 + e^{\frac{\Delta H_L}{R} \left(\frac{1}{T_L} - \frac{1}{T} \right)} + e^{\frac{\Delta H_H}{R} \left(\frac{1}{T_H} - \frac{1}{T} \right)}} \right], \quad (\text{C.22})$$

Notations	Parameters	Units	Values
μ_{\max}^i	specific growth rate	hr ⁻¹	0.3 ~ 1.0 ^{ae,#}
		hr ⁻¹	0.6 ~ 1.8 ^{an,#}
Y_{\max}	apparent yield	fg.fg ⁻¹	0.44 ^{ae}
		fg.fg ⁻¹	0.088 ^{an}
m	maintenance rate	-	0.041 ^{ae}
		-	0.0041 ^{an}
$K_{S,i}^C$	half-saturation constant	mg.l ⁻¹	0.001 ~ 0.1 [#]
$K_{S,i}^O$	half-saturation for O ₂	mg.l ⁻¹	2.3 ^a
$K_{I,i}^O$	inhibition constant for O ₂	mg.l ⁻¹	0.05 ^b
\bar{V}_B	median cell volume	fl	0.4
$V_{B,d}$	cell volume at division	fl	2 \bar{V}_B /1.433
$V_{\min,d}$	minimal active cell volume	fl	\bar{V}_B /5
ρ	cell density (dry mass)	fg.fl ⁻¹	290
R	size of microbial cells	μm	1
D_0^C	substrate diffusion coefficient	mm ² .hr ⁻¹	2.2
D_0^O	oxygen diffusion coefficient	mm ² .hr ⁻¹	7.2
v_0	cell velocity at bulk water	mm.hr ⁻¹	3.6
χ_0	chemotactic sensitivity	mm ² .hr ⁻¹	12.8
$C(z=0)$	substrate boundary concentration	g.l ⁻¹	1

TABLE C.2: **Parameters for individual-based modelling (IBM) for aerobic and anaerobic species**

^{ae} Values assigned for the aerobically growing cells; ^{an} Values assigned for the anaerobically growing cells: Assuming that anaerobic processes are costly; oligotroph-like aerobes and copiotroph-like anaerobes based on observed values (Pirt, 1965; Heijnen, 1999; Stouthamer, 2012). We note that higher maximum growth rates for anaerobes were chosen to compensate the strong inhibition of oxygen

[#] μ_{\max} and $K_{S,i}^C$ are different for each taxon. μ_{\max} are chosen uniformly spaced values and $K_{S,i}^C$ are logarithmically spaced values in the given ranges

^a The growth of obligate aerobes ceases at 25% of atmospheric level

^b The growth of obligate anaerobes is inhibited when oxygen concentration is higher than 0.5% of atmospheric level

Notations	Parameters	Units	Values
ΔH_{Θ}	enthalpy of activation	kJ	-5.43
ΔH_L	enthalpy change for inactivation at low T	kJ	-141.1
ΔH_H	enthalpy change for inactivation at high T	kJ	687.9
T_L	low T inactivation	K	283*
T_H	high T inactivation	K	314.7

TABLE C.3: **Parameters for temperature dependent growth.** Parameters used for the temperature dependent growth (Schoolfield, Sharpe, and Magnuson, 1981; Zwietering et al., 1991), * the enzyme inactivation criterion for the low temperature was modified in this model assuming that microorganisms are adapted to the mean soil temperature

where T_{Θ} is the reference temperature ($25^{\circ}C = 298K$) and ΔH_{Θ} (cal.mol^{-1}) is the activation enthalpy of the reaction. There are two inactivation regimes; low temperature inactivation and high temperature inactivation that are denoted with subscripts, L and H . From the spatially resolved temperature profile from Eq. (D.1), we modified the microbial growth rate accordingly. The used parameters for the temperature dependent growth is given in Table C.3.

C.7 Active cells and potentially active cells before and after wetting event

The model aimed at describing microbial community behaviour under a wide range of matric potential, changes from several kilopascals to megapascals; in other words, the domain can be exposed to very wet conditions after a rainfall event and to very dry conditions after prolonged desiccation. As the soil dries after the rainfall event, the effective water-film thickness can be reduced from 10^{-5} m to 10^{-9} m. This implies that the amount of nutrient flux to a certain location will also be reduced by several orders of magnitude due to thinning of the water film. In the model, this suppresses microbial growth and leads to taxa extinct in the long term. To prevent complete extinction of taxa during simulations with the model, when a cell is starved (i.e., negative growth rate), we count these cells as potentially active cells (Blagodatskaya and Kuzyakov, 2013). This enabled us to track changes in microbial interactions in different hydration states without allowing irreversible extinction of certain taxa and to retain rare members in the microbial community while focusing on the main populations retain rare members in the microbial community while focusing on the main populations during the hydration cycles. Therefore, essentially the model describes dynamics of a community with the constant richness while it tracks the relative abundance changes of the populations.

References

- Blagodatskaya, Evgenia and Yakov Kuzyakov (2013). "Active microorganisms in soil: critical review of estimation criteria and approaches". In: *Soil Biology and Biochemistry* 67, pp. 192–211.
- Castelblanco, JA Muñoz et al. (2012). "The water retention properties of a natural unsaturated loess from Northern France". In: *Geotechnique* 62.2, pp. 95–106.
- Dai, Jing et al. (2013). "Charting microbial phenotypes in multiplex nanoliter batch bioreactors". In: *Analytical chemistry* 85.12, pp. 5892–5899.
- Ferrer, Jordi, Clara Prats, and Daniel López (2008). "Individual-based modelling: an essential tool for microbiology". In: *Journal of Biological Physics* 34.1-2, pp. 19–37.
- Heijnen, Joseph J (1999). "Bioenergetics of microbial growth". In: *Encyclopedia of Bioprocess Technology*.
- Hellweger, Ferdi L and Vanni Bucci (2009). "A bunch of tiny individuals : Individual-based modeling for microbes". In: *Ecological Modelling* 220.1, pp. 8–22.
- Huang, Guan-Hua, Ren-Duo Zhang, and Quan-Zhong Huang (2006). "Modeling soil water retention curve with a fractal method". In: *Pedosphere* 16.2, pp. 137–146.
- Kim, Minsu and Dani Or (2016). "Individual-based model of microbial life on hydrated rough soil surfaces". In: *PLoS ONE* 11.1, e0147394.
- Milington, RJ and JP Quirk (1961). "Permeability of porous media". In: *Nature* 183, pp. 387–388.
- Monod, Jacques (1942). "Recherches sur la croissance des cultures bacteriennes". In: *Hermann and Cie, Paris*.
- (1949). "The growth of bacterial cultures". In: *Annual Reviews in Microbiology* 3.1, pp. 371–394.
- Pirt, SJ (1965). "The maintenance energy of bacteria in growing cultures". In: *Proceedings of the Royal Society of London B: Biological Sciences* 163.991, pp. 224–231.
- Sander, Rolf (1999). *Compilation of Henry's law constants for inorganic and organic species of potential importance in environmental chemistry*.
- Schoolfield, RM, PJH Sharpe, and CE Magnuson (1981). "Non-linear regression of biological temperature-dependent rate models based on absolute reaction-rate theory". In: *Journal of Theoretical Biology* 88.4, pp. 719–731.
- Stouthamer, Adriaan Hendrik (2012). *Quantitative aspects of growth and metabolism of microorganisms*. Springer Science & Business Media.
- Sykes, MF and JW Essam (1964). "Critical percolation probabilities by series methods". In: *Physical Review* 133.1A, A310.
- Tyler, Scott W and Stephen W Wheatcraft (1992). "Fractal scaling of soil particle-size distributions: Analysis and limitations". In: *Soil Science Society of America Journal* 56.2, pp. 362–369.
- Wang, Kang, Renduo Zhang, and Fuqin Wang (2005). "Testing the pore-solid fractal model for the soil water retention function". In: *Soil Science Society of America Journal* 69.3, pp. 776–782.

-
- Zwietering, MH et al. (1991). "Modeling of bacterial growth as a function of temperature".
In: *Applied and Environmental Microbiology* 57.4, pp. 1094–1101.

Appendix D

Hydration Status and Diurnal Trophic Interactions Shape Microbial Community Function in Desert Biocrusts

D.1 Biocrust temperature distribution and dynamics

We implemented the heat equation to calculate temperature gradients within the biocrust and daily variations (in the absence of fluid motion):

$$c_v(\vec{r}) \frac{\partial T(\vec{r}, t)}{\partial t} = \nabla \cdot (\lambda(\vec{r}) \nabla T(\vec{r}, t)) \quad (\text{D.1})$$

where ρ_s and c_s are the density of soil and the specific heat capacity per unit mass, respectively. From the volume fractions and densities of solid, water, and gas, the soil volumetric heat capacity can be written:

$$c_v(\vec{r}) = \rho_s \theta_s(\vec{r}) c_s^s + \rho_w \theta_w(\vec{r}) c_s^w + \rho_g \theta_g(\vec{r}) c_s^g, \quad (\text{D.2})$$

where s, w , and g denote soil grains (solid), water, and gas fractions. We assume that the effective thermal conductivity of a patch, λ is given as a harmonic mean of three conductivities, λ_s, λ_w , and λ_g from different phases.

$$\lambda(\vec{r}) = \left(\frac{\theta_s(\vec{r})}{\lambda_s} + \frac{\theta_w(\vec{r})}{\lambda_w} + \frac{\theta_g(\vec{r})}{\lambda_g} \right)^{-1} \quad (\text{D.3})$$

In the model, the proportion of organic matter (such as EPS, or microbial cells) are ignored for the thermal properties.

D.2 Modelling of chemical reactions within biocrusts

Two main chemical processes are included in the biocrust model; liquid and gas phase partitioning from Henry's law and local acid-base reactions within soil pore water. These

chemical processes are very fast compared with microbial or diffusion processes, therefore we numerically implemented the results of chemical reactions (such as pH estimation) as boundary conditions for reaction diffusion equations (every time step it calculates the new equilibrium solution within a patch).

Firstly, the temperature dependent Henry's law is given as following:

$$C^{l*} = H_{cc}^{\Theta} e^{-\frac{\Delta_{\text{soln}} H}{R} \left(\frac{1}{T} - \frac{1}{T^{\Theta}} \right)} C^{g*}, \quad (\text{D.4})$$

where $H_{cc} \equiv k_H RT$ is the dimensionless Henry's constant, the superscript Θ indicates the standard temperature ($T^{\Theta} = 298.15\text{K}$). $\Delta_{\text{soln}} H$ is the enthalpy of solution and R is the gas constant. In Table D.1, values used for Henry's law constants are given Sander, 1999 together with the partial pressure in the atmosphere. The partial pressure of each element in the atmosphere was set to be constant in the model.

substance	k_H^{Θ} [M/atm]	$-\frac{\Delta_{\text{soln}} H}{R}$ [K]	partial pressure [atm]	reference
O ₂	1.3×10^{-3}	1500	0.2095	-
CO ₂	3.5×10^{-2}	2400	383×10^{-6}	-
NH ₃	6.1×10^1	4200	5×10^{-9}	assumed ^a
HONO	5×10^1	4900	10^{-9}	Su et al., 2011 ^b
N ₂ O	2.5×10^{-2}	2600	5×10^{-7}	assumed ^c

TABLE D.1: Henry's law constants of gaseous elements Sander, 1999 and partial pressure in the atmosphere.

^a The atmospheric level of NH₃ varies depending on the time of the day, season and regions. Generally it is given in a range of 1 ~ 10 ppb.

^b The gas phase concentration of HONO ranges over several orders of magnitude for different regions, 0.1 ~ 600 ppb. In this model, we have chosen the field measurement from semiarid pine forest Su et al., 2011.

^c The atmospheric level of N₂O is in a range of 100 ~ 1000 ppb.

Secondly, acid-base reactions for pH estimation were described as near-equilibrium kinetics with an assumption of local charge neutrality. For instance, the kinetics of the ammonium concentration was written as an ordinary differential equation,

$$\frac{dC_{\text{NH}_4^+}}{dt} = -k_4 \left(C_{\text{NH}_4^+} - C_{\text{NH}_4^+}^* \right) = -k_4 \left(C_{\text{NH}_4^+} - \frac{C_{\text{NH}_3} C_{\text{H}^+}}{K_A} \right), \quad (\text{D.5})$$

where the equilibrium concentration of ammonium, $C_{\text{NH}_4^+}^*$, which will be reached with the rate k_4 . $C_{\text{NH}_4^+}^*$ can be calculated with the acid-base equilibrium with ammonia, $\frac{C_{\text{NH}_3} C_{\text{H}^+}}{K_A}$. K_A is the ammonia dissociation constant, which depends on the temperature and the ionic strength. Here, the concentration of protons, C_{H^+} , holds the local charge neutrality at local scale by satisfying the relation;

$$C_{\text{H}^+} + C_{\text{NH}_4^+} + 2C_{\text{Ca}^{2+}} - C_{\text{OH}^-} - C_{\text{HCO}_3^-} - 2C_{\text{CO}_3^{2-}} - 2C_{\text{NO}_2^-} - C_{\text{NO}_3^-} + C_Z = 0 \quad (\text{D.6})$$

where C_Z is the net concentration of anion and cation that are non-reactive in the model (unknown ions that regulate the soil pH in the model). Furthermore, nitrate, NO_3^- , is also

included in the pH calculation for charge balancing although it does not participate for acid dissociation. Therefore, including the estimation of soil pore water pH, we solved 10 coupled differential algebraic equations at each patch (chemical information of local soil pore water) for the chemical reaction dynamics and applied the solution as boundary conditions every time step in the model. All the chemical reactions and rate constants used in the model are given in Table [D.2](#) and [D.3](#).

process	reaction	rate constant k [day^{-1}]	reaction ID
Autoprotolysis of H_2O	$\text{H}_2\text{O} \rightleftharpoons \text{OH}^- + \text{H}^+$	implemented as equilibrium	R(1)
Hydration of CO_2	$\text{CO}_2(\text{aq}) + \text{H}_2\text{O} \rightleftharpoons \text{HCO}_3^- + \text{H}^+$	$k_2 = 2221$	R(2)
Dissociation of HCO_3^-	$\text{HCO}_3^- \rightleftharpoons \text{CO}_3^{2-} + \text{H}^+$	$k_3 = 10^{10}$ (very fast reaction)	R(3)
Dissociation of NH_3	$\text{NH}_4^+ \rightleftharpoons \text{NH}_3(\text{aq}) + \text{H}^+$	$k_4 = 10^{10}$ (very fast reaction)	R(4)
Dissociation of HNO_2	$\text{HNO}_2(\text{aq}) \rightleftharpoons \text{NO}_2^- + \text{H}^+$	$k_5 = 10^{10}$ (very fast reaction)	R(5)
Solubility of CaCO_3	$\text{CaCO}_3(\text{aq}) \rightleftharpoons \text{Ca}^{2+} + \text{CO}_3^{2-}$	$k_6 = 10^{10}$ (very fast reaction)	R(6)

TABLE D.2: Acid-base reactions considered in the model.

reaction ID	C_{CO_2}	$C_{\text{HCO}_3^-}$	$C_{\text{CO}_3^{2-}}$	C_{NH_3}	$C_{\text{NH}_4^+}$	C_{HNO_2}	$C_{\text{NO}_2^-}$	C_{CaCO_3}	$C_{\text{Ca}^{2+}}$	Rate	K_a^*
R(1)										$C_{\text{H}^+} C_{\text{OH}^-} = K_w$	K_w
R(2)	-1	+1								$k_2 \left(C_{\text{CO}_2} - \frac{C_{\text{HCO}_3^-} C_{\text{H}^+}}{K_{1C}} \right)$	K_{1C}
R(3)		-1	+1							$k_3 \left(C_{\text{HCO}_3^-} - \frac{C_{\text{CO}_3^{2-}} C_{\text{H}^+}}{K_{2C}} \right)$	K_{2C}
R(4)				+1	-1					$k_4 \left(C_{\text{NH}_4^+} - \frac{C_{\text{NH}_3} C_{\text{H}^+}}{K_A} \right)$	K_A
R(5)						-1	+1			$k_5 \left(C_{\text{HNO}_2} - \frac{C_{\text{NO}_2^-} C_{\text{H}^+}}{K_N} \right)$	K_N
R(6)			+1					-1	+1	$k_6 \left(C_{\text{CaCO}_3} - \frac{C_{\text{Ca}^{2+}} C_{\text{CO}_3^{2-}}}{K_{sp}} \right)$	K_{sp}

TABLE D.3: Stoichiometry and kinetics of chemical reactions used in the model. The table of stoichiometry indicates the participation of each soluble in chemical reactions and rate describes the near equilibrium kinetics used in the model. Concentrations of solubles are denoted as $C_{\text{substance}}$ with a unit of [M].
 * The acid dissociation constants for each reaction are assigned with commonly used notations. The values depend on the temperature and the ionic strength during the dynamics following Table D.4 and Equation (D.7).

As the desert biocrust model includes the large variation of temperature, acid dissociation constants, K_a (or $pK_a = -\log_{10} K_a$) are also given as a function of temperature Plummer and Busenberg, 1982; Buhr and Miller, 1983; Ebrahimi et al., 2003. Used expressions for the temperature dependency are summarised in Table D.4. Including the temperature dependency of acid dissociation and ionic interaction in the solution, the equilibrium dissociation constants for partitioning chemical species can be calculated at the given temperature and ionic strength Buhr and Miller, 1983; Yang, 2011. By using the extended Debye-Hückel equation, the negative logarithm of activity coefficients can be written as

$$p\gamma = \frac{G\zeta^2\sqrt{I}}{1 + aB\sqrt{I}}, \quad (\text{D.7})$$

where ζ and I are ionic valency and ionic strength of the solution, a is the effective diameter of the ion in angstrom ($a = 4(\text{HCO}_3^-)$; $4.5(\text{CO}_3^{2-})$; $2.5(\text{NH}_4^+)$; $9(\text{H}^+)$; $3(\text{NO}_2^-)$; $6(\text{Ca}^{2+})$). G , and B are temperature dependent constants Buhr and Miller, 1983.

$$G = 1.825 \times 10^6 (\epsilon T)^{-1.5} \quad (\text{D.8})$$

$$B = 50.3 (\epsilon T)^{-0.5} \quad (\text{D.9})$$

where $\epsilon = 87.74 - 0.40008(T - 273.15) + 9.398 \times 10^{-4}(T - 273.15)^2 - 1.41 \times 10^{-6}(T - 273.15)^3$ is the temperature correction term. With the correction from the activity coefficient, the equilibrium dissociation (protonation) constants for chemical reactions can be calculated as following:

$$K_{1C} = 10^{-pK_{1C}(T) + p\gamma_{\text{H}^+} + p\gamma_{\text{HCO}_3^-}} \quad (\text{D.10})$$

$$K_{2C} = 10^{-pK_{2C}(T) + p\gamma_{\text{H}^+} + p\gamma_{\text{CO}_3^{2-}} - p\gamma_{\text{HCO}_3^-}} \quad (\text{D.11})$$

$$K_A = 10^{-pK_A(T) + p\gamma_{\text{H}^+} - p\gamma_{\text{NH}_4^+}} \quad (\text{D.12})$$

$$K_N = 10^{-pK_N(T) + p\gamma_{\text{H}^+} + p\gamma_{\text{NO}_2^-}} \quad (\text{D.13})$$

$$K_{sp} = 10^{-pK_{sp}(T) + p\gamma_{\text{H}^+} + p\gamma_{\text{CO}_3^{2-}} + p\gamma_{\text{Ca}^{2+}}}. \quad (\text{D.14})$$

These values are used in chemical kinetics described in Table D.3.

reaction ID	temperature dependent pK_a	reference
R(1)	$140.932 - 13446/T - 22.4773 \ln T$	Ebrahimi et al., 2003
R(2)	$3404.71/T - 14.8435 + 0.032786T$	Buhr and Miller, 1983
R(3)	$2902.39/T - 6.498 + 0.02379T$	Buhr and Miller, 1983
R(4)	$2835.76/T - 0.6322 + 0.001225T$	Buhr and Miller, 1983
R(5)	$-\log_{10}(5.6 \times 10^{-4} e^{171217(1/T - 1/298.15)})$	Su et al., 2011 ^a
R(6)	$171.90 + 0.07799T - 2839.3/T - 31.093 \ln T$	Plummer and Busenberg, 1982

TABLE D.4: Temperature dependency of acid dissociation constants used in the model.

^a Phenomenological expressions for the temperature dependency of HONO dissociation are scarce. Following Su et al., 2011, dissociation constant is theoretically calculated using the relation; $K_{a,\text{HNO}_2}(T) = K_{a,\text{HNO}_2}^\ominus \exp \left[-\frac{\Delta H_{a,\text{HNO}_2}}{R} \left(\frac{1}{T} - \frac{1}{T^\ominus} \right) \right]$.

D.3 Activity of photoautotrophs

D.3.1 Photosynthesis and dark respiration

In the main text, the growth rate of species i with limiting factor j was described as following.

$$\mu_i(\vec{r}, t) = \mu_{\max,i} f_T(\vec{r}, t) f_{pH}(\vec{r}, t) \min[f_i^1(\vec{r}, t), f_i^2(\vec{r}, t), \dots, f_i^j(\vec{r}, t)], \quad (\text{D.15})$$

where $\mu_{\max,i}$ is the maximum growth rate of species i with temperature and pH correction terms, $f_T(\vec{r}, t)$ and $f_{pH}(\vec{r}, t)$, respectively. Monod factors are in the minimum function with two types, $f_i^j = \frac{C_j}{K_{s,i}^j + C_j}$ (when nutrient j is a substrate for the growth) or $f_i^j = \frac{K_{i,i}^j}{K_{i,i}^j + C_j}$ (when nutrient j is an inhibitor for the growth) based on the stoichiometry for biomass synthesis. For the growth of phototrophs that uses light as an energy source, Monod factor of light intensity was described differently according to the photoacclimation model Bernard, 2011.

$$f(I(\vec{r})) = \frac{I(\vec{r})}{I(\vec{r}) + K_{s,I} + I(\vec{r})^2/K_{i,I}}, \quad (\text{D.16})$$

where $I(\vec{r})$ is the light intensity at the position \vec{r} , $K_{s,I}$ is the half-saturation coefficient and $K_{i,I}$ is the inhibition coefficient for light. Light inhibition and acclimation mechanisms for photosynthetic activity are considered unlike the other chemical inhibitors to describe the adaptation of pigment (chlorophyll) synthesis and the reduced yields under strong light as a function of light intensity. During the night, phototrophs maintain their biomass by dark respiration controlled by photo-inhibition term with $K_{I,ph}$. Therefore, the total growth of phototrophic organism is obtained as following:

$$\mu_i^p = \mu_{ph} + \mu_{respi} \quad (\text{D.17})$$

$$= \mu_{\max,i} \min[f_i^j, \dots, f(I(\vec{r}))] + \alpha_r \mu_{\max,i} \min[f_i^j, \dots, \frac{K_{I,ph}}{K_{I,ph} + I(\vec{r})}]. \quad (\text{D.18})$$

We note that the maximum respiration rate is linearly proportional to the rate of photosynthesis with the ratio, α_r Tillmann and Rick, 2001; Wolf, Picioreanu, and Loosdrecht, 2007. In Fig. D.1, the normalised growth of photoautotrophs is given as a function of light intensity when the other chemical substances are not limiting. For the light inhibition, $K_{I,ph} \equiv K_{s,I}$ was assumed to describe the activity switch from photosynthetic growth to dark respiration. Under weak light intensity (in a dark environment or deep in the soil domain where light cannot penetrate, i.e. $I(\vec{r}, t) < K_{s,I}$), the dark respiration process is dominant for their growth. During the dark respiration, phototrophs respire like heterotrophic aerobes. The spatio-temporal patterns of phototrophic activity is also depicted in Fig. D.1. The figure shows the temporal changes in optimal depth of phototrophic activity within the domain.

D.3.2 Nitrogen fixation and dynamic yields

The model includes nitrogen fixation by photoautotrophs (e.g. heterocystous cyanobacteria or other diazotrophic cyanobacteria) to provide a primary source of nitrogen to the biocrust

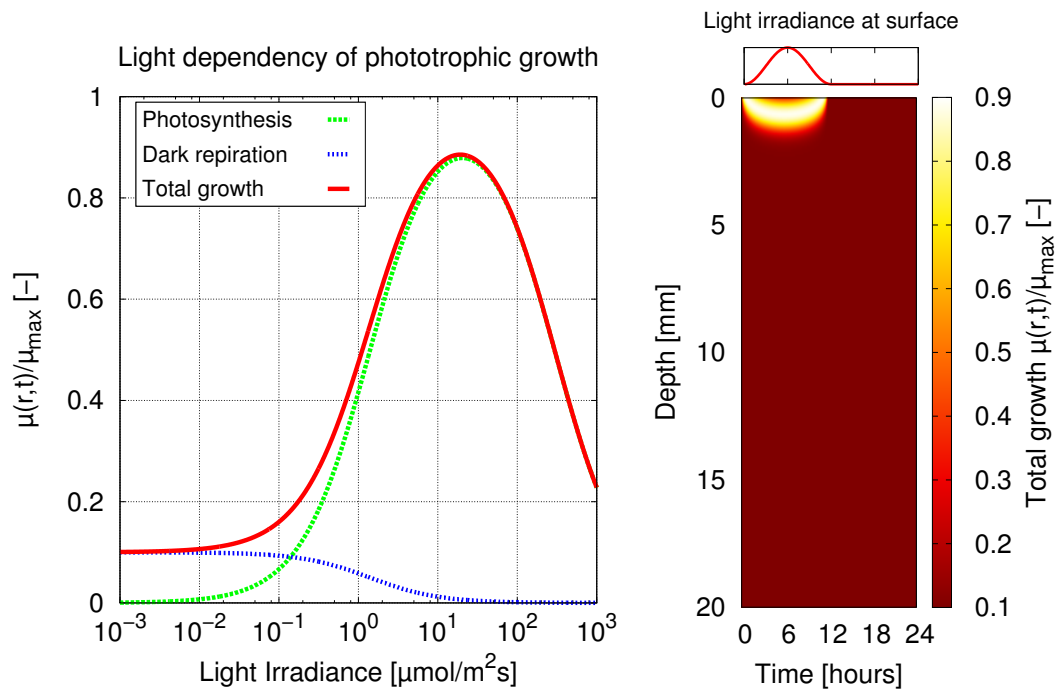


FIGURE D.1: **Activity of photoautotrophs.** (Left) The activity of photoautotrophs as a function of light intensity in the desert biocrust model when other chemical substances are not limiting. Here, the values are normalised based on the maximum growth rate. The growth of phototrophs is partitioned to two processes, photosynthesis (green dash line) and dark respiration (blue dotted line). When $I \approx K_{s,I} = 1.4 [\mu\text{mol}.\text{m}^{-2}\text{s}^{-1}]$ (in the figure), phototrophs switches its growth pattern. (Right) Spatio-temporal changes in potential activity of photoautotrophs. Due to the light decay over the depth, the phototrophic activity is localised in top 2 mm. The light inhibition at the strong light intensity results in the diel cycle of optimal depth for photosynthesis.

community. While cyanobacteria are oxygenic photosynthetic bacteria, the enzyme nitrogenase for N_2 fixation is extremely sensitive to O_2 . Therefore, cyanobacteria have developed several strategies for this by spatially or temporally separating the photosynthesis and N_2 fixation (Berman-Frank, Lundgren, and Falkowski, 2003; Stal, 2015). As the modelling studies on the nitrogen fixing rate during photosynthesis are very scarce, in this work, we propose a simple relation to couple carbon and nitrogen fixation as a dynamic stoichiometry approach.

For a simplification, photoautotrophs in the model were assumed to be heterocystous cyanobacteria taking the strategy of the spatial separation of heterocysts for N_2 fixation within the phototrophic population, which is not explicitly modelled in this study. Instead, by assuming that heterocysts already exist, a certain percentage of energy gain from photosynthesis is assigned for nitrogen fixation to produce ammonium, NH_4^+ . Considering that the heterocysts are located about every tenth cell of a filament, we assume that about 5-15 % of phototrophic biomass will perform N_2 fixation while the rests are vegetative cells providing carbohydrates as a source of electrons to heterocysts. As a whole local population (at a patch), the yield of carbohydrates (fixed C) and ammonium (fixed N) are determined following the local availability of inorganic C and N. The basic idea is that when available C/N is not balanced for photosynthesis, the net yields of carbohydrates and ammonium are adjusted as a feedback. For instance, during C and N fixation by phototrophs that utilises CO_2 and NO_3^- for photosynthesis, the net yield of substrate i at time t , $Y_{i,net}(t)$, is

$$\frac{1}{Y_{i,net}(t)} = \frac{(1 - f(t))}{Y_i^C} + \frac{f(t)}{Y_i^N} \quad (D.19)$$

$$f(t) = r_{N_2} \left[1 + \frac{1}{2} \tanh \left(1 - \frac{Y_{NO_3^-} C_{NO_3^-}(t)}{Y_{CO_2} C_{CO_2}(t)} \right) \right] \quad (D.20)$$

where Y_i^C and Y_i^N are the yields of substrate i via photosynthesis (carbon fixation) and N_2 fixation, respectively. r_{N_2} is the contribution of heterocysts for the net yield (in this work, $r_{N_2} = 0.1(10\%)$). $Y_{NO_3^-}$ [g cell/g NO_3^-] and Y_{CO_2} [g cell/g CO_2] are yields of biomass during photosynthesis (driven from the stoichiometry), in other words, these yields are the inverses of required amount of inorganic C and N in the pore water to synthesise 1 g of biomass. When the local condition was N limited, the ratio of available carbon and nitrogen sources, $\frac{C_{NO_3^-}(t)}{C_{CO_2}(t)}$, will regulate the energy expenses for C and N fixation. Here, a tangent hyperbolic function was chosen as a sigmoid curve with a bound of nitrogen fixation activity between 5-15% with the expected yield of 10% when C and N are balanced. It means that when $\frac{Y_{NO_3^-} C_{NO_3^-}(t)}{Y_{CO_2} C_{CO_2}(t)} < 1$, N is limited, thus the nitrogen fixation rate increases up to 15%.

On the other hand, when $\frac{Y_{NO_3^-} C_{NO_3^-}(t)}{Y_{CO_2} C_{CO_2}(t)} > 1$, N is not limited, thus it decreases to 5%. By using this relation, the net yields of carbohydrates (organic carbon/EPS) and the ammonium are determined based on the local condition as a result of photosynthesis and N_2 fixation. This leads to the positive feedback to the community by levelling the unbalanced C/N ratio within crusts to maximise the primary productivity. In Fig. D.2, the activity of N_2 fixation is depicted as a function of C/N ratio balance, $\frac{Y_N C_N}{Y_C C_C}$.

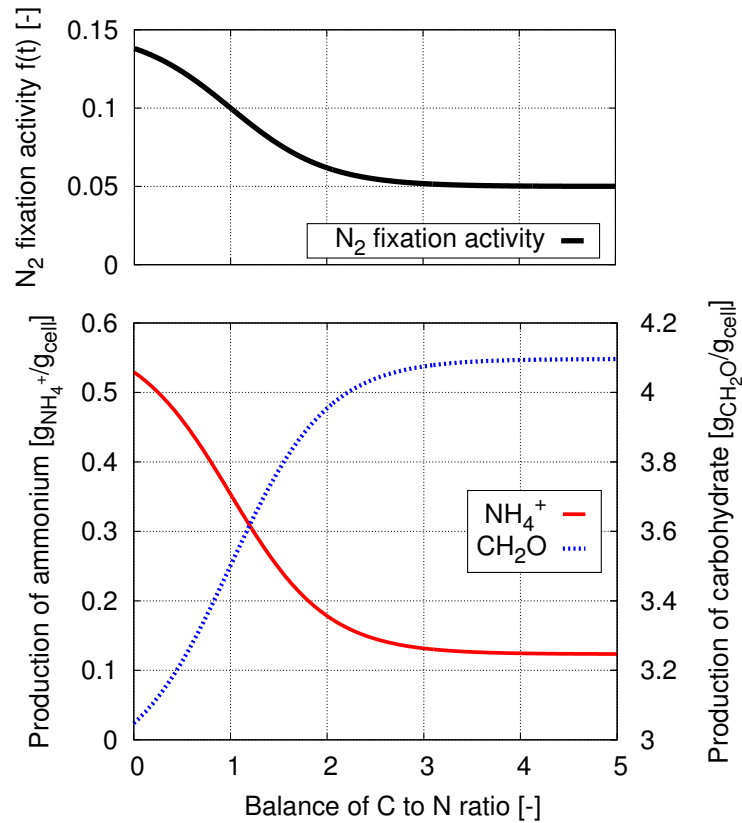


FIGURE D.2: **Modelling the relation of nitrogen fixation and photosynthesis.** (Top) N_2 fixation activity ($f(t)$ in Eq. (D.20)) is depicted as a function of C/N ratio balance, $\frac{Y_N}{Y_C} \frac{C_N}{C_C}$. When the amount of nitrogen is limiting for photosynthesis, the proportion for N_2 fixation increases up to 15%. On the other hand, when the amount of carbon is limiting to maximise photosynthesis, N_2 fixation proportion decreases to 5%. (Bottom) An example of photosynthesis- N_2 fixation regulation. Amounts of produced carbohydrates and ammonium changes depending on the balance of C/N ratio according to Eq. (D.20). In this figure, the amount is given as the inverse of the yield, which is the amount of the product while 1g of biomass is synthesised.

D.3.3 EPS production

Through photosynthesis, photoautotrophs (cyanobacteria) produce EPS increasing the soil carbon pool of biocrusts. The amount of EPS produced by cyanobacteria in drylands varies depending on their environment such as soil types or geological location Hu et al., 2002. It is challenging to predict and to describe how much and how fast EPS can be produced through microbial activity although it plays the most crucial role in the development of biocrusts (for making extreme environments like a home). It is generally accepted that EPS synthesis in cyanobacterial soil crusts is affected by changes in moisture availability and nitrogen level Mager and Thomas, 2011. The most common heterocystous cyanobacteria in biocrusts, *Nostoc* Bowker et al., 2016, were shown to produce more EPS under unbalanced C/N metabolism Otero and Vincenzini, 2004. Moreover, the amount of EPS to cyanobacterial biomass ratio can be increased in the presence of nitrogen source indicating that N metabolism influences carbohydrate yield Huang et al., 1998. Although evidences show a correlation between carbon fixation/EPS production and nitrogen fixation by heterocystous cyanobacteria, however, it is not straightforward to combine these factors in a simple mathematical model. In this current work, the amount of fixed C and N is regulated by the local availability of inorganic C/N. As we mentioned previously, coupling photosynthesis and N_2 -fixation allows to obtain the net production of carbohydrates using the dynamic stoichiometry. We assumed that the net production of carbohydrates determines the EPS production together with the local hydration condition.

When the photosynthetic growth is given as $\mu_{ph}(t)$, Eq. (D.18), the net production of carbohydrate, Δx_{CH_2O} , during Δt , can be calculated as following.

$$\Delta x_{CH_2O} = \frac{\mu_{ph}(t)}{Y_{net, CH_2O}(t)} b(t) \Delta t \quad (D.21)$$

where $\mu_{ph}(t)$ is the photosynthetic growth rate and $b(t)$ is the biomass of a phototrophic cell at time t . Here, Y_{net, CH_2O} [g cell/g CH_2O] is a net yield (from the result of balancing between carbon and nitrogen fixation) representing the amount of synthesised biomass while 1 gram of carbohydrate is produced. The produced carbohydrates are divided into EPS production and organic carbon source that are available for heterotrophs.

Extracellular carbohydrates produced during photosynthesis contribute to the formation of biopolymeric matrix and some fraction of it might not be bounded to the matrix and released to other heterotrophic organisms as available nutrients. The binding probability of the extracellular carbohydrate residues to the polymeric matrix is written as a function of EPS concentration C_{EPS} , and the saturation degree Θ , in the model:

$$f_p(C, \Theta) = \frac{1}{e^{-\frac{C_{EPS} - C_{EPS}^*}{C_{EPS}^* \Theta}} + 1} \quad (D.22)$$

where C_{EPS}^* is the gelation point for EPS as a polymeric substances. The function describes that residual carbohydrate will not be bounded to the polymeric substances anymore as soon as EPS is in a form of weak-gel (reaching C_{EPS}^*). The degree of polymer binding is

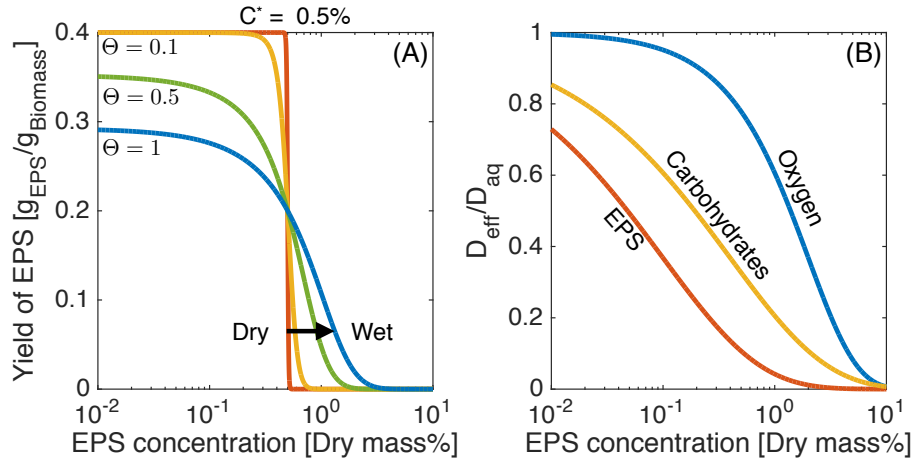
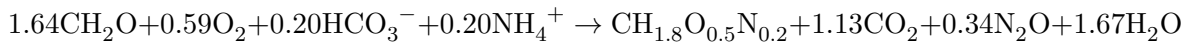


FIGURE D.3: **Modelled EPS production.** (A) The yield of EPS depends on the local EPS concentration and the hydration condition. When the concentration of EPS is higher than the gelation point ($C^* = 0.5\%$ in this figure following the gelation point of xanthan Carnali, 1991), the exopolysaccharides secreted by phototrophs will not attach to the biopolymer matrix and contributes as readily degradable carbon source for heterotrophs (during night, phototrophs also can utilise this as a source for respiration). (B) Diffusion coefficients of each substrates are determined by the concentration of EPS following Equation (11) in the main text.

regulated by the saturation degree. For example, when the domain is wet, the EPS hydrolysis will lower the binding probability of newly produced residual carbohydrates. In Fig. D.3 (A), the yield of EPS, $(Y_{\text{net, CH}_2\text{O}} - Y_{\text{intracellular, CH}_2\text{O}}) f_p(C, \Theta)$, that contributes to the polymer matrix is given. $(Y_{\text{net, CH}_2\text{O}} - Y_{\text{intracellular, CH}_2\text{O}}) (1 - f_p(C, \Theta))$ would be non-bounded organic carbon source that would be available for other organism.

D.4 Stoichiometry and rates of biological processes

Stoichiometry relations of microbial processes are given in Table D.5. Using the given set of stoichiometries, yields of chemical substances can be obtained for diffusion reaction equations. For instance, the stoichiometry of aerobic heterotrophs in the model is given as following:



In this reaction, heterotrophs use CH_2O as an electron donor, O_2 as an electron acceptor, and NH_4^+ as a nitrogen source for biomass synthesis. As 1.64 mol CH_2O is required to synthesise 1 mol $\text{CH}_{1.8}\text{O}_{0.5}\text{N}_{0.2}$ biomass, it gives the biomass yield.

$$Y_{\text{CH}_2\text{O}}^{\text{aerobes}} = \frac{1 \text{ mol } \text{CH}_{1.8}\text{O}_{0.5}\text{N}_{0.2}}{1.64 \text{ mol } \text{CH}_2\text{O}} = \frac{24.63 \text{ g}_{\text{cell}}}{1.64 \times 30.03 \text{ g}_{\text{CH}_2\text{O}}} = 0.5 [g_{\text{cell}}/g_{\text{CH}_2\text{O}}]. \quad (\text{D.23})$$

All yields of substrates can be calculated in the same manner. The reaction rate expressions for each process correspond to the microbial growth rate, Equation (9) in the main text.

Monod parameters, maximum growth rates, half-saturation coefficients, inhibition coefficients are given in Table [D.6](#) and detailed descriptions are listed in Table [D.7](#).

microbial group	process	stoichiometry
phototroph 1	photosynthesis	$4.00\text{CO}_2 + 0.19\text{NO}_3^- + 4.24\text{H}_2\text{O} + 13.9\text{H}^+ \rightarrow \text{CH}_{1.6}\text{O}_{0.4}\text{N}_{0.19} + 3.0\text{CH}_2\text{O} + 1.0\text{O}_2$
phototroph 2	photosynthesis	$4.00\text{CO}_2 + 0.19\text{NH}_4^+ + 4.27\text{H}_2\text{O} + 12.0\text{H}^+ \rightarrow \text{CH}_{1.6}\text{O}_{0.4}\text{N}_{0.19} + 3.0\text{CH}_2\text{O} + 1.0\text{O}_2$
phototroph 3	photosynthesis	$4.00\text{HCO}_3^- + 0.19\text{NO}_3^- + 4.24\text{H}_2\text{O} + 17.9\text{H}^+ \rightarrow \text{CH}_{1.6}\text{O}_{0.4}\text{N}_{0.19} + 3.0\text{CH}_2\text{O} + 1.0\text{O}_2$
phototroph 4	photosynthesis	$4.00\text{HCO}_3^- + 0.19\text{NH}_4^+ + 4.27\text{H}_2\text{O} + 16.0\text{H}^+ \rightarrow \text{CH}_{1.6}\text{O}_{0.4}\text{N}_{0.19} + 3.0\text{CH}_2\text{O} + 1.0\text{O}_2$
all phototrophs	N_2 fixation*	$5.45\text{CH}_2\text{O} + 0.19\text{HCO}_3^- + 2.93\text{N}_2 + 3.66\text{H}_2\text{O} + 5.85\text{H}^+ \rightarrow \text{CH}_{1.6}\text{O}_{0.4}\text{N}_{0.19} + 5.66\text{NH}_4^+ + 4.64\text{CO}_2$
all phototrophs	dark respiration*	$1.59\text{CH}_2\text{O} + 0.54\text{O}_2 + 0.19\text{HCO}_3^- + 0.19\text{NH}_4^+ \rightarrow \text{CH}_{1.6}\text{O}_{0.4}\text{N}_{0.19} + 0.78\text{CO}_2 + 1.27\text{H}_2\text{O}$
aerobic heterotroph	aerobic respiration*	$1.64\text{CH}_2\text{O} + 0.59\text{O}_2 + 0.20\text{HCO}_3^- + 0.20\text{NH}_4^+ \rightarrow \text{CH}_{1.8}\text{O}_{0.5}\text{N}_{0.2} + 1.13\text{CO}_2 + 0.34\text{N}_2\text{O} + 1.67\text{H}_2\text{O}$
anaerobic heterotroph	denitrification*	$2.13\text{CH}_2\text{O} + 0.88\text{NO}_3^- + 0.88\text{H}^+ \rightarrow \text{CH}_{1.8}\text{O}_{0.5}\text{N}_{0.2} + 0.84\text{CO}_2 + 1.24\text{H}_2\text{O}$
nitrifier 1 (AOB)	ammonium oxidation*	$7.63\text{O}_2 + 0.80\text{CO}_2 + 5.99\text{NH}_4^+ \rightarrow \text{CH}_{1.8}\text{O}_{0.5}\text{N}_{0.2} + 5.79\text{NO}_2^- + 5.39\text{H}_2\text{O} + 11.57\text{H}^+$
nitrifier 2 (NOB)	nitrite oxidation*	$12.77\text{O}_2 + 1\text{CO}_2 + 28.44\text{NO}_2^- + 0.80\text{H}_2\text{O} + 0.20\text{H}^+ \rightarrow \text{CH}_{1.8}\text{O}_{0.5}\text{N}_{0.2} + 28.25\text{NO}_3^-$

TABLE D.5: Stoichiometry of microbial reactions used in the model. The elemental composition of phototrophic biomass is assumed as $\text{CH}_{1.6}\text{O}_{0.4}\text{N}_{0.19}$ following a reported composition of photoautotrophic bacteria Shastri and Morgan, 2005 and the biomass composition of other cells were assumed to be the same as *E.coli*, $\text{CH}_{1.8}\text{O}_{0.5}\text{N}_{0.2}$ Grosz and Stephanopoulos, 1983. Photosynthesis was simply assumed based on stoichiometry of biomass synthesis from inorganic carbon and nitrogen sources.

* MBT-tool (Metabolism based on Thermodynamics) was used to calculate yields of chemical substrates during biomass synthesis Araujo, Gras, and Ginovart, 2016. For all reactions, the energy-transfer-efficiency between catabolism and anabolism was assumed to be 0.5.

microbial groups	μ_{\max}	$[\text{hr}^{-1}]^a$	m	$[\text{hr}^{-1}]^a$	K^{O_2}	$K^{\text{CH}_2\text{O}}$	K^{CO_2}	$K^{\text{HCO}_3^-}$	$K^{\text{NH}_4^+}$	$K^{\text{NO}_3^-}$	$K^{\text{NO}_2^-}$	K^{NH_3}	K^{HNO_2}
phototroph1	1.25		0.011				0.88		0.02 ^{ihb}	0.0744			
phototroph2	1.25		0.011				0.88		0.02				
phototroph3	1.25		0.011				0.0088 ^{ihb}	0.88	0.02 ^{ihb}	0.0744			
phototroph4	1.25		0.011				0.0088 ^{ihb}	0.88	0.02				
all phototrophs (DR)	0.125 ^b		0.011		9.60	3.41		0.88	0.02				
aerobic heterotroph	1.25		0.05		1.248 ^c	0.001 ^c		0.88	0.02				
anaerobic heterotroph	0.20		0.05		1.248 ^{ihb,c}	0.001 ^c		0.88	1.7×10^{-6}	0.0022			
nitrifier1 (AOB)	0.2125		0.019		0.5		0.88		0.90		2.96	8.23 ^{ihb}	0.03 ^{ihb}
nitrifier2 (NOB)	0.1250		0.019		0.5		0.88					0.0729 ^{ihb}	0.5036 ^{ihb}

TABLE D.6: Monod coefficients used in the model. The maximum growth rates, μ_{\max} and the maintenance rates, m in the unit of $[\text{hr}^{-1}]$. Half saturation coefficients, K_S , and inhibition coefficients, K_I are given in the unit of $[\text{mg}/\text{L}]$. Inhibition terms are marked with the superscript, *ihb*. Monod coefficients are from the activated sludge model Henze, 2000 with phototrophic activity Wolf, Picoreanu, and Loosdrecht, 2007. The coefficients for ammonia oxidiser (AOB) and nitrite oxidiser (NOB) newly assigned following Blackburne et al., 2007; Park and Bae, 2009.

^a All maximum growth rates are assumed in the model 3 times higher than literature values as the temperature and pH correction terms reducing the maximum rates.

^b Dark respiration rate was assigned as 10% of the maximum growth rate of phototrophs ($\alpha_r = 0.1$ in Eq. (D.18)).

^c Half-saturation /inhibition for oxygen and polyglucose were modified (higher oxygen inhibition for anaerobes and lower half saturation for sugar for both heterotrophs) to reflect the desert environment adaptation (highly aerated environment with lower carbon contents).

microbial group	microbial growth rate
phototroph1	$\mu_{\max,ph1} f_T f_{pH} \min \left[\frac{C_{CO_2} C_{CO_2}^-}{C_{CO_2} + K_{S,1}}, \frac{C_{NO_3}^-}{C_{NO_3}^- + K_{S,1}}, \frac{K_{I,1}^{NH_4^+}}{C_{NH_4^+} + K_{I,1}}, \frac{I}{I + K_{s,I} + I^2 / K_{i,I}} \right]$
phototroph2	$\mu_{\max,ph2} f_T f_{pH} \min \left[\frac{C_{CO_2} C_{CO_2}^-}{C_{CO_2} + K_{S,2}}, \frac{C_{NH_4^+}}{C_{NH_4^+} + K_{S,2}}, \frac{I}{I + K_{s,I} + I^2 / K_{i,I}} \right]$
phototroph3	$\mu_{\max,ph3} f_T f_{pH} \min \left[\frac{K_{I,3}^{CO_2}}{C_{CO_2} + K_{I,3}}, \frac{C_{HCO_3^-}}{C_{HCO_3^-} + K_{I,3}}, \frac{C_{NO_3}^-}{C_{NO_3}^- + K_{S,3}}, \frac{I}{I + K_{s,I} + I^2 / K_{i,I}} \right]$
phototroph4	$\mu_{\max,ph4} f_T f_{pH} \min \left[\frac{K_{I,4}^{CO_2}}{C_{CO_2} + K_{I,4}}, \frac{C_{HCO_3^-}}{C_{HCO_3^-} + K_{S,4}}, \frac{C_{NH_4^+}}{C_{NH_4^+} + K_{S,4}}, \frac{I}{I + K_{s,I} + I^2 / K_{i,I}} \right]$
all phototrophs	$\alpha_T \mu_{\max,ph} f_T f_{pH} \min \left[\frac{C_{O_2}}{C_{O_2} + K_{S,DR}}, \frac{C_{NH_4^+}}{C_{NH_4^+} + K_{S,DR}}, \frac{C_{CH_2O}}{C_{CH_2O} + K_{S,DR}}, \frac{K_{I,ph}}{K_{I,ph} + I(\tilde{r})} \right]$
aerobic heterotrophs	$\mu_{\max,ae} f_T f_{pH} \min \left[\frac{C_{O_2}}{C_{O_2} + K_{S,ae}}, \frac{C_{NH_4^+}}{C_{NH_4^+} + K_{S,ae}}, \frac{C_{CH_2O}}{C_{CH_2O} + K_{S,ae}} \right]$
anaerobic heterotrophs	$\mu_{\max,an} f_T f_{pH} \min \left[\frac{K_{I,an}^{O_2}}{C_{O_2} + K_{I,an}}, \frac{C_{NO_3^-}}{C_{NO_3^-} + K_{S,ae}}, \frac{C_{CH_2O}}{C_{CH_2O} + K_{S,an}} \right]$
nitrifier1 (AOB)	$\mu_{\max,aob} f_T f_{pH} \min \left[\frac{C_{O_2}}{C_{O_2} + K_{S,aob}}, \frac{C_{CO_2}}{C_{CO_2} + K_{S,aob}}, \frac{C_{NH_4^+}}{C_{NH_4^+} + K_{S,aob}}, \frac{K_{I,aob}^{HNO_2}}{K_{I,aob}^{HNO_2} + C_{HNO_2}}, \frac{C_{HNO_2}}{C_{HNO_2} + K_{I,aob}} \right]$
nitrifier2 (NOB)	$\mu_{\max,nob} f_T f_{pH} \min \left[\frac{C_{O_2}}{C_{O_2} + K_{S,nob}}, \frac{C_{CO_2}}{C_{CO_2} + K_{S,nob}}, \frac{C_{NO_3^-}}{C_{NO_3^-} + K_{S,nob}}, \frac{K_{I,nob}^{HNO_2}}{K_{I,nob}^{HNO_2} + C_{HNO_2}}, \frac{C_{HNO_2}}{C_{HNO_2} + K_{I,nob}} \right]$

TABLE D.7: Microbial growth rates used in the model. All growth rates are based on Equation (20) in the main text and stoichiometry for biomass synthesis based on their processes (Table D.5). Here, $f_T = \left[\frac{\frac{T}{T_0} e^{\frac{\Delta H_0}{R} \left(\frac{1}{T_0} - \frac{1}{T} \right)}}{1 + e^{\frac{\Delta H_L}{R} \left(\frac{1}{T_L} - \frac{1}{T} \right)} + e^{\frac{\Delta H_H}{R} \left(\frac{1}{T_H} - \frac{1}{T} \right)}} \right]$ and $f_{pH} = \frac{K_{pH}}{K_{pH} + [H]}$ where $K_{pH} = 10^{-5} [M]$, are temperature and pH correction terms.

D.5 Overview of parameters used in this study

Other parameters used in this study are listed in Table D.8 and Table D.9. Table D.8 summarise control parameters that are environmental specific, such as soil types, light intensity, and soil pH. Other parameters for diffusion and general properties of microbial cells are listed in Table A.2.

parameter	symbol	value	unit
Parameters for physical domain			
fractal dimension for pore size distribution	D	2.65	[-]
mean surface porosity	$\overline{\Phi}$	0.6	[-]
mean porosity	$\overline{\phi}$	0.4	[-]
size of a patch	L_p	100	[μm]
Environmental conditions			
Soil chemical property			
total amount of Ca^{2+} in the domain	$[\text{Ca}^{2+}]$	1.4	[M]
total amount of non-reactive ions in the domain	$[Z]$	1.4	[M]
Light			
maximum light irradiance	I_0	500	[$\mu\text{mol}/\text{m}^2\text{s}$]
light penetration depth	δ_p	0.2	[mm]
Temperature			
average temperature on surface	\overline{T}	25	[$^{\circ}\text{C}$]
amplitude of temperature cycle	A_0	5	[$^{\circ}\text{C}$]

TABLE D.8: Control parameters used in this study. These parameters can vary depending on soil types, location of biocrust considering the environmental conditions.

^a Property of loamy sand was assumed.

^b Alkaline soil is assumed to model desert soil. Diffusible calcium ion is assumed to buffer microbial activity and to see the biologically driven calcium carbonate precipitation. Non-diffusing non-reactive ion is applied uniformly in the domain to determine the set point of soil pH.

^c The typical value of light intensity under overcast sky has been used in this study Garcia-Pichel and Belnap, 1996. The penetration depth for the light is roughly estimated from Figure 2 in Garcia-Pichel and Belnap, 1996.

parameter	symbol	value	unit	reference
Parameters for diffusion				
diffusion coefficient of O_2	$D_0^{O_2}$	2×10^{-9}	$[m^2/s]$	Piciooreanu, Van Loosdrecht, and Heijnen, 1997
diffusion coefficient of CO_2 (aq)	$D_0^{CO_2}$	1.91×10^{-9}	$[m^2/s]$	Ebrahimi et al., 2003
diffusion coefficient of HCO_3^-	$D_0^{HCO_3^-}$	1.18×10^{-9}	$[m^2/s]$	Ebrahimi et al., 2003
diffusion coefficient of CO_3^{2-}	$D_0^{CO_3^{2-}}$	0.91×10^{-9}	$[m^2/s]$	Ebrahimi et al., 2003
diffusion coefficient of NH_4^+	$D_0^{NH_4^+}$	1.86×10^{-9}	$[m^2/s]$	Piciooreanu, Van Loosdrecht, and Heijnen, 1997
diffusion coefficient of NH_3	$D_0^{NH_3}$	1.86×10^{-9}	$[m^2/s]$	same as $D_0^{NH_4^+}$ ^a
diffusion coefficient of NO_2^-	$D_0^{NO_2^-}$	1.9×10^{-9}	$[m^2/s]$	Hirokawa, Kato, and Mafuné, 2008
diffusion coefficient of NO_3^-	$D_0^{NO_3^-}$	1.7×10^{-9}	$[m^2/s]$	Piciooreanu, Van Loosdrecht, and Heijnen, 1997
diffusion coefficient of HNO_2	$D_0^{HNO_2}$	1.9×10^{-9}	$[m^2/s]$	same as $D_0^{NO_2^-}$ ^a
diffusion coefficient of N_2O	$D_0^{N_2O}$	1.84×10^{-9}	$[m^2/s]$	Tamimi, Rinker, and Sandall, 1994
diffusion coefficient of CH_2O	$D_0^{CH_2O}$	0.6×10^{-9}	$[m^2/s]$	Stein, 1990 ^b
diffusion coefficient of EPS	D_0^{EPS}	0.12×10^{-9}	$[m^2/s]$	assumed ^c
diffusion coefficient of Ca^{2+}	$D_0^{Ca^{2+}}$	1.0×10^{-9}	$[m^2/s]$	Ilie, Loosdrecht, and Piciooreanu, 2012
Parameters for IBM				
median cell volume	\bar{V}_B	4	[fl]	Kim and Or, 2016
cell volume at division	$V_{B,d}$	$2\bar{V}_B/1433$	[fl]	in this work
minimal active cell volume	$V_{min,d}$	$\bar{V}_B/5$	[fl]	Kreft, Booth, and Wimpenny, 1998
cell density (dry mass)	ρ	290	[fg/fl]	Kreft, Booth, and Wimpenny, 1998
size of microbial cells	R	1	[μm]	Kreft, Booth, and Wimpenny, 1998
cell velocity at bulk water	v_0	1	[$\mu m/s$]	Kreft, Booth, and Wimpenny, 1998
chemotactic sensitivity	χ_0	3.6×10^{-9}	$[m^2/s]$	in this work
				continued on next page:

TABLE D.9: Parameters used in the model

^a The diffusion coefficients were assigned as their pairs for protonation. As the protonation rate is faster than the diffusion processes, the spatial distribution of these species will be mainly determined by local pH in the model. ^b Assigned with the diffusion rate of glucose. ^c Self-diffusion constant of EPS molecule is assigned as 20% of glucose diffusion.

parameter	symbol	value	unit	reference
continued from previous page:				
Other growth related parameters				
Photoacclimation model				
half-saturation coefficient for light	$K_{I,I}$	1.4	$[\mu\text{mol}/\text{m}^2\text{s}]$	Bernard, 2011
inhibition coefficient for light	$K_{S,I}$	295	$[\mu\text{mol}/\text{m}^2\text{s}]$	Bernard, 2011
photo-inhibition for respiration	$K_{I,ph}$	1.4	$[\mu\text{mol}/\text{m}^2\text{s}]$	assumed to be the same as $K_{I,I}$
Temperature dependent growth rate				
enthalpy of activation	ΔH_Θ	-5.43	$[\text{kJ}]$	Schoolfield, Sharpe, and Magnuson, 1981
enthalpy change for inactivation at low T	ΔH_L	-141.1	$[\text{kJ}]$	Schoolfield, Sharpe, and Magnuson, 1981
enthalpy change for inactivation at high T	ΔH_H	687.9	$[\text{kJ}]$	Schoolfield, Sharpe, and Magnuson, 1981
low T inactivation	T_L	297.7	$[\text{K}]$	Schoolfield, Sharpe, and Magnuson, 1981
high T inactivation	T_H	314.7	$[\text{K}]$	Schoolfield, Sharpe, and Magnuson, 1981
Decay of substances				
decay rate of the cell lysis (phototrophs)	$k_{d,ph}$	0.011	$[\text{hr}^{-1}]$	assumed
decay rate of the cell lysis (other cells)	$k_{d,others}$	0.05	$[\text{hr}^{-1}]$	assumed
EPS degradation rate	$k_{d,EPS}$	0.014	$[\text{hr}^{-1}]$	Wolf, Picioareanu, and Loosdrecht, 2007

TABLE D.9: Parameters used in the model. (Continued from previous page)

D.6 Simulated chemical environment of a fully saturated biocrusts

The chemical dynamics of a fully saturated biocrust differ considerably relative to the more common unsaturated case. A typical results based on dissolved oxygen, pH, total ammonia nitrogen, and nitrate distributions are depicted in Fig. D.4. The chemical dynamics of a fully saturated biocrust differ considerably relative to the more common unsaturated case. The supersaturation of dissolved oxygen and strong alkalisation within top 2 mm during day-time is indicative of oxygen production and inorganic carbon uptake during photosynthesis. Below 2 mm, the domain becomes anoxic due to oxygen consumption by aerobic organisms. During nighttime, in the absence of photosynthesis and oxygen production, dark-respiring phototrophs and aerobic organisms rely on diffusing oxygen from atmosphere. In the absence of inorganic carbon consumption at night, the biocrust pH drops to neutral values near 7. Total ammonia nitrogen and nitrate show complementary behaviour during day and night, indicating the activity of nitrifiers and denitrifiers. The nitrate level in fully saturated biocrust is about 2 orders of magnitude lower than an unsaturated case, indicating a strong denitrification process.

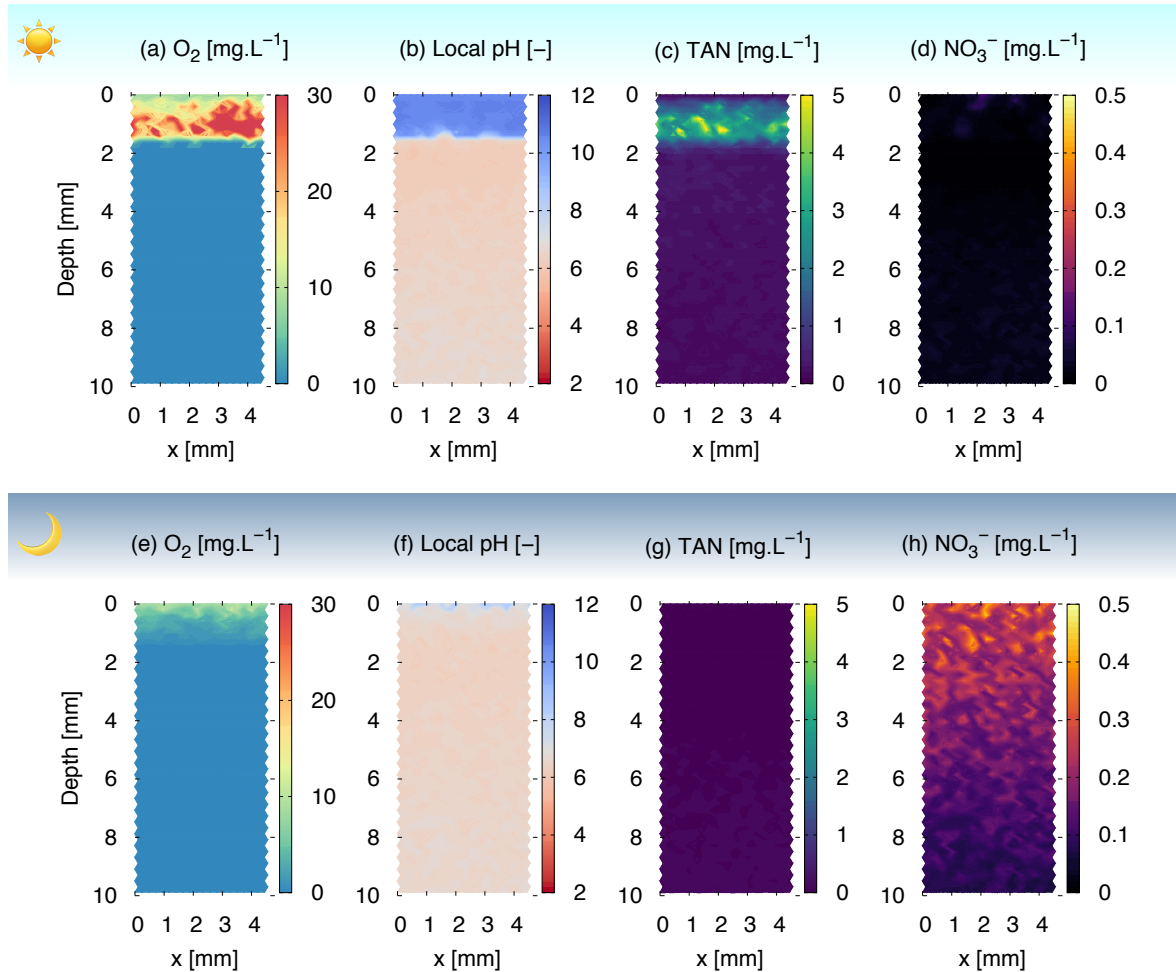


FIGURE D.4: **Diurnal distributions of chemical constituents in the unsaturated biocrust.** A typical simulated chemical profile within a fully saturated biocrust at midday (top panel) and at midnight (bottom panel). The profiles of dissolved oxygen during day (a) and night (e) are shown. During daytime, top 2 mm is supersaturated due to photosynthesis, while below 2 mm becomes anoxic. During night, most of the domain becomes anoxic due to a limited input of oxygen. (b, f) The profile of pH changes similar to the unsaturated case is shown. During day, top of the crust (within 2 mm) exhibits strong alkalisation, marked as blue. During night, pH at the top crust goes back to the similar level as below 2 mm. (c, g) Total ammonia nitrogen (TAN) increases during daytime on the top of the crust due to microbial production (N_2 fixation) and the level decreases during nighttime by microbial consumption. Nitrate profile during day (d) and night (h) shows nitrate production occurs mostly during night. The nitrate concentration drops during daytime again due to the consumption by denitrifiers.

References

- Araujo, Pablo Granda, Anna Gras, and Marta Ginovart (2016). "MbT-Tool: An open-access tool based on Thermodynamic Electron Equivalents Model to obtain microbial-metabolic reactions to be used in biotechnological process". In: *Computational and Structural Biotechnology Journal* 14, pp. 325–332.
- Berman-Frank, Ilana, Pernilla Lundgren, and Paul Falkowski (2003). "Nitrogen fixation and photosynthetic oxygen evolution in cyanobacteria". In: *Research in Microbiology* 154.3, pp. 157–164.
- Bernard, Olivier (2011). "Hurdles and challenges for modelling and control of microalgae for CO₂ mitigation and biofuel production mitigation and biofuel production". In: *Journal of Process Control* 21.10, pp. 1378–1389.
- Blackburne, Richard et al. (2007). "Kinetic characterisation of an enriched *Nitrospira* culture with comparison to *Nitrobacter*". In: *Water Research* 41.14, pp. 3033–3042.
- Bowker, Matthew A et al. (2016). "Controls on distribution patterns of biological soil crusts at micro to global scales". In: *Biological Soil Crusts: An Organizing Principle in Drylands*. Springer, pp. 173–197.
- Buhr, HO and SB Miller (1983). "A dynamic model of the high-rate algal-bacterial wastewater treatment pond". In: *Water Research* 17.1, pp. 29–37.
- Carnali, JO (1991). "A dispersed anisotropic phase as the origin of the weak-gel properties of aqueous xanthan gum". In: *Journal of applied polymer science* 43.5, pp. 929–941.
- Ebrahimi, S et al. (2003). "Rate-based modelling of SO₂ absorption into aqueous NaHCO₃/Na₂CO₃ solutions accompanied by the desorption of CO₂". In: *Chemical engineering science* 58.16, pp. 3589–3600.
- Garcia-Pichel, Ferran and Jayne Belnap (1996). "Microenvironments and Microscale Productivity of Cyanobacterial Desert Crusts¹". In: *Journal of Phycology* 32.5, pp. 774–782.
- Grosz, Ron and Gregory Stephanopoulos (1983). "Statistical mechanical estimation of the free energy of formation of *E. coli* biomass for use with macroscopic bioreactor balances". In: *Biotechnology and bioengineering* 25.9, pp. 2149–2163.
- Henze, Mogens (2000). *Activated Sludge Models ASM1, ASM2, ASM2d and ASM3*. Vol. 9. IWA Publishing.
- Hirokawa, Jun, Takehiro Kato, and Fumitaka Mafuné (2008). "Uptake of gas-phase nitrous acid by pH-controlled aqueous solution studied by a wetted wall flow tube". In: *The Journal of Physical Chemistry A* 112.47, pp. 12143–12150.
- Hu, Chunxiang et al. (2002). "Effect of desert soil algae on the stabilization of fine sands". In: *Journal of Applied Phycology* 14.4, pp. 281–292.
- Huang, Zebo et al. (1998). "Studies on polysaccharides from three edible species of *Nostoc* (Cyanobacteria) with different colony morphologies: comparison of monosaccharide compositions and viscosities of polysaccharides from field colonies and suspension cultures". In: *Journal of Phycology* 34.6, pp. 962–968.

- Ilie, Olga, Mark CM van Loosdrecht, and Cristian Picioreanu (2012). "Mathematical modelling of tooth demineralisation and pH profiles in dental plaque". In: *Journal of Theoretical Biology* 309, pp. 159–175.
- Kim, Minsu and Dani Or (2016). "Individual-based model of microbial life on hydrated rough soil surfaces". In: *PLoS ONE* 11.1, e0147394.
- Kreft, Jan-Ulrich, Ginger Booth, and Julian WT Wimpenny (1998). "BacSim, a simulator for individual-based modelling of bacterial colony growth". In: *Microbiology* 144.12, pp. 3275–3287.
- Mager, DM and AD Thomas (2011). "Extracellular polysaccharides from cyanobacterial soil crusts: A review of their role in dryland soil processes". In: *Journal of Arid Environments* 75.2, pp. 91–97.
- Otero, Ana and Massimo Vincenzini (2004). "*Nostoc* (cyanophyceae) goes nude: extracellular polysaccharides serve as a sink for reducing power under unbalanced C/N metabolism". In: *Journal of Phycology* 40.1, pp. 74–81.
- Park, Seongjun and Wookeun Bae (2009). "Modeling kinetics of ammonium oxidation and nitrite oxidation under simultaneous inhibition by free ammonia and free nitrous acid". In: *Process Biochemistry* 44.6, pp. 631–640.
- Picioreanu, C, MCM Van Loosdrecht, and JJ Heijnen (1997). "Modelling the effect of oxygen concentration on nitrite accumulation in a biofilm airlift suspension reactor". In: *Water Science and Technology* 36.1, pp. 147–156.
- Plummer, L Niel and Eurybiades Busenberg (1982). "The solubilities of calcite, aragonite and vaterite in CO₂–H₂O solutions between 0 and 90°C, and an evaluation of the aqueous model for the system CaCO₃–CO₂–H₂O". In: *Geochimica et Cosmochimica Acta* 46.6, pp. 1011–1040.
- Sander, Rolf (1999). *Compilation of Henry's law constants for inorganic and organic species of potential importance in environmental chemistry*.
- Schoolfield, RM, PJH Sharpe, and CE Magnuson (1981). "Non-linear regression of biological temperature-dependent rate models based on absolute reaction-rate theory". In: *Journal of Theoretical Biology* 88.4, pp. 719–731.
- Shastri, Avantika A and John A Morgan (2005). "Flux balance analysis of photoautotrophic metabolism". In: *Biotechnology progress* 21.6, pp. 1617–1626.
- Stal, Lucas J (2015). "Nitrogen fixation in cyanobacteria". In: *eLS*.
- Stein, WD (1990). "Channels, Carriers, and Pumps: An Introduction to Membrane Transport Academic Press". In: *New York*.
- Su, Hang et al. (2011). "Soil nitrite as a source of atmospheric HONO and OH radicals". In: *Science* 333.6049, pp. 1616–1618.
- Tamimi, A, Edward B Rinker, and Orville C Sandall (1994). "Diffusion coefficients for hydrogen sulfide, carbon dioxide, and nitrous oxide in water over the temperature range 293–368 K". In: *Journal of Chemical and Engineering data* 39.2, pp. 330–332.
- Tillmann, Urban and Hans-Josef Rick (2001). *Synthesis and New Conception of North Sea Research (SYCON): Working Group 7: Phytoplankton*. Zentrum für Meeres-und Klimaforschung.

- Wolf, Gundula, Cristian Picioreanu, and Mark van Loosdrecht (2007). "Kinetic modeling of phototrophic biofilms: The PHOBIA model". In: *Biotechnology and Bioengineering* 97.5, pp. 1064–1079.
- Yang, Aidong (2011). "Modeling and evaluation of CO₂ supply and utilization in algal ponds". In: *Industrial & Engineering Chemistry Research* 50.19, pp. 11181–11192.

Appendix E

Mechanistic Model of Biocrusts under Dynamic Hydration Conditions

E.1 Mechanistic model of biological soil crusts¹

E.1.1 Diffusion processes in the model domain

A spatially explicit model of soil profile was employed to estimate the gaseous efflux. The domain is discretised as a set of spatial elements (hexagonal patches), which represents a local property of soil structure, such as porosity and roughness following the approach of the modified rough surface patch model (Kim and Or, 2016; Št'ovíček et al., 2017; Kim and Or, 2017). At a given hydration condition, local water/gas contents can be determined and these measures shape apparent diffusion rates and mass transfer rates at the gas-liquid interface. As a collection of patches, percolation of gas phase was considered to achieve substrate concentration profiles at top soils. Gas diffusion coefficient is about 10^4 times higher than the diffusion process at the bulk liquid. Thus, we assume that at top soils (near the surface, within a few cm scale), patches that are connected to the atmosphere keep the same mixing ratios (partial pressures) as the atmosphere; therefore, the atmosphere in our model is assumed to be an infinite source. In this work, we only considered the temperature dependent air density which determines the concentration level of each gaseous substrates. Various reactions, such as photoenhanced reactions and diurnal cycles of its rate, are not considered in this model. We focused on the production of gaseous elements from soils and its release to the air from the surface.

The substrate diffusion at the aqueous phase was described as following:

$$\frac{\partial C(\vec{r}, t)}{\partial t} = \nabla \cdot (D(\vec{r}) \nabla C(\vec{r}, t)) - \text{Sink terms} + \text{Source terms} \quad (\text{E.1})$$

where $D(\vec{r})$ is the apparent diffusion coefficient defined from the effective film thickness distribution of adjacent patches and the effective diffusion coefficient including tortuosity as a function of porosity and water content using Millington-Quirk equation (Millington and

¹ We have used previously developed desert biocrust model (DBM) in this work. All the detailed information including equations and parameters are provided in Kim and Or, 2017 and the MATLAB codes are available in <https://github.com/minsughim/DBM/>. In this supplementary information, we briefly introduce and summarise a few processes, diffusion and chemical dissociations, that are especially relevant for this work.

Quirk, 1961).

$$D_{\text{eff}}(\vec{r}) = D_0 \frac{\theta(\vec{r})^2}{\phi(\vec{r})^{4/3}}, \quad (\text{E.2})$$

where D_0 is the diffusion coefficient at the bulk liquid, $\theta(\vec{r})$ and $\phi(\vec{r})$ represent the local water content and the local porosity, respectively. Thus, the net flux between two adjacent patches (for example, patch 1 and patch 2) due to diffusion is calculated as following:

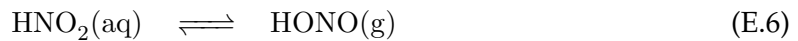
$$\vec{J}_{1 \rightarrow 2} = -\frac{2D_{\text{eff}}(\vec{r}_1)D_{\text{eff}}(\vec{r}_2)}{D_{\text{eff}}(\vec{r}_1) + D_{\text{eff}}(\vec{r}_2)} \min[d_w(\vec{r}_1), d_w(\vec{r}_2)] \frac{C(\vec{r}_2) - C(\vec{r}_1)}{|\vec{r}_2 - \vec{r}_1|} \quad (\text{E.3})$$

where d_w indicates the effective water film thickness. To calculate the flux between heterogeneous medium, we have chosen the harmonic mean of diffusion coefficient and the minimum value of water film thicknesses between neighbouring patches (for the details, see Kim and Or, 2016). In Eq. (E.1), the second and third terms on r.h.s. indicate sink and source of substrates as reaction terms. Source and sink terms are the mass transfer from gas to liquid phases, the net consumption by microorganisms, and the compensation for ionic charge neutrality from chemical reactions. Essentially, all biological, chemical reactions occur within the aqueous phase and distribution of substrates are assigned only with diffusion and mass transfer between gas and liquid phases.

E.1.2 A set of chemical reactions between gas and liquid phases

Gas-liquid partitioning under Henry's law

In this work, following gas and liquid partitionings are included;



Unsaturated soils are characterised with the large specific surface area with the thin water film thickness, thus the mass transfer can be assumed to be a very fast process and the concentration of two phases can be calculated with Henry's equilibria.

$$C^l = H_{cc}(T)C^g = k_H(T)P_g \quad (\text{E.9})$$

where C^l and C^g are concentrations in liquid and gas phases, respectively. $H_{cc}(T)$ is the dimensionless Henry's constant at temperature T ;

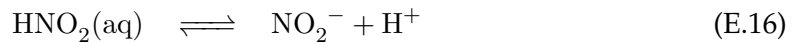
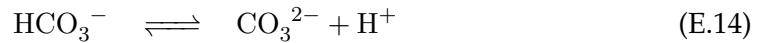
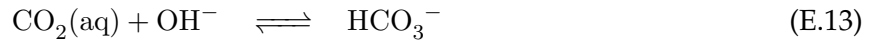
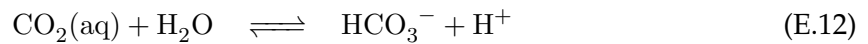
$$H_{cc} = H_{cc}^\Theta e^{-\frac{\Delta_{\text{soln}} H}{R} \left(\frac{1}{T} - \frac{1}{T^\Theta} \right)} \quad (\text{E.10})$$

where $\Delta_{\text{soln}}H$ is the enthalpy of solution, R is the gas constant, and the superscript \ominus refers to the standard condition ($T^\ominus = 298.15\text{K}$) (Sander, 1999). The Henry's constant, k_H , is defined with the partial pressure of the gaseous compound, P_g .

The partial pressure (mixing ratio) of each chemical compound in gas phase is important as it acts as a constant boundary condition in the model. Unlike the atmospheric chemistry, that aims at calculating the equilibrium gas phase concentration from the soil pH value, this proposed work focuses on the soil pore water and its local chemical reactions by assuming that the atmosphere as a well-mixed infinite source. We note that determining atmospheric level of trace gases can be tricky as it varies depending on locations and conditions when it measured. For example, the atmospheric HONO concentrations from the field measurement range from tens of parts per trillion to several parts per billion (Su et al., 2011). In this work, some values from literatures are selected as the fixed atmospheric equilibrium and used to calculate the gaseous efflux. Used values can be found in Kim and Or, 2017.

Acid-base model and local pH determination

Coupled ODEs of chemical acid-base reactions are used to determine chemical status of local water film. Local pH was calculated after net diffusions and microbial reactions with an assumption of local charge neutrality. Considered reactions in aqueous phase are



The detailed rates and the acid-base dissociation constants are given in Kim and Or, 2017. Concentration of protons, pH, was locally determined with an assumption of local charge balance via self-ionisation of water,

$$[\text{H}^+] + [\text{NH}_4^+] + 2[\text{Ca}^{2+}] + [\text{Z}^+] - [\text{OH}^-] - [\text{HCO}_3^-] - [\text{NO}_2^-] - [\text{NO}_3^-] - 2[\text{CO}_3^{2-}] = 0 \quad (\text{E.18})$$

where $[\text{H}^+][\text{OH}^-] = K_W = 10^{-14}$. By solving the differential algebraic equations, local pH values were obtained during the entire dynamics. The unknown cation, Z^+ , is considered to be non-reactive but it is added to the system for charge compensation for pH value of real soil with various minerals. Calcium is selected as a representative reactive cation that participates for inorganic carbon availability. All chemical reactions are coupled with the availability of protons at a given temperature. During the acid-base calculation, the extended Debye-Hückel equation is used for all ionic interactions.

Analytic solution of local pH under Henry's and acid-base equilibria

At the interface between the atmosphere and soil, the fast equilibration of chemical processes can determine local pH of water film. At equilibrium, constraints of gaseous compounds via Henry's law and the acid-base dissociation relations lead to

$$k_H^C P_{\text{CO}_2} = [\text{CO}_2] = \frac{[\text{HCO}_3^-][\text{H}^+]}{K_{1c}} \quad (\text{E.19})$$

$$[\text{HCO}_3^-] = \frac{[\text{CO}_3^{2-}][\text{H}^+]}{K_{2c}} \quad (\text{E.20})$$

$$[\text{CaCO}_3] = \frac{[\text{Ca}^{2+}][\text{CO}_3^{2-}]}{K_{\text{sp}}} \quad (\text{E.21})$$

$$[\text{NH}_4^+] = \frac{[\text{NH}_3][\text{H}^+]}{K_A} = \frac{k_H^A P_{\text{NH}_3}[\text{H}^+]}{K_A} \quad (\text{E.22})$$

$$k_H^N P_{\text{HONO}} = [\text{HONO}] = \frac{[\text{NO}_2^-][\text{H}^+]}{K_N} \quad (\text{E.23})$$

where k_H^C , k_H^A and k_H^N are Henry's constants of CO_2 , NH_3 and HONO , respectively. Dissociation constants are denoted with capital K for each acid-base reaction. We note that Henry's constants and dissociation constants are temperature-dependent. By substituting these relations at equilibrium to the local charge neutrality principal, Eq. (E.18) can be rewritten as following:

$$\left(1 + \frac{k_H^A}{K_A} P_{\text{NH}_3}\right) [\text{H}^+]^3 + Z_{\text{net}} [\text{H}^+]^2 - (K_W + K_N k_H^N P_{\text{HONO}} + K_{1c} k_H^C P_{\text{CO}_2}) [\text{H}^+] - 2K_{1c} K_{2c} k_H^C P_{\text{CO}_2} = 0 \quad (\text{E.24})$$

where $Z_{\text{net}} \equiv 2[\text{Ca}^{2+}] + [\text{Z}^+] - [\text{NO}_3^-]$ denotes the net charge of free cations and anions that are not constrained with gaseous compounds. The pH at equilibrium is the positive real root of the cubic polynomial. Since the partial pressures of gaseous compounds are constants in the model, concentrations of Ca^{2+} , Z^+ and NO_3^- determine the pH value. The calculated analytic solutions of pH under Henry's and acid-base equilibria for varying mixing ratios of NH_3 and HONO are plotted in Fig. E.1. For this plot, the partial pressure of CO_2 was assigned as constant, 383 ppm.

E.1.3 Estimation of gaseous efflux

The gaseous efflux dynamics is obtained simply by using Henry's law and the assumption of immediate equilibration of soil air to the same partial pressures as the atmospheric level when the spatial element is connected to the atmosphere by gas phase percolation. Basically, the amount of local gaseous efflux was calculated element-wise and using the invasion percolation, the emission from atmosphere-connected clusters is summed as the gaseous efflux. When the percolation cluster was not connected to atmosphere directly, it stays locally as the stored gas pocket in the model. This method has a benefit for the system like biocrusts in arid and semi-arid area because; firstly, it considers the sharp gradient over the shallow depth (a few cm) which cannot be estimated by gradient method; secondly,

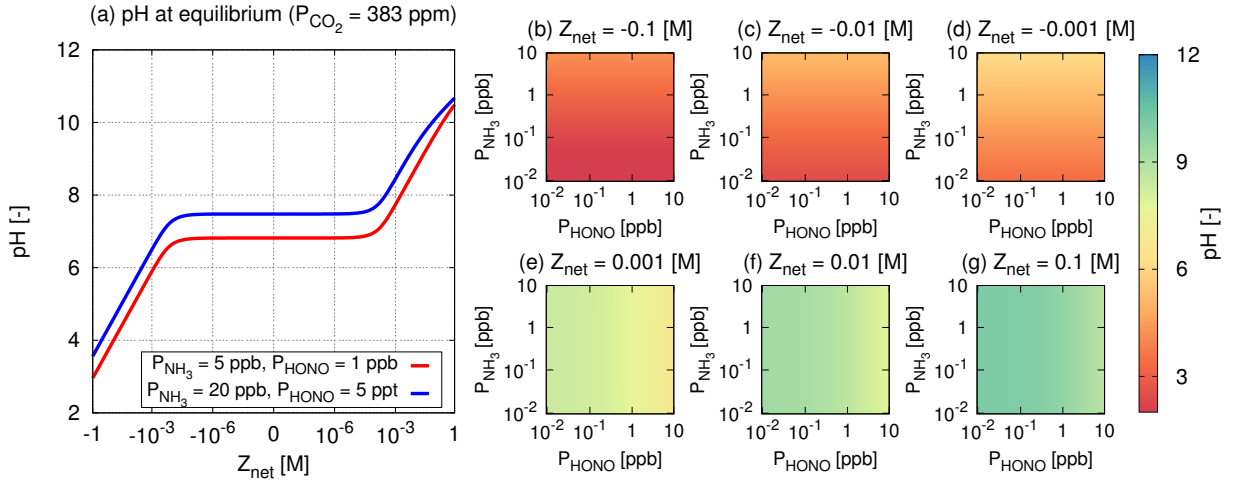


FIGURE E.1: **Analytic solutions of pH.** (a) Analytic solution of pH at Henry's and acid-base dissociation equilibria as a function of $Z_{\text{net}} \equiv 2[\text{Ca}^{2+}] + [\text{Z}^+] - [\text{NO}_3^-]$, which is a net charge of chemical compounds that are not constrained by the air. Under the condition of the constant partial pressure of CO_2 , 383 ppm, two cases are given as examples, $P_{\text{NH}_3} = 5$ ppb, $P_{\text{HONO}} = 1$ ppb (red) and $P_{\text{NH}_3} = 20$ ppb, $P_{\text{HONO}} = 5$ ppt (blue). (b-g) Analytic solution of pH as a function of P_{NH_3} and P_{HONO} for various values of Z_{net} . The results depict that Z_{net} strongly determine the local pH of water film together with partial pressure of pH dependent gaseous compounds. When cations are dominant ($Z_{\text{net}} > 0$), the solution indicates alkaline and when anions are dominant ($Z_{\text{net}} < 0$), the solution indicates acidic. This indicates that the balance between the chemical environments and the activity of microorganisms (such as production of NO_3^-) is crucial for determining local pH.

large temperature variation during diurnal cycles and temperature-dependent-solubility of gaseous elements can be included; lastly, it includes the physical structure of unsaturated soils shaping the water and gas configuration (percolation of gas phases over the soil depth) under dynamic hydration conditions.

The amount of degassed substance is solely determined by Henry's law and local mass conservation during mass transfer. The concentrations at the mass transfer equilibrium, C^{g*} (gas phase) and $C^{l*}(\vec{r}, t)$ (liquid phase), are determined as following:

$$C^{g*}(\vec{r}, t) = \begin{cases} \frac{V_l(\vec{r}, t)C^l(\vec{r}, t) + V_g(\vec{r}, t)C^g(\vec{r}, t)}{H_{cc}(T(\vec{r}, t))V_l(\vec{r}, t) + V_g(\vec{r}, t)} & \text{if } \vec{r} \notin \Omega_a \\ p(\vec{r}, t)\rho_a(T(\vec{r}, t)) & \text{if } \vec{r} \in \Omega_a \end{cases} \quad (\text{E.25})$$

$$C^{l*}(\vec{r}, t) = \begin{cases} H_{cc}(T)C^{g*}(\vec{r}, t) & \text{if } \vec{r} \notin \Omega_a \\ p(\vec{r}, t)\rho_a(T(\vec{r}, t))H_{cc}(T(\vec{r}, t)) & \text{if } \vec{r} \in \Omega_a \end{cases} \quad (\text{E.26})$$

where $V_l(\vec{r}, t)$ and $V_g(\vec{r}, t)$ are the volume of liquid and gas phases of the spatial element (a patch) at location \vec{r} at time t . Ω_a is the cluster region that are connected to the atmosphere. Here the local temperature, $T(\vec{r}, t)$, determines the local solubility and air density. From the concentrations at mass transfer equilibrium, the amount of degassed/dissolved substance can be obtained locally,

$$F(\vec{r}, t) = C^l(\vec{r}, t) - C^{l*}(\vec{r}, t). \quad (\text{E.27})$$

By integrating over the gas percolating region, total gaseous emission can be determined as

$$E_{\text{tot}}(t) = \int_{\Omega_a} F(\vec{r}, t) d\Omega_a. \quad (\text{E.28})$$

E.2 pH measurements of drying soils

E.2.1 Experimental set-up

Use of a planar optode and a microelectrode

We used two commercial devices to measure changes in pH of drying soils; (1) a planar optode sensor for pH (product code SF-HP5-OIW; Presens GmbH, Rosensburg, Germany), a camera (VisiSens detector unit DU02; Presens GmbH) and VisiSens software (PreSens GmbH), (2) a microelectrode with internal reference (PH-200C, Unisense, Aarhus, Denmark) with SensorTracePRO software (Unisense)

Sample preparation

In this study, we used a glass cube (2cm x 2cm x 2cm) filled with (1) Phosphate buffered saline (PBS) solution with agar (2% [w/v]) block or (2) different types of wet soils (desired size/texture of grains). For the planar optode, the sensor foil was glued onto the bottom of the glass cube following the manual provided by PreSens. For the PBS solution, we mixed NaH_2PO_4 and Na_2HPO_4 following the protocol of Sørensen's buffer. For the wet soils, gamma-ray sterilised quartz (0.08- 2 mm) sand were used to avoid the effect of biological activity, and other unknown chemical processes.

Control of the composition of gas phase

The glass cube was designed with a hole on one side, which can be used for inlet/outlet of the airflow to the sample. The composition of the air in the sample was controlled by injecting a gas mixture of air and carbon dioxide (CO_2). For the mixing *in situ*, we used a rotameter (product code: FL-2AB-04SA-04SA; OMEGA Engineering, Manchester, UK). The humidity of the air was controlled with a dew point generator (Product code: LI-610; LICOR, Lincoln, USA). The relative humidity of air was 20% and the flow rate was 1litre/min resulting a turn over rate of the air in the cube to be about 2 sec^{-1} .

Monitoring hydration conditions

The hydration status of the sample was monitored simultaneously by measuring weights while drying wet samples. By mapping the water loss and the water content of the sample, changes in pH can be related with the hydration status. The glass cube was filled with sand grains up to 3mm. Assuming the porosity 0.4 for the sand, at least 0.5ml of water was added to achieve a full saturation. After adding deionised water to the sample, weight of the sample and the response of planar optode and microelectrode were simultaneously recorded until the sample is completely dried.

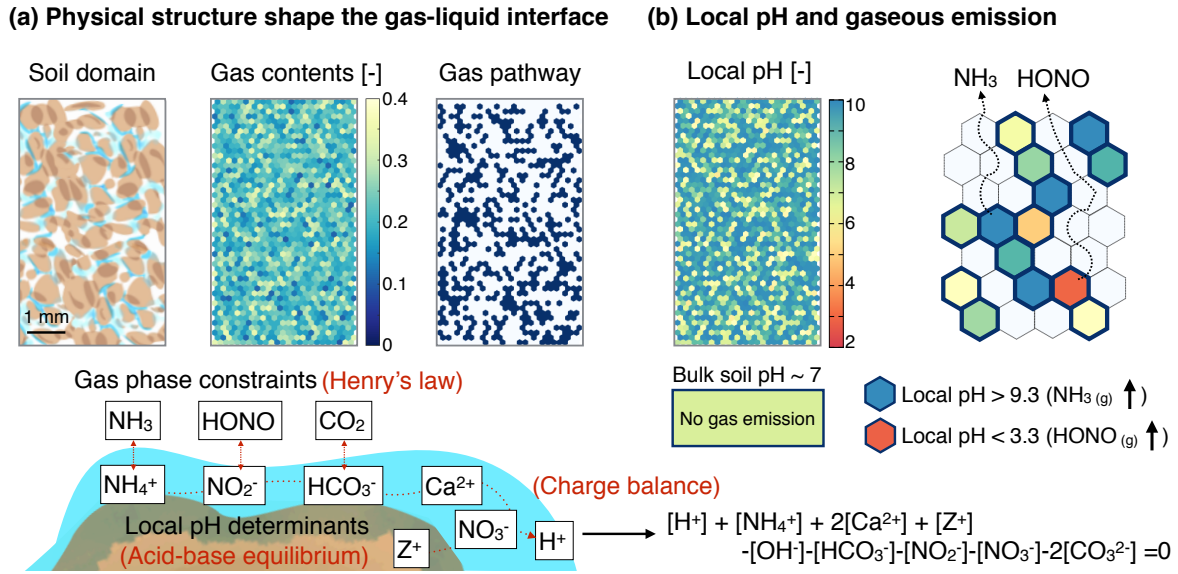


FIGURE E.2: **An example of the physical domain and the scheme for local pH calculation.** (a) Physical structure of a soil domain is abstracted and discretised to spatial elements, hexagons, to fill the domain which we termed as a patch. From the invasion percolation of gas, pathways of gaseous compounds are obtained at a certain hydration condition (In this figure, the matric potential was assigned -3 kPa, after the gas phase percolates through the domain). The connectedness of a patch to the atmosphere is given as gas pathway in white. Navy coloured patches indicate patches with air pockets that are disconnected from the atmosphere. The connectedness of gas pathways shapes the interface between soil water and air, thus constrains concentrations of gaseous compounds that affect local pH within the domain. In the model, inorganic carbon and nitrogen are considered and three principles are applied at patch scale (around $10 \mu\text{m}$), Henry's equilibria, acid-base equilibria, and local charge balance. (b) By solving diffusion equations and mass transfer between gas-liquid phases, a distribution of local pH at steady state can be calculated. Under the absence of biotic processes, the spatial variability of air-soil water interface drives the spatial heterogeneity of local pH, which cannot be captured from the bulk property, such as soil pH. The soil pH (of the entire domain) is about 7 in the figure which is calculated from the total amount of protons in the domain. When the bulk soil pH is considered, simultaneous emissions of NH_3 and HONO cannot be predicted at a static hydration condition.

E.3 Supplementary figures

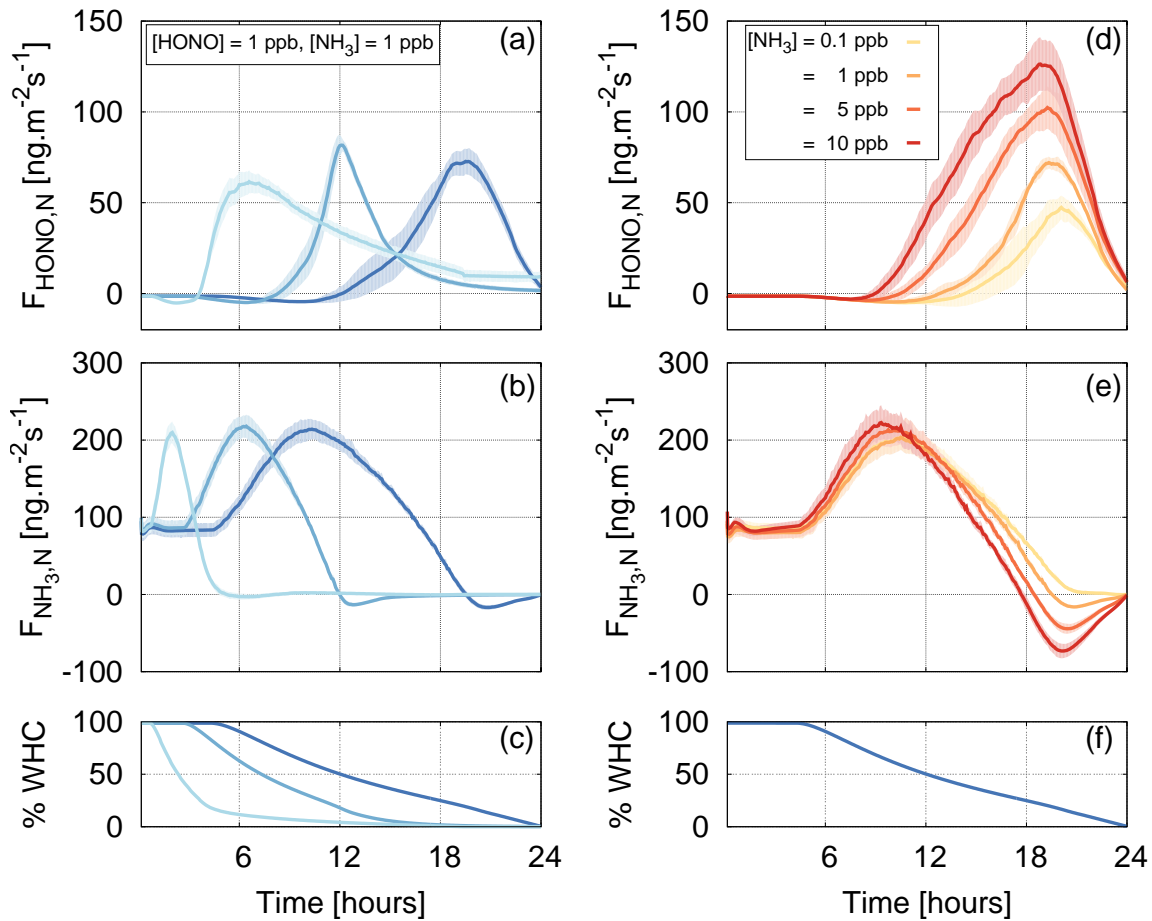


FIGURE E.3: **HONO and NH₃ emissions from simulated desiccation of biocrusts under various conditions.** Solid lines are the averages and shaded areas are 1 s.t.d. of 8 independent simulations under the same boundary conditions. (a) Dynamics of HONO emissions and (b) NH₃ emissions under (c) three different patterns of simulated drying events. Each drying event is given with the corresponding blue colour code. The stronger blue indicates the slower drying rate, thus the biocrust stays hydrated longer. During these simulations, the mixing ratios of HONO and NH₃ are fixed as 1 ppb and 1 ppb, respectively. Effects of dry NH₃ deposition on (d) Dynamics of HONO emissions and (e) NH₃ emissions during (f) a drying event are given with a spectrum of reds, the stronger red indicates higher dry deposition of NH₃. Here, the mixing ratio of HONO was fixed as 1 ppb.

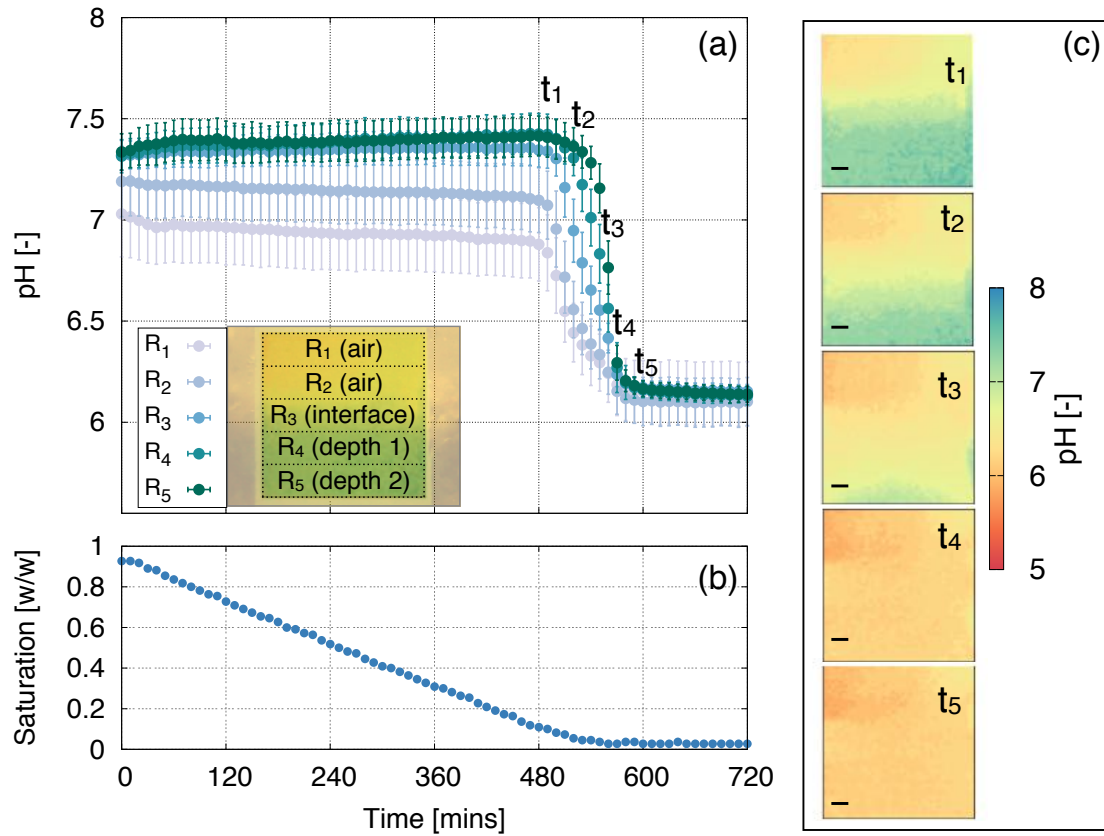


FIGURE E.4: **Vertical patterns of pH changes observed using a planar optode.** The vertical variation indicates that air entry drives acidity of the liquid phase. (a) The response of the optode sensor is analysed for 5 regions, denoted as R_1 to R_5 . From top to bottom, regions indicate air, air-soil interface, and soil. Spatially averaged pH values for each region are given during a course of the desiccation. Error bars indicate one standard deviation of spatial distributions. The inset figure shows an overlay of the sample and pH values. (b) Saturation degree of the soil sample is calculated as the weight ratio of water loss while drying to the amount of applied water. (c) Dynamics of pH distributions at the transition are given every 25 mins ($t_1 = 480, \dots, t_5 = 600$ mins). Corresponding time points are marked in figure (a). The scale bar indicates 1mm.

References

- Kim, Minsu and Dani Or (2016). "Individual-based model of microbial life on hydrated rough soil surfaces". In: *PLoS ONE* 11.1, e0147394.
- (2017). "Hydration status and diurnal trophic interactions shape microbial community function in desert biocrusts". In: *Biogeosciences* 14.23, pp. 5403–5424.
- Milington, RJ and JP Quirk (1961). "Permeability of porous media". In: *Nature* 183, pp. 387–388.
- Sander, Rolf (1999). *Compilation of Henry's law constants for inorganic and organic species of potential importance in environmental chemistry*.
- Šťovíček, Adam et al. (2017). "Microbial community response to hydration-desiccation cycles in desert soil". In: *Scientific Reports* 7.45735.
- Su, Hang et al. (2011). "Soil nitrite as a source of atmospheric HONO and OH radicals". In: *Science* 333.6049, pp. 1616–1618.

Minsu Kim

ETH Zürich

Education

- 2012-2018 **PhD in Environmental systems science**,
Department of Environmental Systems Science (D-USYS), ETH Zürich, (Switzerland).
advisor Prof. Dr. Dani Or (Soil and Terrestrial Environmental Physics (STEP), ETH Zürich)
- 2010-2012 **Erasmus Mundus Masters in Complex Systems**,
Joint master program in Complex Systems Science,
Gothenburg University/Chalmers University (Sweden), University of Warwick (UK).
- 2007-2009 **Master of Science in Physics, (statistical physics)**,
Seoul National University (Republic of Korea).
- 2003-2007 **Bachelor of Science in Physics**,
Seoul National University (Republic of Korea).

Experience

Working & Research

- 2012-2017 **Assistant researcher**, *Prof. Dr. Dani Or*, Soil and Terrestrial Environmental Physics (STEP), Department of Environmental Systems Science (D-USYS), ETH Zürich.
- 2009-2012 **Assistant researcher**, *Korea Research Foundation Project*, Project name : A study on Human Nature and the Basic Forms of Social Life from the Perspective of Consilience.
- 2009-2010 **Internship**, *Prof. Moo Young, Choi*, Seoul National University, Internship in Statistical Physics Group in Seoul National University.
- Jan., 2006 **Assistant researcher**, *Prof. Kee Hoon, Kim*, SNU- eXtreme Multifunctional Physics Lab, Research on multi-ferroic materials.

Teaching

- 2013-2015 **Teaching Assistant**, *Department of Environmental Systems Science*, ETH Zürich.
- Environmental Soil Physics/Vadose Zone Hydrology
- 2007-2008 **Teaching Assistant**, *Department of Physics and Astronomy*, Seoul National University.
- Teaching Assistant of Elementary Physics
- Teaching Assistant of Thermal and Statistical Physics

Honors

Scholarships

- 2010-2012 Erasmus Mundus Scholarship
2007-2009 Brain Korea 21 Scholarship
2003-2007 Presidential Science Scholarship

Awards

Oct. 2014 **Best Poster Award**

International SystemsX.ch conference on Systems Biology in category "Theory and Biophysical Modelling"

Effects of hydration cycles on microbial diversity in soils [5]

Sep. 2014 **Best Student Presentation**

ITES research Day 2014

Microbial biodiversity on hydrated soil surfaces [6]

Jan. 2007 **1st Prize**

KIAS (Korea Institute for Advanced Study)-SNU (Seoul National Univ.) Physics Winter Camp
Synchronization transition - Analysis on the Kuramoto model

Jan. 2006 **1st Prize**

KIAS-SNU Physics Winter Camp

Complex Network Analysis - Transport system in Seoul: Analysing the public bus system using network theory

Projects

— PHD PROJECTS (2012- 2017, SNSF, ERC SOILLIFE)

title *Linking Microbial Diversity in the Vadose Zone Hydrology with Spatial Heterogeneity, Temporally Varying Soil Surface Hydration Status and Bacterial Survival Strategy*

advisor Prof. Dr. Dani Or (ETH Zürich)

description A rough surface patch model is developed during this project [5, 9]. The model is applied to investigate effects of hydration cycles on bacteria diversity and community in desert soils [3-6,12]. The model is further developed to describe diurnal activity patterns and biogeochemical cycles of biological soil crusts [2, 11]. The mechanistic model including physical, chemical, and biological processes can quantify the role of soil hydration conditions for estimating gas emissions, such as CO₂, N₂O, and HONO [10].

— KOREAN RESEARCH FOUNDATION PROJECT (2009-2012)

title *A Study on Human Nature and the Basic Forms of Social Life from the Perspective of Consilience*

- description Participated as an assistant researcher in the interdisciplinary project on human nature. Extended the concept of information exchange to the biological and social aspect from a perspective of physics [13, 15].
- ERASMUS MUNDUS : 2ND YEAR PROJECT (2011-2012)
- title *Modelling the Spatial Spread of Wolbachia Bacteria in Mosquitoes*
- advisor Dr. Penny Hancock and Dr. Leon Danon (University of Warwick, UK)
- description Focused on the dynamics of Wolbachia infection in spatially heterogenous environments by applying mathematical techniques, from two-patch model to network model.
- ERASMUS MUNDUS :1ST YEAR PROJECT (2011)
- title *Measures for Complexity and the Two-dimensional Ising Model*
- advisor Prof. Kristian Lindgren (Chalmers University, Sweden)
- description The measure of complexity of the 2-dimensional Ising model is discussed by using the Grassberger's effective measure from information theory.
- MASTER THESIS (2008-2010)
- title *Information Exchange Dynamics of the Two-dimensional XY model*
- advisor Prof. MooYoung Choi (Seoul National University, Republic of Korea)
- description Discussion on information dynamics of the 2-dim XY model. The model is focused on information-exchange process between a system and its environment to explain evolutionary processes in biological systems [8-9,16].

Computer skills

OS	Mac OS, Linux/Unix, Windows	programming	C, Python
scientific	MATLAB, Mathematica, Gnuplot	job-related	Monte Carlo simulation, Entropic sampling algorithm, Complex network analysis, Individual based modelling, Mass transport in heterogenous media

Scientific Interests

- Soil physics
- Statistical physics
- Information theory
- Computational biology
- Complex systems science
- Microbial ecology
- Nonlinear dynamics
- Theoretical ecology
- Environmental science
- Philosophy of science

Presentations and Publications

Presentations

- [1] M Kim, and D Or. Dynamics of gaseous efflux from biological soil crusts. IBP Congress, 2017.
- [2] M Kim, and D Or. The dynamics and spatial patterns of microbial communities within desert biological soil crusts. ISME, 2016.
- [3] A Stovicek, M Kim, O Gillor, and D Or. Microbial community response to hydration desiccation cycle in desert soil. ISME, 2016.
- [4] M Kim, A Stovicek, O Gillor, and D Or. Effects of wetting-drying cycles on soil microbial diversity. IBP Congress, 2015.
- [5] M Kim, A Stovicek, O Gillor, and D Or. Effects of hydration cycles on microbial diversity in soils. In 2nd International SystemsX.ch conference on systems biology. SystemsX.ch, 2014.
- [6] M Kim, A Stovicek, O Gillor, and D Or. Microbial biodiversity on hydrated soil surfaces. In ITES rDay. ITES rDay, 2014
- [7] M Kim, G Wang, and D Or. Dynamics of microbial communities on patchy hydrated surfaces. STATPHYS25, 2013.
- [8] M Kim, and MY Choi. Information Transfer Dynamics of the Two-dimensional XY model. Korean Physical Society Meeting, 2009.
- [9] M Kim, and MY Choi. Entropy of the Two-dimensional XY model. Korean Physical Society Meeting, 2008.

Publications

- [10] M Kim and D Or. The role of localised pH on HONO and NH₃ emissions from drying soils and desert biocrusts. *in review*, 2018.
- [11] M Kim and D Or. Hydration status and diurnal trophic interactions shape microbial community function in desert biocrusts. *Biogeosciences*, <https://doi.org/10.5194/bg-2017-157>, 2017.
- [12] A Stovicek*, M Kim*, O Gillor, and D Or. Microbial community response to hydration-desiccation cycles in desert soil. *Scientific Reports* 7, 45735, 2017.
- [13] MY Choi and M Kim. Life as a complex system, In *Quantum, Information, and Life*, chapter 13, Hanwool Academy, Seoul, South Korea, 2016.
- [14] M Kim and D Or. Individual-based model of microbial life on hydrated rough soil surfaces. *PLoS ONE*, 11(1):e0147394, 2016.
- [15] MY Choi and M Kim. Physical basis of life phenomena: Self-organisation, emergence, and complexity, In *With Darwin: A Consilience Approach to Human and Society*, chapter 1, Science Books, Seoul, South Korea, 2015.

- [16] M Kim, Daun Jeong, HW Kwon, and MY Choi. Information exchange dynamics of the two-dimensional XY model. *Physical Review E*, 88(5):052134, 2013.